UNIVERSITY OF MIAMI

INVESTIGATIONS OF SUPER-LIFTING CO-FLOW JET AIRFOIL AND DISTRIBUTED ELECTRIC PROPULSION AIRCRAFT

By

Yunchao Yang

A DISSERTATION

Submitted to the Faculty
of the University of Miami
in partial fulfillment of the requirements for
the degree of Doctor of Philosophy

Coral Gables, Florida

May 2018

©2018
Yunchao Yang
All Rights Reserved

UNIVERSITY OF MIAMI

A dissertation submitted in partial fulfillment of
the requirements for the degree of
Doctor of Philosophy

INVESTIGATIONS OF SUPER-LIFTING CO-FLOW JET AIRFOIL AND DISTRIBUTED ELECTRIC PROPULSION AIRCRAFT

Yunchao Yang

Approved:

Ge-Cheng Zha, Ph.D.
Professor of
Mechanical and Aerospace Engineering

Hongtan Liu, Ph.D.
Professor of
Mechanical and Aerospace Engineering

Weiyong Gu, Ph.D.
Professor of
Mechanical and Aerospace Engineering

Guillermo Prado, Ph.D.
Dean of the Graduate School

Wangda Zuo, Ph.D.
Associate Professor of
Civil, Environmental and Architectural Engineering
University of Colorado Boulder

YANG, YUNCHAO (Ph.D., Electrical and Computer Engineering)

Investigations of Super-Lifting Co-Flow Jet Airfoil and Distributed Electric Propulsion Aircraft (May 2018)

Abstract of a dissertation at the University of Miami.

Dissertation supervised by Professor Ge-Cheng Zha.
No. of pages in text. (321)

The objective of this dissertation is to investigate the super-lifting performance of Co-Flow Jet (CFJ) flow control airfoil and its applications to electric aircraft. The CFJ airfoil is promising to transform future aircraft design with extremely short takeoff/landing (ESTOL) and ultra-high cruise efficiency due to its substantial lift enhancement and drag reduction with very low energy expenditure.

To resolve turbulent vortical structures for super-lifting CFJ airfoil flows, the improved delayed detached eddy simulation (IDDES) with high order schemes is developed and implemented in the in-house CFD code, FASIP. The high order schemes used in this study include a fifth-order weighted essentially non-oscillatory (WENO) scheme for the inviscid fluxes reconstruction and a fourth order conservative central differencing scheme for the viscous fluxes. An efficient and low diffusion E-CUSP (LDE) scheme as a Riemann solver designed to minimize numerical dissipation is utilized. The comparative study of the S-A URANS, DES, DDES, and IDDES simulation is performed on the turbulent boundary layer flows over the flat plate and the stalled flows of the NACA0012 airfoil. The validation study indicates that IDDES method can predict the law of the wall accurately for different mesh sizes, Reynolds numbers, and Mach numbers whereas the DES and DDES obtain the velocity profile

in the boundary layer with model stress depletion and log layer mismatched at certain conditions.

The 2D RANS simulation of a CFJ-NACA6421 airfoil discovers for the first time that CFJ airfoil is able to achieve the super-lift coefficient (SLC), which is defined as a lift coefficient that exceeds the theoretical limit based on potential flows. For the CFJ-NACA6421 airfoil, a maximum lift coefficient of 12.6 is achieved at the angle of attack (AoA) of 70° and jet momentum coefficient of $C_\mu = 0.60$. It is 66% higher than the theoretical limit of 7.6 for an airfoil of 21% thickness ($t/c = 0.21$). The circulation achieved around the CFJ airfoil is so large that the stagnation point is detached from the airfoil solid body and the Kutta condition does not apply anymore. For the super-lift condition at AoA of 70°, the vortex structures on the CFJ airfoil suction surface appear to have four counter-rotating vortex layers next to each other from the airfoil wall surface to the far field freestream. The 2D simulation of CFJ airfoil indicates that the C_{Lmax} appears to have no limit. The C_{Lmax} limit from the potential flows is the result of imposing Kutta condition, which is necessary for potential flows, but not a true physical condition. In reality, C_{Lmax} depends on how much energy can be added to the flow to overcome the severe adverse pressure gradient.

To further verify the super-lift coefficient and the vortical structures of the CFJ airfoil, a 3D unsteady IDDES investigation of the CFJ-NACA6421 airfoil is performed with a span length of 10% of the chord. The IDDES results verify that the CFJ airfoil is able to achieve the super-lift coefficient at ultra-high AoAs with attached flow.

The 3D steady RANS simulation of a finite-span super-lift CFJ wing is carried out with different aspect ratios (AR) without using any flaps. The RANS simulation results indicate that the CFJ wing can achieve the maximum lift coefficient of 7.8 at a

very high AoA of 70° with good aerodynamic efficiency. At high AoAs, the outer 25% wingspan is affected more by the wingtip vortex that contributes the lift reduction and drag increase. The ultra-high lift coefficient does not appear to increase the penalty of induced drag due to the negative drag at zero lift. The Oswald efficiency is increased with the AR decreased from 20 to 5 at the same AoA and C_μ. It achieves the value as high as 0.967 at AR of 5, C_μ of 0.25 and AoA of 25°, indicating that the penalty of induced drag for 3D CFJ wing is small even though ultra high lift coefficient is obtained.

Furthermore, the super-lifting CFJ flow control concept is applied to a 2D circular cylinder as a general lifting system to study the fundamental physics of the super-lifting phenomenon. The 2D RANS simulation indicates that the CFJ cylinder can achieve a maximum lift coefficient of 28 at C_μ=0.8, far exceeding the potential limit of 4π where the stagnation point is on the bottom of the cylinder. A trade study of injection and suction slot configurations is performed to obtain the optimum injection and suction slot locations.

An experimental investigation of CFJ airfoil with embedded compressors was conducted at the Low Speed Wind Tunnel of Texas A&M University. The wind tunnel experiment for the first time proves that an airfoil can achieve a lift coefficient exceeding the theoretical limit by CFJ flow control. A high thrust coefficient of the CFJ airfoil was also observed. Both the high lift and thrust are attributed to the super-suction effect with very low pressure at the airfoil leading edge induced by the injection jet. The C_{Lmax} achieved in the experiment varies from 8.0 to 8.6, substantially exceeding the theoretical limit of 7.6. A very large thrust coefficient (negative

drag) of 1.0 is achieved at low AoAs. A thrust is maintained up to the angle of attack of 40° when the airfoil is about to get stalled.

To improve the performance of the CFJ electric airplane (EA), a super-lifting CFJ takeoff airfoil and modified high-efficiency CFJ cruise airfoil are applied to the improved design, CFJ-EA2. The CFJ-EA2 wings are designed to be pivotable to take advantage of ultra-high lift coefficient at high AoA. The 3D steady RANS simulation of CFJ-EA2 at AoA of 30°, 40°, and 50° is performed using the C_μ from 0.2 to 0.6. The simulation results indicate that using the super-lifting wings, the CFJ-EA2 can achieve a maximum lift coefficient of 6.9 at a very high AoA of 50° with a good aerodynamic efficiency. For the cruise performance enhancement, an improved CFJ cruise airfoil is applied on the CFJ-EA2 to have a higher wing loading and better cruise efficiency. The cruise lift coefficient of CFJ-EA2 wings is 1.59 and the corrected aerodynamic efficiency $(L/D)_c$ is increased to 31. The productivity efficiency of $(C_L^2/C_D)_c$ is 50, which is 50% higher than CFJ-EA. The wing loading of the CFJ-EA2 airplane is increased to 214 kg/m^2. In addition to its higher MTOW of 2289 kg because of its high wing loading, the CFJ-EA2 has a range of 531 nm because more batteries are installed.

Finally, a conceptual design of CF Hybrid Electric Regional Aircraft (CFJ-HERA) is conducted. The main purpose of CFJ-HERA airplane is to use CFJ flow control and hybrid electric propulsion to achieve better fuel efficiency and higher payload than the baseline ATR72-500 regional aircraft. The CFJ-HERA airplane uses CFJ wings with an aspect ratio of 12 based on CFJ-NACA6421-INJ13-SUC20 airfoil with the original fuselage and empennage design of ATR72-500. The lift coefficient of 1.158 is achieved at AoA of 4° and C_μ of 0.02 based on a RANS simulation of the CFJ wing.

The CFJ-HERA cruises at the Mach number of 0.46 with the range of 2500 nm. The MTOW is increased to 39500 kg since the CFJ wing a high wing loading of 660 kg/m^2. The hybrid propulsion system is analyzed with various components including electric motors, inverter/converter, electric cable, and CFJ micro-compressor.

In conclusion, this dissertation demonstrates that the CFJ airfoil can achieve both the super lift coefficient during takeoff and landing and ultra-high cruise efficiency during cruise. The super-lift coefficient of CFJ airfoil with embedded micro-compressor was proved in the wind tunnel testing. It expands the high lift theory of fluid mechanics to a new area, which may foster industrial applications that are very different from today's technology. The novel CFJ aircraft design combined with the benefits of distributed electric propulsion (DEP) has the potential to transform the aviation industry.

Dedicated to my wife, my parents, and my sisters

for their love, support, encouragement and inspiration.

Acknowledgements

I sincerely express my gratitude and respect to my academic advisor, Professor Ge-Cheng Zha for his continuous academic support, invaluable comments and suggestions throughout my Ph.D. study at the University of Miami. His contagious passion inspired me all the time.

I thank my fellow students for the stimulating and useful discussions and their tremendous help, especially Dr. Jiaye Gan, Dr. Daniel Espinal, and Dr. Alexis Lefebvre. The computing resource support from the Center for Computational Sciences at University of Miami is greatly appreciated. This Defense Advanced Research Projects Agency project on the ESTOL Performance for Heavy Lift Transports is appreciated for providing resources for the investigation.

Most importantly, I would like to thank my family, especially my wife Ruogu Fang, my parents, and my sisters for sporting me throughout my PhD study and my life in general. Your support and understanding are greatly appreciated.

Yunchao Yang

University of Miami

May 2018

Table of Contents

LIST OF FIGURES **xiii**

LIST OF TABLES **xxix**

List of Symbols **xxxii**

1 INTRODUCTION **1**

1.1 Background 1

1.1.1 Market Forecasts 1

1.1.2 Sky Taxis 3

1.2 Emerging Technologies in Aviation 4

1.2.1 Hybrid Wing Body 5

1.2.2 Boundary Layer Ingestion 8

1.2.3 Distributed Propulsion 9

1.2.4 Electric/Hybrid-Electric Propulsion 12

1.2.5 Extreme Short Takeoff/Landing Performance 20

1.3 Turbulence Modeling 23

1.4 Co-Flow Jet Flow Control 24
1.5 Research Strategy 29
1.5.1 Objectives 29
1.5.2 Outline of Dissertation 30

2 OVERVIEW OF AIRCRAFT FLOW CONTROL 31

2.1 Extremely Short Takeoff and Landing 31
2.2 Maximum Lift Coefficient C_{Lmax} 33
2.2.1 Theoretical Background 33
2.2.2 Lift Coefficient Limit in Potential Flow 35
2.2.3 Flow Past an Ellipse Airfoil 38
2.3 Conventional High Lift Systems 40
2.3.1 Passive High Lift Systems 40
2.3.2 Active Lift Enhancement Systems 42
2.4 Flow Control Overview 44
2.5 High Lift Flow Control 46
2.5.1 Boundary Layer Control 46
2.5.2 Circulation Control 57
2.6 Drag Reduction Flow Control 67
2.6.1 Laminar Flow Control 69
2.6.2 Turbulent Drag Reduction 70
2.6.3 Lift-induced drag reduction 73

3 GOVERNING EQUATIONS **74**

3.1 The Navier-Stokes Equations 74

3.2 Spalart-Allmaras Turbulence Model 78

3.3 Improved Delayed Detached Eddy Simulation (IDDES) 83

3.3.1 DES 83

3.3.2 DDES 83

3.3.3 IDDES 84

4 NUMERICAL METHODOLOGY **88**

4.1 Implicit Discretization 88

4.2 Upwind Characteristics 94

4.3 The Low Diffusion E-CUSP (LDE) Scheme 99

4.4 The 5th Order WENO Scheme 103

4.5 The 4th Order Central Differencing for Viscous Terms 104

4.6 Implicit Time Integration 110

4.6.1 Implicit Time Accurate Flow Solver 110

5 CFJ AIRFOIL PARAMETERS **112**

5.1 Lift, Drag and Moment Calculation 112

5.2 Jet Momentum Coefficient 114

5.3 Power Coefficient 114

5.4 Corrected Aerodynamic Efficiency 115

5.5 Aircraft Productivity 115

6 VALIDATION OF IDDES **118**

6.1 Hybrid RANS/LES Simulation 118

6.2 IDDES Validation of the 3D Flat Plate Boundary Layer 120

6.3 IDDES Investigation of the NACA0012 Airfoil Stalled Flows 126

6.4 Conclusions 140

7 SUPER-LIFT COEFFICIENT OF 2D CFJ AIRFOIL **141**

7.1 Maximum Lift Coefficient 141

7.1.1 What is the C_{Lmax} Limit? 143

7.1.2 ESTOL Performance with Flow Control 145

7.2 CFD Simulation Setup 147

7.2.1 Boundary Conditions 148

7.2.2 Mesh 148

7.3 Results and Discussion 150

7.3.1 Maximum Lift Coefficient 152

7.3.2 Cruise Efficiency 165

7.4 Parametric Study of Super-Lift CFJ Airfoil 173

7.4.1 Effects of SST 173

7.4.2 Effects of CFJ Suction Slot Size 180

7.4.3 Effects of CFJ Injection Slot Size 183

7.4.4 Flow Field Analysis at Super-Lift Coefficient Conditions . . . 188

7.5 Conclusion 191

8 IDDES SIMULATION OF A SUPER-LIFTING CFJ AIRFOIL 194

8.1 3D IDDES Simulation of Super-Lifting CFJ Airfoil 194

8.2 Results and Discussion 195

8.2.1 Computational Mesh and Flow Conditions 195

8.2.2 CFJ wing at AoA = 62° 198

8.2.3 CFJ-NACA6421 and baseline NACA6421 flows at AoA = 18° 202

8.3 Conclusion 205

9 INVESTIGATION OF ULTRA-HIGH LIFT CFJ WING 206

9.1 3D Ultra-High Lift CFJ Wing 206

9.2 Results and Discussion 207

9.2.1 Mesh 207

9.2.2 Lift and Drag Coefficient, AR=20 208

9.2.3 High Lift CFJ Wing Flow Structures, AR=20 210

9.2.4 High Lift CFJ Wing Pressure Distribution, AR=20 211

9.2.5 Induced Drag and Tip Vortex Structures 212

9.2.6 Oswald Efficiency 213

9.3 Conclusion 216

10 INVESTIGATION OF CFJ CYLINDER 226

10.1 Maximum Lift Coefficient of a Circular Cylinder 226

10.1.1 The Co-Flow Jet Concept 229

10.1.2 Geometry and Mesh 230

10.2 Results and Discussion 232
10.2.1 CFJ Cylinder Trade Study 233
10.3 Conclusion 237

11 WIND TUNNEL TESTING OF SUPER-LIFTING AND THRUSTING CFJ AIRFOIL ACTUATED BY MICRO-COMPRESSORS 244

11.1 Motivation 244
11.2 The CFJ Airfoils 246
11.2.1 Subsonic Wind Tunnel at TAMU 247
11.3 Results and Discussion 251
11.4 Conclusion 256

12 PERFORMANCE IMPROVEMENT OF CFJ ELECTRIC AIRPLANE 259

12.1 CFJ Electric Airplane 259
12.2 Super-Lifting Performance at Takeoff/Landing 260
12.2.1 Super-lifting CFJ Wing Geometry for Takeoff/Landing 260
12.2.2 Flow Structures 262
12.3 Cruise Efficiency Improvement 266
12.3.1 CFJ Wing Geometry for Cruise 267
12.3.2 Flow Structures for Cruise Condition 268
12.4 Conclusion 270

13 CONCEPTUAL DESIGN OF CFJ REGIONAL AIRCRAFT WITH HYBRID ELECTRIC PROPULSION **272**

13.1 Overview 272

13.2 Conceptual Design Method 273

13.2.1 Conventional Propulsion 273

13.2.2 Full Electric Propulsion 274

13.2.3 Hybrid Electric Propulsion 278

13.3 CFJ Hybrid Electric Regional Airplane 282

13.4 Conclusion 290

14 CONCLUSIONS **292**

14.1 Summary 292

14.2 Conclusions 293

14.2.1 IDDES 293

14.2.2 Super-Lift Coefficient 294

14.2.3 IDDES Investigation of CFJ Super-Lift Coefficient 296

14.2.4 Study of 3D High Lift CFJ Wings 296

14.2.5 CFJ Cylinder 297

14.2.6 Wind Tunnel Experimental Study of CFJ Airfoil 298

14.2.7 Full CFJ Electric Aircraft 298

14.2.8 Hybrid Electric CFJ Aircraft 299

14.3 Summary of Contributions 299

14.4 Future Work 301
14.4.1 CFJ Development on Transonic and Supersonic Flows 301
14.4.2 Validation of CFJ Cylinder using LES/IDDES and Wind Tunnel Testing 301

APPENDIX **303**

BIBLIOGRAPHY **309**

List of Figures

1.1 NASA's global growth in aviation: opportunities and challenges [1]. . 3

1.2 NASA N3-X conceptual design with HWB configuration and turbo-electric propulsion 6

1.3 Discrete BWB airframe and the high by-pass ratio conventional aircraft [2]. 7

1.4 A partial list of various HWB concept aircraft reported recently. . . . 7

1.5 Boundary layer Ingestion concept [3] 8

1.6 The D8 conceptual aircraft 8

1.7 Distributed propulsion implementation examples summarized in [4]. 11

1.8 A historical overview of electric aircraft summarized in [5]. 13

1.9 Airbus E-Fan X demonstrator. 15

1.10 Zunum Aero hybrid electric airplane 15

1.11 Lilium Jet all electric airplane 15

1.12 NASA X-57 experimental aircraft 15

1.13 Summary of the hybrid-electric and universally-electric aircraft concepts targeting YEIS 2030+ unveiled (summarized in [5]). 16

1.14 A partial summary of electric aircraft released in 2017. 16

1.15 Various types of electric-based propulsion strategies (Turboelectric, parallel hybrid electric, series hybrid electric, and all electric) [6]. . . . 18
1.16 ESTOL runway layout [7] 21
1.17 Baseline and CFJ airfoil. 25
1.18 Attached flow of CFJ NACA 6415 airfoil at AoA=25° measured by PIV in experiment, C_μ of 0.06, M=0.1 (Plot adopted from [8]). 25
1.19 Measured drag polars of discrete CFJ airfoils at mass flow $\dot{m} = 0.06$ kg/s (Plot adopted from [8]). 26
1.20 Computed power coefficient compared with experiment at M=0.03 and $C_\mu = 0.08$ (Plot adopted from [8]). 26
1.21 The features and benefits of CFJ aircraft 28

2.1 Effect of aerodynamic lift on landing distance. [9] 32
2.2 The effect of aft airfoil on the trailing edge velocity of the front airfoil [10]. 34
2.3 Superposition of flow over a cylinder.(Plot adopted from [11]) 37
2.4 Conformal mapping from cylindrical plane (X, Z) to physical plane (x, z). (Plot is from [12]) 37
2.5 Commercial airplane high lift systems. (Plot is from [13]) 40
2.6 Typical high lift devices in use (Plot is from [14]) 41
2.7 Effect of various types of high-lift devices on airfoil section maximum lift coefficient. 41
2.8 Lift and drag enhancement using different lift enhancement devices (IBF, USB, EBF, and Vectored thrust). [15] 42
2.9 Prandtl's photograph of suction flow control of a cylinder 44

2.10 Boundary layer development on an airfoil. 46
2.11 The actuation systems implemented on the DLR F15 model and lift coefficient vesus [16] 51
2.12 Lift curves of two-element airfoil with drooped spoiler; setting optimization without and with VGJs [17]. 52
2.13 Working principle of a sweeping jet actuator internal flow [18]. . . . 52
2.14 Sweeping jet actuator arrangement on the 757 vertical tail [19] 54
2.15 Synthetic jet evolution during forward and backward motion of a diaphragm [20]. 55
2.16 Various rotating-cylinder configurations. [21] 58
2.17 Coandă effect over a cylinder over airfoil around trailing edge. 58
2.18 BLC and super-circulation regimes for CC airfoil [9] 60
2.19 Circulation control flow regimes showing sensitivities and influence of wall blowing [22] 60
2.20 Maximum Lift coefficient at different thickness/chord ratio [23] 61
2.21 Example of two Coanda surfaces. [22] 61
2.22 Lift and drag variation with C_μ at $\alpha = 0°$ [24]. 62
2.23 Equivalent Lift-Drag ratio with C_μ at $\alpha = 0°$. [24] 62
2.24 Lift results obtained at GTRI and NASA LaRC experiments. [24] . . 62
2.25 Comparison between pulsed and steady blowing circulation control [25]. 64
2.26 FAST-MAC model in high-lift mode(left), FAST-MAC model in cruise mode mounted on the sidewall (right) [26] 64

2.27 Typical result from the wind tunnel test of the FAST-MAC model (a) C_L takeoff condition at $\delta_f = 60°$, Ma = 0.10, 0.20, Re = 5 million . [27], (b) aerodynamic efficiency increments at Re = 30 million for M = 0.85. [28] 66
2.28 Boundary layer control and supercirculation control [29] 66
2.29 Breakdown of drag components. [9] 68
2.30 Hybrid Laminar Flow Concept (Reneaux, 2004). [30] 70
2.31 Wingtip modifications on existing aircraft [31]. 73

4.1 Discretization domain indicating the cell center(i,j) 89

6.1 Computational coarse and fine mesh for flat plate 121
6.2 Typical mesh size and boundary layer thickness in the test section for coarse and fine mesh, shown are simulations with Reynolds number of 20,000,000 121
6.3 Mean velocity profiles calculated at Re=1000000, comparing to the law of the wall(Mach = 0.1(top figure), 0.6(bottom figure), coarse mesh(Left figure) and fine mesh(Right figure)) 122
6.4 Mean velocity profiles calculated at Re=2000000, comparing to the law of the wall(Mach = 0.1(top figure), 0.6(bottom figure), coarse mesh(Left figure) and fine mesh(Right figure)) 123
6.5 Mean velocity profiles calculated at Re=6500000, comparing to the law of the wall(Mach = 0.1(top figure), 0.6(bottom figure), coarse mesh(Left figure) and fine mesh(Right figure)) 124

6.6 Mean velocity profiles calculated at Re=10000000, comparing to the law of the wall(Mach = 0.1(top figure), 0.6(bottom figure), coarse mesh(Left figure) and fine mesh(Right figure)) 125
6.7 Mean velocity profiles calculated at Re=20000000, comparing to the law of the wall(Mach = 0.1(top figure), 0.6(bottom figure), coarse mesh(Left figure) and fine mesh(Right figure)) 126
6.8 Distributions of $u/U_\infty, 0.002\frac{\nu_t}{\nu}, f_d, f_e$ in the flat plate boundary layer . 127
6.9 Computational meshes of NACA0012 computation 128
6.10 Calculated wall normal distance on the NACA 0012 airfoil surface. . . 128
6.11 Time-averaged lift and drag coefficients of all NACA0012 computations and comparison with experimental data. 129
6.12 Lift and drag coefficient history at AoA = 5°. 130
6.13 Time-averaged Mach contours at AoA = 5° in simulation with coarse(top) and fine(bottom) mesh. 131
6.14 Viscous and pressure drag coefficient history at AoA = 5°. 131
6.15 Lift and drag coefficient history at AoA = 17°. 132
6.16 Time-averaged Mach contours at AoA = 17° in simulation with coarse(left) and fine(right) mesh. 133
6.17 Iso-surfaces of the instantaneous Q-criterion=0, shown are the results of the S-A URANS, DDES and IDDES at AoA = 17°. 134
6.18 Lift and drag coefficient history at AoA = 45°. 135
6.19 Time-averaged Mach contours at AoA = 45° in simulation with coarse(left) and fine(right) mesh. 136

6.20 Iso-surfaces of the instantaneous Q-criterion=0, shown are the results of the S-A URANS, DDES and IDDES at AoA = 45°. 136
6.21 Mach contours at different spans in S-A URANS coarse mesh simulation at AoA = 45° 136
6.22 Mach number contours at three different spans in the IDDES coarse mesh simulation at AoA = 45° 137
6.23 Vorticity contours at three different spans in the IDDES coarse mesh simulation at AoA = 45° 137
6.24 Lift and drag coefficient history at AoA = 60°. 138
6.25 Time-averaged Mach contours at AoA = 60° in simulation with coarse(left) and fine(right) mesh. 139
6.26 Iso-surfaces of the instantaneous Q-criterion=0, shown are the results of the S-A URANS, DDES and IDDES at AoA = 60°. 139

7.1 Lift coefficient C_L vs cylinder rotating speed in the rotating cylinder experiment. (Plot is adopted from [32]) 144
7.2 Lifting cylinder using tangential blowing from surface slots. (Plot is adopted from [33]) 144
7.3 C-17 aircraft with STOL performance. 146
7.4 The double bubble concept 146
7.5 The SAX-40 concept aircraft 146
7.6 Computational mesh for CFJ calculation (AoA = 5°) 149
7.7 CFJ6421 airfoil geometry 150
7.8 Lift and Drag coefficient vs AoA for the baseline and CFJ6421-SST016-SUC053-INJ009 airfoil. 153

7.9 Aerodynamics efficiency L/D vs AoA for the baseline and CFJ6421-SST016-SUC053-INJ009 airfoil. 154
7.10 Moment coefficient C_M vs AoA for the baseline and CFJ6421-SST016-SUC053-INJ009 airfoil. 154
7.11 Corrected aerodynamic efficiency $(L/D)_c$ vs AoA for the baseline and CFJ6421-SST016-SUC053-INJ009 airfoil. 155
7.12 Corrected productivity efficiency $({C_L}^2/C_D)_c$ vs AoA for the baseline and CFJ6421-SST016-SUC053-INJ009 airfoil. 155
7.13 Power coefficient P_c for the CFJ6421-SST016-SUC053-INJ009 airfoil. 156
7.14 Total pressure ratio PR for the CFJ6421-SST016-SUC053-INJ009 airfoil. 156
7.15 The lift coefficient C_L at different C_μ for the CFJ6421-SST016-SUC053-INJ009 airfoil. 156
7.16 The jet velocity V_J/V_{inf} at different C_μ for the CFJ6421-SST016-SUC053-INJ009 airfoil. 156
7.17 Variation of C_{Lmax} with C_μ for different CFJ airfoils. 158
7.18 Variation of C_{Lmax} with V_J/V_{inf} for different CFJ airfoils. 158
7.19 Variation of C_{Lmax} with P_c for different CFJ airfoils. 158
7.20 Surface pressure coefficient C_p distribution for the baseline airfoil at AoA=18° (left) and CFJ6421-SST016-SUC053-INJ009 airfoil at AoA=70°, $C_\mu = 0.25$ and 0.35 (right). 160
7.21 Surface isentropic Mach number M_{is} distribution for the baseline(left) and CFJ6421-SST016-SUC053-INJ009 airfoil(right). 161
7.22 Static pressure distribution at $C_\mu = 0.35$ and AoA = 70° for the CFJ6421-SST016-SUC053-INJ009 airfoil. 161

7.23 Mach number contours and streamlines at the momentum coefficient C_μ = 0.25 (left) and 0.35 (right) and AoA=70° for the CFJ6421-SST016-SUC053-INJ009 airfoil. 162

7.24 Mach number contours and streamlines at C_μ = 0.35 and AoA =70° for the CFJ6421-SST016-SUC053-INJ009 airfoil. 163

7.25 Vorticity contour at $C_\mu = 0.35$ and AoA =70° for the CFJ6421-SST016-SUC053-INJ009 airfoil. 163

7.26 Sketch of the vortex distribution near the leading edge of CFJ airfoil at $C_\mu = 0.35$ and AoA =70°. 164

7.27 Lift and drag coefficient vs AoA at different C_μ for the baseline and CFJ6421-SST143-SUC133-INJ065 airfoil. 166

7.28 Drag polar at different C_μ for the baseline and CFJ6421-SST143-SUC133-INJ065 airfoil. 166

7.29 Moment coefficient C_M vs AoA at different C_μ for the baseline and CFJ6421-SST143-SUC133-INJ065 airfoil. 166

7.30 Aerodynamic efficiency (L/D) vs AoA at different C_μ for the baseline and CFJ6421-SST143-SUC133-INJ065 airfoil. 166

7.31 Corrected aerodynamic efficiency $(L/D)_c$ vs AoA at different C_μ for the baseline and CFJ6421-SST143-SUC133-INJ065 airfoil. 167

7.32 Corrected productivity efficiency $({C_L}^2/C_D)_c$ vs AoA at different C_μ for the baseline and CFJ6421-SST143-SUC133-INJ065 airfoil. 167

7.33 Power coefficient P_c vs AoA at different C_μ for the CFJ6421-SST143-SUC133-INJ065 airfoil. 168

7.34 Total pressure ratio PR vs AoA at different C_μ for the CFJ6421-SST143-SUC133-INJ065 airfoil. 168
7.35 Surface pressure coefficient C_p (left) and isentropic Mach number M_{is} (right) distribution for the baseline and CFJ6421-SST143-SUC133-INJ065 airfoil at C_μ=0.04 and AoA = 6°, 10°. 170
7.36 Mach number contours at AoA = 6°, 10° for baseline(bottom) and CFJ6421-SST143-SUC133-INJ065 airfoil(top). 171
7.37 Static pressure contours at AoA = 6°, 10° for baseline(bottom) and CFJ6421-SST143-SUC133-INJ065 airfoil(top). 172
7.38 Lift coefficient vs AoA at different SSTs (SST016, SST026, SST057). 174
7.39 Drag coefficient vs AoA at different SSTs (SST016, SST026, SST057). 174
7.40 Power coefficient for CFJ6421 at different SSTs (SST016, SST026, SST057). 175
7.41 Normalized jet velocity for CFJ6421 at different SSTs (SST016, SST026, SST057). 176
7.42 Corrected aerodynamic efficiency for CFJ6421 at different SSTs (SST016, SST026, SST057). 177
7.43 Lift and drag coefficient C_L , C_D vs C_μ at AoA = 70°. 178
7.44 P_c, L/Dc, and C_L^2/C_{Dc} vs C_μ at AoA = 70°. 178
7.45 Mach contours of for CFJ6421-SST016 airfoil with AoA=70° at different $C_\mu = 0.20, 0.25, 0.35$. 179
7.46 Productivity efficiency C_L^2/C_{Dc} vs AoA at different SSTs. 179
7.47 The correlation between the maximum lift coefficient and jet velocity. 179

7.48 Modified suction slot size geometry from the CFJ6421-SST016 airfoil, (SUC018 (original), SUC036 (2×), SUC053 (3×)). 180
7.49 Lift and drag coefficient at different suction slot sizes CFJ airfoils (SUC018, SUC036, SUC053). 181
7.50 Aerodynamic efficiency $(L/D)_c$ (left) and productivity efficiency coefficient C_L^2/C_{DC} (right) at different suction slot sizes CFJ airfoils (SUC018, SUC036, SUC053). 181
7.51 Mach contours and streamlines of suction slot at different suction slot sizes (SUC018, SUC036, SUC053) ($C_\mu = 0.25$, AoA=70°). 182
7.52 C_{Lmax} at different suction slot size with C_μ at AoA = 70°. 183
7.53 C_{Lmax} at different suction slot size with C_{JK} at AoA = 70°. 183
7.54 The modified CFJ6421-SST016-SUC053 airfoil geometry of enlarged injection slot sizes. (INJ009 (original), INJ018 (2×), INJ027 (3×), INJ055 (6×)). 184
7.55 Lift and drag coefficient for the different CFJ airfoils with different injection slot sizes (INJ018, INJ027, INJ055). 185
7.56 Aerodynamic efficiency $(C_L/C_D)_c$ (left) and productivity efficiency $(C_L^2/C_D)_c$ (right) at different injection slot sizes CFJ airfoils (INJ018, INJ027, INJ055). 186
7.57 C_{Lmax} with different injection slot sizes. (INJ009, INJ018, INJ027) . . 187
7.58 Normalized jet velocity with different injection slot sizes (INJ009, INJ018, INJ027). 187
7.59 Static pressure contour and streamlines at $C_\mu = 0.35$. 188
7.60 Vorticity contour at $C_\mu = 0.25$, 0.35 and AoA =70°. 189

7.61 Vorticity contour at the LE for $C_\mu = 0.25$ and 0.35 and AoA =70°. . 190

8.1 Computational mesh for IDDES calculation 196

8.2 Lift and drag coefficient history at AoA = 62 ° and $C\mu = 0.5$. 199

8.3 The time-averaged and instantaneous streamlines and Mach number contours at AoA = 62 ° and $C_\mu = 0.5$. 199

8.4 Comparison of time-averaged Mach number distribution for different jet momentum coefficient C_μ. 200

8.5 Turbulent flow structures of instantaneous flow field using iso-surface of Lambda-2 criterion colored by Mach number for the CFJ wing with different C_μ. 201

8.6 Multiple leading edge vortex layers at $C_\mu = 0.5$ and AoA = 62° . . . 202

8.7 Lift and drag coefficient history for the baseline NACA6421 wing at AoA = 18° 203

8.8 Instantaneous Mach number contour with streamlines and vorticity visualized by the Q=5 criterion for the baseline NACA6421 wing at AoA = 18° 204

8.9 Instantaneous turbulent flow structures represented by Lambda-2 criterion λ_2=-100 colored by the Mach number 204

8.10 Mach number contour and streamlines for CFJ6421 wing at AoA = 18° and C_μ=0.25 204

9.1 Computational mesh 217

9.2 Lift and drag coefficient of 3D CFJ wing and 2D airfoil 218

9.3 Three-dimensional streamlines on CFJ wing with finite span 218

9.4 Mach number contours at AoA=25° and C_μ=0.25 218

9.5 Mach number contours at AoA=45° and C_μ=0.25 219
9.6 Mach number contours at AoA=70° 219
9.7 Pressure contours of different spanwise crosssection at AoA=25° and C_μ=0.25 220
9.8 Pressure contours of different spanwise crosssection at AoA=45° and C_μ=0.25 220
9.9 Pressure contours of different spanwise crosssection at AoA=70° and C_μ=0.25 221
9.10 streamlines near the wing tip showing the interaction of CFJ and tip vortex 221
9.11 Pressure distribution on the wing surface at 3 angles of attack. 221
9.12 Pressure coefficient C_p at different span at the AoA of 25 °, 45 °, and 70 °. 222
9.13 Isentropic Mach number M_{is} at different span at the AoA of 25 °, 45 °, and 70 ° 222
9.14 Iso-pressure surfaces at the wing-tip 222
9.15 Vorticity magnitude distribution at different location of x/chord = 1, 3, 5, and 7. 223
9.16 Pressure distribution at different crosssection of x/chord = 1, 3, 5, and 7. 223
9.17 Spanwise vorticity ω_z and streamlines at the wingtip 224
9.18 Induced drag coefficient C_{Di} vesus C_L^2 (left) and vesus AR (right). . . 224
9.19 Oswald efficiency e_0 vesus aspect ratio AR. 225

10.1 Flow field around a rotating cylinder. (Figures are adapted from reference [11] 227
10.2 Rotating cylinder application examples, rotor airplane concept(left) and sailing boat(right).(Figures are adapted from [34]) 228
10.3 Lifting cylinder using tangential blowing from surface slots. (Plot is adopted from [33]) 228
10.4 Lift coefficient C_L vs cylinder rotating speed in the rotating cylinder experiment. (Plot is adopted from [32]) 228
10.5 Baseline airfoil and CFJ airfoil. 229
10.6 Mach number contours and streamlines at $C_\mu = 0.35$ and AoA =70° for the CFJ6421-SST016-SUC053-INJ009 airfoil. 229
10.7 CFJ flow control illustration on circular cylinder 231
10.8 Computational mesh for CFJ cylinder calculation. 238
10.9 Pressure coefficient plotted as a function of the azimuth angle for one semi-circle of the cylinder's surface 239
10.10streamlines of steady state RANS results for the stationary cylinder flow 239
10.11Lift and drag coefficient vs C_μ for the cylinder with CFJ flow control at different suction locations. 239
10.12Aerodynamic efficiency C_L/C_{Dc} vesus C_μ 240
10.13Productivity efficiency C_L^2/C_{Dc} vesus C_μ 240
10.14Power coefficient C_L vs C_μ 240
10.15Pressure ratio PR vs C_μ 240
10.16The Mach number and streamlines at the jet momentum coefficient C_μ of 0.2, 0.3 and 0.5 241

10.17Mach contours and streamlines at $C_\mu = 0.6$ 241
10.18Pressure distribution at different suction configurations 242
10.19Lift and drag coefficient with different suction slot sizes 242
10.20Lift and drag coefficient with different injection location 242
10.21Lift and drag coefficients with different injection slot sizes 243

11.1 Mach number contours and streamlines at $C_\mu = 0.35$ and AoA =70° for the CFJ-NACA6421 airfoil. 245
11.2 Vorticity contour at $C_\mu = 0.35$ and AoA =70° for the CFJ-NACA6421 airfoil. 245
11.3 Schematic view of the LSWT at TAMU. 248
11.4 Photo of the tested CFJ-NACA-6421 airfoil with 5 micro-compressors embedded. 252
11.5 Sketch of the CFJ airfoil with the micro-compressor and the suction and injection duct. 252
11.6 Photo of the CFJ-NACA-6421 airfoil tested. 255
11.7 Photo of the baseline NACA 6421 airfoil tested. 255
11.8 Lift coefficient of the cruise CFJ and baseline airfoil vs AoA. 257
11.9 Drag coefficient of the cruise CFJ and baseline airfoil vs AoA. 257
11.10Pitching Moment coefficient of the cruise CFJ and baseline airfoil vs AoA. 257
11.11Lift coefficient of the TOL CFJ and baseline airfoil vs AoA. 257
11.12Drag coefficient of the TOL CFJ and baseline airfoil vs AoA. 257
11.13Pitching Moment coefficient of the TOL CFJ and baseline airfoil vs AoA. 257

11.14Lift coefficient of the Super-Lift CFJ airfoil and baseline airfoil vs AoA. 258
11.15Drag coefficient vs AoA. 258
11.16Pitching Moment coefficient vs AoA. 258

12.1 The original design of CFJ-EA isometric view [35]. 260
12.2 CFJ-EA with rotatable wing 261
12.3 Mesh topology at AoA = 50° 261
12.4 The streamlines of CFJ-EA at AoA = 50° and C_μ of 0.5 263
12.5 Mach number contours with streamlines 264
12.6 Pressure coefficient C_p distribution at different wingspan for the AoA of 50° and C_μ of 0.50. 264
12.7 The pressure contour at the wing root between the fuselage and CFJ wing 265
12.8 Pressure distribution on the surface of CFJ wing and fuselage 265
12.9 The modified design of the CFJ-EA2 cruise airfoil. 266
12.10Lift, drag and power coefficient of the baseline, CFJ-EA, CFJ-EA2 at cruise. 268
12.11Aerodynamic and Productivity efficiency of the baseline, CFJ-EA, CFJ-EA2 at cruise. 269
12.12Mach number contours for the CFJ-EA and CFJ-EA2 airfoils 269
12.13Pressure contours for the CFJ-EA and CFJ-EA2 airfoils 270
12.14C_p distribution at different wingspan for the AoA of 5° and C_μ of 0.04. 270
12.15Mach number and pressure distributions along the CFJ-EA2 wing. . . 271

13.1 Volume and mass specific energy characteristics of different energy storage systems [36] 275

13.2 The Mass and equivalent energy density of propulsion systems providing a shaft power of 50 kW for 2 hours [36]. (E*: the equivalent energy density) 277
13.3 Typical on-board conversion chains with typical component efficiencies and total chain efficiency [36]. 278
13.4 Diagram of series hybrid electric propulsion 279
13.5 The isometric view and dimension of ATR72 regional airliner [37]. . 284
13.6 CFJ-HERA regional airliner. 285
13.7 The weight decomposition of a conventional and CFJ airliner with hybrid electric propulsion 287
13.8 CFJ-HERA wing with Micro-compressors 287
13.9 Pressure coefficient C_p and isentropic Mach number Ma_{is} of the CFJ-HERA wing at AoA of 4° and C_μ of 0.02. 289
13.10 The Mach number and pressure contour of the CFJ-HERA wing . . . 289
13.11 Pressure coefficient C_p and isentropic Mach number Ma_{is} of the CFJ-HERA wing at AoA of 30° and C_μ of 0.4. 290
13.12 The Mach number and pressure contours of the CFJ-HERA wing at the takeoff condition 290

1 Diagram of series hybrid electric propulsion 304

List of Tables

1.1 NASA N+3 metrics 5

1.2 ESTOL regional aircraft requirement [38] 22

1.3 CESTOL aircraft operating characteristics [39] 23

4.1 The coefficients of C_l^I 107

4.2 The coefficients of D_l^I 107

4.3 The coefficients of C_l^c 108

6.1 Computational parameters for the flat plate validation 120

6.2 Simulation cases setup for NACA0012 127

7.1 Mesh for CFJ 6421 airfoil calculation 149

7.2 Mesh independence study for the baseline NACA6421 airfoil at AoA=5° 150

7.3 Mesh independence study for the CFJ6421 SST016-SUC053-INJ009 airfoil at AoA=70° and $C_\mu = 0.25$ 150

7.4 CFJ6421 airfoil geometry parameters for takeoff/landing and cruise condition 151

7.5 Takeoff/Landing simulation parameters 152

7.6 Cruise simulation parameters 165

7.7 Comparison of parameters for baseline and CFJ airfoils at the best aerodynamic efficiency point $(L/D)_{c_{max}}$. (CFJ pumping efficiency η =100%) 168
7.8 Comparison of parameters for CFJ airfoils at the best aerodynamic efficiency point $(L/D)_{c_{max}}$. (CFJ pumping efficiency η =80%) 169
7.9 CFJ airfoils geometry with various SST, injection and suction slot sizes 173

8.1 Computational parameters for IDDES study of CFJ6421 airfoil 196
8.2 Mesh details for CFJ6421 airfoil 197
8.3 CFJ-NACA6421 airfoil geometry parameters for takeoff/landing and cruise condition 197
8.4 Takeoff/Landing simulation parameters 198
8.5 Time-averaged simulation results 198
8.6 Time-averaged simulation results of NACA6421 airfoil 203

9.1 Computational parameters 3D CFJ wing 207
9.2 Mesh details for the CFJ Wing 208
9.3 Mesh independence study for the CFJ6421 wing at AoA=45° and C_μ=0.15. 208
9.4 Lift and drag coefficients at different angle of attacks 209
9.5 The zero-lift drag coefficient C_{D0} at different C_μ. 214
9.6 Oswald efficiency e_0 calculated for the finite CFJ wing 215

10.1 Geometry parameters for the CFJ cylinder. 232
10.2 Grid size distribution CFJ cylinder 232
10.3 Simulation parameters for CFJ cylinder 233

11.1 CFJ6421 airfoil geometry parameters for takeoff/landing and cruise condition 247
11.2 Wind Tunnel Testing Conditions 251

12.1 Takeoff/Landing simulation parameters 261
12.2 Simulation results for CFJ-EA at the takeoff condition 262
12.3 Design parameters for the CFJ-EA2. 267
12.4 CFJ-EA2 wing design. 267
12.5 CFJ-EA2 overall performance. 267

13.1 Comparison of ATR72-500 and CFJ-HERA regional turboprop airliner mission performance 286
13.2 Weight decomposition of CFJ regional aircraft electric propulsion . . 288
13.3 The cruise parameters for CFJ Regional Aircraft 288

List of Symbols

a, c	speed of sound, $\sqrt{\gamma p/\rho}$
A, B, C	Jacobian matrix of inviscid flux $\mathbf{E}, \mathbf{F}, \mathbf{G}$ in ξ, η, ζ direction
C	speed of sound in generalized coordinates, $c\sqrt{l_\xi^2 + l_\eta^2 + l_\zeta^2}$
$\mathbf{C}$	absolute velocity vector
C_D	Drag coefficient
C_{DES}	DES coefficient, 0.65
C_L	Lift coefficient
C_{Lmax}	Maximum lift coefficient
C_m	Pitch moment coefficient
C_p	specific heat capacity at constant pressure
C_x, C_θ, C_r	absolute velocities in x, θ, r direction
C_t	tip chord of the compressor rotor
d	distance from the closest wall
$\tilde{d}$	length scale of DES, $min(d, C_{DES}\Delta)$
dQ	head added to system
dW	total work done of the system
dE	change in total energy of system
D	source term of Navier-Stokes equations in generalized coordinates

$\mathbf{E}, \mathbf{F}, \mathbf{G}$	inviscid flux vectors in ξ, η, ζ direction
e	total energy per unit mass
$\mathbf{e}_x, \mathbf{e}_y, \mathbf{e}_z$	unit normal vector in reference xyz
$\mathbf{F}$	sum of fluid force acting on the structure or on a finite control volmue
$\mathbf{F}_b$	body force acting on a finite control volmue
$\mathbf{F}_s$	surface force acting on a finite control volmue
I	identity matrix
I_o	rothalpy
J	Jacobian of the coordinate transformation, $\frac{\partial(\xi,\eta,\zeta)}{\partial(x,y,z)}$
L	reference or characteristic length
$\mathbf{l}, \mathbf{m}, \mathbf{n}$	normal vector on ξ, η, ζ surface with its magnitude equal to the elemental surface area and pointing to the direction of increasing ξ, η, ζ
l_t	grid moving velocity
L, M, N	Jacobian matrix of viscous flux $\mathbf{R}, \mathbf{S}, \mathbf{T}$ in ξ, η, ζ
$\mathbf{M}, \mathbf{C}, \mathbf{K}$	vibration mass, damping, stiffness matrices
m	pseudo time marching step
M_∞	reference Mach number, $\frac{V_\infty}{a_\infty}$
M_ξ	contravariant Mach number in ξ direction, $M_\xi = \frac{U}{C}$
n	physical time marching step
N_B	number of blade
N_D	number of nodal diameter
p, P	static pressure
p_o, P_o	total pressure
$\bar{p}_o, \bar{P}_o$	pitchwise mass averaged total pressure

Pr	Prandtl number
Pr_t	turbulent Prandtl number
$\mathbf{Q}$	conservative variable vector
q_k	total heat flux in Cartesian coordinates
R	gas constant
$\mathbf{R}, \mathbf{S}, \mathbf{T}$	viscous flux vectors in ξ, η, ζ direction
R_e	Reynolds number, $\frac{\rho_\infty V_\infty L_\infty}{\mu_\infty}$
R_o	Rossby number, $\frac{\Omega L_\infty}{V_\infty}$
S	Wing span length
S_v	S-A turbulence model source term
T	static temperature, or period
$\mathbf{T}$	surface stress vector, $\sigma \cdot \mathbf{n}$
T_o	total temperature
t	time
U, V, W	contravariant velocities in ξ, η, ζ direction
V_∞	freestream reference velocity
u, v, w	relative velocities in x, y, z direction
u^+	dimensionless velocity, u/u_τ
u_τ	friction velocity, $\sqrt{\tau_w/\rho}$
$\mathbf{V}$	relative velocity vector
V	cell volume
x, y, z	cartesian coordinates in moving frame of reference
X, Y, Z	cartesian coordinates in fixed frame of reference
y^+	dimensionless wall normal distance, $\frac{u_\tau y}{\nu}$

- Greek Symbols -

θ, r, x	Cylindrical coordinates
ΔS	Change of entropy, $C_p ln\frac{To}{To_\infty} - Rln\frac{Po}{Po_\infty}$
Δt	physical time step
δ_{ik}	Kronecker delta function
γ	specific heat ratio
μ	viscosity
μ_{DES}	turbulent eddy viscosity determined by DES, DDES or IDDES
ν	kinematic viscosity
$\tilde{\nu}$	working variable of the S-A model related to turbulent eddy viscosity
ρ	fluid density
τ_{ik}	shear stress in Cartesian coordinates
τ_w	fluid shear stress at the wall surface
φ	position vector in reference xyz
ξ, η, ζ	generalized coordinates

- Subscripts -

b	computational domain outer boundary
i	computational domain inner boundary
i, j, k	indices
∞	reference point

- Abbreviations -

AoA	Angle of Attack
AFC	Active Flow Control
BC	Boundary Condition

BLC	Boundary Layer Control
BLI	Boundary Layer Injection
BWB	Blended Wing Body
CC	Circulation Control
$CESTOL$	Cruise Efficient Short Take-Off and Landing
CFD	Computational Fluid Dynamics
CFJ	Co-Flow Jet
CFL	Courant-Friedrichs-Lewy number
CSD	Computational Structural Dynamics
$CUSP$	Convective Upwind and Split Pressure
$DDES$	Delayed Detached Eddy Simulation
DES	Detached Eddy Simulation
DNS	Direct Numerical Simulation
EA	Electric Aircraft
$ESTOL$	Extreme Short Take-Off and Landing
FSI	Fluid-Structural Interaction
FVS	Flux Vector Splitting
HEP	Hybrid Electric Propulsion
HWB	Hybrid Wing Body
ICE	Internal Combustion Engine
$IDDES$	Improved Delayed Detached Eddy Simulation
LCO	Limit Cycle Oscillation
LDE	Low Diffusion E-CUSP scheme
LE	Leading Edge

LES	Large Eddy Simulation
LFC	Laminar Flow Control
LHS	Left Hand Side
LLM	Log Layer Mismatch
MSD	Modeled-Stress Depletion
$MTOW$	Maximum TakeOff Weight
$MUSCL$	Monotone Upstream-centered Schemes for Conservation Laws
NSV	Non-Synchronous Vibration
$RANS$	Reynolds Averaged Navier-Stokes equations
RHS	Right Hand Side
$S-A$	Spalart-Allmaras (S-A) one equation turbulence model
SLC	Super Lift Coefficient
TE	Trailing Edge
TFC	Turbulent Flow Control
TOL	Takeoff/Landing
$URANS$	Unsteady Reynolds Averaged Navier-Stokes equations
$WENO$	Weighted Essentially Non-Oscillatory scheme
$WMLES$	Wall Modeled Large Eddy Simulation
$ZNMF$	Zero-net mass flux

CHAPTER 1

Introduction

1.1 Background

1.1.1 Market Forecasts

In the past several decades, the population and goods transportation via air vehicles have been increased rapidly. In the near future, the aviation industry will continue to be the backbone of the United States and global economies. According to NASA's prediction (Fig. 1.1), global aviation is forecast to grow from today's 3.5 billion passenger trips per year to 7 billion passenger trips by the mid-2030s, and to 11 billion passenger trips by mid-2050s. Over 36000 new aircraft will be required for the next twenty years with a worth of 6 trillion dollar GDP produced [1]. The market growth could produce the direct economic potential of trillions of dollars in the fields of manufacturing, operations and maintenance, and numerous high-quality jobs. At the same time, the international competition for leadership of this critical industry is growing, as more nations invest in developing their own aviation technology and industrial capabilities.

The surge in demand for commercial aircraft also creates substantial operational and environmental challenges. A confluence of factors is powering a drive toward

"green technologies" for cleaner, more efficient and smarter aircraft [40]. The first factor is always that all airlines' quest to reduce fuel costs, whereas the second is to meet the strict regulations for environmental protection. For example, European Union Emissions Trading System targets to cut net carbon emissions by 50% by 2050 and increases annual fuel efficiency by 1.5% through 2020. By 2050s, the aviation industry will need to build and fly enough new aircraft to accommodate more than three times as many passenger trips while at the same time reducing total emissions by half. By some measures, it appears that the aviation industry is entering a "second golden age" [40].

The ever-exploding number of airlines for passengers and cargo puts tremendous pressure beyond the airport capacity in the lack of runway and terminals, which will lead to airport congestion and resulting in travel delays. Almost all the major airports in the United States are struggling with growing number of air traffic congestion. In the next 50 years, both current hub and spoke infrastructure will fail to withstand the capacity for the expected high rise in air travel, and would need major changes to maintain the same level of service. With the increase in air traffic predicted, congestion will worsen. One possible resolution for the airport congestion is redesigning the airport infrastructure [41]. Another major solution is the revolution of next-generation's air vehicles.

In 2002, NASA published its blueprint for aeronautics that revolutionary new air vehicles [42] will be required for the future of aviation. The future vehicles would produce the possibility for new large, long haul concepts, increased speed, autonomous operations, and the necessity for new vehicle concepts that provide runway independence. The blueprint described some new technologies that will enable the increased

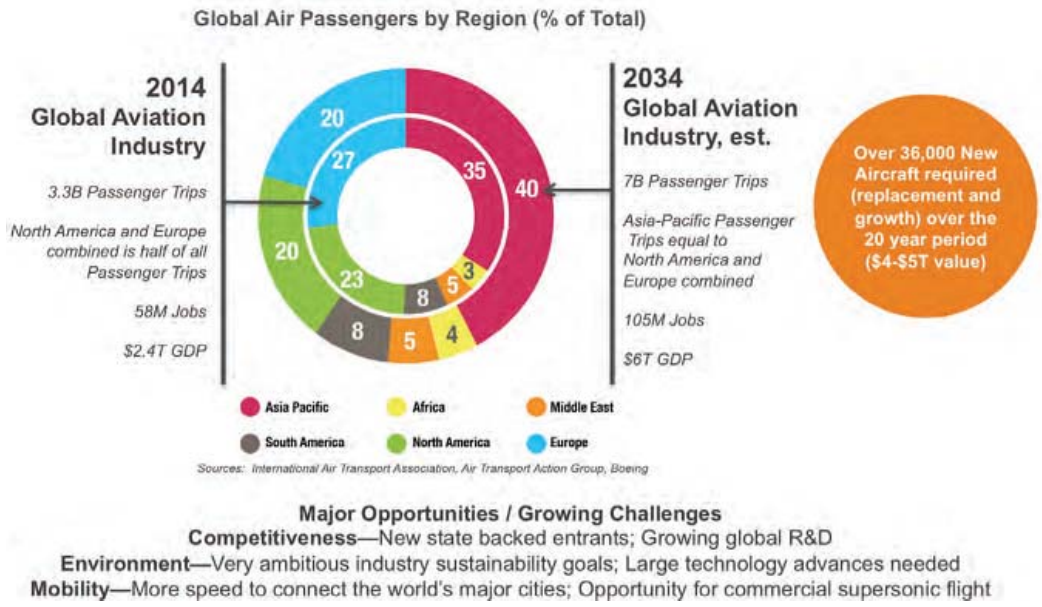

Figure 1.1: NASA's global growth in aviation: opportunities and challenges [1].

capabilities of these revolutionary air vehicles [43]. Another emerging market is to provide the doorstep air traffic, or called "Sky Taxi". Doorstep-to-destination mobility will drive vehicle requirements and provide multi-level highways in the sky. For this purpose, new concept air vehicles, such as vertical-lift or extremely short takeoff and landing (ESTOL) capabilities will provide a degree of runway independence.

1.1.2 Sky Taxis

Flying automobiles could make the leap from science fiction to reality in the very near future. In May 2010, Comparative Aircraft Flight Efficiency Foundation (CAFE) [44] presented a formal colloquium at NASA Langley Research Center describing how such an aircraft, which CAFE named the Sky Taxi, could transform transportation and substantially reduce greenhouse gas emissions. The business need for on-demand Sky Taxis can be made based on their substantial time, fuel, and maintenance savings, plus the extended reach that they can provide. As its popularity grows, the travel

by Sky Taxi will likely to provide all citizens the affordable availability of on-demand travel that is faster than a bizjet. Then CAFE held the 2011 Green Flight Challenge especially for electric aircraft. The name "Sky Taxi" is adopted to describe the electric-powered aircraft that combine these capabilities. The point-to-point Sky Taxi operates at pocket airports, and there are big potential economic and societal benefits of such operations. As its popularity grows, it will become affordable enough for the near 245,000,000 Americans who are at least 15 years old.

One business example is that Uber has started to build a flying taxi system on the Uber Elevate Summit in April 2017. Their vision is to develop on-demand aviation, which has the potential to radically improve urban mobility space.The program will start testing sky taxi in 2020 and is anticipated to get into service as soon as 2023. Dubai is a pioneering city to test its Sky Taxi in September 2017. The Dubai Civil Aviation Authority tested a proof-of-concept autonomous air taxi built by the German company Volocopter, flying for 5 minutes approximately 650 ft above a windy residential neighborhood. Their autonomous air taxi's goal is to provide 30-minute trip for passengers.

1.2 Emerging Technologies in Aviation

In a rigorous attempt to meet projected national aviation goals in noise, emissions, and performance, NASA has conducted an N+3 case study intended to foster advanced aircraft concepts and technologies projected to enter service in the 2030 to 2035 timeframe. The project metrics included a 52 dB cumulative reduction in aircraft noise, an 80% reduction in Takeoff/Landing NOx emissions, and an 80% re-

duction in mission fuel burn relative to a state of the art reference aircraft [45]. These goals are summarized in Table 1.1.

Table 1.1: NASA N+3 metrics

TECHNOLOGY BENEFITS*	TECHNOLOGY GENERATIONS (Technology Readiness Level = 4-6)		
	N+1 (2015)	N+2 (2020**)	N+3 (2025)
Noise (cum margin rel. to Stage 4)	-32 dB	-42 dB	-52 dB
LTO NOx Emissions (rel. to CAEP 6)	-60%	-75%	-80%
Cruise NOx Emissions (rel. to 2005 best in class)	-55%	-70%	-80%
Aircraft Fuel/Energy Consumption‡ (rel. to 2005 best in class)	-33%	-50%	-60%

* Projected benefits once technologies are matured and implemented by industry. Benefits vary by vehicle size and mission. N+1 and N+3 values are referenced to a 737-800 with CFM56-7B engines, N+2 values are referenced to a 777-200 with GE90 engines
** ERA's time-phased approach includes advancing "long-pole" technologies to TRL 6 by 2015
‡ CO2 emission benefits dependent on life-cycle CO2e per MJ for fuel and/or energy source used

To meet NASA's N+3 goals in 2035 for subsonic fixed wing aircraft, NASA has proposed a N3-X aircraft with turbo-electric distributed propulsion (TeDP), and hybrid-wing-body (HWB) configuration for Cruise Efficient Short Takeoff/Landing (CESTOL) performance [46] (Fig. 1.2). The purpose is to achieve high aerodynamic performance and potential of reductions in fuel consumption, noise, and emissions. The N3-X aircraft has the synergistic benefits of distributed propulsion and airframe integration with respect to cruise efficiency and noise reduction. The propulsion system is composed of 2 turbogenerators (turboshaft engine and generators), 14 motors and inverters, and a cooling system [46] .

1.2.1 Hybrid Wing Body

A hybrid wing body (HWB) is an appealing fixed-wing aircraft design technology, with no clear splitting lines between the wings and the main body of the aircraft.

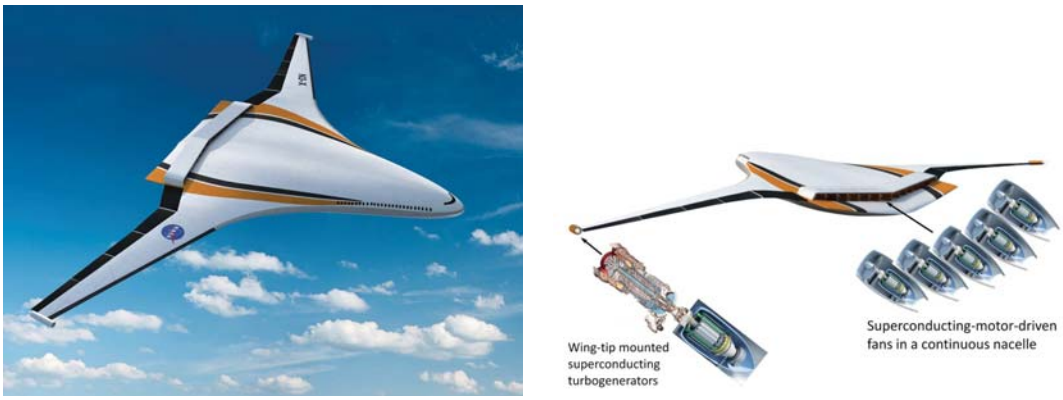

Figure 1.2: NASA N3-X conceptual design with HWB configuration and turboelectric propulsion

It is formed by a distinct wing and body structures, though the wings are smoothly blended into the body, which is different from a flying wing with no distinct fuselage (See Fig. 1.3). It is also named blended wing body (BWB). The HWB configuration is to improve aerodynamic performance, and hence the dramatic reductions in fuel consumption, noise, and emissions. The entire aircraft is expected to generate lift. As a result, the size of the wings will be reduced, leading to smaller weight and drag. Therefore, the HWB configuration reduces the total wetted area of the aircraft surface and skin frictional drag. A conventional tubular fuselage carries 12-13% of the total lift compared to 31-43% carried by the centerbody in an HWB. Modern HWB aircraft, as it is known today, was initialized in 1988 by Robert Liebeck of Boeing Company [2]. NASA has performed tje study of HWB tailless aircraft on commercial airliners, the BWB-450 in 2003. The BWB450 concept has the mission of 450 passenger capacity with using boundary layer ingestion (BLI) technology. They explored the possibility of applying the HWB tailless aircraft concept to commercial passenger transport. Various companies have proposed their own commercial airplane prototypes with HWB configurations respectively, such as X-48B BWB concept tested by Boeing. More HWB examples are given in Fig. 1.4.

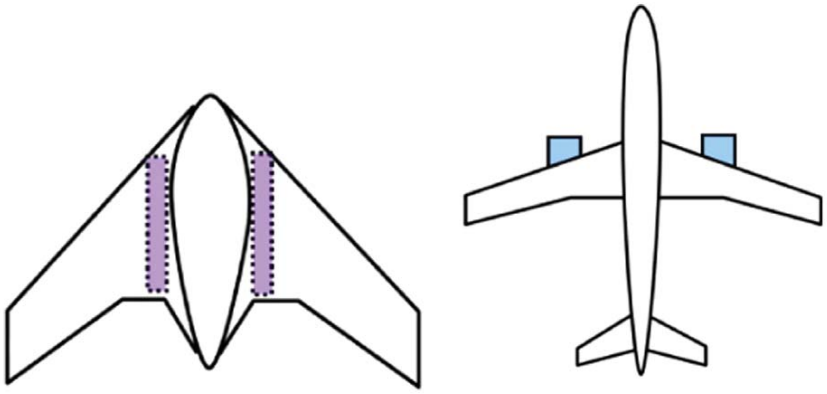

(a) Discrete BWB

(b) High By - pass Ratio Conventional Air craft

Figure 1.3: Discrete BWB airframe and the high by-pass ratio conventional aircraft [2].

Figure 1.4: A partial list of various HWB concept aircraft reported recently.

1.2.2 Boundary Layer Ingestion

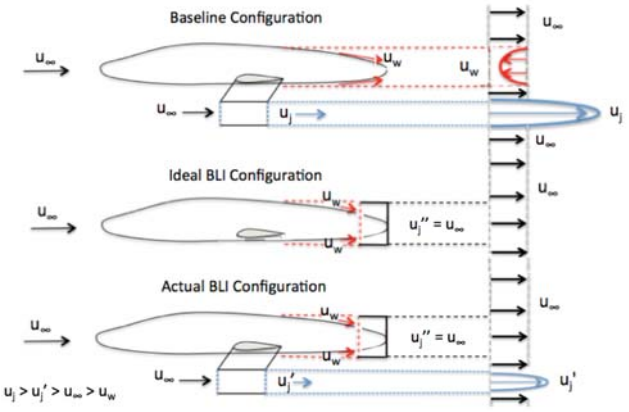

Figure 1.5: Boundary layer Ingestion concept [3]

Figure 1.6: The D8 conceptual aircraft

Boundary layer ingestion (BLI) is a promising idea to reduce fuel burn in jet engines, thus reducing emissions and the cost of operating the aircraft. The main principle of this BLI concept is to reduce the overall propulsive power required by the aircraft by integrating an additional propulsor in the aft section of the fuselage, where the lower velocity boundary layer can be ingested by the engine intake [3]. By re-energizing the wake produced by the airframe through the use of Boundary-Layer Ingestion, the overall energy efficiency of the system will be improved.

With BLI, an airplane's engines are located near the rear of the aircraft. The accelerated air flow through the engine fills the wake produced by the flow over the aircraft fuselage. In a conventional tube and wing airplane, the high-speed flow behind the engine and drag-inducing airflow mixed with the undisturbed air behind. The velocity deficit in the wake profile creates energy loss to the aircraft. The purpose of BLI is to reduce the total drag of an airplane by redistributing the velocity profile behind the whole aircraft. Further discussion of the BLI benefits are elaborated in references [3]

A. M. O. Smith and H. Roberts (1947) [47] first examined an aircraft that used suction slots located along the wing and fuselage to ingest the boundary layer in order to prevent or delay the turbulence transition. Their tests showed that the engine included Boundary-Layer Ingestion, had a reduced fuel consumption of almost 33% as well as an increased C_L and L/D compared to the turbojet without Boundary-Layer Ingestion for the same aircraft. More recent studies have combined BLI technology with HWB geometry configurations in order to improve energy efficiency for the aircraft [3, 48]. A reduction in the mechanical power required by the propulsor is achieved as compared to a typical podded nacelle configuration. Several airplane concepts that employ BLI could be incorporated into a series of X-planes in NASA. A novel conceptual design employing the BLI concept is the "Double Bubble" by NASA/MIT/Aurora as shown in Fig. 1.6.

Though boundary layer ingestion can bring some potential benefits for aircraft, it also comes with difficult challenges. One significant issue is that the non-uniform flow drawn from the boundary layer into the engine fan inlet could cause a decrease in engine efficiency and thrust due to inlet distortion. Also, the aerodynamic instability from the boundary layer integrated with the airframe could possibly lead to forced response (and flutter) aeromechanical limits [49].

1.2.3 Distributed Propulsion

The innovation in the propulsion system for aircraft could also provide a potential solution for the future aviation. The propulsion system is a key element of future aircraft due to its significant role in reducing emissions, fuel burn, and noise. Distributed propulsion is based on dividing up the thrust generation to achieve the beneficiary

gain of noise reduction, shorter take-off and landing, enhanced specific fuel consumption and flight range [4]. Distributed propulsion has been considered recently as a promising direction to improve fuel efficiency and address stringent environmental regulations.

Several fixed wing aircrafts using distributed propulsion have been proposed and flown. As defined by Kim (2010) [50], distributed propulsion in aircraft application is the spanwise distribution of the propulsive thrust stream such that overall vehicle benefits in terms of aerodynamic, propulsive, structural, and/or other efficiencies are mutually maximized to enhance the vehicle mission. With this definition, Kim listed a number of fixed-wing aircraft using distributed propulsion studied by NASA, such as the jet flap, cross-flow fan, and multiple discrete engines (such as the CESTOL aircraft in Fig. 1.7). Another famous Distributed Electric Propulsion (DEP) Aircraft example is SCEPTOR X-Plane. A broader review and evaluation of various distributed propulsion system is given by Gohardani et al. (2011) [4].

NASA has conducted researches on various aspects of distributed propulsion technology in collaboration with a number of partner universities, companies and research institutes. One of the adjacent research of distributed propulsion is to combine distributed and with electric power. As a consequence of this quest, electric motors and high-temperature superconductivity are proposed for future aviation. Fig. 1.7 illustrates a number of distributed propulsion concepts and components [4].

Benefits of Distributed Propulsion

As suggested by Kim from NASA Subsonic Fixed Wing (SFW) Project [50], the benefits of using distributed propulsion for aircraft could be found in improvement in

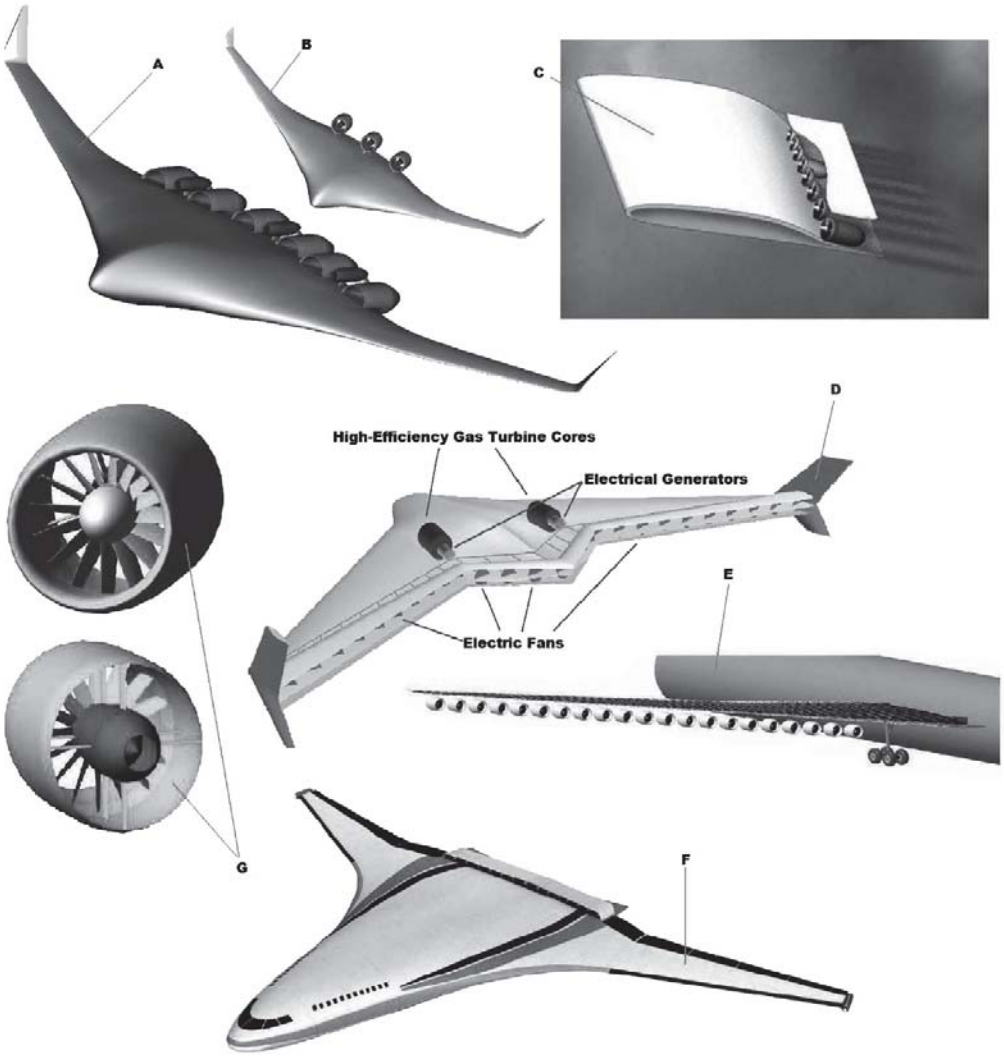

Figure 1.7: Distributed propulsion implementation examples summarized in [4].

aircraft performance, noise reduction to the surrounding community, and/or providing the capability of STOL. Specifically, the following possible benefits of distributed propulsion concepts have been identified by Kim [50]:

- Reduction in fuel consumption by ingesting the thick boundary layer flow and filling in the wake.
- Enable STOL capability by spanwise high lift via high-aspect-ratio distributed flow control.
- Better integration of the propulsion system with the airframe to reduce the aircraft noise.
- Reduction in aircraft propulsion installation weight.
- Elimination of aircraft control surfaces through differential and vectoring thrust.
- High production rates and easy replacement of propulsors that are small and light.

1.2.4 Electric/Hybrid-Electric Propulsion

To combat the global warming and reduce emissions, the electric aircraft industry is being developed rapidly. In the last decade, the full electric propulsion and hybrid electric systems are attracting more and more research and industry investigations all over the world. The electric propulsion aircraft has the remarkable features of zero-emission and high energy conversion efficiency. The full electric propulsion can be considered as locally zero-emission aircraft in the sky, albeit depending on how the electric energy is produced.

Figure 1.8: A historical overview of electric aircraft summarized in [5].

Full electric propulsion relies solely on electric power stored in batteries. However, the low power density of batteries is currently limiting the range of a fully electric aircraft to be economically viable. Hybrid electric propulsion (HEP) is defined more broadly, which is a fusion of internal combustion engine and electric propulsion system. HEP airplanes are powered by the electric motors combined with the conventional fuel engines.

Recent Development of Electric Aircraft

Electrically powered aircraft have been flown since the 1970s. However, even today a successful commercial electric airplane is still not available. Progress for the fixed-wing aircraft using electric propulsion has been made rapidly since the year 2000. The electric aircraft industry is still in its early stage with various challenges. One well-known event is the 2011 Green Flight Challenge (GFC) held in Santa Rosa,

California. The desirable mission for an electric aircraft is to fly 200 miles in less than 2 hours using the energy equivalent of a gallon of gasoline per passenger. The Pipistrel Taurus G4 demonstrator won the 2011 CAFE/NASA GFC. It is designed with twin fuselage and four-seats general aviation aircraft.

The emerging electric aircraft market has attracted research efforts and investment throughout the globe. In 2017, numerous electric airplanes sprout out in the aviation industry. Airbus, Rolls-Royce and Siemens partnered on a hybrid electric aircraft prototype, the E-Fan X, which demonstrated how the blending of conventional and electric engines could work. The E-Fan X demonstrator will use modified four-engine BAe-146 by replacing one or two of its gas turbine engines with a 2 MW electric motor (see Fig. 1.9). EasyJet announced it was developing an electric 180-seater with Wright Electric. Wright Electric proposed a 10-seater, eventually an at least 120 passengers single aisle, short haul airliner and targets 50% lower noise and 10% lower costs. Zunum Aero (by Boeing and JetBlue) formally launched the development of a six-to-12-seat aircraft aimed to fly in 2020 and be delivered in 2022 (See Fig. 1.10). Lilium Jet tested the first all-electric aircraft which can take off vertically like a helicopter, and then accelerating into forward flight using wing-borne lift (See Fig. 1.11). Lilium Jet is powered by 36 separate jet engines mounted on its 10-meter long wings via 12 movable flaps. At take-off, the flaps are pointed downwards to provide vertical lift. And once airborne, the flaps gradually tilt into a horizontal position, providing forward thrust.

A fully-electric X-plane X-57 “Maxwell” is developed by NASA, which features Distributed Electric Propulsion (DEP) wings mounted with small electric propellers on the leading edge. The NASA X-57 Maxwell with two seats has a range of ap-

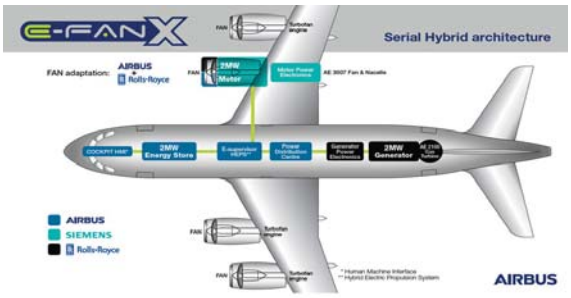

Figure 1.9: Airbus E-Fan X demonstrator.

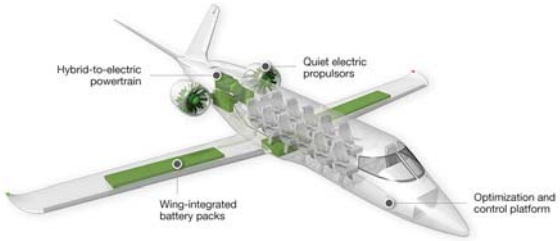

Figure 1.10: Zunum Aero hybrid electric airplane

Figure 1.11: Lilium Jet all electric airplane

Figure 1.12: NASA X-57 experimental aircraft

proximately 100 miles (160 km) and a maximum flight time of approximately 1 hour. The NASA X-57 Maxwell has 14 electric motors driving propellers mounted on the wing leading edges. During takeoff and landing, all of the 14 electric motors provide the necessary lift, with only the outer 2 electric motors used during cruise. Once the X-57 gains designed altitude and velocity, the inner 12 lift motors shut down and the propellers fold back into a more aerodynamic position. During cruise, the propulsion is drawn solely from the two large electrically-driven propellers mounted on the tips of each wing.

Pornet and Isikveren (2015) [5] presented some hybrid-electric and universally-electric aircraft concepts unveiled in recent years before 2015 in Fig. 1.13. A more recent summary of electric aircraft recently released in 2017-2018 is given in Fig. 1.14.

Figure 1.13: Summary of the hybrid-electric and universally-electric aircraft concepts targeting YEIS 2030+ unveiled (summarized in [5]).

Figure 1.14: A partial summary of electric aircraft released in 2017.

1.2.4.1 Hybrid Electric Propulsion

To integrate the power supplied by fuel engines and batteries, various types of configurations are adopted for the hybrid electric propulsion systems. Fig. 1.15 presents four different electric-based propulsion configurations among turboelectric, parallel hybrid-electric, series hybrid electric, and pure electric systems [6]. The power generation and distribution strategies are determined by their powertrain respectively.

The turboelectric propulsion has single power source from the combustion engine. The chemical energy is converted into the electricity through combustion engine and generators. The electricity is supplied to the motors to drive the fans/propellers. No extra batteries are required to store energy for aircraft propulsion.

On the contrary, in the full electric propulsion system, the propulsion power comes solely from the energy stored in the pre-charged batteries or equivalent.
The whole propulsion is electric-powered, which does not include the combustion engine and related components.

Other than the above strategies with a single energy source, most of the HEP strategies use both the fuel and batteries. The HEP strategies are categorized into series or parallel connection, and the series-hybrid combination, depending on their power transferring system respectively. For the series HEP strategy, the electric power from the battery and generated from the combustion engine are combined to drive the electric motor, and then the fan/propulsor. The energy from fuel combustion is produced to power motor or to charge the batteries. The engine is not connected to the fans/propulsors. Therefore, no mechanical power is supplied from the combustion engine to the fans/propulsors. For the parallel HEP strategy, the power for the fan/propulsor has two sources independently, the shaft power from the electric motor

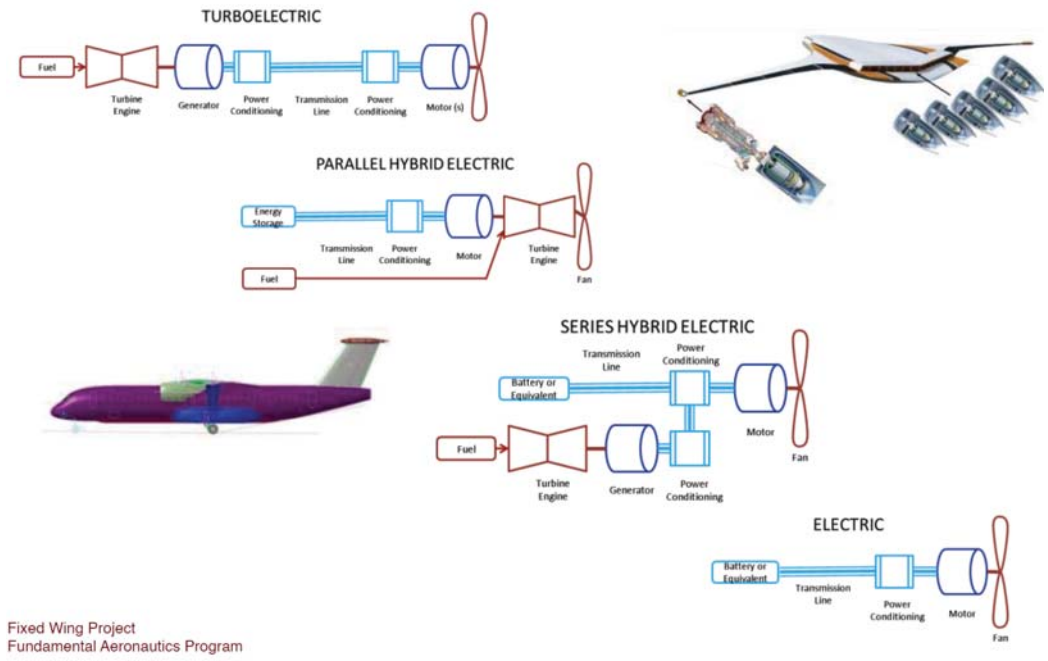

Figure 1.15: Various types of electric-based propulsion strategies (Turboelectric, parallel hybrid electric, series hybrid electric, and all electric) [6].

and the shaft power directly output from the turbine engine. The major difference for the parallel hybrid strategy is that the mechanical power can be directly supplied to the fan/propulsor.

For the hybrid electric system, the Degree-of-Hybridization (DoH) is proposed by Pornet and Isikveren (2015) [5]. The DoH is represented by two parameters H_P and H_E, defined as

$$\begin{aligned} H_P &= \frac{P_{ELEC}}{P_{TOT}} \\ H_E &= \frac{E_{ELEC}}{E_{TOT}} \end{aligned} \tag{1.1}$$

where $H_P$represents the ratio of maximum installed electrical power to the total installed power; H_E is the ratio of total stored the electric energy to the total stored energy.

1.2.4.2 Benefits of Hybrid Electric Propulsion

The integration of electric power with distributed propulsion has a significant merit, which leads to the emergence of distributed electric propulsion (DEP) system. Distributed propulsion is created by a spanwise distribution of partially or fully embedded multiple propulsion units along the wing/fuselage. The electricity transits through electric cables efficiently, which is naturally coupled with power distribution system. The electric power from the fuel engines can be easily and flexibly transited to the multiple propulsion units, such as motors and fans without much energy loss. Moreover, the power generator and the propulsors can be placed anywhere on the vehicle to optimize overall system performance [51]. The hybrid electric distributed propulsion can also be well integrated into the hybrid wing body configuration. Therefore, overall distributed electric propulsion has better fuel efficiency and hence less operating costs. Despite their great potentials, the development of fully electric and hybrid electric propulsion in aviation is still in its embryonic stage.

The benefits for a hybrid electric propulsion airplane can be summarized as follows.

- With the complimentary electric propulsion system, the internal combustion engine always operates at its optimum operating point. Therefore, the energy conversion efficiency is higher than that of the conventional engine, which have to sacrifice efficiency to trade for a broad operating range in the whole flying envelope. At the same time, electric motors work efficiently in a wide operating range.

- Since the whole power output depends on the combined power of the combustion engine and electric motors, the maximum power required for the combustion engine is reduced (e.g. maximum power for takeoff).

- The electric-based propulsion system can be straightforwardly incorporated with the distributed propulsion. The power distributed propulsion system can be achieved using electric systems instead of complicated mechanical systems. Moreover, the power generator and the propulsors can be placed anywhere on the vehicle to optimize overall system performance [51]. Therefore, overall distributed electric propulsion has better fuel efficiency and hence less operating costs.

- The overall reduced fuel consumption due to higher system efficiency and decreased weight of the core combustion engines of HEP offset the weight increase due to the added motors and generators.

1.2.5 Extreme Short Takeoff/Landing Performance

To break the bottleneck in the limited space at major airports, the extremely short takeoff/landing (ESTOL) performance is desirable for airliners. The ESTOL aircraft is supposed to allow more efficient of limited airport infrastructure. According to Bauhaus Luftfahrt, by rearrangement of existing runway area for conventional takeoff and landing (CTOL) aircraft, the airport capacity could be substantially increased by employing the ESTOL-capable aircraft (See Fig. 1.16).

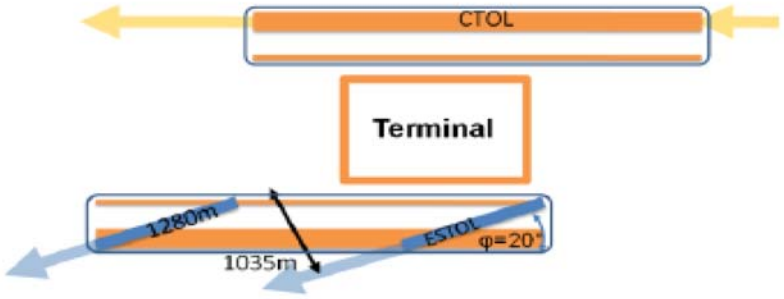

Figure 1.16: ESTOL runway layout [7]

1.2.5.1 Extreme Short Takeoff/Landing Aircraft

The requirement for Extreme Short Takeoff/Landing Aircraft(ESTOL) performance presents a unique challenge for the existing leading-edge high-lift technologies. The ESTOL goals are set for a commercial vehicle, to move from today's state of the art (SOA) and within the next 15 years provide the technology for a vehicle that can operate with a take-off and landing distance of $\leq$ 2,000 feet, cruise at Mach 0.80, carry 90-100 passengers, have a range of 1,400-2,000 nm, noise containment within an airport footprint, and low speed maneuverability [9, 52]. To accomplish this task and simultaneously open up new airports for commercial travel, the vehicle will require a takeoff and landing speed of 50 knots and a 1/4 nm turn radius in the terminal area [9]. Another crucial consideration is noise reduction, which requires an ESTOL vehicle a good neighbor at community airports. The NASA vehicle sector has identified specific technology targets that include a C_{Lmax} of 10, an L/D of 16, a 20 EPNdB reduction in noise from today's SOA, and reduce the empty weight fraction to 0.43. The propulsion system will need improvements in engine T/W of 120% and a 10% reduction in thrust specific fuel consumption (TSFC). Improving C_{Lmax} from the current SOA of 7 will most likely require flow control and innovative new powered

Table 1.2: ESTOL regional aircraft requirement [38]

Take-off field length [m]	1000
Range [nm]	1200
Cruise Mach number [-]	0.78
Passengers	90
Cruise altitude [ft]	37,000

lift concepts [9] [38]. According to the results above, typical mission requirements for an ESTOL regional jet are derived in [38] and summed up in Table 1.2.

1.2.5.2 Cruise-Efficient Short Takeoff and Landing Concept

The Cruise-Efficient Short Takeoff and Landing (CESTOL) aircraft concept was introduced into a future U.S. National Airspace System (NAS) civil aviation environment by NASA [39]. The CESTOL aircraft design is to increase capacity and reduce emissions for future aviation system. The CESTOL capability provides flexible climb, descent, and runway performance and high-speed cruise capabilities. It is intended to provide service for various airports. It is capable of serving the hub airports, satellite airports, and regional airports. It is required to leverage fuel-efficient, low-noise, and low-emission technologies and operating procedures. The operating capabilities of the CESTOL aircraft are envisioned to be compatible with standard procedures, as well as alternative procedures that take advantage of its unique performance characteristics. In general, the CESTOL aircraft will be in harmony with conventional aircraft and procedures that fit the above description is one of sufficient size, range, and speed to be commercially feasible on a NAS-wide scale with technological and operational performance characteristics to be economically efficient and environmentally effective. The preliminary CESTOL capabilities are listed in Table 1.3, which guided by from NASA [39].

Table 1.3: CESTOL aircraft operating characteristics [39]

One-way Operating Range (nm)	2,000
Minimum Runway Length (ft)	2,000
Cruise Mach number:	0.8
Aircraft Seat Size	120-130 seats

1.3 Turbulence Modeling

Turbulence has inherently nonlinear, complex features in the nature of Navier-Stokes equation. Reynolds-averaged Navier-Strokes (RANS) methods are not appropriate for simulating stalled vortical flow structures due to its universal scale filtering. As an alternative, large eddy simulation (LES) is developed to directly simulate the large flow structures and model the small eddy structures that are more isotropic. However, LES is much more CPU expensive. The hybrid RANS/LES approach is a promising compromise for engineering applications by taking the advantages of RANS's high efficiency and LES's high accuracy with more affordable computational cost.

The detached eddy simulation (DES, or DES97) is the first and most popular non-zonal hybrid RANS/LES strategy suggested by Spalart et al. in 1997 [53]. Near the solid surface within the wall boundary layer, the unsteady RANS(URANS) turbulence modeling is utilized. Away from the boundary layer, the DES97 model is automatically converted to LES. The Delayed detached-eddy simulation (DDES) suggested by Spalart et al. [54] is improved to resolve model stress depletion(MSD) and grid induced separation(GIS) problems. The more recently improved DDES(IDDES) model is formulated by Travin et al. [55] and Shur et al. [56] by coupling wall-modeled LES(WMLES) and DDES to eliminate the log layer mismatch (LLM) problem, and maintain the compatibility with the general DES approach. The major improvement

of IDDES can be summarized as a near-wall modification of the LES filter Δ, and a more rapid transition between the RANS and LES length scales than DES97 or DDES. The IDDES method utilizes more sensors in the boundary layer region and a new blending function based on theoretical considerations and empirical tuning [57].

Computational simulations of airfoil stall flows have been conducted extensively by various researchers [55, 58–60]. Travin et al. [55] simulate the massively separated flows over an airfoil, and observe that the DDES performs similarly to the original DES97 for their cases. Morton et al. [58] employed DES97 to simulate a full F/A-18E aircraft experiencing massively separated flows with good agreement with the experiment. Durrani et al. [59] applied DES97 and DDES to simulate the flow around the A-airfoil at the maximum lift condition(AoA=13.3°). They observed that for the flow with a relatively thick boundary layer and a mild trailing-edge separation, DES97 performs better than DDES due to its relatively lower turbulence dissipation levels.

1.4 Co-Flow Jet Flow Control

The Co-Flow Jet (CFJ) active flow control concept was firstly suggested by Zha [61] in 2004 in the NASA/ONR 2004 Circulation Control Workshop. The CFJ flow control method can substantially enhance lift, reduce drag and increase stall margin at low energy expenditure. The CFJ airfoil has an injection slot near the LE and a suction slot near the TE on the airfoil suction surface as sketched in Fig. 1.17. A small amount of mass flow is withdrawn into the airfoil near the TE, pressurized and energized by a pumping system inside the airfoil, and then injected near the LE in the direction tangent to the main flow. The whole process does not add any mass flow

to the system. And hence CFJ airfoil is a zero-net mass-flux (ZNMF) flow control. The CFJ system is a self-contained high lift system with no moving parts.

The fundamental mechanism of the CFJ airfoil is that the turbulent mixing between the jet and main flow energizes the wall boundary-layer, which dramatically increases the circulation, augmenting lift, and reducing the total drag (or generates thrust) by filling the wake velocity deficit.

The CFJ airfoil has a unique low energy expenditure mechanism because the jet gets injected at the leading edge suction peak location, where the main flow pressure is the lowest and makes it easy to eject the flow, and the flow is sucked at near the trailing edge, where the main flow pressure is the highest and makes it easy to withdraw the flow. The turbulent shear layer between the main flow and the jet causes strong turbulence mixing, which enhances lateral transport of energy from the jet to main flow and allows the main flow to overcome severe adverse pressure gradient and remain attached at a high angle of attack.

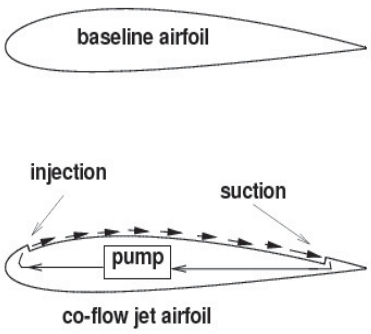

Figure 1.17: Baseline and CFJ airfoil.

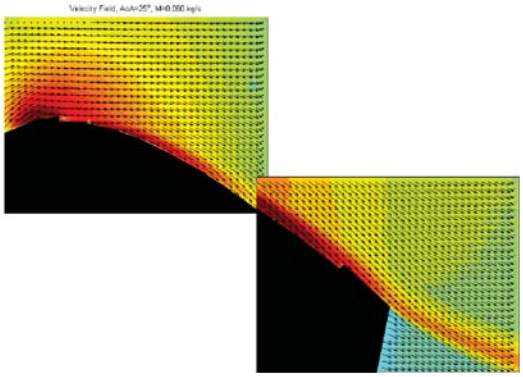

Figure 1.18: Attached flow of CFJ NACA 6415 airfoil at AoA=25° measured by PIV in experiment, C_μ of 0.06, M=0.1 (Plot adopted from [8]).

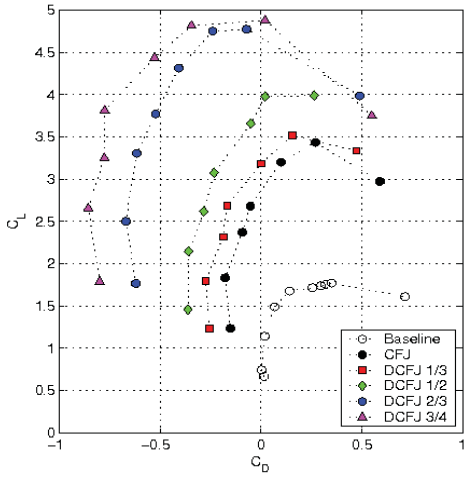

Figure 1.19: Measured drag polars of discrete CFJ airfoils at mass flow $\dot{m} = 0.06$ kg/s (Plot adopted from [8]).

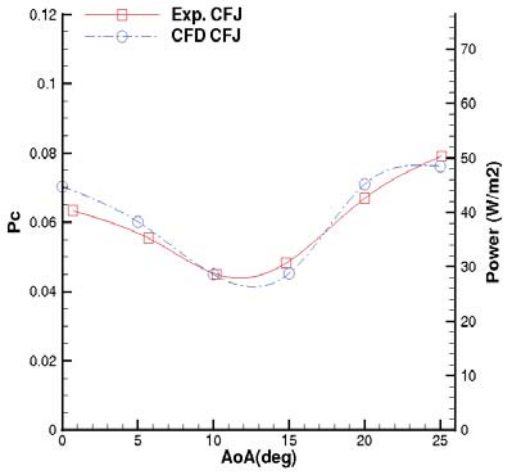

Figure 1.20: Computed power coefficient compared with experiment at M=0.03 and $C_\mu = 0.08$ (Plot adopted from [8]).

Fig. 1.18 adopted from [8] is the PIV measured velocity field of the CFJ-NACA-6415 airfoil at the AoA of 25° and C_μ of 0.06, which has the flow attached and a higher speed within the wake than in the freestream. In this case, thrust is generated. The baseline NACA-6415 airfoil has massive flow separation at this AoA. Fig. 1.19 shows the wind tunnel test results of several CFJ airfoils at Mach number of 0.1. The CFJ airfoil achieves a C_{Lmax} of about 5, more than 3 times higher than the baseline airfoil. It also obtains an enormous thrust coefficient of about 0.8. A CFJ wing is hence can be used as a distributed thrust system.

Fig. 1.20 from [8] shows the computed power coefficient compared with the experiment. The power coefficient decreases with the increase of AoA up to 15° and then rises at higher AoA. It is because when the AoA is increased and the flow still remains attached, the airfoil LE suction effect becomes stronger with lower static pressure in the region of the injection jet, and hence less power is needed to generate the jet with the same momentum coefficient. However, when the AoA is beyond the

separation value, the boundary layer is deteriorated with large energy loss and the suction power is significantly increased. More information on CFJ airfoil can be found in [8, 35, 61–70]

Benefits of CFJ Aircraft

The overall benefits of using Co-Flow Jet flow control aircraft could be summarized in improvement in aircraft performance, noise reduction to the surrounding community, and/or providing the capability of ESTOL. Specifically, the following possible benefits have been identified:

- Super-high lift coefficient ($C_L > 10$) across the wingspan with supercirculation around the wing, providing the ESTOL capacity
- Reduction in fuel consumption by improving the aerodynamic/productivity efficiency (high C_L/C_D, C_L^2/C_D) during cruise;
- Requires a smaller wing span for easy storage, light weight and reduced skin friction and form drag;
- Supersonic aircraft to have small wing size matching cruise need, but also have high subsonic performance (e.g. high lift low drag at $M < 1$);
- The distributed propulsion system intrinsically integrated with the airframe, created counter-rotating vortex layer to remove the wake generated by the airframe.
- integration of propulsion system with boundary layer, re-energize the boundary layer and remove the wake velocity deficit, thus reduce drag, improve fuel efficiency.

- Elimination of aircraft control surfaces through differential and vectoring thrust for pitch, roll, and yaw moments.
- Reduction in aircraft propulsion installation weight through inlet/nozzle/wing structure integration.
- Integration of propulsion system with the airframe for noise reduction to the surrounding community through airframe shielding
- With more propulsors, higher production rates and better reliability

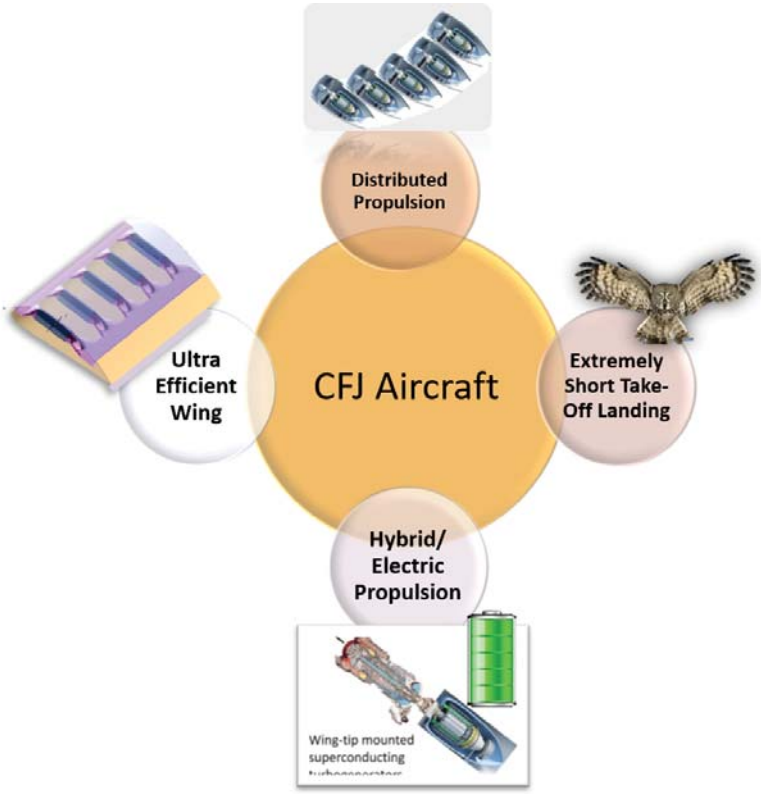

Figure 1.21: The features and benefits of CFJ aircraft

1.5 Research Strategy

1.5.1 Objectives

The objective of this dissertation is to investigate the super-lifting performance of CFJ airfoils and its applications on electric aircraft. The research strategies of this dissertation are described as follows:

1. Unsteady 3D compressible Navier-Stokes equations are solved with the low diffusion ECUSP scheme with a 5th order WENO reconstruction for the inviscid flux and a set of 2nd order central differencing for the viscous terms are used to accurately capture the shock wave/turbulent boundary layer interaction of the vibrating wing and blades.

2. The advanced hybrid LES/RANS turbulence model, Improved Delayed Detached Eddy Simulation (IDDES) is developed and implemented for high fidelity CFD simulation with turbulence modeling.

3. Develop an iterative subroutine for the CFJ injection and suction boundary condition for multiple CFJ with various targeted C_μ .

4. Validate the IDDES method on a flat plate turbulent boundary layer and NACA0012 detached flow.

5. Perform the parametric trade study of a 2D CFJ6421 airfoil, obtain the super lift coefficient and analyze the flow behavior with multiple vortex layers in the super-lift CFJ flows.

6. Investigate the ultra high-lift finite-span CFJ wing and apply it on a general aviation electric aircraft, analyze the lift enhancement for the takeoff condition.

7. Perform wind tunnel testing of super-lifting flow over CFJ wing with embedded Micro-compressors.

8. A conceptual design of CFJ hybrid electric regional aircraft will be performed using high-efficiency CFJ airfoil and hybrid electric distributed propulsion system.

1.5.2 Outline of Dissertation

The outline of this dissertation is organized as followed, Chapter 2 presents the overview of aircraft flow control methods, Chapter 3 introduces the derivation of the time accurate Navier-Stokes equations as the governing equations the fluid dynamics, followed by the CFD numerical methodology are presented in Chapter 4. The parameters used in CFJ performance analysis are given in Chapter 5, The validation of the IDDES method is given in Chapter 6. The parametric trade study of 2D super-lifting CFJ airfoil is given Chapter 7. The 3D unsteady IDDES investigations of super-lifting CFJ airfoil are given in Chapter 8, followed by a 3D steady RANS study of 3D super-lifting CFJ wing is given Chapter 9. The 2D RANS simulation of the CFJ cylinder is given in Chapter 10. Chapter 11 presents the experimental investigation of the super-lifting CFJ airfoil with embedded Micro-compressors in a subsonic wind tunnel.

After the investigations of super-lifting airfoils and wings, a super-lifting CFJ airfoil and a modified high-efficiency cruise CFJ airfoil are applied on a CFJ Electric Airplane to improve its takeoff performance and cruise efficiency. A conceptual design of CFJ hybrid electric regional airplane is performed in Chapter 13. The final concluding remarks and future work are summarized in Chapter 14.

CHAPTER 2

Overview of Aircraft Flow Control

2.1 Extremely Short Takeoff and Landing

The requirement for High Lift Flow Control

The design of a high-lift system is crucial for a modern airplane, since the high-lift system can bring significant performance enhancement and operating cost reduction. As Wimpress [71] stated that achieving adequate low-speed aerodynamic characteristics for takeoff and landing of modern high-performance airplanes is one of the most challenging goals in subsonic aerodynamic technology. Small changes in high-lift aerodynamic gains will exert tremendous economic benefits. For the takeoff situation, the takeoff path consists of the ground roll for acceleration to flying speed, a flare, and a climb to an altitude and the speed that are adequate to clear local obstacles. The ground roll length is determined by the installed thrust-to-weight ratio (T/W), wing loading, and the maximum lift coefficient C_{Lmax} available. The landing distance generally is defined as the overall distance covered from a 50 feet height to a final stop on the ground [71]. The landing approach speed is determined by wing loading and the maximum lift coefficient C_{Lmax}. The lift-to-drag ratio (L/D) of the landing configuration cannot be ignored. Wimpress [71] has examined the effect of

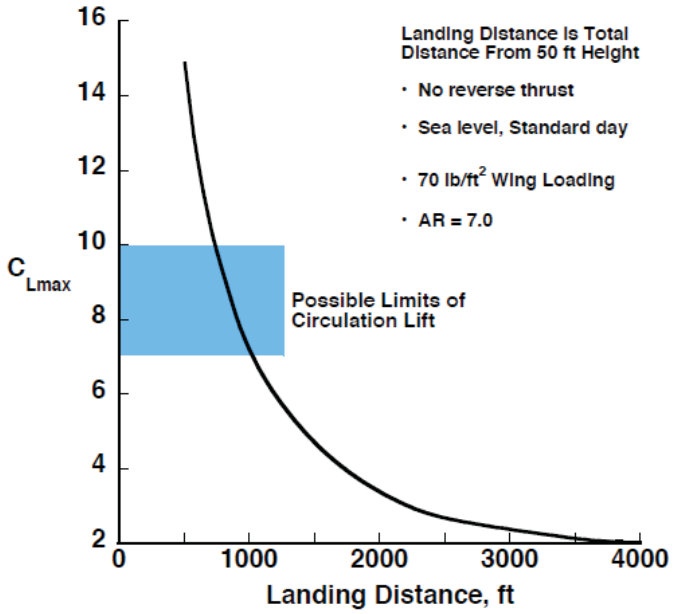

Figure 2.1: Effect of aerodynamic lift on landing distance. [9]

small changes in the aerodynamics of takeoff by an example of a vehicle that is weight limited by the available field length. At takeoff, a five percent increase in C_{Lmax} will cause 20% increase in allowable payload. At climb out, a five percent reduction in drag (increased L/D) results in a 40% increase in payload carried and 77% profit increase. For landing performance, approach speed is the most important parameter, and it can be greatly influenced by increasing C_{Lmax}. It is very clear that the landing distance decreased with the C_{Lmax} (Fig 2.1). A five percent increase in C_{Lmax} will cause the payload carried into the field increased by 65%.

The take-off distance is a function of the value of maximum lift coefficient C_{Lmax}, wing loading W/S, thrust-weight ratio T/W. One formula of take-off distance calculation given by Corke [15] is

$$s_{TO} = 20.9\frac{W}{S}\frac{W}{T}\frac{1}{C_{Lmax}} + 87\sqrt{\frac{W}{S}\frac{1}{C_{Lmax}}} \tag{2.1}$$

Corke [15] estimated that for a medium size aircraft to achieve the STOL performance that $s_{TO} \leq 1000$ feet, $C_{Lmax} \geq 5.47$. The assumption is that the altitude at take-off is sea level($\sigma = \rho_{TO}/\rho_{SL} = 1$), $W/S \approx 40$ lb/ft^2, and $T/W \approx 0.2$. For a long range aircraft, with a wind loading $W/S \approx 140$ lb/ft^2 and $T/W \approx 0.3$ (similar to Boeing 737-900, with $W/S \approx 138$ lb/ft^2 and $T/W \approx 0.310$), to accomplish the goal of $s_{TO} \leq 2000$ feet, $C_{Lmax} \geq 6.153$.

2.2 Maximum Lift Coefficient C_{Lmax}

2.2.1 Theoretical Background

The original question was asked by A. M. O. Smith (1975) [10]:" What is the maximum lift which can be obtained from an airfoil, and what is the shape of that airfoil." The pioneering researches in response to this fundamental question were conducted by A.M.O. Smith (1975) [10] and Robert H. Liebeck (1978) [72] in the 1970s. Their contribution lay the theoretical grounds for the maximum achievable lift of a single or multi-element airfoil using the classical aerodynamics. Smith (1975) [10] explained that the maximum 2D lift coefficient of a potential flow about a cylinder is 4π. Such flow has two stagnation points that move closer to each other with increasing circulation. Maximum circulation and thus lift is obtained when they coincide. Typical maximum lift coefficient of a single airfoil used in aircraft wings is about 1.5. Typical real-world application is not potential flow. Due to the viscous, rotational and compressible effects, the maximum lift coefficient in potential flow theory is far from reached.

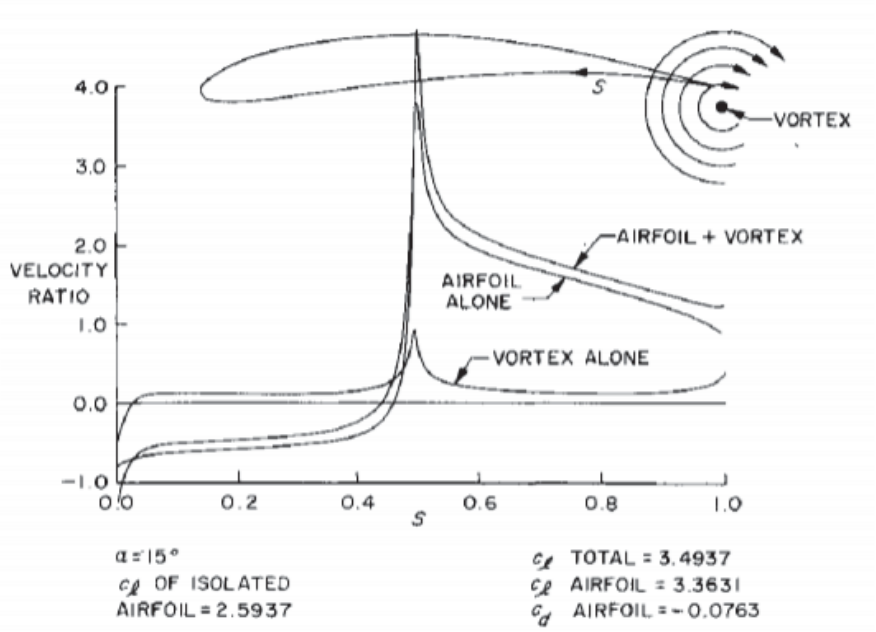

Figure 2.2: The effect of aft airfoil on the trailing edge velocity of the front airfoil [10].

Due to the flow viscosity, the airfoil boundary layer separates given a certain amount of adverse pressure gradient. The lift coefficient of an airfoil is limited by flow separation conditions. To analyze the lift limit, Liebeck (1978) [72] studied the pressure distribution along a single or multi-element airfoil which could represent the maximum lift conditions at a given Reynolds number. The Stratford pressure recovery distribution was employed as the limit that the boundary layer can sustain before separation. Flow is assumed laminar up to the start of deceleration and turbulent from there on. And the Kutta condition is applied at the trailing edge. Using the above conditions, the optimized airfoil velocity distribution was discovered, satisfying the boundary-layer theory.

For multi-element airfoils, Smith (1975) [10] indicates that the two closely positioned airfoils can be represented replacing one with a vortex which has the same

circulation. The rear airfoil has influenced on the front-airfoil in that the circulation from the rear-airfoil will increase the trailing edge velocity of the front-airfoil (see Fig. 2.2). Therefore, the front-airfoil flow will allow a delayed deceleration and a larger area of suction surface on its Cp curve. On the other hand, the flow over the rear-airfoil can again sustain the limiting Stratford pressure recovery. The combination effect makes the two-element airfoil provide a larger area on the Cp distribution is obtained with two airfoils, and hence lift force. Following this derivation, the airfoil with more elements could increase the maximum lift coefficient. The development for multi-element airfoil involving the the number of airfoil element and the chord length of each one was studied by Liebeck (1978) [72]. He indicated that the flow over the main element should be accelerated to the critical Mach number. And then the optimum design is dependent on the freestream Mach number. The chord length of the main element and the development of other elements are adjusted to gradually decrease the trailing edge velocities of the following elements (i.e. flaps) to avoid separation. From the above discussion, the single or multi-element wings in the demand of the highly efficient and short-takeoff and landing aircraft has reached a roof derived in the potential flow. Besides, building simpler and lighter high-lift systems is the trend due to the intrinsic penalty of extra weight and drag, extreme complexity, and difficulty in installation [73].

2.2.2 Lift Coefficient Limit in Potential Flow

The theoretical limit of lift coefficient is critical to provide the guidance for engineering design. This section gives the brief review of the study on the maximum limit coefficient for potential flows.

2.2.2.1 Flow Past a Circular Cylinder

Consider the inviscid flow around a circular cylinder where no separation occurs. The flow is synthesized by a uniform flow, a doublet and a vortex of strength Γ. Superposition of flow over a cylinder is shown in Fig. 2.3. The velocity stream function for the flow is

$$\psi = V_\infty r\left(1 - \frac{R^2}{r^2}\right)\sin\theta + \frac{\Gamma}{2\pi}\ln\frac{r}{R} \tag{2.2}$$

The corresponding flow field is

$$V_r = V_\infty\left(1 - \frac{R^2}{r^2}\right)\cos\theta;\ V_\theta = -V_\infty\left(1 + \frac{R^2}{r^2}\right)\sin\theta - \frac{\Gamma}{2\pi r} \tag{2.3}$$

The stagnation points can be obtained when $V_r = 0$ and $V_\theta = 0$. The resulting stagnation points depend on the value of $\Gamma/4\pi V_\infty R$. For $\Gamma/4\pi V_\infty R < 1$, both of the two stagnation points are located on the cylinder surface at (R, θ), where θ is given by $\theta = arcsin\left(-\frac{\Gamma}{4\pi V_\infty R}\right)$. If $\Gamma/4\pi V_\infty R = 1$, there is only one stagnation point on the bottom$(R, -\pi/2)$ on the cylinder surface. Larger circulation $(\Gamma/4\pi V_\infty R > 1)$ moves the stagnation points off the surface [11, 12].

For the potential flow over a lifting circular cylinder, there are infinite numbers of possible solutions, depending on the infinite number of Γ values.

2.2.2.2 Conformal Mapping

The conformal mapping is able to map any airfoil profile of a physical plane $p(x, z)$ onto a circular cylinder plane $P(X, Z)$, as shown in Fig. 2.4. The inverse transformation will therefore describe the exact solution of the flow past the original profile [12].

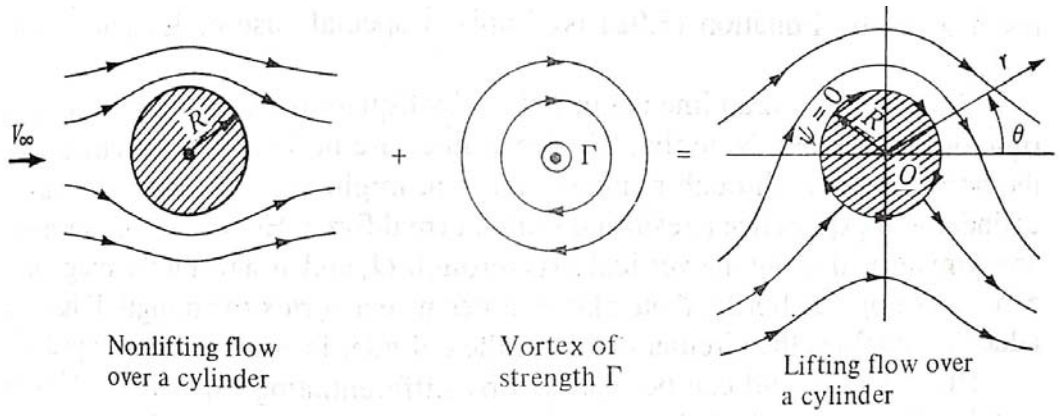

Figure 2.3: Superposition of flow over a cylinder.(Plot adopted from [11])

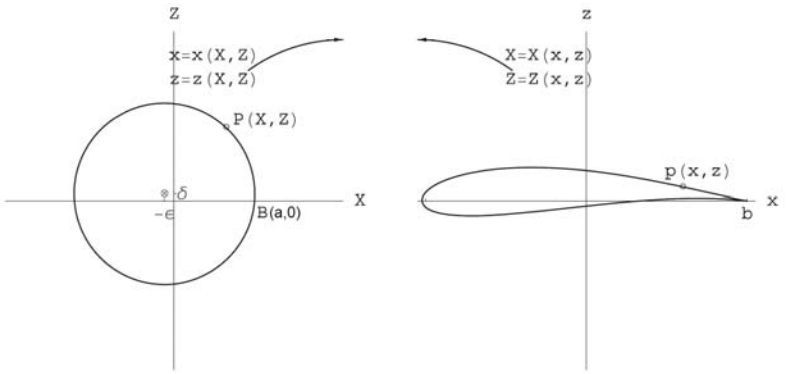

Figure 2.4: Conformal mapping from cylindrical plane (X, Z) to physical plane (x, z). (Plot is from [12])

$$x = X\left(1 + \frac{a^2}{X^2 + Z^2}\right);\ z = Z\left(1 - \frac{a^2}{X^2 + Z^2}\right) \tag{2.4}$$

where (x, z) represents the physical plane and (X, Z) represents the cylindrical plane. The cylinder of radius R, where $R^2 = (a + \epsilon)^2 + \delta^2$, centered at $X = \epsilon, Z = \delta$ and passing through point $B(a, 0)$ maps onto a family of Joukowski airfoils depending on ϵ and δ [12]. The profile has a cusp at the trailing edge, point b.

2.2.2.3 The Kutta Condition

By the Joukowski transformation, the mapping of a cylinder to an airfoil profile is singular at $B(a, 0)$, which corresponds to the cusp at the trailing edge b of the Joukowski profile. For a realistic airfoil, the fluid particle is not able to come around the trailing edge, and hence separate from the profile there. This makes the inviscid flow solution unique by fixing the circulation Γ. The Kutta condition states that the flow must leave the airfoil at the sharp trailing edge "smoothly". From the Joukowski transformation, for any flow with an incidence of α and an arbitrary circulation Γ around the cylinder, the rear stagnation point will be located at an arbitrary point. The velocity at the cusp of trailing edge is infinite. To enforce the Kutta condition, the circulation Γ is adapted to make the rear stagnation point located at the trailing edge [12].

2.2.3 Flow Past an Ellipse Airfoil

The conformal mapping from a circle centered at the origin $(0, 0)$ and of radius $b(\geq a)$ in the cylindrical plane gives an ellipse airfoil.

The velocity potential with flow incidence of α, is

$$\Phi = V_\infty(r + \frac{b^2}{r})\cos(\theta - \alpha) - \frac{\Gamma}{2\pi(\theta - \alpha)} \tag{2.5}$$

The velocity components on the cylindrical plane are,

$$V_r = 0, \quad V_\theta = -2V_\infty \sin(\theta - \alpha) - \frac{\Gamma}{2\pi b} \tag{2.6}$$

Using the Kutta condition, the circulation is obtained by $\Gamma = 4V_\infty b \sin\alpha$. Therefore, the lift coefficient is

$$C_L = \frac{2\Gamma}{V_\infty c} \tag{2.7}$$

Substituting the circulation,

$$C_L = 4\pi \frac{b^2}{b^2 + a^2} \sin\alpha = 2\pi \Big(1 + \frac{t}{c}\Big) \sin\alpha \tag{2.8}$$

where c is chord length, $c = 2(b^2 + a^2)/b$; t is the thickness, $t = 2(b^2 - a^2)/b$.

The maximum lift coefficient is achieved when the angle of attack reaches maximum $\alpha = 90°$, which is $C_{L_{max}} = 2\pi \Big(1 + \frac{t}{c}\Big)$.

A.M.O.Smith (1975) [10] states that for any airfoil, the maximum possible lift is 4π for the maximum thickness is no greater than 1. Maximum circulation and thus lift coefficient is obtained when the two stagnation points coincide. Also, the Kutta condition sets the circulation to such strength that the rear stagnation point is already at the trailing edge. It is called a natural flow [10]. For the ellipses family with no sharp trailing edge, the circulation may not be at the trailing edge. Thwaites [10] proposed the airfoil by suction to force the rear stagnation point to the rear end. Following the thought, greater circulation moves the stagnation point off the body. For instance, a Flettner Rotor generates such flows that move the stagnation off the body. However, it is considered as not realistic analog for a natural aerodynamic airfoil without flow control, where both of two stagnation points are on the surface [10].

Therefore, it can be generalized that, for an airfoil with certain thickness t and rear stagnation point at the trailing edge, the maximum possible lift coefficient is obtained for potential flow over ellipse airfoils with Kutta condition at $\sin\alpha = 1$, which is

$$C_{L_{max}} = 2\pi\left(1 + \frac{t}{c}\right) \tag{2.9}$$

where $\frac{t}{c}$ represents the airfoil thickness. The maximum lift coefficient for a cylinder can be recovered from Eq. (2.9), which is 4π for an airfoil with $t/c = 1$ at $\alpha = 90°$. It is a much higher value than what is typically obtained. The maximum lift coefficient of a single airfoil used in aircraft wings is typically about 1.5.

2.3 Conventional High Lift Systems

2.3.1 Passive High Lift Systems

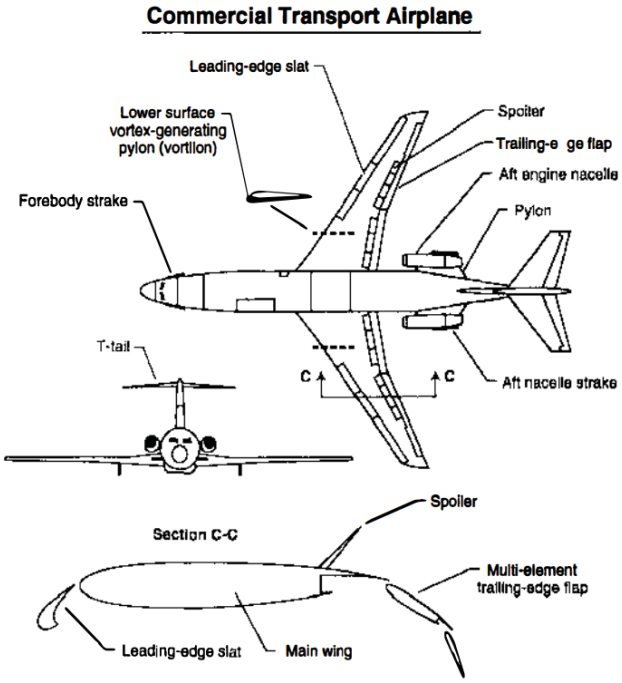

Figure 2.5: Commercial airplane high lift systems. (Plot is from [13])

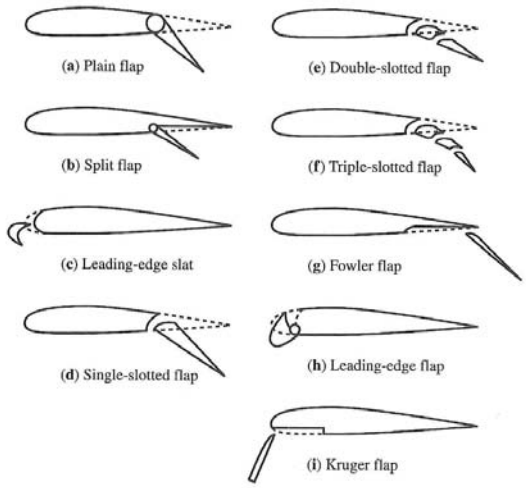

Figure 2.6: Typical high lift devices in use (Plot is from [14])

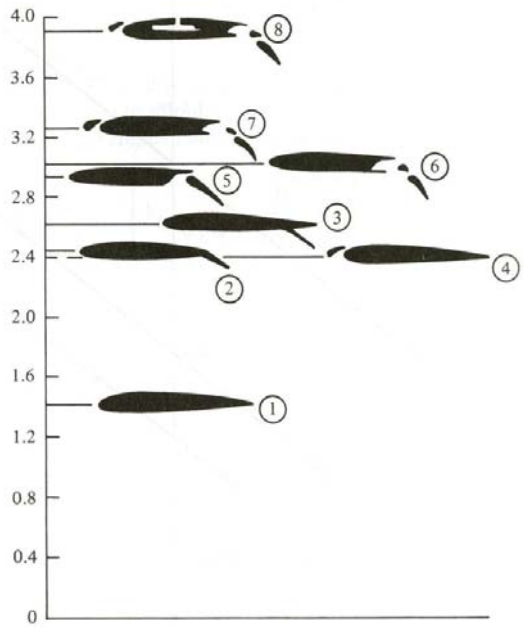

Figure 2.7: Effect of various types of high-lift devices on airfoil section maximum lift coefficient.

The high-lift system design is a critical part of the configuration design of aircraft. To achieve acceptable takeoff/landing performance as well as cruise efficiency requires a sophisticated high lift system. Conventional high-lift devices fall into two categories: passive and active. Passive lift enhancement is used in most of the modern aircraft designs, including the leading edge and trailing edge treatment (Fig. 2.5). The design principle for trailing edge is to increase its airfoil camber, for leading edge is to prevent the leading edge separation [13]. The most common types of leading-edge devices are fixed slot, leading-edge flap, Krueger flap and plain slat (slotted leading edge flap). The effectiveness of these devices depends on their deflection angle. Although trailing edge flaps gain lift enhancement at a given angle of attack, the flow stall margin is not increased. Actually, the stall margin will be decreased, which could result in leading edge separation. To resolve the this, increase the leading edge radius is generally used. The Krueger flaps with hinged flap on wing leading edge are widely employed

on large aircraft. Various flap and slat treatments are illustrated in Fig. 2.6. The section maximum lift coefficient achieved by different types of passive high-lift devices is displayed in Fig. 2.7. The 2D maximum lift coefficient C_{Lmax} attainable by these passive devices is approximately 4.0. The passive lift enhancement devices will not provide a sufficient C_{Lmax} for STOL or ESTOL capable aircraft. Therefore, active (powered-lift) approaches are needed is aircraft of this type are to be able to achieve such short take-off distances [15].

2.3.2 Active Lift Enhancement Systems

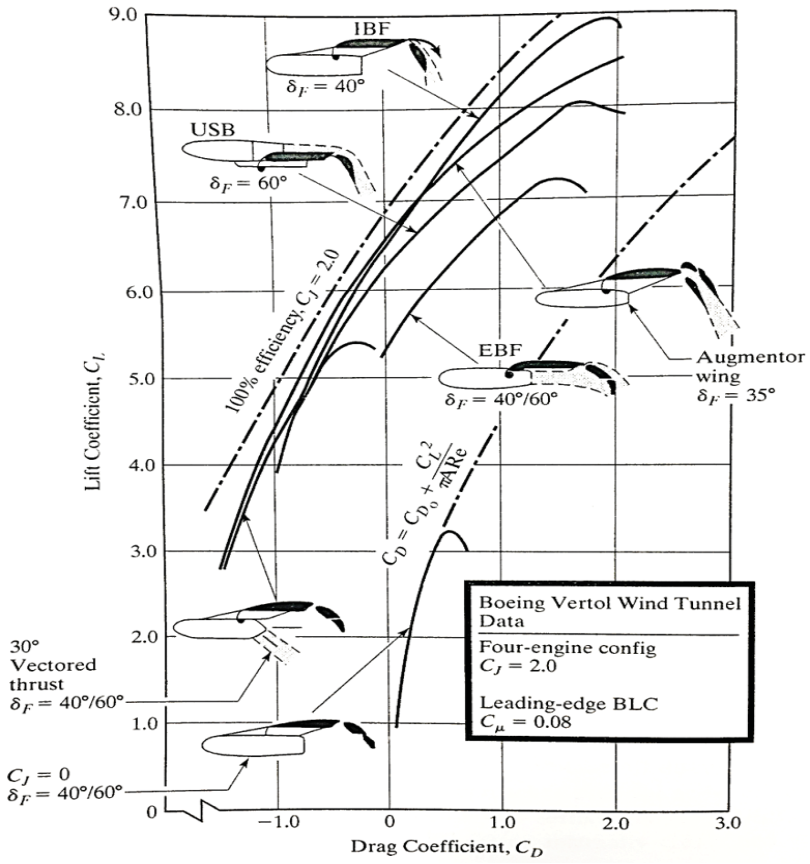

Figure 2.8: Lift and drag enhancement using different lift enhancement devices (IBF, USB, EBF, and Vectored thrust). [15]

Fig.2.8 shows some common active high-lift systems and their corresponding achievable lift coefficients [15]. Three categories are identified: upper surface blowing (USB), externally blown flaps (EBF), and internally blown flaps (IBF). The upper surface blowing (USB) uses a high velocity air stream directed over the upper surface of the main wing. The engines are installed above and forward of the main wing to provide the high-speed flow. The principle for the blown flaps is that a high velocity air stream is directed specifically at the trailing edge flaps. For externally blown flaps (EBF), the air stream is directly obtained from the engine exhaust. The boundary layer over the flaps can be energized by the engine exhaust. The YC-15 and C-17 Globemaster used this arrangement. On the other hand, the Internally blown flaps (IBF) use duct system to direct a certain amount of the engine exhaust, onto the upper surface of the trailing-edge flaps. The IBF is used in Boeing YC-14. In addition to the enhanced aerodynamic lift that these three approaches provide, they also generate A component of downward thrust is generated by the aforementioned powered-lift approaches. Note that the Coanda effect is used; it means that an air stream will follow a curved surface of a body.

The effectiveness of these active approaches is also summarized in Fig. 2.8 in terms of the drag polar C_L vesus C_D. Any of these are capable of providing lift coefficient in excess of 7.0. The vectored thrust, USB, and IBF have lower drag coefficients than EBF. Also, the effectiveness of the USB is a function of the jet coefficient defined as $C_J = \frac{Thrust}{q\ S_W}$.

There are different requirements for each of those active lift enhancement method respectively [15]. The IBF requires internal ducting that can be heavy and result in internal momentum loss. The USB blown flap generally requires a heat-resistant

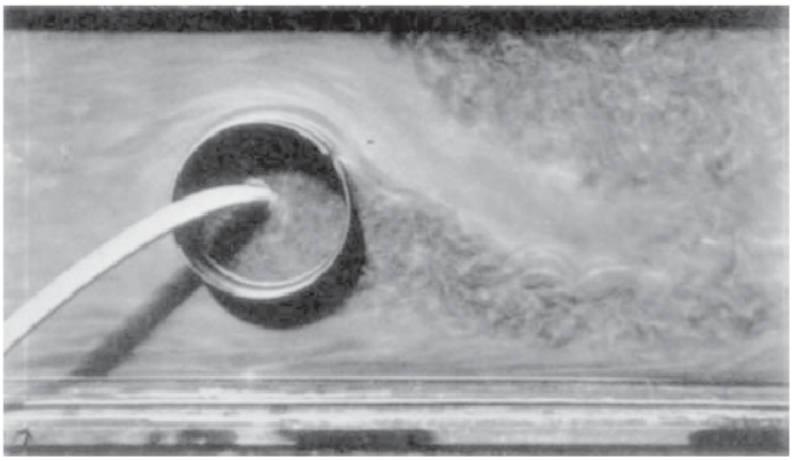

Figure 2.9: Prandtl's photograph of suction flow control of a cylinder

material on the wing flap because of the hot exhaust air, which adds much weight. The EBF approach only directs the hot exhaust over the flaps which requires heat-resistant materials covered on the wing and flap. The weight penalty increases. Consequently, the power-lift devices are not used widely on commercial aircraft because of those unfavorable features, i.e., increased complexity, weight penalty, noise production, and reduced Payloads.

2.4 Flow Control Overview

In 1904, Prandtl developed the epoch-making boundary-layer theory. In Prandtl's experiment, he firstly used the suction flow control method to suppress flow separation on a circular cylinder as the famous flow-visualization (Fig. 2.9) As Gad-el-Hak (1996) [74] stated, the flow control science originates with Prandtl's explanation of the boundary layer. The researchers in the field of aeronautics explored the boundary-layer control method to delay separation and achieve lift enhancement for aircraft thereafter [75].

Flow control methods can be categorized into the passive and active, dependent on whether external energy is introduced in the flow system. The passive control technique is an important part in that it has wide applicability as well as the various advantages. Besides, the passive techniques can provide a benchmark against which to evaluate active methods [43]. Also, the passive devices is popular in real-world applications for its light weight, less complexity and expenses in design and manufacture, and easier maintenance. For instance,vortex generators (VG) is a typical passive boundary layer control technique, which is commonly used in aviation and automobiles. The vortex generators use vane-type device with height h on the order of the boundary-layer thickness, δ to control flow separation. The flow control mechanism is to increase the near-wall momentum through the momentum transfer from the free-stream flow.

Active Flow Control (AFC) has attracted tremendous interests in the last few decades [43]. Tremendous advancement has been achieved of AFC, which is provided by innovation, experience and sheer luck. Therefore, AFC is sometimes interpreted as "The ART of Flow Control" [74]. Though many of these technologies are in their embryonic stage and will require many more years of development plus advances in the supporting technologies, the potential benefit of AFC materialized their potential payoffs which is desirable for future aviation. Plenty of potential applications are identified, such as boundary layer (separation) control, mixing control, vortex control, circulation control, boundary layer control and shock/boundary layer interactions. Several comprehensive reviews has been conducted by Gad el-Hak (1996) [74], Kral(2000) [76], and Jahanmiri (2010) [30].

In contrast to the passive techniques, two primary advantages of AFC can be identified [76]. The first advantage of AFC is that it can leverage and control flow stability to achieve desired flow control effectiveness at the expense of a small amount of energy input. On the contrary, the passive control techniques are aimed at certain operating conditions, since the passive flow control is a point design. As conditions vary during flight, the effectiveness of passive techniques may diminish [43]. At some certain conditions, the passive techniques may have adverse effects on the system performance [77].

2.5 High Lift Flow Control

Due to the drawback of complicated high-lift systems and powered-lift enhancement, the persistent pursuing for high lift flow control has been conducted for decades.

2.5.1 Boundary Layer Control

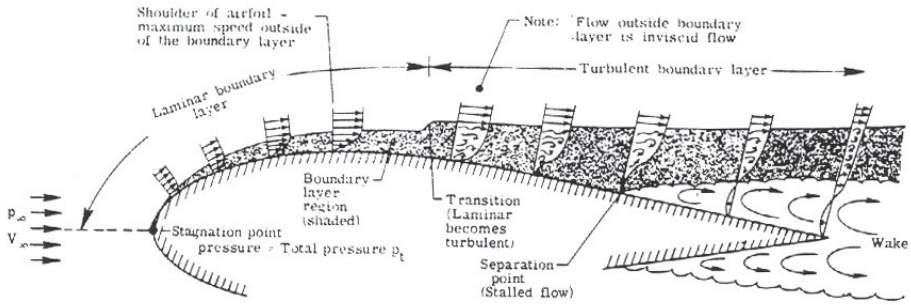

Figure 2.10: Boundary layer development on an airfoil.

It is believed that the first flow control design was to use suction to delay flow separation by Prandtl. Fig. 2.10 shows the boundary layer on an airfoil, where, for reasons of clarity, the dimension in the transverse direction is enlarged greatly.

The laminar boundary layer increases in thickness with increased distance from the wing leading edge. As with the plate, a laminar boundary layer begins to develop at the nose of the airfoil. Some distance back from the leading edge, the laminar flow begins an oscillatory disturbance which is unstable. After a certain distance x_{crit} along the contour of the body, the laminar-turbulent transition occurs, so that the boundary layer is turbulent for $x > x_{crit}$. Thus, a transition takes place in which the laminar boundary layer decays into a turbulent boundary layer. The thin layer of air adjacent to the surface of an airfoil shows reduced local velocities due to the effect of skin friction. At high angles of attack, the boundary layer on the upper surface can not sustain flow attachment because of large adverse pressure gradient. When this happens, the flow separates from the surface and stall occurs.

Boundary Layer Control (BLC), refers to the flow control technique in an attempt to achieve lift enhancement based on boundary layer theory. Various BLC methods have been widely investigated since the born of boundary layer theory from the 1920s until the 1970s [75]. In the 1970s, the coherent vortex structures and turbulent instabilities were discovered. These findings incubated a variety of instability control methods for large-scale performance improvements.

2.5.1.1 Traditional Boundary Layer Control Method

Steady Blowing and Suction

Various boundary layer control were explored by pioneer researchers in the aeronautical area. Blowing and suction are considered as most common boundary layer control methods. After Prandtl's boundary layer suction experiment, Baumann (1921) used air jets emanating from slots to control the flow separation. Knight

and Bamber (1929) explored the effect of the geometry of air jet slot (slot width, slot location), and the jet flow rate on the lift enhancement. Their experiment demonstrated that for a 2D airfoil, the aerodynamic efficiency L/D can be increased by a 151%. Regarding suction flow control, Ackeret et al. (1926) and Schrenk (1928, 1931) performed experiment on airfoils with steady suction. [75, 78]

To remove the leading edge separation associated with the thinner airfoil, leading-edge suction is applied in a flight test by Hunter and Johnson (1954) [75]. The distributed suction was attempted to control laminar boundary layer transition and turbulent boundary layers separation by Raspet and his coworkers at Mississippi State University in the 1950s. Raspet et al. was able to achieve a laminar boundary layer over 95% of the chord of a TG-3A glider wing up to a section lift coefficient of 0.93 (Raspet, 1951, 1952). Cornish (1953) deployed the distributed suction on a TG-3A glider, which could increase the maximum lift coefficient from 1.38 to 2.28. Distributed suction was next applied to a powered aircraft, an L-21, which was the military version of the Piper PA-18 "Super Cub" (Raspet et al., 1956). The maximum flaps-down lift coefficient obtained was 3.98. An overview of development of blowing and suction boundary layer control is given in [75].

Through the investigation process of flow control, the momentum coefficient C_μ was discovered as an effective measurement for the effectiveness of the blowing and suction jets, which directly affect lift enhancement. It is defined as $C_\mu = \frac{q_m V_j}{q_0 S}$, firstly determined by Poisson-Quinton (1948) [75]. In the definition, q_m and V_j are the mass flow rate and jet velocity, respectively. The normalization procedure uses the dynamic pressure $q = 0.5\rho V^2$and planform area S.

2.5.1.2 Unsteady Flow Control

Due to the high momentum and power requirements for steady flow control method, unsteady boundary-layer separation control was studied extensively. Periodic excitation Unsteady periodic excitation flow control is based on the natural flow instability phenomena (such as control of flow separation), has the potential to reduce the mass flux and improve efficacy.

Oscillatory Blowing Research in NASA

The boundary-layer separation control on 2D airfoils using periodic excitation momentum through a slot was demonstrated in both low [79] and high [80] Reynolds number wind-tunnel experiments by Seifert et al. The mechanism of the periodic excitation is because mixing enhancement between the higher momentum fluid above the otherwise separated region and the lower momentum fluid near the surface. In the wind tunnel tests, two unswept NACA 0015 models were constructed. Two excitation locations are tested: the trailing edge of the main element and the leading edge of the flap. The results indicated that oscillatory blowing at 10% chord location delays airfoil stall. And oscillatory blowing at the flap shoulder also improves the flap performance. In this experiment, an oscillatory blowing valve was used to generate the periodic disturbance. It is also indicated that other type of actuators can also be used as an alternative to generate the periodic excitation [79, 81]. Greenblatt et al. [82] studied the effectiveness of periodic excitation on lift enhancement with flap on. The flap deflection angle of δ_f ¿ 40 ° was selected, and excitation was at the flap shoulder. The wind tunnel testing indicated that if the flap deflection δ_f ¿ 20 °, a lift increment of $\Delta C_L = 0.82$ was generated using the periodic excitation. The advantages of

oscillatory blowing over steady tangential blowing is that to obtain comparable gains, oscillatory blowing generally requires much smaller amount of oscillatory momentum [76].

Pulsed Blowing and Vortex Generator Jets by DLR

The pulsed blowing methods by skewed round jet at leading edge and slot actuator for flap trailing edge for separation control has been investigated by Ciobaca (2013) at DLR. The flow control implementation involves constant blowing vortex generator jets(VGJs) on the leading edge and pulsed blowing slot actuation at the flap [16]. The leading edge flow control employs round inclined holes, which is known as vortex generator jet. At the trailing edge flap, the actuator chambers have a rectangular-exit shape that is used for the pulsed blowing flow control method. A pulsed blowing application on the flap of a 2-element high-lift airfoil DLR-F15 is sketched in Fig. 2.11 , for a moderate angle of attack. The time-averaged vorticity distribution shows that the size of flow separation is reduced significantly by the pulsed blowing flow control.

Fig. 2.11 illustrates the simulation results for different blowing momentum coefficient C_μ. The maximum lift coefficient achieved by the current actuation system is ≈ 3.15 There is a minimum blowing momentum that must be exceeded in order to obtain a benefit from the actuation. In other words, the actuation system has no effect on lift enhancement when $C_\mu \approx 0.1$. Also, saturation can be reached, which corresponds to an attached flow downstream the actuation.

Radespiel et al. (2016) [17] reviewed recent progress in the steady blowing using tangential blowing and oblique blowing strategy (or, Vortex Generators Jet (VGJs)).

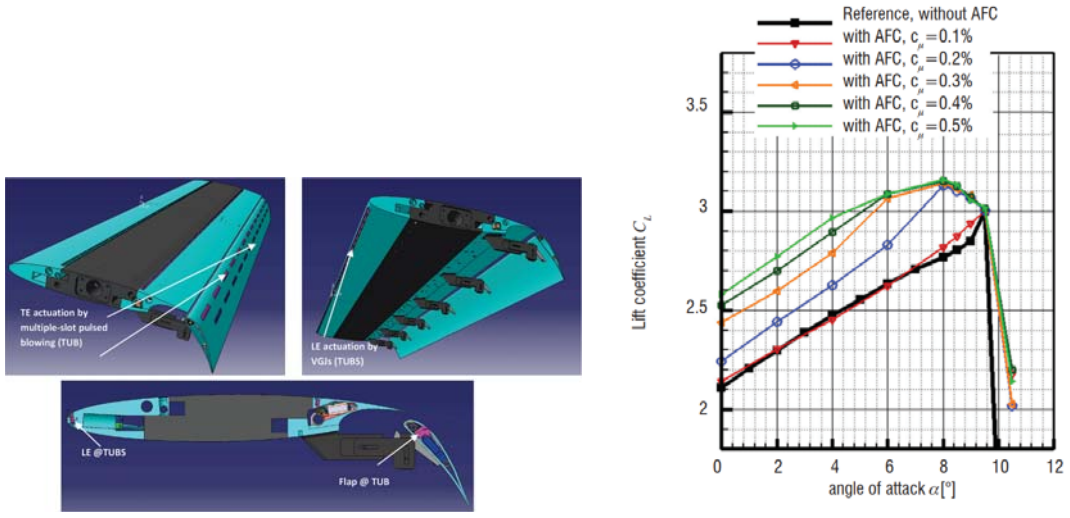

Figure 2.11: The actuation systems implemented on the DLR F15 model and lift coefficient vesus [16]

The tangential blowing strategy uses thin wall jets to overcome the adverse pressure gradients usually from large flow turning rates. It usually exploits the potentials of the Coanda effect, such as using blown flap. In contrast to tangential blowing, the working principle of the oblique blowing air jets is to generate longitudinal vortices in the boundary layer. The longitudinal vortices lead to the convective redistribution of momentum in the boundary layer and enhance turbulent momentum transport. This method re-arranges momentum in boundary layers, using the localized blowing from orifices, that produces desired longitudinal vorticity at certain locations. The VGJs were implemented to delay flow separation and airfoil stall on the DLR-F15 two-element airfoil with a slotted Fowler flap [17] .

Radespiel et al. (2016) states that the oblique blowing has the benefits of maximum lift coefficients enhancement and higher lift gain factors. However, the VGJs has limited capacity of maximum lift coefficient enhancement which is attributed to limited ability to rearrange momentum by tangential blowing. In other words, VGJs can be effective to control flow separation to a limited extent. Therefore, the max-

imum achievable lift coefficient is comparatively lower than the tangential blowing. It is also noted that the lift gain factors of VGJs decrease as the C_{Lmax} approaches 3.5. The lift enhancement using VGJs upstream of a drooped spoiler was plotted in Fig. 2.12. The potentials of tangential blowing to obtain lift enhancement are larger, as tangential blowing could provide large flow turning on airfoils. The achievable lift coefficients by VGJs are in the range of 2-5.

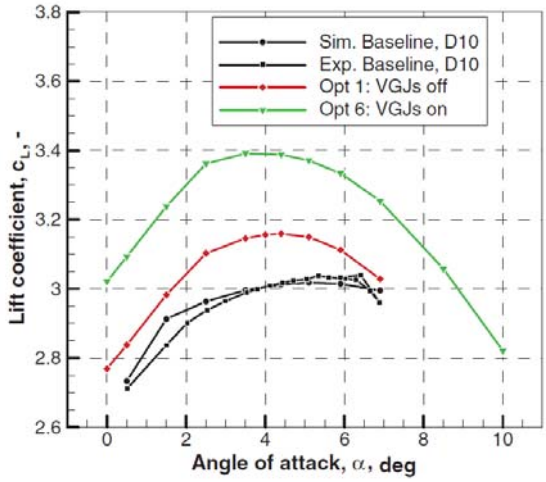

Figure 2.12: Lift curves of two-element airfoil with drooped spoiler; setting optimization without and with VGJs [17].

Sweeping Jet

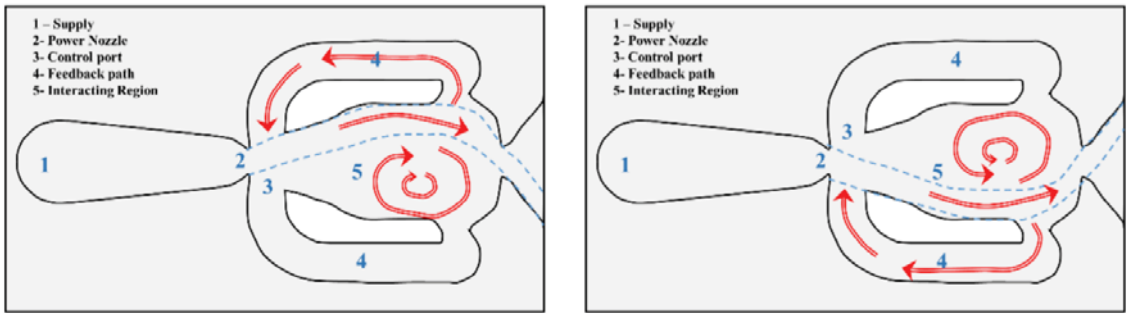

Figure 2.13: Working principle of a sweeping jet actuator internal flow [18].

The Sweeping Jet was introduced in 1950s. The main advantages of sweeping jets is that it only needs a small amount of steady compressed air supply and no moving parts required for the actuation system. Sweeping jet actuators can re-energize the boundary layer and sweep jet flow smoothly to cover a wide wing area in the spanwise direction. The working principal is illustrated in Fig. 2.13. The benefit for sweeping jets is that even with a low level of C_μ, they have the capacity to remove airflow separation on an airfoil. With an increased C_μ, it even causes a general augmentation of the lift over drag ratio.

The recent implementation of sweeping jet is targeted at the vertical tail of a civil aircraft [19]. The flow control efficiency of sweeping jet actuator was tested on a subscale and full-scale vertical tail of a civil aircraft in wind tunnel tests [83–85]. Seele et al. (2012-2013) [83,84] tested sweeping jet system to a subscale (14%) vertical tail model at Caltech Lucas wind tunnel. Total 32 sweeping jet actuators were placed on the rudder and on the stabilizer trailing edge, respectively, in two series of wind tunnel tests. Graff et al. (2013) [85] further examined different actuator size and spacing effects and discussed the effects of the sweeping jet actuators on the spanwise flow over swept wings. The researches [19, 85] reported a significant side force enhancement of approximately 50% at large rudder deflections ($\delta_{Rudder} = 30°$), zero sideslip ($\beta = 0$), and a momentum coefficient C_μ of 1.7%.

A Boeing 757 vertical tail [18, 19] were tested in the National Full-Scale Aerodynamics Complex (NFAC) (Fig. 2.14). The vertical tail model was tested at a nominal speed of Ma $\approx$ 0.15 and Re $\approx$ 15 million. Greater than 20% increments in side force were achieved at the two sideslip angles with a 31-actuator AFC configuration [86]. The flow is attached on the rudder, which resulted in 20% and greater increases in side

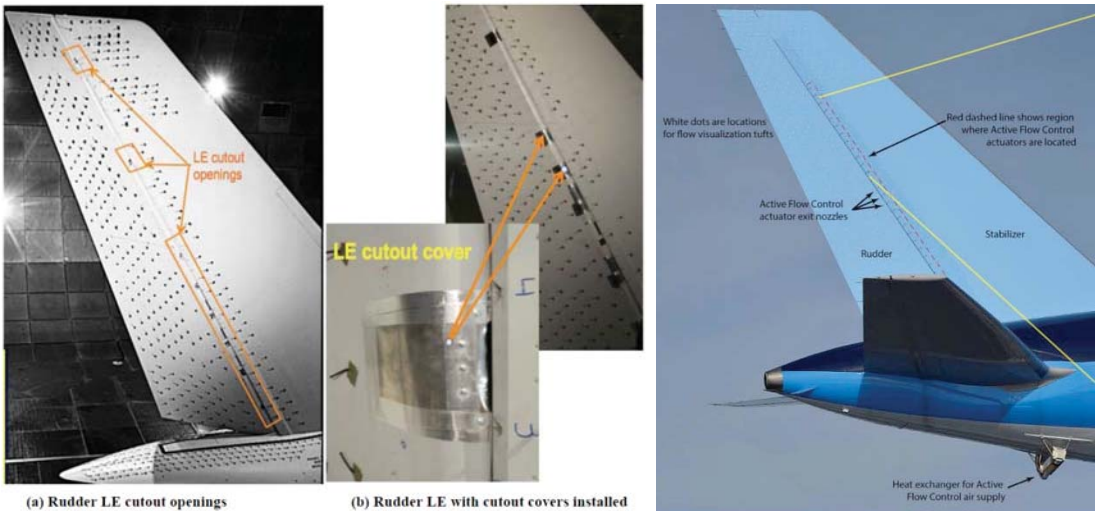

Figure 2.14: Sweeping jet actuator arrangement on the 757 vertical tail [19]

force for the maximum rudder deflection of 30° at 0° and -7.5° sideslip angles. The AFC-enhanced vertical tail technology was flown on the Boeing 757 ecoDemonstrator in the spring of 2015 [18]. It is noted that the flow cones on the rudder indicated strong flow alignment (flow attachment) along the rudder span with the AFC turned on, as opposed to massive flow separation observed for AFC off. It was estimated that the induced reduction in fuel consumption can achieve 15,500 gallons/airplane/year [19].

Synthetic Jet

The name "Synthetic Jet" was defined by Glezer [87], since the jet-like flow is synthesized from the working fluid surrounding in the system. The synthetic jet is generated by the periodic expulsion and suction of fluid from an orifice as shown in Fig. 2.15. A schematic of this actuator is shown in 2.15. The expulsion and suction at the orifice is droved by the back and forth movement of a diaphragm inside the cavity. In the expulsion phase, fluid is ejected out from the orifice, rolls up and forms a vortex ring. The ambient fluid surrounding the orifice drawn back into the cavity while the

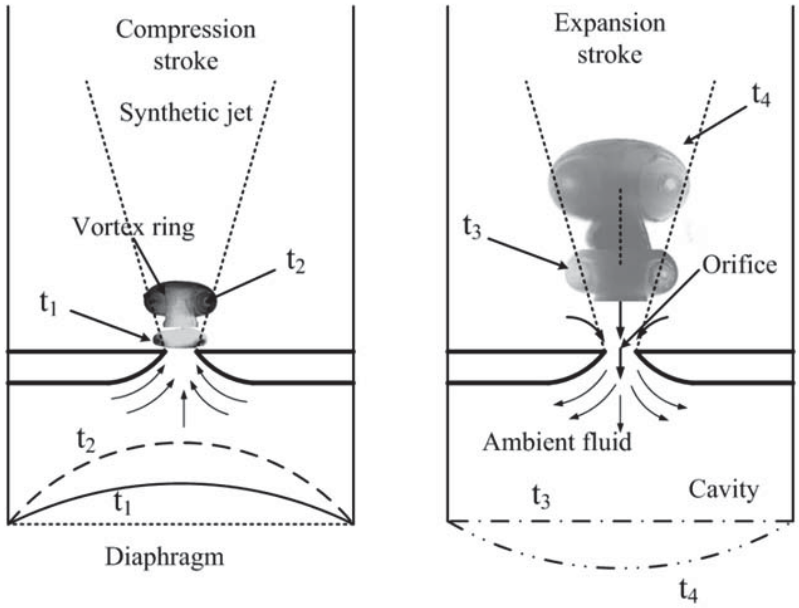

Figure 2.15: Synthetic jet evolution during forward and backward motion of a diaphragm [20].

vortex ring is moved away from the orifice due to its self-induced velocity during the suction phase at the design conditions An isolated synthetic jet is produced by the interactions of a train of vortices that are typically formed by alternating momentary ejection and suction of fluid across an orifice such that the net mass flux is zero [20]. No mass injection is needed for the oscillatory surfaces within a cavity. The flow field of synthetic jet flow control can be separated into two regions based on its highly transient characteristics, which is the developing region and developed region. In the developing region close to the orifice, the flow is dominated by the formation of periodic vortex rings and their interactions. In the developed region away from the orifice, the vortical flow structures break down into turbulence [88] Synthetic jet can be produced using different activation methods such as piezoelectric (thunder actuators, bimorphs, plasma actuators), acoustics (loudspeakers), electromagnetic (solenoids) and mechanical driver (piston). Piston and loudspeaker can be used for generating the SJ where the response time and jet size are less critical.

Smith et al. (1998) [89] investigate the flow separation control with a synthetic jet using experimental study. The synthetic jet is placed at the leading edge of a thick airfoil to reattach the separated shear layer. The lift coefficient was obtained more than doubled.The effect of jet location and amplitude on the separation control efficiency was also examined. Smith and Glezer (1997) and Smith et al. (1999) studied the effect of adjacent synthetic jets on controlled interactions. The jet formation near the orifice has a strong entrainment of ambient fluid. By this the dynamic vectoring of adjacent jets is exploited by varying the relative phases of driving waveforms. [76] Amitay et al. (2002) performed a wind tunnel study on the synthetic jets pairing and cross flows. The cross flow attached separated shear layer to the airfoil similar to Coanda effect. A specially designed periodic array of synthetic jet actuators by Rathnasingham et al. (2003) [90] placed an array of synthetic jet actuators in the near-wall region of a turbulent boundary layer. The wall pressure fluctuations and the mean wall shear stress were also reduced by up to 15% and 7% respectively and streamwise velocity fluctuations were reduced by 30%. Amitay et al. (2006) [91] studied the suppression of post-stall separation over an unconventional 2-D airfoil using synthetic jet actuators showed a complete suppression of separation over a range of AoAs. The airfoil stalled at the angle of attack greater than 5° could continue to get attached to the surface up to 25° using the synthetic jets. It was also discovered that the synthetic jets are most effective as the frequencies exceed the characteristic vortex shedding frequency downstream the airfoil.

Moving Surface

The concept of moving surface boundary-layer control, as applied to a Joukowsky airfoil, is investigated by Modi and colleagues [21]. The implementation was applied at different locations, the leading edge and/or trailing edge, and upper surface of the airfoil. The results shows rotating cylinder can lead to a significant lift enhancement and a delay in stall AoA. The combinations of cylinder geometry, rotating speed and location, can be manipulated to satisfy the desired performance to obtain favorable results over range of AoA. The momentum injection through moving surfaces, achieved here by introduction of bearing mounted, motor driven, hollow cylinders, can reduce the pressure drag as well as delay separation onset. Fig.2.16 shows a variety of rotating flow control family on a 2D airfoils at different positions used to inject momentum. Modi [21] has conducted a series of wind tunnel experiment over an extended range of the AoA a and cylinder rotational speeds at a Reynolds number of 4.62×10^4. The effects of modification of the airfoil with the different configurations has been tested. The leading-edge cylinder is quite effective in extending the lift curve,substantially increasing the maximum lift coefficient C_{Lmax} of 2, as compared to the C_{Lmax} of 0.88 for baseline airfoil.

2.5.2 Circulation Control

Circulation Control (CC) flow control method was discovered in 1935 when Henry Coandă The circulation control technology has been in the research and development phase for almost 80 years since it is first recorded by H. Hagedorn and P. Ruden, in 1938, who noticed a significant increase in lift at high blowing rates during investigations into boundary layer control on a flap . The circulation control method is

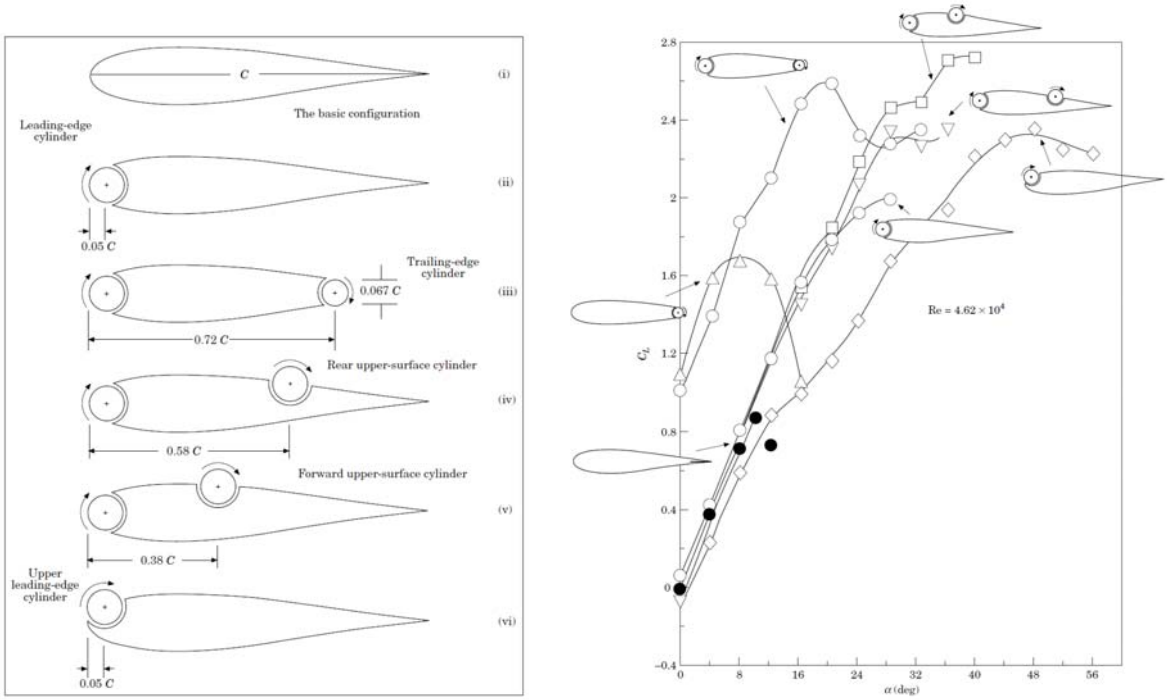

(a) Different configurations (b) Lift coefficient

Figure 2.16: Various rotating-cylinder configurations. [21]

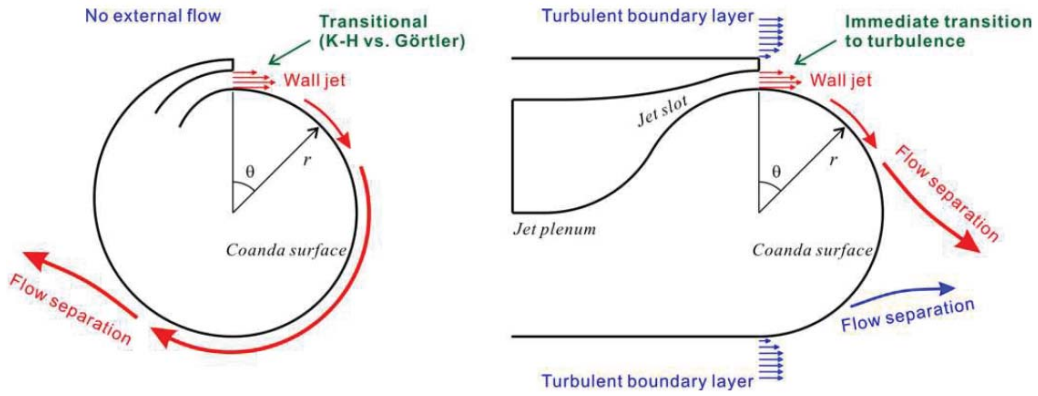

Figure 2.17: Coandă effect over a cylinder over airfoil around trailing edge.

primarily for fixed wing aircraft with the early models referred to as “blown flaps”. In the early stage, circulation control technology was used on the main wing of an aircraft in conjunction with a Coanda surface, such as a rounded trailing edge or a deployable flap [92]. Those fundamental research during this time proved a that small amount of exit jet velocity could have a large impact on the aerodynamics of an airfoil. Circulation control has been successfully experimentally tested in generating high lift [9].

The jet was initially designed to entrains the boundary layer to prevent aft flow separation at very low amount of jet mass flow rates, and thus is an effective form of boundary layer separation control. As the jet strength are enhanced, the blowing jet continues to wrap around the Coanda surface causing a rise in the local static pressure. The pressure increases, along with viscous shear stress, and centrifugal forces, lead to jet separation from the rounded trailing edge, detach a new stagnation point off the airfoil.

Traditional circulation control wings (CCW) use steady blowing at the trailing edge to turn the flow over a curved trailing edge. Supercirculation flow field and high lift are generated by the steady blowing. Despite the favorable lift enhancement ,due to the systems penalties dealing with engine bleed requirements, CCW is rarely applied on a real aircraft [9].

Physical regimes for CC airfoil

To split the boundary layer control and circulation control, the most commonly used parameter is the momentum coefficient, C_μ. The performance of the flow controlled airfoil is determined C_μ, which characterizes the jet characteristics and the

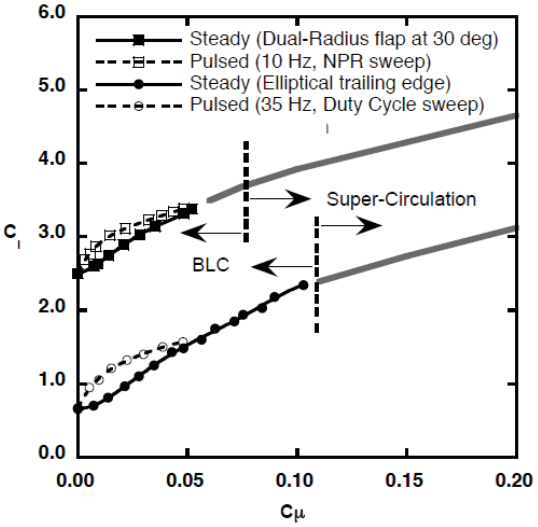

Figure 2.18: BLC and super-circulation regimes for CC airfoil [9]

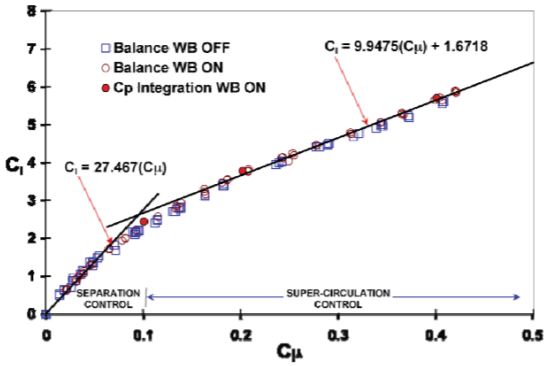

Figure 2.19: Circulation control flow regimes showing sensitivities and influence of wall blowing [22]

airfoil geometry, particularly on the surface near the jet exit. The circulation control has two physical regimes as a function of blowing jet strength. The two regimes are commonly referred to as separation control, or boundary layer control and supercirculation control. Different global efficiencies determined by the change in unit lift due to the change in unit blowing are shown by the data in Fig. 2.18 [9] and 2.19 [22].

The physical description of the efficiencies of these regimes is demonstrated by the relationship of the jet separation location on the trailing edge surface and the interaction of the jet with the incoming flow. The flow separation is typically dependent on the pressure gradient along the surface. The flow separation is delayed when a thin jet is applied on a airfoil. This thin jet entrains and accelerates the flow resulting in increase in flow turning. The leading edge stagnation region is also altered. Thus, the overall circulation around the airfoil and the lift will be enhanced. The regime transition can not be clearly identified for some airfoil with various sharpness of the trailing edge Different trailing edge geometries that include a hinged flapped

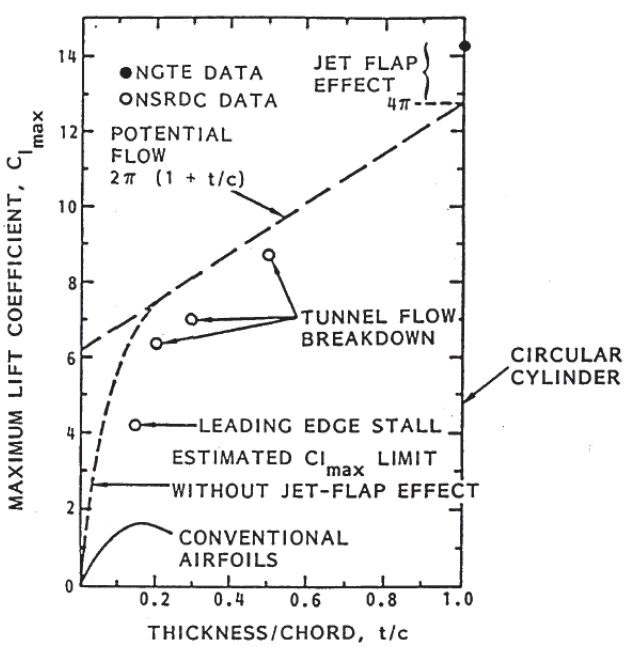

Figure 2.20: Maximum Lift coefficient at different thickness/chord ratio [23]

geometry and a circular geometry was studied as shown in Fig. 2.21 [22]. Englar [23] analyzed the flow phenomena at different thickness ratios of an airfoil as compared to the potential flow lift coefficient limit.

Englar et al. (2009) [24] presented and discussed the significance of results from two benchmark experimental wind-tunnel evaluations that were conducted to provide physics and performance characteristics to improve the CFD simulation tools.

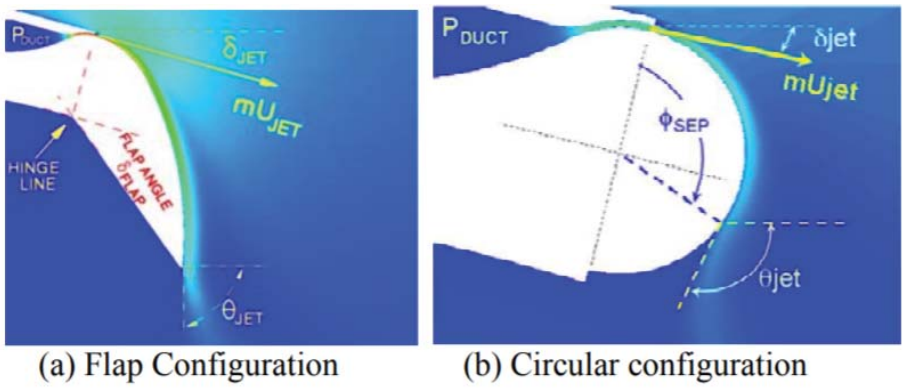

Figure 2.21: Example of two Coanda surfaces. [22]

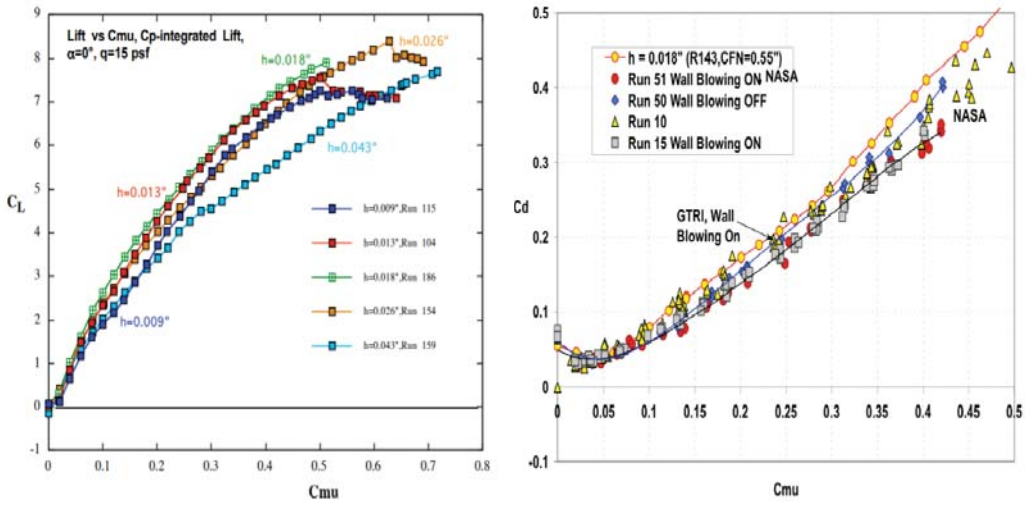

Figure 2.22: Lift and drag variation with C_μ at $\alpha = 0°$ [24].

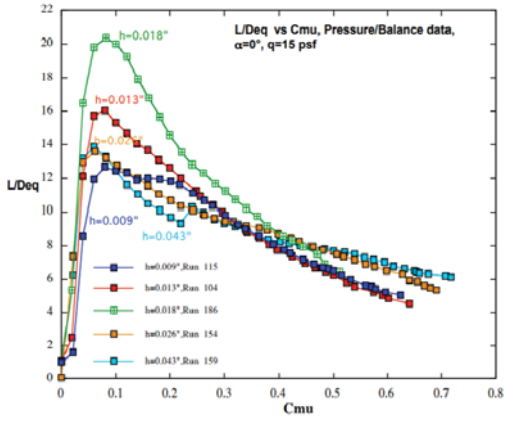

Figure 2.23: Equivalent Lift-Drag ratio with C_μ at $\alpha = 0°$. [24]

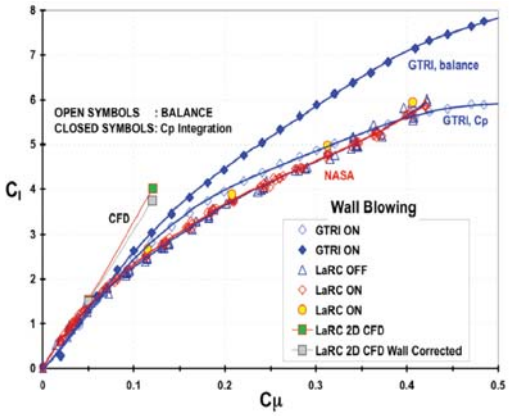

Figure 2.24: Lift results obtained at GTRI and NASA LaRC experiments. [24]

The experimental data has highlighted the physics of separation and supercirculation related to Circulation Control on high lift and drag-control airfoils. Lift coefficients over 8 at α=0° have been demonstrated, as has drag increase or decrease by variation in blowing. Fig.2.22 show lift variation with blowing at $\alpha = 0°$ for a family of nominal slot heights. The equivalent aerodynamic efficiency is defined as L/D_{eq} $= C_L/(C_D + C_\mu)$ to account for the jet momentum expended. The L/D_{eq} variation

with C_μ is shown in Fig. 2.23. The most efficient configuration is found to be the intermediate slot height h = 0.018 inch in the C_L range of 1.5 to 2.5.

2.5.2.1 Pulsed Blowing Circulation Control

Jones et al. [93] performed an investigation on unsteady pulsed circulation control (pulsed CC). The purpose is to reduce the mass flow requirements, which is considered as a major concern to the steady blowing technology [9]. A novel dual-blowing concept for the trailing edge was introduced in a General Aviation Circulation Control (GACC) airfoil. The idea is to reduce the cruise performance penalty by creating a "virtual trailing edge" at the trailing edge using two streams of simultaneous blowing air from both the upper and lower surface. Their results indicated a 48% reduction in mass flow rates can be obtained with pulsed CC. Another advantage for the dual blowing concept is providing the opportunity to make the entire wing into a distributed control surface. Therefore, spanwise variation of the upper and lower surface blowing may provide a distributed or tailored load distribution, pneumatic ailerons and split flaps [43].

Jones and Englar [25] investigated pulsed circulation control for traditional rounded Coanda surfaces (circular and elliptical) and for a dual-radius simply hinged Coanda flap. The lift coefficient C_μ is shown in Fig. 2.25. Both configurations show the mass flow reductions of about 50% for ΔC_L of 0.3 to 0.4 can be achieved. They demonstrated that the pulsed jet with different frequencies and duty cycles, could have a significant impact on the required mass flow to achieve a desired performance. However, their results are limited to the boundary layer control (BLC) region shown

in Fig. 2.18. It is not clear the effects and benefits of pulsing blowing in the super-circulation range with higher ΔC_L for higher ΔC_L [9].

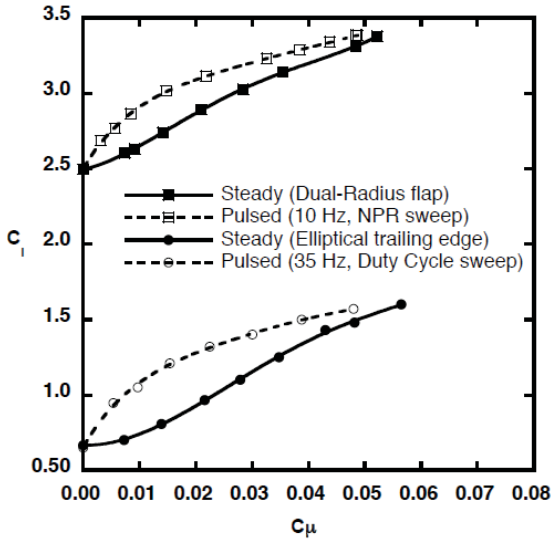

Figure 2.25: Comparison between pulsed and steady blowing circulation control [25].

2.5.2.2 Transonic CCW Wing

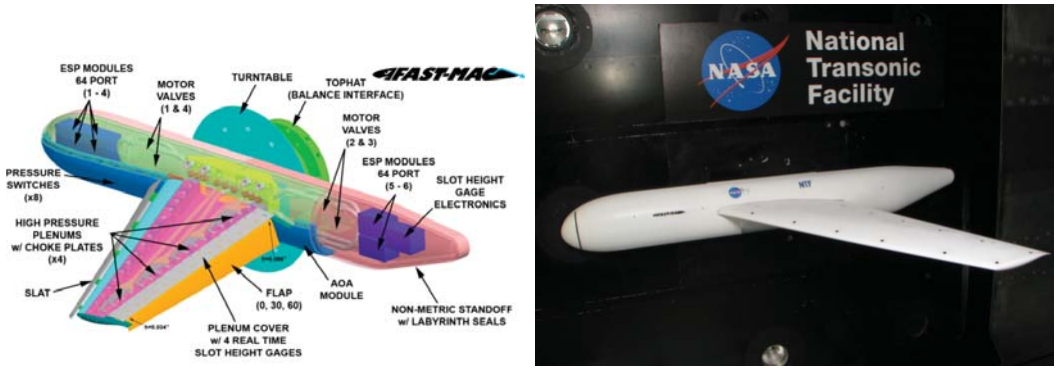

Figure 2.26: FAST-MAC model in high-lift mode(left), FAST-MAC model in cruise mode mounted on the sidewall (right) [26]

Due to the lack of Reynolds number scaling data, the application of CCW technique is limited. To resolve this, NASA has launched a new circulation control study [26], FAST-MAC model in the National Transonic Facility (NTF) at the NASA

Langley Research Center. And a series of wind tunnel testing have been conducted. The FAST-MAC model is depicted in Fig. 2.26. This model is designed to be tested at realistic flight Reynolds numbers. The model is uniquely designed in that it will allow circulation control strategies to be evaluated at transonic Mach numbers during cruise. The outer mold line of the model was designed for a cruise Mach number of 0.85, a lift coefficient of 0.50, at a Reynolds number based on mean aerodynamic chord. In the low-speed high-lift mode, the circulation control is applied where a high momentum jet from a blowing slot is directed over a simple short-chord hinged flap.

For the low-speed high-lift testing, the circulation control was directed over a 30°-60° simple hinged trailing edge flap, while a conventional slat was mounted on the leading edge. Three wind tunnel testing [26–28] have been performed from 2012 to 2018. The low speed testing was primarily conducted at a Mach number of 0.10 and 0.20. The chord Reynolds number was varied from 5×10^6 to 15×10^6. In the first experiment (2012), at zero degrees angle-of-attack, the circulation control nearly doubled the lift coefficient of the model in the separation control regime (Fig. 2.27). The circulation control blowing was still shown to provide a near constant lift increment over the linear portion of the lift curve, and increased the uncorrected maximum lift coefficient by 33% at the highest Reynolds number. The stall pattern of the wing was observed to begin with flow separation on the outboard portion of the actively blown flap. The transonic cruise testing was performed with a zero degree trailing edge deflection, at freestream Mach numbers ranging from 0.70 to 0.88, while the chord Reynolds number was varied from 10×10^6 to 30×10^6. The addition of low blowing rates at the Mach of 0.85, design condition of the wing resulted in a loss of lift and forward movement of the shock wave. The lift and drag increments due to

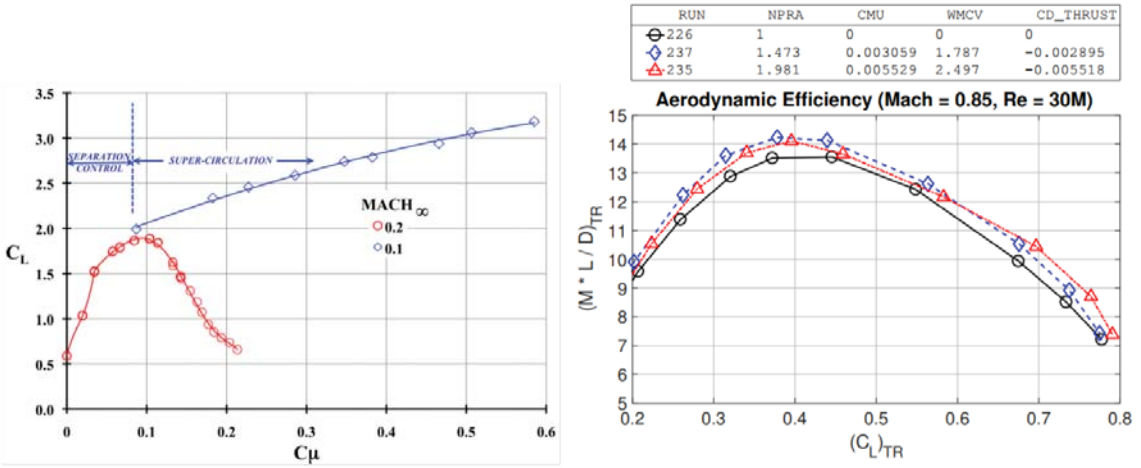

Figure 2.27: Typical result from the wind tunnel test of the FAST-MAC model (a) C_L takeoff condition at $\delta_f = 60°$, Ma = 0.10, 0.20, Re = 5 million . [27], (b) aerodynamic efficiency increments at Re = 30 million for M = 0.85. [28]

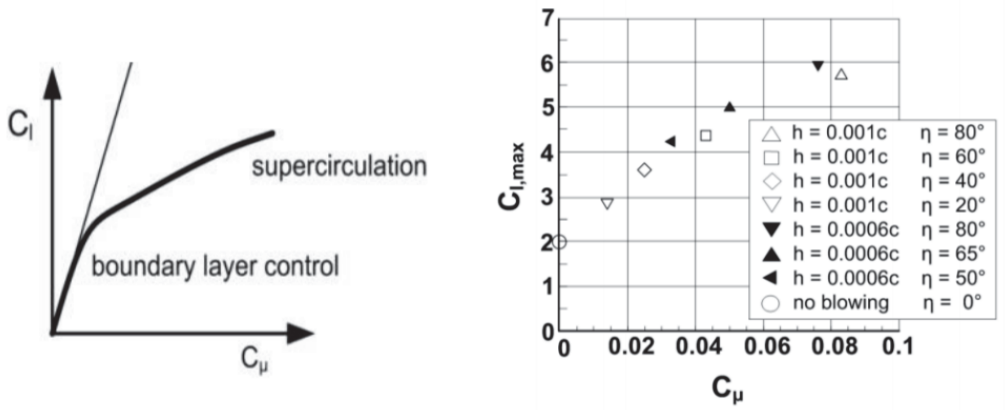

Figure 2.28: Boundary layer control and supercirculation control [29]

blowing were presented with the increased lift and reduced drag. it shows that the overall aerodynamic efficiency ($Ma \times L/D$) of the configuration would increase as a result of the blowing. The thrust-removed corrected data results with uncertainty bounds showed that an overall drag reduction and increased aerodynamic efficiency was realized as a consequence of the blowing for both Mach numbers especially at the flight Reynolds numbers of 30 million [28].

Supercirculation

The distinction between BLC at low C_μ and circulation control at high C_μ has been identified, named "supercirculation". The supercirculation phenomenon refers to achieving lift greater than the theoretical value achievable with a fully attached potential flow around the airfoil (Fig. 2.28). According to Poisson-Quinton and Lapage (1961), the first use of supercirculation was by Valensi et al. (1942), who used slot-jet blowing with momentum-coefficient values much larger than necessary to maintain an attached boundary layer on a wing flap [75]. Those experiments showed that reattachment of a boundary layer depended not only on the mass flow of the jet, but also identified the effect of jet velocity. The adverse effects of low jet velocity relative to the external flow were recognized by Kelly (1956) [75], and an effective correction to C_μ was found. Using

$$C_{\mu_{net}} = C_\mu(1 - \frac{V_0}{V_{jet}}) \tag{2.10}$$

where V_0 is the free stream velocity and V_{jet} is the boundary-layer control-jet velocity, the lift-coefficient data were properly scaled at low momentum coefficients ($C_\mu < 0.025$).

2.6 Drag Reduction Flow Control

The requirement for Drag Reduction Control

Fuel economy is a measure of how much fuel an aircraft needs to operate, which could be directly affected by the aerodynamic drag of the aircraft. The aerodynamic drag, which exerts a force on the aircraft in the opposite direction from the velocity, is a principal determinant of energy consumption in aircraft because they operate at

such high speeds. Therefore, to improve the fuel economy, drag reduction flow control is a desirable tool.

The drag buildup on a modern transonic aircraft is typically divided into major categories such as skin friction, induced drag, interference, and wave drag as indicated in Fig. 2.29 [9]. Skin friction and induced drag represent the form drag of a modern transonic aircraft. Skin friction reduction technology depends on whether one is working with laminar or turbulent boundary layers [9]. The wave drag is significantly different for various aircraft. The wave drag is associated with the flow physics of the shock waves and boundary layer interactions. Drag reduction flow control has obvious benefit for aircraft, reduce fuel consumption, achieve a longer range with greater endurance, and higher achievable speeds. For an aerodynamic drag breakdown of a transport aircraft, skin friction drag, and the lift-induced drag are the two main contributions of drag, approximately one half and one third of the total drag [30].

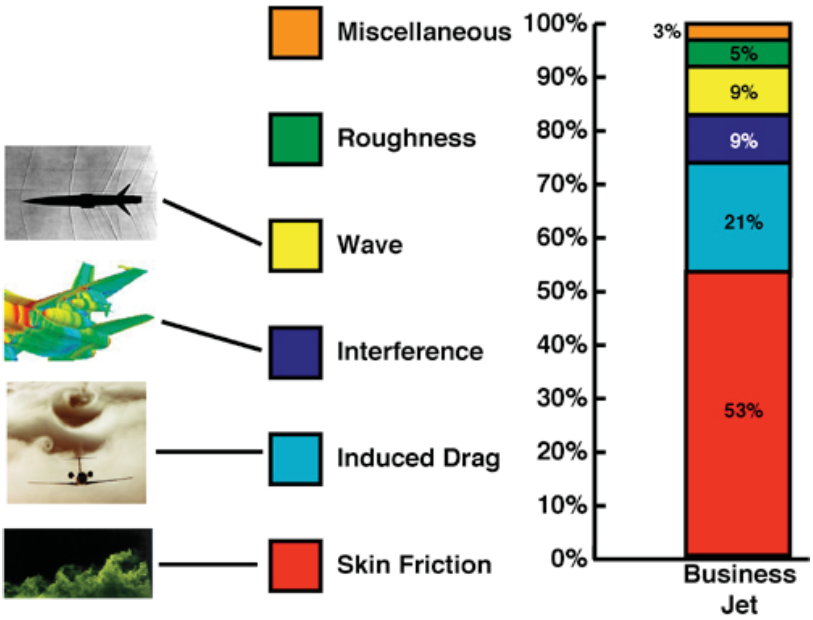

Figure 2.29: Breakdown of drag components. [9]

2.6.1 Laminar Flow Control

Laminar Flow Control (LFC) has been investigated extensively from lab test to flight demonstration. It shows a substantial benefit in terms of drag reduction LFC aims to keep a boundary layer from transitioning to much higher Reynolds number than would occur normally. Joslin [94] provides a detailed review of the historical development and validation of LFC research over the past half century. He defines the LFC categories that include Natural Laminar Flow (NLF), in which wing shaping is used to discourage the growth of instabilities, and Hybrid Laminar Flow Control (HLFC), which combines active laminar flow control with NLF. Natural laminar flow (NLF) implies delaying transition via controlling the body shape to provide long runs of favorable pressure-gradient, and has been applied since the 1930s on airfoil sections to achieve lower skin-friction drag. LFC uses suction, wall heating/cooling and other active means of control to suppress the proper instability modes. Active LFC is rarely used alone and is almost always combined with appropriate wing shaping. Joslin [94] points out that issues of LFC applications on commercial aircraft today include: resolution of some of the potential performance penalties versus the benefits, demonstration of the reliability, maintainability, and operational characteristics, development of an HLFC compatible ice-protection system, and viable high Reynolds number test techniques [43].

Fig.2.30 gives the Hybrid Laminar Flow concept, where the natural laminar flow can be sustained by leading edge suction to maintain the development of cross-flow and Tollmien-Schlichting instabilities combined with favorable pressure gradients in the spar box region [30]. It is indicated that anti-contamination devices are required for HLFC.

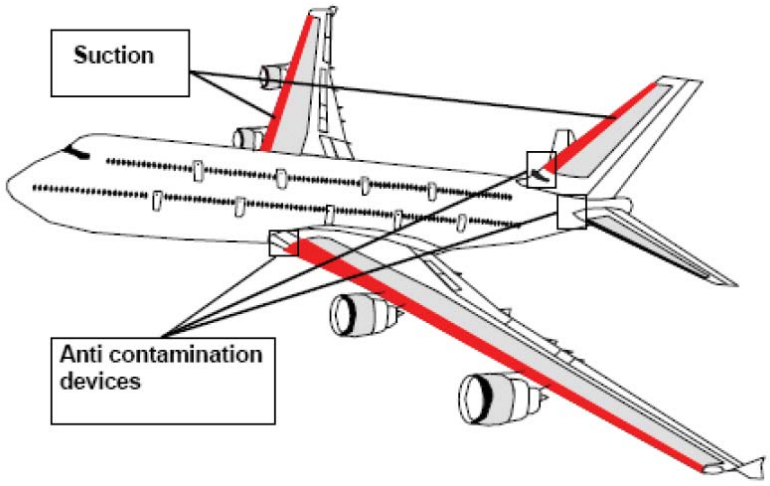

Figure 2.30: Hybrid Laminar Flow Concept (Reneaux, 2004). [30]

2.6.2 Turbulent Drag Reduction

Though LFC could delay transition and provide large drag reduction for aircraft, the real critical (for application) maintenance and reliability issues were never successfully addressed [95]. Various real-world issues, such as wing surface roughnesses, insect debris, and other occurrence of waviness under loading kept LFC in the category of a 'laboratory curiosity" [95]. The turbulent drag reduction (TDR) initiated from the late 1930s. Bushnell (2003) [95] reviewed the turbulent drag reduction methods across the speed range for the 'conventional' drag components of viscous drag, lift-induced drag, and wave drag. In general, turbulent drag reduction can be passive, active but steady state and active dynamic, both phased with, and independent from, the turbulence dynamics. Several turbulent drag reduction technologies are discussed below.

2.6.2.1 Riblets

The most extensively studied passive TDR method is riblets. Riblets are small longitudinal striations on the surface. By imposition of a spanwise viscous force, Riblets can reduce local skin friction and effectively convert the turbulence dynamics to a slip velocity on wing surfaces. Riblets were developed at NASA Langley in the early 1980's. It was originally designed as a viscous drag reduction method that can combine with large eddy breakup (LEBU) devices. Their wind tunnel experiment [9] showed that riblets have a 6% drag reduction in low speeds as well as at flight conditions. The 6% drag reduction can be translated into approximately a 1-2% total drag reduction if riblets could be applied to a large commercial transport. Although a 1-2% reduction in total drag is significant for a commercial aircraft, aircraft designer may have other considerations are such as possible increased maintenance cost and application time required to cover the aircraft that have resulted in a very limited number of actual applications of the riblet technology to commercial aircraft [9].

2.6.2.2 Micro Vortex Generators

Vortex generators (VG) have been and are still widely used for postponing boundary layer separation for improving wing stall characteristics. The working principal for vortex generators is to make the boundary layer more resistant to separation due to adverse pressure gradient by generating streamwise vortices near the edge of the boundary layer that 'reenergize' the boundary layer flow [30]. The conventional vortex generators may incur excess residual drag through conversion of aircraft forward momentum into unrecoverable turbulence in the aircraft wake. Therefore, the micro VG design, or low-profile VG, could be used to achieve separation control at certain

applications where the separation location is fairly fixed and does not require covering a large downstream distance by the devices. [96] Lin [96] has reviewed micro vortex generators (MVGs), or low-profile VGs, development. He evaluated numerous devices and found that a small vane type generator extending only 20% of the boundary layer height is still effective. Operationally they were small enough that when the flaps retract they can be stowed in the flap cove and thereby avoid a cruise drag penalty. In terms of separation control, when applied to a modern multi-element high-lift system they provided an L/D improvement of 100%, and a lift increase of 10% [43].

2.6.2.3 Active turbulent drag reduction

For active turbulent boundary layer reduction control, NASA Langley has conducted numerous experiments and simulations [9]. Since the flow is benign at cruise condition, the drag reduction performance is comparatively lower for active flow control compared to the lift enhancement performance. Researchers have conducted studies showing that turbulent boundary layer drag reductions of 20-70% can be achieved by active flow control [9]. The majority of drag reduction methods are generated as minimization of the fluctuation energy [97]. Choi, Mon, and Kim (1994) [98] observed 25-30 % drag reduction for suction and blowing at the wall; Choi, DeBisschop, and Clayton (1998) [99] experimentally measured a 45% reduction with spanwise oscillation. Rathnasingham and Breuer (2003) [90] report a 7 % reduction in shear stress using a spanwise array of synthetic jets aligned with the free stream.

2.6.3 Lift-induced drag reduction

For finite-span wing, a significant contribution of aircraft drag is lift-induced drag. Increasing the aspect ratio of the wing can be effective to reduce the influence of lift-induced drag. However, high AR wing comes with the penalty of weight and friction drag increase. Therefore, there is a balance for the aspect ratio determination. The commonly used method is to design the wingtip device. Various wingtip devices have been developed to suppress the influence of wingtip vortex as shown in Fig. 2.31.

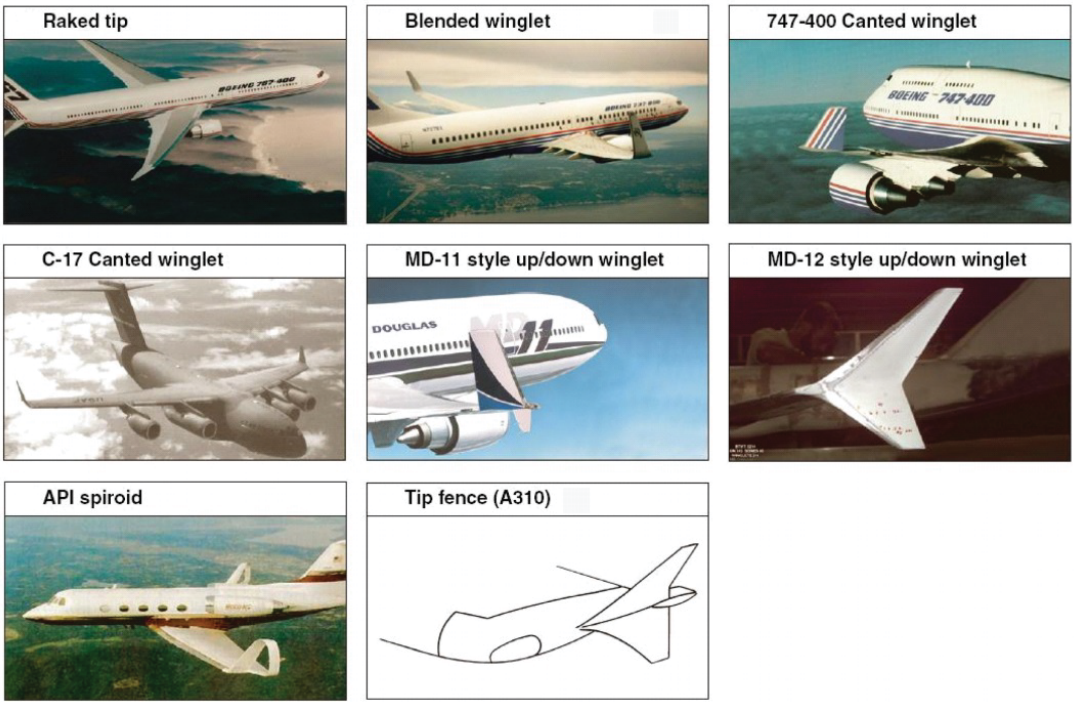

Figure 2.31: Wingtip modifications on existing aircraft [31].

CHAPTER 3

Governing Equations

The governing equations for fluid flow are Navier-Stokes equations, which are a system of unsteady and non-linear partial differential equations for the conservation of mass, momentum, and energy. This chapter describes the governing equations compressible aerodynamics in detail.

3.1 The Navier-Stokes Equations

Following the derivation of Knight et al. [100], the filtered compressible Navier-Stokes equations in Cartesian coordinates can be expressed as:

$$\frac{\partial \mathbf{Q}}{\partial t} + \frac{\partial \mathbf{E}}{\partial x} + \frac{\partial \mathbf{F}}{\partial y} + \frac{\partial \mathbf{G}}{\partial z} = \frac{1}{Re}\left(\frac{\partial \mathbf{E_v}}{\partial x} + \frac{\partial \mathbf{F_v}}{\partial y} + \frac{\partial \mathbf{G_v}}{\partial z}\right) \tag{3.1}$$

where t is time,Re is the Reynolds number. The variable vector $\mathbf{Q}$, inviscid flux vectors $\mathbf{E}$, $\mathbf{F}$, $\mathbf{G}$, and the viscous fluxes $\mathbf{E_v}$, $\mathbf{F_v}$, $\mathbf{G_v}$ are given as the following.

$$\mathbf{Q} = \begin{pmatrix} \bar{\rho} \\ \bar{\rho}\tilde{u} \\ \bar{\rho}\tilde{v} \\ \bar{\rho}\tilde{w} \\ \bar{\rho}\tilde{e} \end{pmatrix}, \ \mathbf{E} = \begin{pmatrix} \bar{\rho}\tilde{u} \\ \bar{\rho}\tilde{u}^2 + \bar{p} \\ \bar{\rho}\tilde{u}\tilde{v} \\ \bar{\rho}\tilde{u}\tilde{w} \\ (\bar{\rho}\tilde{e} + \bar{p})\tilde{u} \end{pmatrix}, \ \mathbf{F} = \begin{pmatrix} \bar{\rho}\tilde{v} \\ \bar{\rho}\tilde{v}\tilde{u} \\ \bar{\rho}\tilde{v}^2 + \bar{p} \\ \bar{\rho}\tilde{v}\tilde{w} \\ (\bar{\rho}\tilde{e} + \bar{p})\tilde{v} \end{pmatrix}, \ \mathbf{G} = \begin{pmatrix} \bar{\rho}\tilde{w} \\ \bar{\rho}\tilde{w}\tilde{u} \\ \bar{\rho}\tilde{w}\tilde{v} \\ \bar{\rho}\tilde{w}^2 + \bar{p} \\ (\bar{\rho}\tilde{e} + \bar{p})\tilde{w} \end{pmatrix}$$

$$\mathbf{E_v} = \begin{pmatrix} 0 \\ \bar{\tau}_{xx} + \sigma_{xx} \\ \bar{\tau}_{xy} + \sigma_{xy} \\ \bar{\tau}_{xz} + \sigma_{xz} \\ Q_x \end{pmatrix}, \ \mathbf{F_v} = \begin{pmatrix} 0 \\ \bar{\tau}_{yx} + \sigma_{yx} \\ \bar{\tau}_{yy} + \sigma_{yy} \\ \bar{\tau}_{yz} + \sigma_{yz} \\ Q_y \end{pmatrix}, \ \mathbf{G_v} = \begin{pmatrix} 0 \\ \bar{\tau}_{zx} + \sigma_{zx} \\ \bar{\tau}_{zy} + \sigma_{zy} \\ \bar{\tau}_{zz} + \sigma_{zz} \\ Q_z \end{pmatrix}$$

The overbar denotes a regular filtered variable, and the tilde is used to denote the Favre filtered variable. In above equations, $\rho$is the density, u, v, w are the Cartesian velocity components in x, y, z directions , p is the static pressure, and e is the total energy per unit mass .

The $\bar{\tau}$ is the molecular viscous stress tensor and is estimated as:

$$\bar{\tau}_{ij} = -\frac{2}{3}\tilde{\mu}\frac{\partial \tilde{u}_k}{\partial x_k}\delta_{ij} + \tilde{\mu}(\frac{\partial \tilde{u}_i}{\partial x_j} + \frac{\partial \tilde{u}_j}{\partial x_i}), \qquad i, j = 1, 2, 3 \tag{3.2}$$

The above equation is in tensor form, where the subscript 1, 2, 3 represent the coordinates, x, y, z, and the Einstein summation convention is used.

The molecular viscosity $\tilde{\mu} = \tilde{\mu}(\tilde{T})$ is determined by Sutherland law.

The σ is the subgrid scale stress tensor due to the filtering process and is expressed as:

$$\sigma_{ij} = -\bar{\rho}(\widetilde{u_i u_j} - \tilde{u}_i \tilde{u}_j) \tag{3.3}$$

The energy flux Q is expressed as:

$$Q_i = \tilde{u}_j(\bar{\tau}_{ij} + \sigma_{ij}) - \bar{q}_i + \Phi_i \tag{3.4}$$

where Φ is the subscale heat flux:

$$\Phi_i = -C_p \bar{\rho}(\widetilde{u_i T} - \tilde{u}_i \tilde{T}) \tag{3.5}$$

The $\bar{q}_i$ is the molecular heat flux:

$$\bar{q}_i = -\frac{C_p \tilde{\mu}}{Pr} \frac{\partial \tilde{T}}{\partial x_i} \tag{3.6}$$

$$\bar{\rho}\tilde{e} = \frac{\bar{p}}{(\gamma - 1)} + \frac{1}{2}\bar{\rho}(\tilde{u}^2 + \tilde{v}^2 + \tilde{w}^2) + \rho k \tag{3.7}$$

where γ is the ratio of specific heats, ρk is the subscale kinetic energy per unit volume.

$$\rho k = \frac{1}{2}\bar{\rho}(\widetilde{u_i u_i} - \tilde{u}_i \tilde{u}_i) = -\frac{1}{2}\sigma_{ii} \tag{3.8}$$

In the present calculation, the ρk in Eq.(3.7) is omitted based on the assumption that the effect is small.

In generalized coordinates, Eq.(3.1) can be expressed as the following:

$$\frac{\partial \mathbf{Q}'}{\partial t} + \frac{\partial \mathbf{E}'}{\partial \xi} + \frac{\partial \mathbf{F}'}{\partial \eta} + \frac{\partial \mathbf{G}'}{\partial \zeta} = \frac{1}{\mathrm{Re}} \left(\frac{\partial \mathbf{E}'_{\mathbf{v}}}{\partial \xi} + \frac{\partial \mathbf{F}'_{\mathbf{v}}}{\partial \eta} + \frac{\partial \mathbf{G}'_{\mathbf{v}}}{\partial \zeta} \right) \tag{3.9}$$

where

$$\mathbf{Q}' = \frac{\mathbf{Q}}{J} \tag{3.10}$$

$$\mathbf{E}' = \frac{1}{J}(\xi_t \mathbf{Q} + \xi_x \mathbf{E} + \xi_y \mathbf{F} + \xi_z \mathbf{G}) \tag{3.11}$$

$$\mathbf{F}' = \frac{1}{J}(\eta_t \mathbf{Q} + \eta_x \mathbf{E} + \eta_y \mathbf{F} + \eta_z \mathbf{G}) \tag{3.12}$$

$$\mathbf{G}' = \frac{1}{J}(\zeta_t \mathbf{Q} + \zeta_x \mathbf{E} + \zeta_y \mathbf{F} + \zeta_z \mathbf{G}) \tag{3.13}$$

$$\mathbf{E}'_{\mathbf{v}} = \frac{1}{J}(\xi_x \mathbf{E}_{\mathbf{v}} + \xi_y \mathbf{F}_{\mathbf{v}} + \xi_z \mathbf{G}_{\mathbf{v}}) \tag{3.14}$$

$$\mathbf{F}'_{\mathbf{v}} = \frac{1}{J}(\eta_x \mathbf{E}_{\mathbf{v}} + \eta_y \mathbf{F}_{\mathbf{v}} + \eta_z \mathbf{G}_{\mathbf{v}}) \tag{3.15}$$

$$\mathbf{G}'_{\mathbf{v}} = \frac{1}{J}(\zeta_x \mathbf{E}_{\mathbf{v}} + \zeta_y \mathbf{F}_{\mathbf{v}} + \zeta_z \mathbf{G}_{\mathbf{v}}) \tag{3.16}$$

where J is the transformation Jacobian. The inviscid fluxes in generalized coordinate system are expressed as:

$$\mathbf{E}' = \begin{bmatrix} \bar{\rho}U \\ \bar{\rho}\tilde{u}U + l_x\bar{p} \\ \bar{\rho}\tilde{v}U + l_y\bar{p} \\ \bar{\rho}\tilde{w}U + l_z\bar{p} \\ (\bar{\rho}\tilde{e} + \bar{p})\,U - l_t\bar{p} \end{bmatrix}, \; \mathbf{F}' = \begin{bmatrix} \bar{\rho}V \\ \bar{\rho}\tilde{u}V + m_x\bar{p} \\ \bar{\rho}\tilde{v}V + m_y\bar{p} \\ \bar{\rho}\tilde{w}V + m_z\bar{p} \\ (\bar{\rho}\tilde{e} + \bar{p})\,V - m_t\bar{p} \end{bmatrix}, \; \mathbf{G}' = \begin{bmatrix} \bar{\rho}W \\ \bar{\rho}\tilde{u}W + n_x\bar{p} \\ \bar{\rho}\tilde{v}W + n_y\bar{p} \\ \bar{\rho}\tilde{w}W + n_z\bar{p} \\ (\bar{\rho}\tilde{e} + \bar{p})\,W - n_t\bar{p} \end{bmatrix}$$

where U, V and W are the contravariant velocities in ξ, η and ζ directions.

$$
\begin{aligned}
U &= l_t + \mathbf{l} \bullet \mathbf{V} = l_t + l_x\tilde{u} + l_y\tilde{v} + l_z\tilde{w} \\
V &= m_t + \mathbf{m} \bullet \mathbf{V} = m_t + m_x\tilde{u} + m_y\tilde{v} + m_z\tilde{w} \\
W &= n_t + \mathbf{n} \bullet \mathbf{V} = n_t + n_x\tilde{u} + n_y\tilde{v} + n_z\tilde{w}
\end{aligned} \tag{3.17}
$$

$\mathbf{l}$, $\mathbf{m}$, $\mathbf{n}$ are the normal vectors on ξ, η, ζ surfaces with their magnitudes equal to the elemental surface area and pointing to the directions of increasing ξ, η, ζ.

$$
\mathbf{l} = \frac{\nabla\xi}{J},\ \mathbf{m} = \frac{\nabla\eta}{J},\ \mathbf{n} = \frac{\nabla\zeta}{J} \tag{3.18}
$$

$$
l_t = \frac{\xi_t}{J},\ m_t = \frac{\eta_t}{J},\ n_t = \frac{\zeta_t}{J} \tag{3.19}
$$

For simplicity, all the overbar and tilde in above equations will be dropped in the rest of this thesis. Please note that the Navier-Stokes equations, Eq.(3.9), are normalized based on a set of reference parameters.

3.2 Spalart-Allmaras Turbulence Model

The transport equation of the Spalart-Allmaras one equation turbulence model is derived by using empiricism, dimensional analysis, Galilean invariance and selected dependence on the molecular viscosity [101]. The working variable $\tilde{\nu}$ is related to the eddy viscosity ν_t. The transport equation is expressed as

$$
\begin{aligned}
\tfrac{D\tilde{\nu}}{Dt} = \ & c_{b1}\tilde{S}\tilde{\nu}\,(1 - f_{t2}) - [c_{w1}f_w - \tfrac{c_{b1}}{k^2}f_{t2}][\tfrac{\tilde{\nu}}{d}]^2 \\
& + \tfrac{1}{\sigma}[\nabla\cdot((\nu+\tilde{\nu})\nabla\tilde{\nu}) + c_{b2}(\nabla\tilde{\nu})^2] + f_{t1}\,(\Delta q)^2
\end{aligned} \tag{3.20}
$$

In generalized coordinate system, the dimensionlessed conservative form of Eq.(3.20) is given as the following:

$$\frac{\partial \frac{1}{J}\rho\tilde{\nu}}{\partial t} + \frac{\partial \rho\tilde{\nu}U}{\partial \xi} + \frac{\partial \rho\tilde{\nu}V}{\partial \eta} + \frac{\partial \rho\tilde{\nu}W}{\partial \zeta} = \frac{1}{Re}\left(\frac{\partial \frac{\rho}{\sigma}(\nu+\tilde{\nu})(\mathbf{l}\bullet\nabla\tilde{\nu})}{\partial \xi} + \frac{\partial \frac{\rho}{\sigma}(\nu+\tilde{\nu})(\mathbf{m}\bullet\nabla\tilde{\nu})}{\partial \eta} + \frac{\partial \frac{\rho}{\sigma}(\nu+\tilde{\nu})(\mathbf{n}\bullet\nabla\tilde{\nu})}{\partial \zeta} + \frac{1}{J}S_\nu\right) \tag{3.21}$$

where

$$\begin{aligned} S_\nu = {} & \rho c_{b1}(1-f_{t2})\tilde{S}\tilde{\nu} + \tfrac{1}{Re}\left[-\rho\left(c_{w1}f_w - \tfrac{c_{b1}}{\kappa^2}f_{t2}\right)\left(\tfrac{\tilde{\nu}}{d}\right)^2\right. \\ & \left. + \tfrac{\rho}{\sigma}c_{b2}(\nabla\tilde{\nu})^2 - \tfrac{1}{\sigma}(\nu+\tilde{\nu})\nabla\tilde{\nu}\bullet\nabla\rho\right] + Re\left[\rho f_{t1}(\Delta q)^2\right] \end{aligned} \tag{3.22}$$

The eddy viscosity ν_t is obtained from:

$$\nu_t = \tilde{\nu}f_{v1} \qquad f_{v1} = \frac{\chi^3}{\chi^3 + c_{v1}^3} \qquad \chi = \frac{\tilde{\nu}}{\nu} \tag{3.23}$$

where ν is the kinematic viscosity. The production term is:

$$\tilde{S} = S + \frac{\tilde{\nu}}{k^2d^2}f_{v2}, \qquad f_{v2} = 1 - \frac{\chi}{1+\chi f_{v1}} \tag{3.24}$$

where S is the magnitude of the vorticity. The function f_w is given by

$$f_w = g\left(\frac{1+c_{w3}^6}{g^6+c_{w3}^6}\right)^{1/6}, \qquad g = r + c_{w2}(r^6 - r), \qquad r = \frac{\tilde{\nu}}{\tilde{S}k^2d^2} \tag{3.25}$$

The function f_{t2} is given by

$$f_{t2} = c_{t3}exp\left(-c_{t4}\chi^2\right) \tag{3.26}$$

and the trip function f_{t1} is

$$f_{t1} = c_{t1}g_t exp\left[-c_{t2}\frac{\omega_t^2}{\Delta U^2}\left(d^2 + g_t^2 d_t^2\right)\right], \; g_t = min\left(0.1, \frac{\Delta q}{\omega_t \Delta x_t}\right) \tag{3.27}$$

where, ω_t is the wall vorticity at the wall boundary layer trip location, d is the distance to the closest wall. d_t is the distance of the field point to the trip location, Δq is the difference of the velocities between the field point and the trip location, Δx_t is the grid spacing along the wall at the trip location.

The values of the coefficients are: $c_{b1} = 0.1355, c_{b2} = 0.622, \sigma = \frac{2}{3}, c_{w1} = \frac{c_{b1}}{k^2} + (1 + c_{b2})/\sigma, c_{w2} = 0.3, c_{w3} = 2, k = 0.41, c_{v1} = 7.1, c_{t1} = 1.0, c_{t2} = 2.0, c_{t3} = 1.1, c_{t4} = 2.0$.

In S-A one equation turbulence model, the trip point need to be specified before computation. This is not straightforward to do because the exact position of the trip point is not known in most of the cases. Thus, a full turbulent boundary layer is used by setting $c_{t1} = 0$ and $c_{t3} = 0$. No trip point needs to be specified.

It is observed that the S-A one equation turbulence model is sensitive to initial field. If the initial field of $\tilde{\nu}$ is set to a small value, e.g. $\tilde{\nu} < 1$, the solution may converge with $\tilde{\nu} = 0$, which is the trivial solution of $\tilde{\nu}$ when $c_{t1} = c_{t3} = 0$. This will result in a laminar flow solution. If the initial value is too large ($\tilde{\nu} > 3$), the computation may diverge. In addition, setting up the initial value of $\tilde{\nu}$ also depends on the schemes to be used. In our computation, it is found that it is generally safe to set the initial value of $\tilde{\nu}$ to 2.

The boundary conditions of $\tilde{\nu}$ are given as the following

$$
\begin{aligned}
&at\ walls: && \tilde{\nu} = 0 \\
&far\ field\ inflow: && \tilde{\nu} = 0.02 \\
&far\ field\ outflow: && \tilde{\nu}\ is\ extrapolated
\end{aligned}
$$

Coupled Eqs.(3.9) with the S-A model Eq.(3.21), the conservative form of the governing equations are given as the following:

$$\frac{\partial Q}{\partial t}+\frac{\partial \mathbf{E}}{\partial \xi}+\frac{\partial \mathbf{F}}{\partial \eta}+\frac{\partial \mathbf{G}}{\partial \zeta}=\frac{1}{Re}\left(\frac{\partial \mathbf{R}}{\partial \xi}+\frac{\partial \mathbf{S}}{\partial \eta}+\frac{\partial \mathbf{T}}{\partial \zeta}+D\right) \tag{3.28}$$

where,

$$Q=\frac{1}{J}\begin{bmatrix}\rho\\ \rho u\\ \rho v\\ \rho w\\ \rho e\\ \rho\tilde{\nu}\end{bmatrix} \tag{3.29}$$

$$\mathbf{E}=\begin{bmatrix}\rho U\\ \rho uU+l_x p\\ \rho vU+l_y p\\ \rho wU+l_z p\\ (\rho e+p)\,U-l_t p\\ \rho\tilde{\nu}U\end{bmatrix},\ \mathbf{F}=\begin{bmatrix}\rho V\\ \rho uV+m_x p\\ \rho vV+m_y p\\ \rho wV+m_z p\\ (\rho e+p)\,V-m_t p\\ \rho\tilde{\nu}V\end{bmatrix},\ \mathbf{G}=\begin{bmatrix}\rho W\\ \rho uW+n_x p\\ \rho vW+n_y p\\ \rho wW+n_z p\\ (\rho e+p)\,W-n_t p\\ \rho\tilde{\nu}W\end{bmatrix} \tag{3.30}$$

$$\mathbf{R} = \begin{bmatrix} 0 \\ l_k\tau_{xk} \\ l_k\tau_{yk} \\ l_k\tau_{zk} \\ l_k\beta_k \\ \frac{\rho}{\sigma}\left(\nu+\tilde{\nu}\right)\left(\mathbf{l}\bullet\nabla\tilde{\nu}\right) \end{bmatrix}, \ \mathbf{S} = \begin{bmatrix} 0 \\ m_k\tau_{xk} \\ m_k\tau_{yk} \\ m_k\tau_{zk} \\ m_k\beta_k \\ \frac{\rho}{\sigma}\left(\nu+\tilde{\nu}\right)\left(\mathbf{m}\bullet\nabla\tilde{\nu}\right) \end{bmatrix}, \ \mathbf{T} = \begin{bmatrix} 0 \\ n_k\tau_{xk} \\ n_k\tau_{yk} \\ n_k\tau_{zk} \\ n_k\beta_k \\ \frac{\rho}{\sigma}\left(\nu+\tilde{\nu}\right)\left(\mathbf{n}\bullet\nabla\tilde{\nu}\right) \end{bmatrix} \tag{3.31}$$

$$D = \frac{1}{J}\begin{bmatrix} 0 \\ 0 \\ 0 \\ 0 \\ 0 \\ S_\nu \end{bmatrix} \tag{3.32}$$

where, U, V, W are defined as in Eq.(3.17).

$$\beta_k = u_i\tau_{ki} - q_k \tag{3.33}$$

The shear stress $\bar{\tau}_{ik}$ and total heat flux $\bar{q}_k$ in Cartesian coordinates is given by

$$\bar{\tau}_{ik} = \left(\mu+\mu_{DES}\right)\left[\left(\frac{\partial\tilde{u}_i}{\partial x_k}+\frac{\partial\tilde{u}_k}{\partial x_i}\right)-\frac{2}{3}\delta_{ik}\frac{\partial\tilde{u}_j}{\partial x_j}\right] \tag{3.34}$$

$$\bar{q}_k = -\left(\frac{\mu}{Pr}+\frac{\mu_{DES}}{Pr_t}\right)\frac{\partial\tilde{T}}{\partial x_k} \tag{3.35}$$

where μ is from Sutherland's law. For DES family in general, the eddy viscosity is represented by $\mu_{DES}(=\bar{\rho}\tilde{\nu}f_{v1})$.

3.3 Improved Delayed Detached Eddy Simulation (IDDES)

3.3.1 DES

For the original detached eddy simulation (DES) model, a modification of a S-A RANS model is made to switch the model to a subgrid scale formulation in regions for LES calculations. The coefficients c_{t1} and c_{t3} in the S-A model are set to zero and the distance to the nearest wall, d, is replaced by $\tilde{d}$ as

$$\tilde{d} = min(d, C_{DES}\Delta) \tag{3.36}$$

3.3.2 DDES

The DDES model is suggested by Spalart et al. [54] to overcome the modeled stress depletion (MSD) for ambiguous grids. The DDES redefines the distance scale transition from RANS mode to LES mode $\tilde{d}$. The mechanism was identified as an encroachment of the RANS-LES interface inside the boundary layer, giving rise to reduced level of eddy viscosity on the LES-mode side.

$$\tilde{d} = d - f_d max(0, d - C_{DES}\Delta) \tag{3.37}$$

where

$$f_d = 1 - tanh([8r_d]^3) \tag{3.38}$$

$$r_d = \frac{\nu_t + \nu}{(U_{i,j}U_{i,j})^{0.5}k^2d^2R_e} \tag{3.39}$$

$$U_{i,j} = \frac{\partial u_i}{\partial x_j} \tag{3.40}$$

where Δ is the local grid filter scale, $U_{i,j}$ is the velocity gradient, and k denotes the Karmann constant.

3.3.3 IDDES

The Improved DDES(IDDES) is introduced by extending the DDES with the WMLES capacity. The IDDES has two branches, DDES and WMLES, including a set of empirical functions of subgrid length-scales designed to achieve good performance from these branches themselves and their coupling. By switching the activation of RANS and LES in different flow regions, IDDES significantly expands the scope of application of DDES with well-balanced and powerful numerical approach to complex turbulent flows at high Reynolds numbers.

The three aspects of IDDES are presented below: the DDES branch , the WMLES branch and hybridization of DDES and WMLES.

DDES branch of IDDES

This branch is responsible for the DDES-like functionality of IDDES and should become active only when the inflow conditions do not have any turbulent content (if a simulation has spatial periodicity, the initial conditions rather than the inflow conditions set the characteristics of the simulation), in particular when a grid of "boundary-layer type" precludes the resolution of the dominant eddies. The DDES formulation from Eq.(3.37) can be reformulated as

$$l_{DDES} = l_{RANS} - f_d max\{0, l_{RANS} - l_{LES}) \tag{3.41}$$

where the delaying function, f_d, is defined the same as

$$f_d = 1 - tanh[(8r_d)^3] \tag{3.42}$$

and the quantity r_d borrowed from the S-A RANS turbulence model:

$$r_d = \frac{\nu_t + \nu}{k^2 d_w^2 max[(U_{i,j}U_{i,j})^{0.5}, 10^{-10}]} \tag{3.43}$$

is a marker of the wall region, which is equal to 1 in a log layer and 0 in a free shear flow.

In Eq. (3.43), $U_{i,j}$ represents the velocity gradient, and k denotes the Karmann constant. Based on the general DES concept, in order to create a seamless hybrid model, the length-scale IDDES defined by Eq.3.41 is substituted into the background RANS model to replace the RANS length-scale, l_{RANS}, which is explicitly or implicitly involved in any such model. For instance, for the S-A model the length-scale is equal to the distance to the wall $l_{RANS} = d_w$. In the original DES97, the length-scale depends only on the local grid. In DDES and IDDES, it also depends on the solution of Eq. (3.41) and (3.43).

As far as the LES length-scale, l_{LES}, in Eq. (3.41) is concerned, it is defined via the subgrid length-scale as

$$l_{LES} = C_{DES}\Phi\Delta \tag{3.44}$$

where C_{DES} is the fundamental empirical constant of DES, 0.65. Φ is a low-Reynolds number correction introduced in order to compensate the activation of the low-Reynolds number terms of some background RANS model in LES mode. Both C_{DES} and Φ depend on the background RANS model, and Ψ is equal to 1 if the RANS model does not include any low-Reynolds number terms.

WMLES branch of IDDES

This branch is intended to be active only when the inflow conditions used in the simulation are unsteady and impose some turbulent content with the grid fine enough

to resolve boundary-layer dominant eddies. It presents a new seamless hybrid RANS-LES model, which couples RANS and LES approaches via the introduction of the following blended RANS-LES length-scale:

$$l_{WMLES} = f_B(1 + f_e)l_{RANS} + (1 - f_B)l_{LES} \tag{3.45}$$

The empirical blending-function f_B depends upon d_w/h_{max} and is defined as

$$f_B = min\{2exp(-9\alpha^2), 1.0\}, \alpha = 0.25 - d_w/h_{max} \tag{3.46}$$

It varies from 0 to 1 and provides rapid switching of the model from RANS mode ($f_B = 1.0$) to LES mode ($f_B = 0$) within the range of wall distance $0.5h_{max} < d_w < h_{max}$

The second empirical function involved in Eq. (3.45), elevating-function, f_e, is aimed at preventing the excessive reduction of the RANS Reynolds stresses observed in the interaction of the RANS and LES regions in the vicinity of their interface. It is intended to eliminating the log-layer mismatch(LLM) problem.

$$f_e = max\{(f_{e1} - 1), 0\}\Phi f_{e2} \tag{3.47}$$

where the function f_{e1} is defined as

$$f_{e1}(d_w/h_{max}) = \begin{cases} 2exp(-11.09\alpha^2) & \text{if } \alpha \geq 0 \\ 2exp(-9.0\alpha^2) & \text{if } \alpha < 0 \end{cases} \tag{3.48}$$

It provides a grid-dependent "elevating"device for the RANS component of the WMLES length-scale.

The function f_{e2} is:

$$f_{e2} = 1.0 - max\{f_t, f_l\} \tag{3.49}$$

Blending DDES and WMLES branches

The DDES length-scale defined by Eq. (3.41) and that of the WMLES-branch defined by Eq. (3.45) do not blend directly in a way to ensure an automatic choice of the WMLES or DDES mode by the combined model, depending on the type of the simulation (with or without turbulent content) and the grid used.

However a modified version of equivalent length scale combination, namely,

$$\tilde{l}_{DDES} = \tilde{f}_d l_{RANS} + (1 - \tilde{f}_d) l_{LES} \tag{3.50}$$

where the blending function $\tilde{f}_d$ is defined by

$$\tilde{f}_d = max\{(1 - f_{dt}), f_B\} \tag{3.51}$$

with $f_{dt} = 1 - tanh[(8r_{dt})^3]$

With the use of Eq. (3.50), the required IDDES length-scale combining the DDES and WMLES length scales defined by Eq. (3.50) and (3.45) is straightforward and can be implemented as

$$l_{hyb} = \tilde{f}_d(1 + f_e) l_{RANS} + (1 - \tilde{f}_d) l_{LES} \tag{3.52}$$

With inflow turbulent content, f_{dt} is close to 1.0, $\tilde{f}_d$ is equal to f_B, so Eq. (3.52) is reducted to $l_{hyb} = l_{WMLES}$ in Eq. (3.45). Otherwise, f_e is zero, Eq. (3.52) is interpreted as $l_{hyb} = l_{DDES}$ in Eq. (3.50)

CHAPTER 4

Numerical Methodology

In this chapter, an implicit finite difference discretization for the flow governing equations is described. The inviscid fluxes are discretized using a low diffusion E-CUSP scheme [102]. The fifth-order WENO scheme [103, 104] is used to reconstruct the conservative variables at volume interfaces. A set of fully conservative fourth-order accurate finite central differencing schemes for the viscous terms is employed in this research [105, 106].

4.1 Implicit Discretization

Let $J = \frac{1}{\Delta V}$, then 3D Navier-Stokes equations (3.28) is rewritten in a conservative flux vector form as

$$\frac{\partial \Delta V \mathbf{Q}}{\partial t} + \frac{\partial (\mathbf{E} - \mathbf{R}')}{\partial \xi} + \frac{\partial (\mathbf{F} - \mathbf{S}')}{\partial \eta} + \frac{\partial (\mathbf{G} - \mathbf{T}')}{\partial \zeta} = \Delta V \mathbf{D} \tag{4.1}$$

where ΔV denotes the volume of the cell and $\mathbf{R}' = \mathbf{R}/Re$, $\mathbf{S}' = \mathbf{S}/Re$, $\mathbf{T}' = \mathbf{T}/Re$. For steady state solutions, the governing equation will be elliptic type at subsonic and hyperbolic at supersonic. This will make it difficult to discretize the Navier-Stokes equations using a consistent scheme. The temporal term is thus included for steady

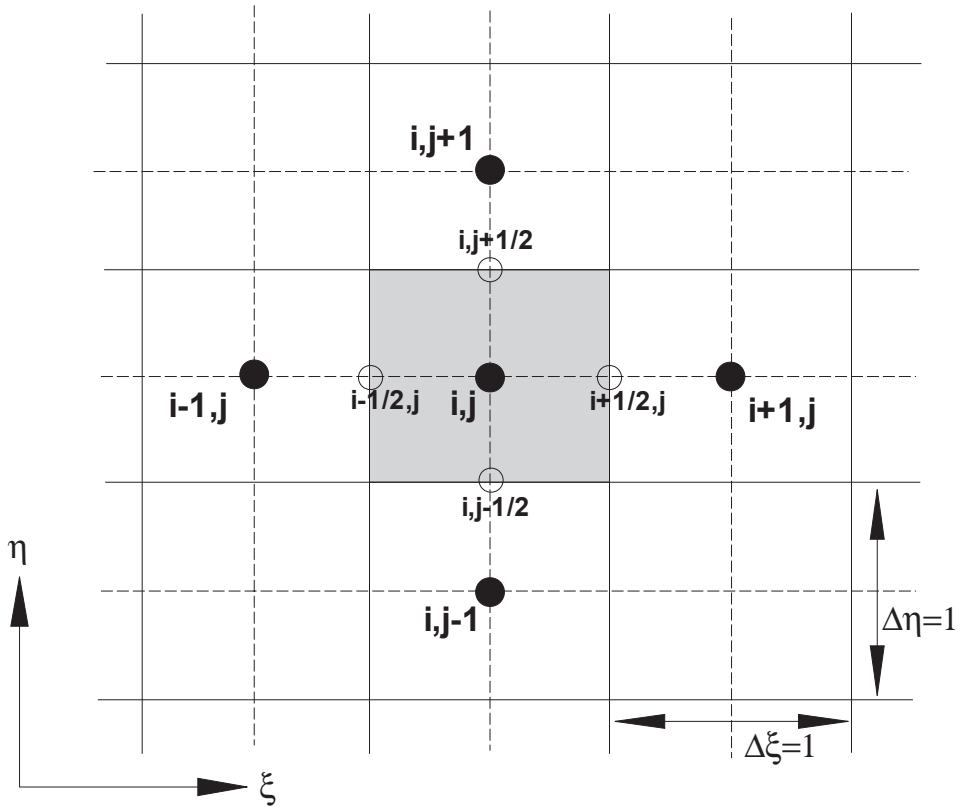

Figure 4.1: Discretization domain indicating the cell center(i,j)

state solutions to keep the governing equations to have the same hyperbolic type across Mach number 1. For steady state solution, the accuracy of the temporal term is irrelevant since it must be zero when it is converged. Hence, the temporal term is discretized using first order Euler method for its simplicity. The discretized temporal term becomes

$$\frac{\Delta V(\mathbf{Q}^{n+1}-\mathbf{Q}^{n})}{\Delta t}+[\frac{\partial(\mathbf{E}-\mathbf{R}')}{\partial\xi}]^{n+1}+[\frac{\partial(\mathbf{F}-\mathbf{S}')}{\partial\eta}]^{n+1}+[\frac{\partial(\mathbf{G}-\mathbf{T}')}{\partial\zeta}]^{n+1}=\Delta V\mathbf{D}^{n+1} \tag{4.2}$$

where n and $n+1$ are two sequential time levels, which have a time interval of Δt. Eq. (4.2) can be further discretized in space using a conservative differencing as the following:

$$\begin{aligned}
&\frac{\Delta V_{ijk}(\mathbf{Q}_{ijk}^{n+1}-\mathbf{Q}_{ijk}^{n})}{\Delta t} \\
&+(\mathbf{E}_{i+\frac{1}{2}}-\mathbf{E}_{i-\frac{1}{2}})^{n+1}-(\mathbf{R}'_{i+\frac{1}{2}}-\mathbf{R}'_{i-\frac{1}{2}})^{n+1} \\
&+(\mathbf{F}_{j+\frac{1}{2}}-\mathbf{F}_{j-\frac{1}{2}})^{n+1}-(\mathbf{S}'_{j+\frac{1}{2}}-\mathbf{S}'_{j-\frac{1}{2}})^{n+1} \\
&+(\mathbf{G}_{k+\frac{1}{2}}-\mathbf{G}_{k-\frac{1}{2}})^{n+1}-(\mathbf{T}'_{k+\frac{1}{2}}-\mathbf{T}'_{k-\frac{1}{2}})^{n+1} \\
&=\Delta V_{ijk}\mathbf{D}_{ijk}^{n+1}
\end{aligned} \tag{4.3}$$

To evaluate the inviscid fluxes at the cell interface $\mathbf{E}, \mathbf{F}, \mathbf{G}$, the characteristic based upwind schemes are usually employed due to importance of capturing strong shocks and careful treatment of discontinuity, while the central differencing is used for the viscous fluxes $\mathbf{R}, \mathbf{S}, \mathbf{T}$. For implicit methods, a Jacobian must be introduced at time level $n+1$ for linearization. This Jacobian is formed by the derivatives of the flux values with respect to each conservative variable at a cell center point.

The implicit matrices will result in 9 elements around the diagonal element for 3D with first order upwind for inviscid fluxes and second order central differencing scheme. The first order upwind scheme for the implicit matrix will have the diagonal dominance required by Gauss-Seidel iteration [107]. Using Gauss-Seidel line relaxation, a block tri-diagonal matrix is inversed along each mesh line.

With an upwind scheme, the numerical flux is split into its left(L) and right(R) side fluxes. For example, the inviscid flux $\mathbf{E}$ at $i+\frac{1}{2}$ can be expressed as

$$\mathbf{E}_{i+\frac{1}{2}}=\mathbf{E}_L+\mathbf{E}_R=\mathbf{E}^{+}_{i+\frac{1}{2}}+\mathbf{E}^{-}_{i+\frac{1}{2}} \tag{4.4}$$

Since Eq. (4.1) is nonlinear, a linearization procedure is necessary. Let us apply a Taylor series expansion to the flux vectors at time level $n+1$ as

$$\mathbf{E}^{n+1} \cong \mathbf{E}^n + \frac{\partial \mathbf{E}}{\partial t}\Delta t + O[(\Delta t)^2] \tag{4.5}$$

$$\frac{\partial \mathbf{E}}{\partial t} = \frac{\partial \mathbf{E}}{\partial \mathbf{Q}}\frac{\partial \mathbf{Q}}{\partial t} \cong \frac{\partial \mathbf{E}}{\partial \mathbf{Q}}\frac{\Delta \mathbf{Q}}{\Delta t} \tag{4.6}$$

$$\mathbf{E}^{n+1} \cong \mathbf{E}^n + A \bullet \Delta \mathbf{Q} \tag{4.7}$$

where $A(= \frac{\partial \mathbf{E}}{\partial \mathbf{Q}})$ is the inviscid flux Jacobian matrix and the change in the conservative variable vector, $\Delta \mathbf{Q}$, is defined by

$$\Delta \mathbf{Q} = \mathbf{Q}^{n+1} - \mathbf{Q}^n \tag{4.8}$$

The inviscid flux $\mathbf{E}$ at the cell interface $i + \frac{1}{2}$ can be given as

$$\mathbf{E}^{n+1}_{i+\frac{1}{2}} = \mathbf{E}^n_{i+\frac{1}{2}} + (\tfrac{\partial \mathbf{E}^+}{\partial \mathbf{Q}})_L \bullet \Delta \mathbf{Q}_L + (\tfrac{\partial \mathbf{E}^-}{\partial \mathbf{Q}})_R \bullet \Delta \mathbf{Q}_R \tag{4.9}$$

where $\Delta \mathbf{Q}$ approaches zero when it is converged. Hence the accuracy order for $\Delta \mathbf{Q}$ is not important. The first order accuracy is used to evaluate $\Delta \mathbf{Q}$.

$$\Delta \mathbf{Q}_L = \Delta \mathbf{Q}_i, \quad \Delta \mathbf{Q}_R = \Delta \mathbf{Q}_{i+1} \tag{4.10}$$

Let

$$A^L_{i+\frac{1}{2}} = (\frac{\partial \mathbf{E}^+}{\partial \mathbf{Q}})_L, \quad A^R_{i+\frac{1}{2}} = (\frac{\partial \mathbf{E}^-}{\partial \mathbf{Q}})_R \tag{4.11}$$

Then,

$$\mathbf{E}^{n+1}_{i+\frac{1}{2}} = \mathbf{E}^n_{i+\frac{1}{2}} + A^L_{i+\frac{1}{2}}\Delta \mathbf{Q}_i + A^R_{i+\frac{1}{2}}\Delta \mathbf{Q}_{i+1} \tag{4.12}$$

Thus,

$$\begin{gathered}\mathbf{E}^{n+1}_{i+\frac{1}{2}} - \mathbf{E}^{n+1}_{i-\frac{1}{2}} = \\ (\mathbf{E}^n_{i+\frac{1}{2}} - \mathbf{E}^n_{i-\frac{1}{2}}) + A^R_{i+\frac{1}{2}}\Delta \mathbf{Q}_{i+1} + (A^L_{i+\frac{1}{2}} - A^R_{i-\frac{1}{2}})\Delta \mathbf{Q}_i - A^L_{i-\frac{1}{2}}\Delta \mathbf{Q}_{i-1}\end{gathered} \tag{4.13}$$

The viscous fluxes are linearized using central differencing.

$$\begin{aligned}(\mathbf{R}'_{i+\frac{1}{2}})^{n+1} &= (\mathbf{R}'_{i+\frac{1}{2}})^{n} + \frac{\partial \mathbf{R}'_{i+\frac{1}{2}}}{\partial \mathbf{Q}_{i+1}}\Delta\mathbf{Q}_{i+1} + \frac{\partial \mathbf{R}'_{i+\frac{1}{2}}}{\partial \mathbf{Q}_{i}}\Delta\mathbf{Q}_{i} \\ &= (\mathbf{R}'_{i+\frac{1}{2}})^{n} + L^{R}_{i+\frac{1}{2}}\Delta\mathbf{Q}_{i+1} + L^{L}_{i+\frac{1}{2}}\Delta\mathbf{Q}_{i}\end{aligned} \tag{4.14}$$

Thus,

$$\begin{aligned}&(\mathbf{R}'_{i+\frac{1}{2}})^{n+1} - (\mathbf{R}'_{i-\frac{1}{2}})^{n+1} = \\ &(\mathbf{R}'_{i+\frac{1}{2}})^{n} - (\mathbf{R}'_{i-\frac{1}{2}})^{n} + L^{R}_{i+\frac{1}{2}}\Delta\mathbf{Q}_{i+1} + (L^{L}_{i+\frac{1}{2}} - L^{R}_{i-\frac{1}{2}})\Delta\mathbf{Q}_{i} - L^{L}_{i-\frac{1}{2}}\Delta\mathbf{Q}_{i-1}\end{aligned} \tag{4.15}$$

The source term can be linearized by

$$\mathbf{D}^{n+1}_{i,j,k} \cong \mathbf{D}^{n}_{i,j,k} + (\frac{\partial \mathbf{D}}{\partial \mathbf{Q}})_{i,j,k} \bullet \Delta\mathbf{Q}_{i,j,k} \tag{4.16}$$

To apply above linearization to the fluxes in η and ζ direction, then the integrated governing equations are written as

$$\begin{aligned}&(I-\Theta)\Delta\mathbf{Q}_{i,j,k} + \hat{A}^{+}\Delta\mathbf{Q}_{i+1,j,k} + \hat{A}\Delta\mathbf{Q}_{i,j,k} + \hat{A}^{-}\Delta\mathbf{Q}_{i-1,j,k} \\ &+\hat{B}^{+}\Delta\mathbf{Q}_{i,j+1,k} + \hat{B}\Delta\mathbf{Q}_{i,j,k} + \hat{B}^{-}\Delta\mathbf{Q}_{i,j-1,k} \\ &+\hat{C}^{+}\Delta\mathbf{Q}_{i,j,k+1} + \hat{C}\Delta\mathbf{Q}_{i,j,k} + \hat{C}^{-}\Delta\mathbf{Q}_{i,j,k-1} = \mathbf{RHS}^{n}\end{aligned} \tag{4.17}$$

where $\Theta = \Delta t \bullet (\frac{\partial \mathbf{D}}{\partial \mathbf{Q}})^{n}_{i,j,k}$. The coefficients A, A^{+}, A^{-}, B, B^{+}, B^{-}, and C, C^{+}, C^{-} are called the left hand side (LHS) coefficient matrices and given as

$$
\begin{aligned}
\hat{A}^{+} &= \tfrac{\Delta t}{\Delta V}(A^{R}_{i+\frac{1}{2}} - L^{R}_{i+\frac{1}{2}}) \\
\hat{A} &= \tfrac{\Delta t}{\Delta V}(A^{L}_{i+\frac{1}{2}} - L^{L}_{i+\frac{1}{2}} - A^{R}_{i-\frac{1}{2}} + L^{R}_{i-\frac{1}{2}}) \\
\hat{A}^{-} &= -\tfrac{\Delta t}{\Delta V}(A^{L}_{i-\frac{1}{2}} - L^{L}_{i-\frac{1}{2}}) \\
\hat{B}^{+} &= \tfrac{\Delta t}{\Delta V}(B^{R}_{j+\frac{1}{2}} - M^{R}_{j+\frac{1}{2}}) \\
\hat{B} &= \tfrac{\Delta t}{\Delta V}(B^{L}_{j+\frac{1}{2}} - M^{L}_{j+\frac{1}{2}} - B^{R}_{j-\frac{1}{2}} + M^{R}_{j-\frac{1}{2}}) \\
\hat{B}^{-} &= -\tfrac{\Delta t}{\Delta V}(B^{L}_{j-\frac{1}{2}} - M^{L}_{j-\frac{1}{2}}) \\
\hat{C}^{+} &= \tfrac{\Delta t}{\Delta V}(C^{R}_{k+\frac{1}{2}} - N^{R}_{k+\frac{1}{2}}) \\
\hat{C} &= \tfrac{\Delta t}{\Delta V}(C^{L}_{k+\frac{1}{2}} - N^{L}_{k+\frac{1}{2}} - C^{R}_{k-\frac{1}{2}} + N^{R}_{k-\frac{1}{2}}) \\
\hat{C}^{-} &= -\tfrac{\Delta t}{\Delta V}(C^{L}_{k-\frac{1}{2}} - N^{L}_{k-\frac{1}{2}})
\end{aligned}
\tag{4.18}
$$

In Eq. (4.17), $\mathbf{RHS}^n$ is the summation of all terms on the right hand side (RHS) of the discretized equation and written as

$$
\begin{aligned}
\mathbf{RHS}^n = -\tfrac{\Delta t}{\Delta V}[(\mathbf{E}_{i+\frac{1}{2}} - \mathbf{E}_{i-\frac{1}{2}})^n + (\mathbf{F}_{i+\frac{1}{2}} - \mathbf{F}_{i-\frac{1}{2}})^n + (\mathbf{G}_{i+\frac{1}{2}} - \mathbf{G}_{i-\frac{1}{2}})^n \\
-(\mathbf{R'}_{i+\frac{1}{2}} - \mathbf{R'}_{i-\frac{1}{2}})^n - (\mathbf{S'}_{i+\frac{1}{2}} - \mathbf{S'}_{i-\frac{1}{2}})^n - (\mathbf{T'}_{i+\frac{1}{2}} - \mathbf{T'}_{i-\frac{1}{2}})^n] + \Delta t \bullet \mathbf{D}^n
\end{aligned}
\tag{4.19}
$$

Since the delta formulation($\Delta\mathbf{Q}$), the left hand side (LHS) in Eq. (4.17) constructed by employing 1st order scheme, does not affect the final solution, the accuracy of the converged solution relies on the accuracy of $\mathbf{RHS}^n$. The 5th order WENO scheme with an efficient upwind Riemann solver, so called the low diffusion E-CUSP (LDE) scheme [102], is used to evaluate the interface inviscid fluxes in $\mathbf{RHS}^n$. A fully conservative 4th order central differencing scheme [106] is used to evaluate the viscous fluxes. The unfactored Gauss-Seidel line iteration method is adopted to solve the Eq. (4.17) because the diagonal dominance is achieved through the 1st order implicit discretization and it is shown to be the most efficient relaxation method for transonic flow simulation [108].

4.2 Upwind Characteristics

Upwind schemes are designed to resolve the flow physics reasonably by accounting for the wave propagation, in which the flux vector is decomposed into a negative and a positive contributions according to the signs of the eigenvalues of the Jacobian matrices. Forward difference is then applied for the negative flux and backward difference for the positive flux. In the present study the Van Leer scheme [109] as a family of CUSP scheme is used for the LHS side in Eq. (4.17) and the LDE scheme [102] is applied for the RHS side in Eq. (4.17), which is described in detail in the following sections.

Before the upwind schemes are proposed to solve the LHS coefficients and RHS fluxes shown in Eq. (4.17), the characteristics of hyperbolic system as basis of the upwind schemes are explored. For example, the inviscid Jacobian matrix in ξ-direction can be computed as

$$\begin{aligned}\frac{\partial \mathbf{E}}{\partial \mathbf{Q}} &= \frac{\partial(E_1,E_2,E_3,E_4,E_5)}{\partial(Q_1,Q_2,Q_3,Q_4,Q_5)} \\ &= \begin{bmatrix} \frac{\partial E_1}{\partial Q_1} & \frac{\partial E_1}{\partial Q_2} & \frac{\partial E_1}{\partial Q_3} & \frac{\partial E_1}{\partial Q_4} & \frac{\partial E_1}{\partial Q_5} \\ \frac{\partial E_2}{\partial Q_1} & \frac{\partial E_2}{\partial Q_2} & \frac{\partial E_2}{\partial Q_3} & \frac{\partial E_2}{\partial Q_4} & \frac{\partial E_2}{\partial Q_5} \\ \frac{\partial E_3}{\partial Q_1} & \frac{\partial E_3}{\partial Q_2} & \frac{\partial E_3}{\partial Q_3} & \frac{\partial E_3}{\partial Q_4} & \frac{\partial E_3}{\partial Q_5} \\ \frac{\partial E_4}{\partial Q_1} & \frac{\partial E_4}{\partial Q_2} & \frac{\partial E_4}{\partial Q_3} & \frac{\partial E_4}{\partial Q_4} & \frac{\partial E_4}{\partial Q_5} \\ \frac{\partial E_5}{\partial Q_1} & \frac{\partial E_5}{\partial Q_2} & \frac{\partial E_5}{\partial Q_3} & \frac{\partial E_5}{\partial Q_4} & \frac{\partial E_5}{\partial Q_5} \end{bmatrix} \end{aligned} \tag{4.20}$$

$$\mathbf{Q} = \frac{1}{J}\begin{bmatrix} \rho & \rho u & \rho v & \rho w & \rho e \end{bmatrix} = \begin{bmatrix} Q_1 & Q_2 & Q_3 & Q_4 & Q_5 \end{bmatrix} \tag{4.21}$$

$$\mathbf{E} = \begin{bmatrix} \rho\bar{U} \\ \rho u\bar{U} + l_x P \\ \rho v\bar{U} + l_y P \\ \rho w\bar{U} + l_z P \\ (\rho e + P)\bar{U} \end{bmatrix} = \begin{bmatrix} \rho(l_x u + l_y v + l_z w) \\ \rho u(l_x u + l_y v + l_z w) + l_x P \\ \rho v(l_x u + l_y v + l_z w) + l_y P \\ \rho w(l_x u + l_y v + l_z w) + l_z P \\ (\rho e + P)(l_x u + l_y v + l_z w) \end{bmatrix} = \begin{bmatrix} E_1 \\ E_2 \\ E_3 \\ E_4 \\ E_5 \end{bmatrix} \tag{4.22}$$

where $\bar{U} = U - l_t$ and the static pressure for a perfect gas can be stated as

$$P = (\gamma - 1)[\rho e - \rho\frac{1}{2}(u^2 + v^2 + w^2 - \Omega^2 r^2)] \tag{4.23}$$

then, Eq. (4.22) and Eq. (4.23) can be reconstructed using the conservative variable vector $\mathbf{Q}$ as

$$E_1 = l_x Q_2 + l_y Q_3 + l_z Q_4 \tag{4.24}$$

$$E_2 = \frac{Q_2}{Q_1}(l_x Q_2 + l_y Q_3 + l_z Q_4) + l_x(\gamma - 1)(Q_5 - q) \tag{4.25}$$

$$E_3 = \frac{Q_3}{Q_1}(l_x Q_2 + l_y Q_3 + l_z Q_4) + l_y(\gamma - 1)(Q_5 - q) \tag{4.26}$$

$$E_4 = \frac{Q_4}{Q_1}(l_x Q_2 + l_y Q_3 + l_z Q_4) + l_z(\gamma - 1)(Q_5 - q) \tag{4.27}$$

$$E_5 = [\gamma Q_5 - (\gamma - 1)q](l_x \frac{Q_2}{Q_1} + l_y \frac{Q_3}{Q_1} + l_z \frac{Q_4}{Q_1}) \tag{4.28}$$

where

$$q = \frac{1}{2}(\frac{Q_2^2}{Q_1} + \frac{Q_3^2}{Q_1} + \frac{Q_4^2}{Q_1} - Q_1 \Omega^2 r^2) \tag{4.29}$$

The resulting Jacobian matrix A is obtained.

The eigenvalues($\lambda_{1,2,3,4,5}$) of the Jacobian matrix A that represent the characteristic direction of propagation are determined by

$$A = X_A \Lambda_A X_A^{-1} \tag{4.30}$$

$$\Lambda_A = \begin{bmatrix} \lambda_1 & 0 & 0 & 0 & 0 \\ 0 & \lambda_2 & 0 & 0 & 0 \\ 0 & 0 & \lambda_3 & 0 & 0 \\ 0 & 0 & 0 & \lambda_4 & 0 \\ 0 & 0 & 0 & 0 & \lambda_5 \end{bmatrix} = \begin{bmatrix} \bar{U} & 0 & 0 & 0 & 0 \\ 0 & \bar{U} & 0 & 0 & 0 \\ 0 & 0 & \bar{U} & 0 & 0 \\ 0 & 0 & 0 & \bar{U} + C & 0 \\ 0 & 0 & 0 & 0 & \bar{U} - C \end{bmatrix} \tag{4.31}$$

where Λ_A is a diagonal matrix with its element being the eigenvalues of A, X_A is the eigenvector matrix. C is the contravariant speed of sound given as

$$C = c\sqrt{l_x^2 + l_y^2 + l_z^2} \tag{4.32}$$

The eigenvector X_A is

$$X_A = [\vec{X}_1 \quad \vec{X}_2 \quad \vec{X}_3 \quad \vec{X}_4 \quad \vec{X}_5]$$

$$= \begin{pmatrix} 0 & 1 & 0 & 1 & 1 \\ -\frac{l_y}{l_x} & \frac{\bar{U}}{l_x} & -\frac{l_z}{l_x} & u + c\hat{l_x} & u - c\hat{l_x} \\ 1 & 0 & 0 & v + c\hat{l_y} & v - c\hat{l_y} \\ 0 & 0 & 1 & w + c\hat{l_z} & w - c\hat{l_z} \\ \frac{l_y u - lxv}{lx} & \frac{2u(l_y v + l_z w) - (v^2 + w^2 - u^2) l_x}{2 l_x} & \frac{l_x w - l_z u}{l_x} & I_o + \frac{c\bar{U}}{\sqrt{l_x^2 + l_y^2 + l_z^2}} & I_o - \frac{c\bar{U}}{\sqrt{l_x^2 + l_y^2 + l_z^2}} \end{pmatrix} \tag{4.33}$$

where

$$\hat{l_x} = \frac{l_x}{\sqrt{l_x^2 + l_y^2 + l_z^2}}$$

$$\hat{l_y} = \frac{l_y}{\sqrt{l_x^2 + l_y^2 + l_z^2}} \tag{4.34}$$

$$\hat{l_z} = \frac{l_z}{\sqrt{l_x^2 + l_y^2 + l_z^2}}$$

X_A^{-1} is the inverse eigenvector matrix of X_A such that

$$X_A^{-1} X_A = I \tag{4.35}$$

Note that the flux vector $\mathbf{E}$ equals $A\mathbf{Q}$ and is homogeneous function of degree one. The eigenvalues are real and consist of positive and negative eigenvalues. The signs of the eigenvalues indicate the direction of wave propagation; hence the flux vector can be split into positive or negative characteristics.

For example, for the subsonic flow where $M_\xi (= \frac{U}{C}) < 1$, the eigenvalues U, U, U and $U + C$ are positive, and $U - C$ is negative. If the Steger-Warming flux vector

splitting (FVS) scheme [110] is considered, then split of the Jacobian matrix A is shown as,

$$A = A^+ + A^- \tag{4.36}$$

where

$$A^+ = X_A \Lambda_A^+ X_A^{-1} \tag{4.37}$$

$$A^- = X_A \Lambda_A^- X_A^{-1} \tag{4.38}$$

Λ_A^+ is a diagonal matrix whose elements are the positive eigenvalues of A and Λ_A^- is a diagonal matrix whose elements are the negative eigenvalues of A. For example, if $\lambda_1 (= U)$ is positive, then

$$\Lambda_A^+ = \begin{bmatrix} \bar{U} & 0 & 0 & 0 & 0 \\ 0 & \bar{U} & 0 & 0 & 0 \\ 0 & 0 & \bar{U} & 0 & 0 \\ 0 & 0 & 0 & \bar{U}+C & 0 \\ 0 & 0 & 0 & 0 & 0 \end{bmatrix} \tag{4.39}$$

where $\Lambda_A^- = \Lambda_A - \Lambda_A^+$. Then, the flux vector $\mathbf{E}$ can be split as

$$\mathbf{E}^+ = A^+ \mathbf{Q} \tag{4.40}$$

$$\mathbf{E}^- = A^- \mathbf{Q} \tag{4.41}$$

The other inviscid coefficients matrices, B and C are determined in the same manner as the matrix A. For the supersonic flow ($M_\xi > 1$), all five eigenvalues are positive and which results in

$$A^+ = A \tag{4.42}$$

$$A^- = 0 \tag{4.43}$$

4.3 The Low Diffusion E-CUSP (LDE) Scheme

The Low Diffusion E-CUSP (LDE) Scheme [102] is used to evaluate the inviscid fluxes. The basic idea of the LDE scheme is to split the inviscid flux into the convective flux E^c and the pressure flux E^p based on the upwind characteristics. In generalized coordinate system, the flux $\mathbf{E}$ can be split as the following:

$$\mathbf{E}' = E^c + E^p = \begin{pmatrix} \rho U \\ \rho u U \\ \rho v U \\ \rho w U \\ \rho e U \\ \rho \tilde{\nu} U \end{pmatrix} + \begin{pmatrix} 0 \\ l_x p \\ l_y p \\ l_z p \\ p\overline{U} \\ 0 \end{pmatrix} \tag{4.44}$$

where, U is the contravariant velocity in ξ direction and is defined as the following:

$$U = l_t + l_x u + l_y v + l_z w \tag{4.45}$$

$\overline{U}$ is defined as:

$$\overline{U} = l_x u + l_y v + l_z w \tag{4.46}$$

The convective term, E^c is evaluated by

$$E^c = \rho U \begin{pmatrix} 1 \\ u \\ v \\ w \\ e \\ \tilde{\nu} \end{pmatrix} = \rho U f^c, \; f^c = \begin{pmatrix} 1 \\ u \\ v \\ w \\ e \\ \tilde{\nu} \end{pmatrix} \tag{4.47}$$

let

$$C = c\left(l_x^2 + l_y^2 + l_z^2\right)^{\frac{1}{2}} \tag{4.48}$$

where $c = \sqrt{\gamma RT}$ is the speed of sound.

Then the convective flux at interface $i + \frac{1}{2}$ is evaluated as:

$$E^c_{i+\frac{1}{2}} = C_{\frac{1}{2}} \left[\rho_L C^+ f^c_L + \rho_R C^- f^c_R\right] \tag{4.49}$$

where, the subscripts L and R represent the left and right hand sides of the interface. The Mach number splitting of Edwards [111] is borrowed to determine C^+ and C^- as the following:

$$C_{\frac{1}{2}} = \frac{1}{2}\left(C_L + C_R\right) \tag{4.50}$$

$$C^+ = \alpha^+_L \left(1 + \beta_L\right) M_L - \beta_L M^+_L - M^+_{\frac{1}{2}} \tag{4.51}$$

$$C^- = \alpha^-_R \left(1 + \beta_R\right) M_R - \beta_R M^-_R + M^-_{\frac{1}{2}} \tag{4.52}$$

$$M_L = \frac{U_L}{C_{\frac{1}{2}}},\ M_R = \frac{U_R}{C_{\frac{1}{2}}} \tag{4.53}$$

$$\alpha_{L,R} = \tfrac{1}{2}\left[1 \pm sign\left(M_{L,R}\right)\right] \tag{4.54}$$

$$\beta_{L,R} = -max\left[0, 1 - int\left(\left|M_{L,R}\right|\right)\right] \tag{4.55}$$

$$M^{+}_{\frac{1}{2}} = M_{\frac{1}{2}}\frac{C_R + C_L\Phi}{C_R + C_L},\ M^{-}_{\frac{1}{2}} = M_{\frac{1}{2}}\frac{C_L + C_R\Phi^{-1}}{C_R + C_L} \tag{4.56}$$

$$\Phi = \frac{\left(\rho C^2\right)_R}{\left(\rho C^2\right)_L} \tag{4.57}$$

$$M_{\frac{1}{2}} = \beta_L\delta^{+}M^{-}_{L} - \beta_R\delta^{-}M^{+}_{R} \tag{4.58}$$

$$M^{\pm}_{L,R} = \pm\tfrac{1}{4}\left(M_{L,R} \pm 1\right)^2 \tag{4.59}$$

$$\delta^{\pm} = \tfrac{1}{2}\left\{1 \pm sign\left[\tfrac{1}{2}\left(M_L + M_R\right)\right]\right\} \tag{4.60}$$

The pressure flux, E^p is evaluated as the following

$$E^p_{i+\frac{1}{2}} = \begin{pmatrix} 0 \\ \mathcal{P}^+ p\, l_x \\ \mathcal{P}^+ p\, l_y \\ \mathcal{P}^+ p\, l_z \\ \frac{1}{2} p \left[\overline{U} + \overline{C}_{\frac{1}{2}} \right] \\ 0 \end{pmatrix}_L + \begin{pmatrix} 0 \\ \mathcal{P}^- p\, l_x \\ \mathcal{P}^- p\, l_y \\ \mathcal{P}^- p\, l_z \\ \frac{1}{2} p \left[\overline{U} - \overline{C}_{\frac{1}{2}} \right] \\ 0 \end{pmatrix}_R \tag{4.61}$$

The contravariant speed of sound $\overline{C}$ in the pressure vector is consistent with $\overline{U}$. It is computed based on C as the following,

$$\overline{C} = C - l_t \tag{4.62}$$

The use of $\overline{U}$ and $\overline{C}$ instead of U and C in the pressure vector is to take into account of the grid speed so that the flux will transit from subsonic to supersonic smoothly. When the grid is stationary, $l_t = 0$, $\overline{C} = C$, $\overline{U} = U$.

The pressure splitting coefficient is:

$$\mathcal{P}^{\pm}_{L,R} = \frac{1}{4} \left(M_{L,R} \pm 1 \right)^2 \left(2 \mp M_L \right) \tag{4.63}$$

The LDE scheme can capture crisp shock profile and exact contact surface discontinuities as accurately as the Roe scheme [112]. With an extra equation from the DES, the splitting is basically the same as the original scheme for the Euler equation. This is an advantage over the Roe scheme [113], for which the eigenvectors need to be derived when any extra equation is added to the governing equations. In addition, it is simpler and more CPU efficient than the Roe scheme due to no matrix operation.

4.4 The 5th Order WENO Scheme

The interface flux, $E_{i+\frac{1}{2}} = E(Q_L, Q_R)$, is evaluated by determining the conservative variables Q_L and Q_R using fifth-order WENO scheme [103, 104]. For example,

$$(Q_L)_{i+\frac{1}{2}} = \omega_0 q_0 + \omega_1 q_1 + \omega_2 q_2 \tag{4.64}$$

where

$$\begin{aligned} q_0 &= \tfrac{1}{3}Q_{i-2} - \tfrac{7}{6}Q_{i-1} + \tfrac{11}{6}Q_i \\ q_1 &= -\tfrac{1}{6}Q_{i-1} + \tfrac{5}{6}Q_i + \tfrac{1}{3}Q_{i+1} \\ q_2 &= \tfrac{1}{3}Q_i + \tfrac{5}{6}Q_{i+1} - \tfrac{1}{6}Q_{i+2} \end{aligned} \tag{4.65}$$

$$\omega_k = \frac{\alpha_k}{\alpha_0 + \ldots + \alpha_{r-1}} \tag{4.66}$$

$$\begin{aligned} &\alpha_k = \tfrac{C_k}{\epsilon + IS_k},\ k = 0, \ldots, r-1 \\ &C_0 = 0.1,\ C_1 = 0.6,\ C_2 = 0.3 \\ &IS_0 = \tfrac{13}{12}\left(Q_{i-2} - 2Q_{i-1} + Q_i\right)^2 + \tfrac{1}{4}\left(Q_{i-2} - 4Q_{i-1} + 3Q_i\right)^2 \\ &IS_1 = \tfrac{13}{12}\left(Q_{i-1} - 2Q_i + Q_{i+1}\right)^2 + \tfrac{1}{4}\left(Q_{i-1} - Q_{i+1}\right)^2 \\ &IS_2 = \tfrac{13}{12}\left(Q_i - 2Q_{i+1} + Q_{i+2}\right)^2 + \tfrac{1}{4}\left(3Q_i - 4Q_{i+1} + Q_{i+2}\right)^2 \end{aligned} \tag{4.67}$$

where, ϵ is originally introduced to avoid the denominator becoming zero and is supposed to be a very small number. In [104], it is observed that IS_k will oscillate if ϵ is small and also shift the weights away from the optimum values in the smooth region. The higher the ϵ values, the closer the weights approach the optimum weights, C_k, which will give the symmetric evaluation of the interface flux with minimum numerical

dissipation. When there are shocks in the flow field, ϵ can not be too large to maintain the sensitivity to shocks. In [104], the optimized value of $\epsilon = 10^{-2}$ is recommended for the transonic flow with shock waves.

4.5 The 4th Order Central Differencing for Viscous Terms

A set of conservative fourth-order accurate finite central differencing schemes for the viscous terms is suggested [106]. These central differencing schemes are constructed so that the stencil widths are within the WENO scheme stencil. This requires that the central differencing achieves their maximum order accuracy in the WENO stencil.

We take the viscous flux derivative in ξ-direction as the example to explain how the schemes are constructed. To conservatively discretize the viscous derivative term in Navier-Stokes equations Eq. (3.28), we have

$$\frac{\partial R}{\partial \xi}|_i = \frac{\tilde{R}_{i+1/2} - \tilde{R}_{i-1/2}}{\Delta \xi} \tag{4.68}$$

To obtain 4th order accuracy, $\tilde{R}$ needs to be reconstructed as

$$\tilde{R}_{i-1/2} = \sum_{I=i-3/2}^{i+1/2} \alpha_I R_I \tag{4.69}$$

where

$$\alpha_{i-3/2} = -\frac{1}{24},\ \alpha_{i-1/2} = \frac{26}{24},\ \alpha_{i+1/2} = -\frac{1}{24}$$

$$R_{i-1/2} = \left[(\xi_x \tau_{xx}) + (\eta_y \tau_{xy}) + (\zeta_z \tau_{xz})\right]_{i-1/2}$$

$$
\begin{aligned}
(\tau_{xx}) = \quad & \mu\{\tfrac{4}{3}\left[(\xi_x\tfrac{\partial u}{\partial \xi}) + (\eta_x\tfrac{\partial u}{\partial \eta}) + (\zeta_x\tfrac{\partial u}{\partial \zeta})\right] \\
& -\tfrac{2}{3}[(\xi_y\tfrac{\partial v}{\partial \xi}) + (\eta_y\tfrac{\partial v}{\partial \eta}) + (\zeta_y\tfrac{\partial v}{\partial \zeta}) \\
& (\xi_z\tfrac{\partial w}{\partial \xi}) + (\eta_z\tfrac{\partial w}{\partial \eta}) + (\zeta_z\tfrac{\partial w}{\partial \zeta})]\}
\end{aligned} \tag{4.70}
$$

If R in Eq. (4.69) can be approximated with the accuracy order not lower than 4th order, the Taylor series expansion analysis of (4.68) and (4.69) will give

$$
\frac{1}{\Delta\xi}(\tilde{R}_{i+1/2} - \tilde{R}_{i-1/2}) = R^{'}(\xi_i) + O(\Delta\xi^4) \tag{4.71}
$$

and the 4th order accuracy is achieved (to be proved later). It needs to point out that in Eq. (4.68), $\tilde{R}_{i-1/2}$ can not be replaced by $R_{i-1/2}$. Otherwise, the 4th order accuracy can not be achieved even though the high order approximation of $R_{i-1/2}$ is used. The 4th order accuracy from Eq. (4.68)-(4.71) is also based on the uniform spacing $\Delta\xi = C$.

In order to achieve the highest order accuracy of R_I with $I = i-3/2, i-1/2, i+1/2$, the approximation of each term in Eq. (4.69) using the same points is given below:

$$
\mu_I = \sum_{l=m}^{n} C_l^I \mu_{i+l}, \tag{4.72}
$$

$$
\frac{\partial u}{\partial \xi}|_I = \frac{1}{\Delta\xi}\sum_{l=r}^{s} D_l^I u_{i+l}, \tag{4.73}
$$

$$
\frac{\partial u}{\partial \eta}|_I = \sum_{l=m}^{n} C_l^I \frac{\partial u}{\partial \eta}|_{i+l,j} \tag{4.74}
$$

where

$$
\frac{\partial u}{\partial \eta}|_{i,j} = \frac{1}{\Delta\eta}\sum_{l=p}^{q} C_l^c u_{i,j+l}, \tag{4.75}
$$

By choosing different ranges for $(m,n),(r,s),(p,q)$ and different coefficients C_l^I, D_l^I, C_l^c, one can obtain different order accuracy approximation to the viscous terms. The principle of choosing $(m,n),(r,s),(p,q)$ is to ensure that the approximation of $\frac{\partial R}{\partial \xi}|_i$ in Eq. (4.68) is a central differencing. For example, let $(m,n)=(-2,1),(r,s)=(-3,2), and\ (p,q)=(-2,2)$, and they give

$$\mu_I = \sum_{l=m}^{n} C_l^I \mu_{i+l} + O(\Delta\xi^4), \tag{4.76}$$

$$\frac{\partial u}{\partial \xi}|_I = \frac{1}{\Delta\xi}\sum_{l=r}^{s} D_l^I u_{i+l} + O(\Delta\xi^5), \tag{4.77}$$

$$\frac{\partial u}{\partial \eta}|_I = \sum_{l=m}^{n} C_l^I \frac{\partial u}{\partial \eta}|_{i+l,j} + O(\Delta\xi^4, \Delta\eta^4), \tag{4.78}$$

where

$$\frac{\partial u}{\partial \eta}|_{i,j} = \frac{1}{\Delta\eta}\sum_{l=p}^{q} C_l^c u_{i,j+l} + O(\Delta\eta^4) \tag{4.79}$$

the coefficients C_l^I, D_l^I, C_l^c can be obtained by Taylor's series expansion and are given in Tables 4.1-4.3. For example,

$$\begin{cases} \mu_{i-3/2} = \frac{1}{16}(5\mu_{i-2} + 15\mu_{i-1} - 5\mu_i + \mu_{i+1}) + O(\Delta\xi^4) \\ \mu_{i-1/2} = \frac{1}{16}(-\mu_{i-2} + 9\mu_{i-1} + 9\mu_i - \mu_{i+1}) + O(\Delta\xi^4) \\ \mu_{i+1/2} = \frac{1}{16}(\mu_{i-2} - 5\mu_{i-1} + 15\mu_i + 5\mu_{i+1}) + O(\Delta\xi^4) \end{cases} \tag{4.80}$$

$$\begin{cases} \frac{\partial u}{\partial \xi}|_{i-3/2} = \frac{1}{\Delta\xi}(\frac{71}{1920}u_{i-3} - \frac{141}{128}u_{i-2} + \frac{69}{64}u_{i-1} + \frac{1}{192}u_i - \frac{3}{128}u_{i+1} + \frac{3}{640}u_{i+2}) + O(\Delta\xi^5) \\ \frac{\partial u}{\partial \xi}|_{i-1/2} = \frac{1}{\Delta\xi}(-\frac{3}{640}u_{i-3} + \frac{25}{384}u_{i-2} - \frac{75}{64}u_{i-1} + \frac{75}{64}u_i - \frac{25}{384}u_{i+1} + \frac{3}{640}u_{i+2}) + O(\Delta\xi^5) \\ \frac{\partial u}{\partial \xi}|_{i+1/2} = \frac{1}{\Delta\xi}(-\frac{3}{640}u_{i-3} + \frac{3}{128}u_{i-2} - \frac{1}{192}u_{i-1} - \frac{69}{64}u_i + \frac{141}{128}u_{i+1} - \frac{71}{1920}u_{i+2}) + O(\Delta\xi^5) \end{cases} \tag{4.81}$$

The other terms are determined similarly. For comparison, the terms used in Ref. [114, 115] by De Rango and Zingg et al. are given as the following,

$$\begin{cases} \mu_{i-3/2} = \frac{1}{16}(-\mu_{i-3} + 9\mu_{i-2} + 9\mu_{i-1} - \mu_i) + O(\Delta\xi^4) \\ \mu_{i-1/2} = \frac{1}{16}(\mu_{i-2} + 9\mu_{i-1} + 9\mu_i - \mu_{i+1}) + O(\Delta\xi^4) \\ \mu_{i+1/2} = \frac{1}{16}(\mu_{i-1} + 9\mu_i + 9\mu_{i+1} - \mu_{i+2}) + O(\Delta\xi^4) \end{cases} \tag{4.82}$$

$$\begin{cases} \frac{\partial u}{\partial \xi}|_{i-3/2} = \frac{1}{24\Delta\xi}(-u_{i-3} - 27u_{i-2} + 27u_{i-1} - u_i) + O(\Delta\xi^4) \\ \frac{\partial u}{\partial \xi}|_{i-1/2} = \frac{1}{24\Delta\xi}(-u_{i-2} - 27u_{i-1} + 27u_i - u_{i+1}) + O(\Delta\xi^4) \\ \frac{\partial u}{\partial \xi}|_{i+1/2} = \frac{1}{24\Delta\xi}(-u_{i-1} - 27u_i + 27u_{i+1} - u_{i+2}) + O(\Delta\xi^4) \end{cases} \tag{4.83}$$

Compare Eqs. (4.80),(4.81) and Eqs. (4.82),(4.83), it can be seen that μ_I in present paper has the same accuracy order, as that of De Rango and Zingg et al., but has small stencil width $(i-2, \cdots, i+1)$, $\frac{\partial u}{\partial \xi}|_I$ has the same stencil width, but obtains one accuracy order higher than that in Ref. [114, 115].

Table 4.1: The coefficients of C_l^I

I	C_{-2}^I	C_{-1}^I	C_0^I	C_1^I
$i-3/2$	5/16	15/16	-5/16	1/16
$i-1/2$	-1/16	9/16	9/16	-1/16
$i+1/2$	1/16	-5/16	15/16	5/16

Table 4.2: The coefficients of D_l^I

I	D_{-3}^I	D_{-2}^I	D_{-1}^I	D_0^I	D_1^I	D_2^I
$i-3/2$	71/1920	-141/128	69/64	1/192	-3/128	3/640
$i-1/2$	-3/640	25/384	-75/64	75/64	-25/384	3/640
$i+1/2$	-3/640	3/128	-1/192	-69/64	141/128	-71/1920

It can be proved that the scheme Eq. (4.68) is symmetric with respect to cell i. For example, the coefficients of $\mu_{i-2}u_{i-3}$, $\mu_{i+2}u_{i+3}$, $\mu_{i-1}u_{i-2}$, and $\mu_{i+1}u_{i+2}$ can be

Table 4.3: The coefficients of C_l^c

C_{-2}^c	C_{-1}^c	C_0^c	C_1^c	C_2^c
1/12	-8/12	0	8/12	-1/12

found as (in the following formula, $\tilde{C}_l^I$ and $\tilde{D}_l^I$ are the coefficients of μ_{i+l}, u_{i+l} in R_I for $\tilde{R}_{i+1/2}$, respectively. It's clear that there are $\tilde{C}_l^I = C_{l-1}^{I-1}$ and $\tilde{D}_l^I = D_{l-1}^{I-1}$, $\tilde{\alpha}_I = \alpha_{I-1}$, $I = i - 1/2, i + 1/2, i + 3/2$):

$$
\begin{aligned}
C_{i-2,i-3} &= -\sum_{I=i-3/2}^{i+1/2} \alpha_I C_{-2}^I D_{-3}^I \\
&= -\left[(\tfrac{-1}{24}) \cdot \tfrac{5}{16} \cdot \tfrac{71}{1920} + \tfrac{26}{24} \cdot (\tfrac{-1}{16}) \cdot (\tfrac{-3}{640}) + (\tfrac{-1}{24}) \cdot \tfrac{1}{16} \cdot (\tfrac{-3}{640}) \right] \\
&= \tfrac{7}{46080}
\end{aligned}
$$

$$
\begin{aligned}
C_{i+2,i+3} &= \sum_{I=i-1/2}^{i+3/2} \tilde{\alpha}_I \tilde{C}_2^I \tilde{D}_3^I \\
&= (\tfrac{-1}{24}) \cdot \tfrac{1}{16} \cdot \tfrac{3}{640} + \tfrac{26}{24} \cdot (\tfrac{-1}{16}) \cdot \tfrac{3}{640} + (\tfrac{-1}{24}) \cdot \tfrac{5}{16} \cdot (\tfrac{-71}{1920}) \\
&= \tfrac{7}{46080}
\end{aligned}
$$

$$
\begin{aligned}
C_{i-1,i-2} &= \textstyle\sum_{I=i-1/2}^{i+3/2} \tilde{\alpha}_I \tilde{C}_{-1}^I \tilde{D}_{-2}^I - \sum_{I=i-3/2}^{i+1/2} \alpha_I C_{-1}^I D_{-2}^I \\
&= (\tfrac{-1}{24}) \cdot \tfrac{5}{16} \cdot \tfrac{71}{1920} + \tfrac{26}{24} \cdot (\tfrac{-1}{16}) \cdot (\tfrac{-3}{640}) + (\tfrac{-1}{24}) \cdot \tfrac{1}{16} \cdot (\tfrac{-3}{640}) \\
&\quad - \left[(\tfrac{-1}{24}) \cdot \tfrac{15}{16} \cdot (\tfrac{-141}{128}) + \tfrac{26}{24} \cdot \tfrac{9}{16} \cdot \tfrac{25}{384} + (\tfrac{-1}{24}) \cdot (\tfrac{-5}{16}) \cdot \tfrac{3}{128} \right] \\
&= -\tfrac{479}{5760}
\end{aligned}
$$

$$
\begin{aligned}
C_{i+1,i+2} &= \textstyle\sum_{I=i-1/2}^{i+3/2} \tilde{\alpha}_I \tilde{C}_{1}^I \tilde{D}_{2}^I - \sum_{I=i-3/2}^{i+1/2} \alpha_I C_{1}^I D_{2}^I \\
&= (\tfrac{-1}{24}) \cdot (\tfrac{-5}{16}) \cdot (\tfrac{-3}{128}) + \tfrac{26}{24} \cdot \tfrac{9}{16} \cdot (\tfrac{-25}{384}) + (\tfrac{-1}{24}) \cdot \tfrac{15}{16} \cdot \tfrac{141}{128} \\
&\quad - \left[(\tfrac{-1}{24}) \cdot \tfrac{1}{16} \cdot \tfrac{3}{640} + \tfrac{26}{24} \cdot (\tfrac{-1}{16}) \cdot \tfrac{3}{640} + (\tfrac{-1}{24}) \cdot \tfrac{5}{16} \cdot (\tfrac{-71}{1920}) \right] \\
&= -\tfrac{479}{5760}
\end{aligned}
$$

So we have $C_{i-2,i-3} = C_{i+2,i+3}$, $C_{i-1,i-2} = C_{i+1,i+2}$, and so on. Hence the scheme Eq. (4.68) is symmetric with respect to grid node i. The symmetry of central differencing for Eq. (4.68) satisfies the diffusion property of the viscous flux.

Next, we prove that the order of accuracy given by Eq.(4.71) is satisfied. Take the term $T^- = \mu \partial u / \partial \xi$ in Eq.(4.71) as the example,

In $\tilde{R}_{i-1/2}$, at $I = i - 3/2$, based on Taylor's series expansion

$$
\begin{aligned}
T_{i-3/2}^- &= \textstyle\sum_{l=m}^{n} C_l^I \mu_{i+l} (\frac{1}{\Delta\xi} \sum_{l=r}^{s} D_l^I u_{i+l}) \\
&= \left[\mu_{i-3/2} + A_I \mu_{i-3/2}^{(4)} \Delta\xi^4 + O(\Delta\xi^5) \right] \left[\tfrac{\partial u}{\partial \xi}|_{i-3/2} + O(\Delta\xi^5) \right] \\
&= \mu_{i-3/2} \tfrac{\partial u}{\partial \xi}|_{i-3/2} + A_I \mu_{i-3/2}^{(4)} \tfrac{\partial u}{\partial \xi}|_{i-3/2} \Delta\xi^4 + O(\Delta\xi^5)
\end{aligned}
$$

A_I is the coefficient of Taylor's series expansion.

The corresponding term T^+ in $\tilde{R}_{i+1/2}$ is at $I = i - 1/2$, and

$$
\begin{aligned}
T_{i-1/2}^+ &= \textstyle\sum_{l=m}^{n} \tilde{C}_l^I \mu_{i+1+l} (\frac{1}{\Delta\xi} \sum_{l=r}^{s} \tilde{D}_l^I u_{i+1+l}) \\
&= \left[\mu_{i-1/2} + \tilde{A}_I \mu_{i-1/2}^{(4)} \Delta\xi^4 + O(\Delta\xi^5) \right] \left[\tfrac{\partial u}{\partial \xi}|_{i-1/2} + O(\Delta\xi^5) \right] \\
&= \mu_{i-1/2} \tfrac{\partial u}{\partial \xi}|_{i-1/2} + \tilde{A}_I \mu_{i-1/2}^{(4)} \tfrac{\partial u}{\partial \xi}|_{i-1/2} \Delta\xi^4 + O(\Delta\xi^5)
\end{aligned}
$$

Note that $A_I = \tilde{A}_I$, hence

$$T^+_{i-1/2} - T^-_{i-3/2} = \mu_{i-1/2}\frac{\partial u}{\partial \xi}|_{i-1/2} - \mu_{i-3/2}\frac{\partial u}{\partial \xi}|_{i-3/2} + O(\Delta\xi^5)$$

The other two terms can be analyzed similarly as above, then Eq.(4.71)

$$\frac{1}{\Delta\xi}(\tilde{R}_{i+1/2} - \tilde{R}_{i-1/2}) = R^{'}(\xi_i) + O(\Delta\xi^4)$$

is proved, i.e. the constructed schemes are formally 4th order accuracy.

4.6 Implicit Time Integration

When a unsteady solution is considered, higher order approximation for the time derivative is desirable. For unsteady flow, Jameson formulated so called the 2nd order dual time stepping scheme [116]. By introducing a pseudo time term, the unsteady problem at each physical time step is treated as a steady state problem for pseudo time. Without losing time accuracy, the dual time stepping scheme can greatly improve the computation efficiency by enhancing diagonal dominance [117].

4.6.1 Implicit Time Accurate Flow Solver

The time accurate governing equations are solved using dual time stepping method suggested by Jameson [116]. To achieve high convergence rate, the implicit pseudo time marching scheme is used with the unfactored Gauss-Seidel line relaxation [118]. The physical temporal term is discretized implicitly using a three point, backward differencing as the following:

$$\frac{\partial Q}{\partial t} = \frac{3Q^{n+1} - 4Q^n + Q^{n-1}}{2\Delta t} \tag{4.84}$$

where $n-1$, n and $n+1$ are three sequential time levels, which have a time interval of Δt. The first-order Euler scheme is used to discretize the pseudo temporal term to enhance diagonal dominance. The semi-discretized equations of the governing equations are finally given as the following:

$$\begin{aligned}\left[\left(\tfrac{1}{\Delta\tau}+\tfrac{1.5}{\Delta t}\right)I-\left(\tfrac{\partial R}{\partial Q}\right)^{n+1,m}\right]\delta Q^{n+1,m+1}\\ =R^{n+1,m}-\tfrac{3Q^{n+1,m}-4Q^{n}+Q^{n-1}}{2\Delta t}\end{aligned} \tag{4.85}$$

where the $\Delta\tau$ is the pseudo time step, R is the net flux evaluated on a grid point using the fifth-order WENO scheme.

CHAPTER 5

CFJ Airfoil Parameters

This chapter describes the definitions of parameters that are used to measure the CFJ implementation and to evaluate the performance of CFJ airfoil.

5.1 Lift, Drag and Moment Calculation

The momentum and pressure at the injection and suction slots produce a reactionary force, which is automatically measured by the force balance in wind tunnel testing. However, for CFD simulation, the full reactionary force needs to be included. Using a control volume analysis, the reactionary forces can be calculated using the flow parameters at the injection and suction slot opening surfaces. Zha et al. [62] give the following formulations to calculate the lift and drag due to the jet reactionary force for a CFD simulation. By considering the effects of injection and suction jets on the CFJ airfoil, the expressions for these reactionary forces are given as :

$$F_{x_{cfj}} = (\dot{m}_j V_{j1} + p_{j1} A_{j1}) * cos(\theta_1 - \alpha) - (\dot{m}_j V_{j2} + p_{j2} A_{j2}) * cos(\theta_2 + \alpha) \quad (5.1)$$

$$F_{y_{cfj}} = (\dot{m}_{j1} V_{j1} + p_{j1} A_{j1}) * sin(\theta_1 - \alpha) + (\dot{m}_{j2} V_{j2} + p_{j2} A_{j2}) * sin(\theta_2 + \alpha) \quad (5.2)$$

where the subscripts 1 and 2 stand for the injection and suction respectively, and θ_1 and θ_2 are the angles between the injection and suction slot surfaces and a line normal to the airfoil chord. α is the angle of attack.

The total lift and drag on the CFJ airfoil can then be expressed as:

$$D = R'_x - F_{x_{cfj}} \tag{5.3}$$

$$L = R'_y - F_{y_{cfj}} \tag{5.4}$$

where R'_x and R'_y are the surface integral of pressure and shear stress in x (drag) and y (lift) direction excluding the internal injection and suction ducts.

Let us introduce the CFJ reactionary forces components in the x and y direction for the injection (inj subscript) and suction (sub subscript) as :

$$F_{x_{inj}} = (\dot{m}_j V_{j1} + p_{j1} A_{j1}) * cos(\theta_1 - \alpha) \tag{5.5}$$

$$F_{x_{suc}} = (\dot{m}_j V_{j2} + p_{j2} A_{j2}) * cos(\theta_2 + \alpha) \tag{5.6}$$

$$F_{y_{inj}} = (\dot{m}_{j1} V_{j1} + p_{j1} A_{j1}) * sin(\theta_1 - \alpha) \tag{5.7}$$

$$F_{y_{suc}} = (\dot{m}_{j2} V_{j2} + p_{j2} A_{j2}) * sin(\theta_2 + \alpha) \tag{5.8}$$

The total pitching moment of the CFJ airfoil can be expressed as:

$$M_z = M'_z + F_{x_{inj}}.L_{y_{inj}} + F_{y_{inj}}.L_{x_{inj}} - F_{x_{suc}}.L_{y_{suc}} - F_{y_{suc}}.L_{x_{suc}} \tag{5.9}$$

where M'_z is the pitching moment generated by the airfoil surface pressure and shear stress excluding the internal injection and suction ducts. $L_{x_{inj}}$ and $L_{y_{inj}}$, respectively $L_{x_{suc}}$ and $L_{y_{suc}}$, are the moment arm in x and y direction for the injection, respectively suction. By convention, we define a pitch up moment as a positive moment and a pitch down moment as a negative moment.

For the CFD simulation, the total lift, drag and moment are calculated using Eqs. (5.3), (5.4) and (5.9) respectively.

5.2 Jet Momentum Coefficient

The jet momentum coefficient C_μ is a parameter used to quantify the jet intensity. It is defined as :

$$C_\mu = \frac{\dot{m} V_j}{\frac{1}{2}\rho_\infty {V_\infty}^2 S} \tag{5.10}$$

where $\dot{m}$ is the injection mass flow, V_j the injection velocity, ρ_∞ and V_∞ denote the free stream density and velocity, and S is the planform area.

5.3 Power Coefficient

The CFJ can be implemented by mounting a pumping system inside the wing that withdraws air from the suction slot and blows it into the injection slot. The power consumption can be determined by the jet mass flow and total enthalpy change as the following :

$$P = \dot{m}(H_{t1} - H_{t2}) \tag{5.11}$$

where H_{t1} and H_{t2} are the total enthalpy in the injection cavity and suction cavity respectively, P is the Power required by the pump and $\dot{m}$ the jet mass flow rate. Introducing the pump efficiency η and total pressure ratio of the pump $\Gamma = \frac{P_{t1}}{P_{t2}}$, the power consumption can be expressed as :

$$P = \frac{\dot{m} C_p T_{t2}}{\eta}(\Gamma^{\frac{\gamma-1}{\gamma}} - 1) \tag{5.12}$$

where γ is the specific heat ratio equal to 1.4 for air. The power consumption can be expressed as a power coefficient below:

$$P_c = \frac{P}{\frac{1}{2}\rho_\infty V_\infty^3 S} \tag{5.13}$$

5.4 Corrected Aerodynamic Efficiency

The conventional airfoil aerodynamic efficiency is defined as :

$$\frac{L}{D} \tag{5.14}$$

For the CFJ airfoil, the ratio above still represents the pure aerodynamic relationship between lift and drag. However since CFJ active flow control consumes energy, the ratio above is modified to take into account the energy consumption of the pump. The formulation of the corrected aerodynamic efficiency for CFJ airfoils is :

$$(\frac{L}{D})_c = \frac{L}{D + \frac{P}{V_\infty}} \tag{5.15}$$

where V_∞ is the free stream velocity, P is the pumping power, and L and D are the lift and drag generated by the CFJ airfoil. The formulation above converts the power consumed by the CFJ into a force $\frac{P}{V_\infty}$ which is added to the aerodynamic drag D. If the pumping power is set to 0, this formulation returns to the aerodynamic efficiency of a conventional airfoil.

5.5 Aircraft Productivity

The transportation ability of an airplane is measured by how much total weight the aircraft can move for the maximum distance. We use a term "productivity" defined as the product of the total weight by the maximum range to represent the transportation ability of an airplane.

For a jet engine airplane, the total weight of the aircraft decreases during flight. A non-dimensional productivity parameter is hence defined using the aircraft averaged weight as below:

$$C_{RW} = \frac{R\overline{W}}{\frac{1}{2c_t}\bar{\rho}V_\infty^3 S} = \frac{C_L^2}{C_D}\ln\frac{W_0}{W_f} \tag{5.16}$$

where R is the aircraft range, $\overline{W}$ is the averaged weight of the aircraft during cruise, c_t is the engine cruise thrust specific fuel consumption[fuel weight(N)/(thrust(N) s)], $\bar{\rho}$ is the averaged air density during cruise due to altitude variation, S is the wing platform area, W_0 is the aircraft initial gross weight at takeoff, W_f is the final weight at landing. This formulation is obtained from the Breguet Range Equation. The productivity parameter represents the productivity of the aircraft with the fuel consumed per unit time.

For a propeller engine airplane, the productivity parameter is defined as:

$$C_{RW} = \frac{R\overline{W}}{\frac{1}{2c}\bar{\rho}V_\infty^2 S} = \eta\frac{C_L^2}{C_D}\ln\frac{W_0}{W_f} \tag{5.17}$$

where c is the specific fuel consumption of the propeller, η is the propeller efficiency.

For a full electric battery powered propeller airplane, the aircraft weight will not change during flight. The productivity parameter is defined as:

$$C_{RW} = \frac{RW}{\frac{1}{2c}\rho V_\infty^2 S E_c/g} = \eta\frac{C_L^2}{C_D}\frac{W_b}{W_0} \tag{5.18}$$

where E_c is the battery specific energy density (Wh/kg), W_b is the total battery weight.

To compare aircraft that have the same ratio of initial weight to final weight with the same engine fuel consumption or battery energy density, the only factor affecting their productivity parameter is C_L^2/C_D. We hence name C_L^2/C_D as productivity efficiency.

We consider the productivity efficiency $C_L^2/C_D = C_L(C_L/C_D)$ as a more comprehensive parameter than the conventional aerodynamic efficiency C_L/C_D to measure the merit of an airplane aerodynamic design for cruise performance. The former includes not only the information of C_L/C_D, but also the information of the aircraft weight C_L. For example, for two airplane designs having the same C_L/C_D with one C_L twice larger than the other, if the wing sizes are the same, one airplane will be able to carry twice more weight than the other with productivity and wing loading increased by 100%. Such a large difference is not reflected by C_L/C_D, but very well reflected by C_L^2/C_D.

The definition of C_L/C_D in general is a suitable measure of merit for conventional aircraft design. This is because at a certain Mach number regime, the maximum C_L/C_D is usually achieved at low angle of attack within the drag bucket and is more or less the same for different airfoil designs. In other words, for the same optimum C_L/C_D, the C_L is about the same. A typical C_L for subsonic airfoil is about 0.4 and for transonic airfoil is about 0.7.

For CFJ airfoil, the minimum CFJ pumping power occurs at a fairly high AoA as shown in Fig. 1.20 [67, 68]. With the augmentation of CFJ, the subsonic cruise lift coefficient of a CFJ airfoil is typically 2 to 3 times higher than the conventional airfoil with about the same $(C_L/C_D)_c$ [70]. Such a high lift coefficient is unattainable for conventional airfoil since they would be either stalled or near stalled with very high drag. Hence for CFJ aircraft design, the productivity efficiency $C_L^2/C_D = C_L(C_L/C_D)$ is more informative to be used to reflect the aerodynamic performance. The corrected productivity efficiency for CFJ airfoils is $(C_L^2/C_D)_c = C_L^2/(C_D + P_c)$.

CHAPTER 6

Validation of IDDES

6.1 Hybrid RANS/LES Simulation

Airfoil stall flows at the high angle of attack with massive flow separation are very challenging to simulate accurately [119]. Large vortex structures are formed around the airfoil leading edge and travel along the airfoil suction surface as they grow, and get separated from the airfoil surface near the trailing edge.

Reynolds-averaged Navier-Strokes (RANS) methods are not appropriate for simulating stalled vortical flow structures due to its universal scale filtering. As an alternative, large eddy simulation (LES) is developed to directly simulate the large flow structures and model the small eddy structures that are more isotropic. However, LES is much more CPU expensive. The hybrid RANS/LES approach is a promising compromise for engineering applications by taking the advantages of RANS's high efficiency and LES's high accuracy with more affordable computational cost.

The detached eddy simulation (DES, or DES97) is the first and most popular non-zonal hybrid RANS/LES strategy suggested by Spalart et al. in 1997 [53]. Near the solid surface within the wall boundary layer, the unsteady RANS(URANS) turbulence modeling is utilized. Away from the boundary layer, the DES97 model is automati-

cally converted to LES. The Delayed detached-eddy simulation (DDES) suggested by Spalart et al. [54] is improved to resolve model stress depletion(MSD) and grid induced separation(GIS) problems. The more recently improved DDES(IDDES) model is formulated by Travin et al. [55] and Shur et al. [56] by coupling wall-modeled LES(WMLES) and DDES to eliminate the log layer mismatch(LLM) problem, and maintain the compatibility with the general DES approach. The major improvement of IDDES can be summarized as a near-wall modification of the LES filter Δ, and a more rapid transition between the RANS and LES length scales than DES97 or DDES. The IDDES method utilizes more sensors in the boundary layer region and a new blending function based on theoretical considerations and empirical tuning [57].

Computational simulations of airfoil stall flows have been conducted extensively by various researchers [55, 58–60]. Travin et al. [55] simulate the massively separated flows over airfoil, and observe that the DDES performs similarly to the original DES97 for their cases. Morton et al. [58] employed DES97 to simulate a full F/A-18E aircraft experiencing massively separated flows with good agreement with the experiment. Durrani et al. [59] applied DES97 and DDES to simulate the flow around the A-airfoil at the maximum lift condition(AoA=13.3°). They observed that for the flow with a relatively thick boundary layer and a mild trailing-edge separation, DES97 performs better than DDES due to its relatively lower turbulence dissipation levels.

The objective of this study is two-folds: 1) Apply the high order accuracy schemes to IDDES with different mesh sizes to demonstrate their performance at different conditions; 2) Compare the IDDES turbulence modeling with advantages over RANS model and DDES for airfoil stalled flows.

6.2 IDDES Validation of the 3D Flat Plate Boundary Layer

Table 6.1: Computational parameters for the flat plate validation

#	Mach	Re	Δx^*	Δy_1	Δz	Δx^+	Δy_1^+	Δz^+
c-Ma1Re1	0.1	$1e^6$	0.0084	1.0e-5	0.0022	336	0.40	88
c-Ma1Re2	0.1	$2e^6$	0.0084	1.0e-6	0.0022	672	0.08	176
c-Ma1Re6	0.1	$6.5e^6$	0.0084	1.0e-6	0.0022	1764	0.21	462
c-Ma1Re10	0.1	$10e^6$	0.0084	1.0e-6	0.0022	3024	0.36	792
c-Ma1Re20	0.1	$20e^6$	0.0084	1.0e-6	0.0022	7392	0.88	1936
f-Ma1Re1	0.1	$1e^6$	0.00133	1.0e-5	0.0022	53.3	0.40	88
f-Ma1Re2	0.1	$2e^6$	0.00133	1.0e-6	0.0022	106.4	0.08	176
f-Ma1Re6	0.1	$6.5e^6$	0.00133	1.0e-6	0.0022	279.3	0.21	462
f-Ma1Re10	0.1	$10e^6$	0.00133	1.0e-6	0.0022	478.8	0.36	792
f-Ma1Re20	0.1	$20e^6$	0.00133	1.0e-6	0.0022	1170.4	0.88	1936
c-Ma6Re1	0.6	$1e^6$	0.0084	1.0e-5	0.0022	336	0.40	88
c-Ma6Re2	0.6	$2e^6$	0.0084	1.0e-6	0.0022	672	0.08	176
c-Ma6Re6	0.6	$6.5e^6$	0.0084	1.0e-6	0.0022	1764	0.21	462
c-Ma6Re10	0.6	$10e^6$	0.0084	1.0e-6	0.0022	3024	0.36	792
c-Ma6Re20	0.6	$20e^6$	0.0084	1.0e-6	0.0022	7392	0.88	1936
f-Ma6Re1	0.6	$1e^6$	0.00133	1.0e-5	0.0022	53.3	0.40	88
f-Ma6Re2	0.6	$2e^6$	0.00133	1.0e-6	0.0022	106.4	0.08	176
f-Ma6Re6	0.6	$6.5e^6$	0.00133	1.0e-6	0.0022	279.3	0.21	462
f-Ma6Re10	0.6	$10e^6$	0.00133	1.0e-6	0.0022	478.8	0.36	792
f-Ma6Re20	0.6	$20e^6$	0.00133	1.0e-6	0.0022	1170.4	0.88	1936

*All the grid distance information refers to the local grid size denoted in Fig. 6.1.

To test the IDDES implementation, simulation of the 3D flat plate turbulent boundary layer flow is conducted to validate with the law of the wall. The simulations are conducted at different Mach numbers, Reynolds numbers and mesh sizes. To study the sensitivity of turbulence models on compressibility, two Mach number of 0.1 and 0.6 are used in the simulation. Four different Reynolds number in the range of 1,000,000 to 20,000,000 are simulated. Since mesh sizes have a significant impact on the DES-family models, different meshes are constructed for comparison. As shown in Fig. 6.1, two computational meshes are constructed with size of $120 \times 120 \times 5$

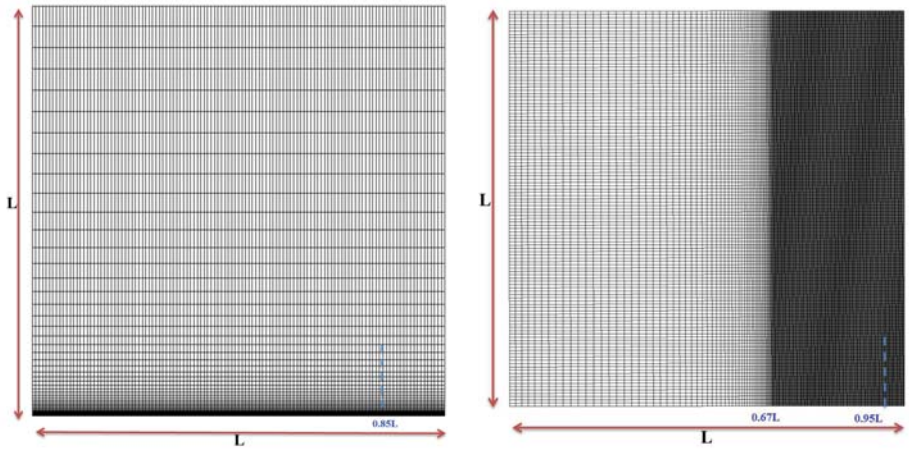

Figure 6.1: Computational coarse and fine mesh for flat plate

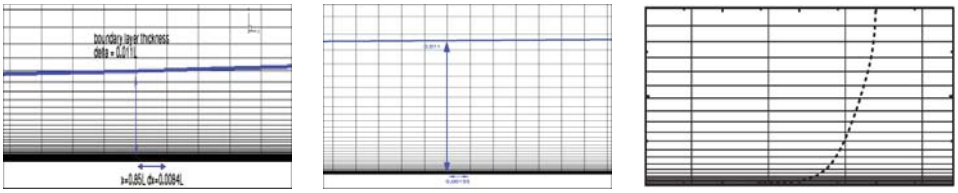

coarse mesh fine mesh ambiguous grid spacing

Figure 6.2: Typical mesh size and boundary layer thickness in the test section for coarse and fine mesh, shown are simulations with Reynolds number of 20,000,000

and $300 \times 120 \times 5$ in streamwise, normal to the wall and spanwise direction. The computational meshes are constructed to test the ambiguous grid spacing, as indicated by Spalart [54]. The coarse mesh is constructed to have streamwise grid spacing, $\Delta_{\|}$ (or Δx for the present 3D flat plate) about 0.63-0.75 of the turbulent boundary layer thickness, calculated by $\delta = 0.37(Re_L)^{-0.2}L$. The fine mesh is constructed to have streamwise grid spacing, $\Delta_{\|}$ (or Δx and Δz for the present 3D flat plate) about 0.09-0.118 of the turbulent boundary layer thickness. The first grid dimensionless distance normal to the wall has the $y^+(= \frac{u_\tau y}{\nu})$ is less than unity. Periodic boundary conditions are applied in the spanwise directions. No-slip wall boundary conditions are implemented on the flat plate surface. The 3D flat plate boundary layer test cases are summarized in table 6.1.

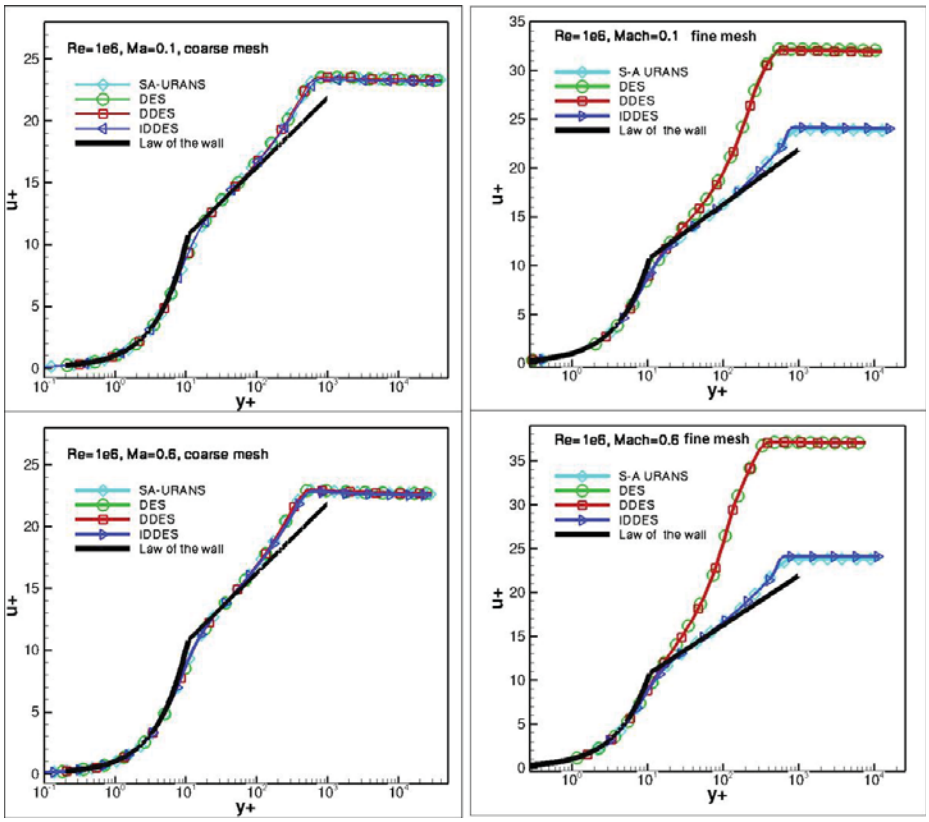

Figure 6.3: Mean velocity profiles calculated at Re=1000000, comparing to the law of the wall(Mach = 0.1(top figure), 0.6(bottom figure), coarse mesh(Left figure) and fine mesh(Right figure))

Fig. 6.3, 6.4, 6.5, 6.6 and 6.7 present the turbulent boundary layer profiles computed by the S-A URANS model, and DES family models(DES97, DDES and IDDES) at different Reynolds numbers with coarse and fine meshes. In order to demonstrate the IDDES improvement on the MSD and LLM problems over the DES97 and DDES, the meshes are specifically generated in the ambiguous grid size range. The boundary layer size and mesh size in the test region are illustrated as in Fig. 6.2

The first case has the Reynolds number of 1,000,000 and the results are shown in Fig. 6.3. For the coarse mesh simulation at both Mach number of 0.1 and 0.6, all the simulated boundary layer profiles are in good agreement with the law of the wall. However, for the fine mesh simulation, the profiles calculated by DES97 and DDES are

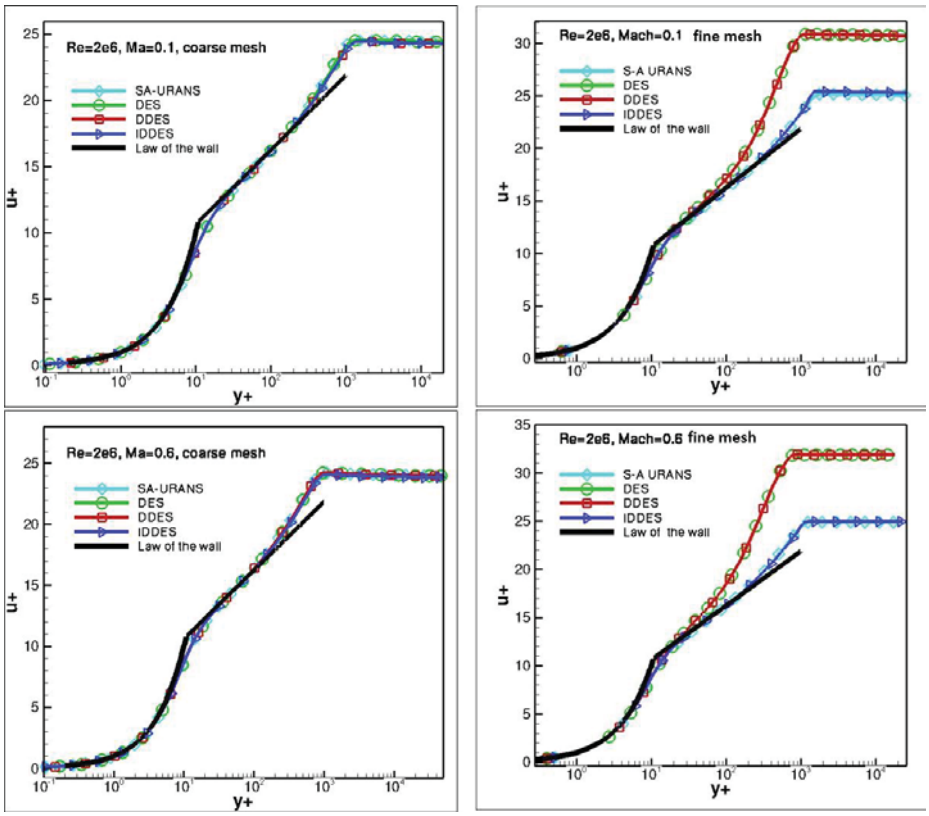

Figure 6.4: Mean velocity profiles calculated at Re=2000000, comparing to the law of the wall(Mach = 0.1(top figure), 0.6(bottom figure), coarse mesh(Left figure) and fine mesh(Right figure))

significantly deviated away from the velocity log profile for both two Mach numbers. This phenomena is referred as the Log Layer Mismatch (LLM) [54], [56], [120]. The higher u_+ obtained by the DES97 and DDES calculation indicates that the wall shear stress τ_w is underpredicted. Similar trends are observed in the Reynolds numbers of 2,000,000 and 6,500,000.

At the Reynolds numbers of 10,000,000, the accuracy of DES97 and DDES has a significant difference for the fine mesh at the Mach number of 0.1. This observation is referred as the Model Stress Depletion (MSD) by Spalart [54]. However, at the high Mach number of 0.6, the predicted velocity profiles show little difference between

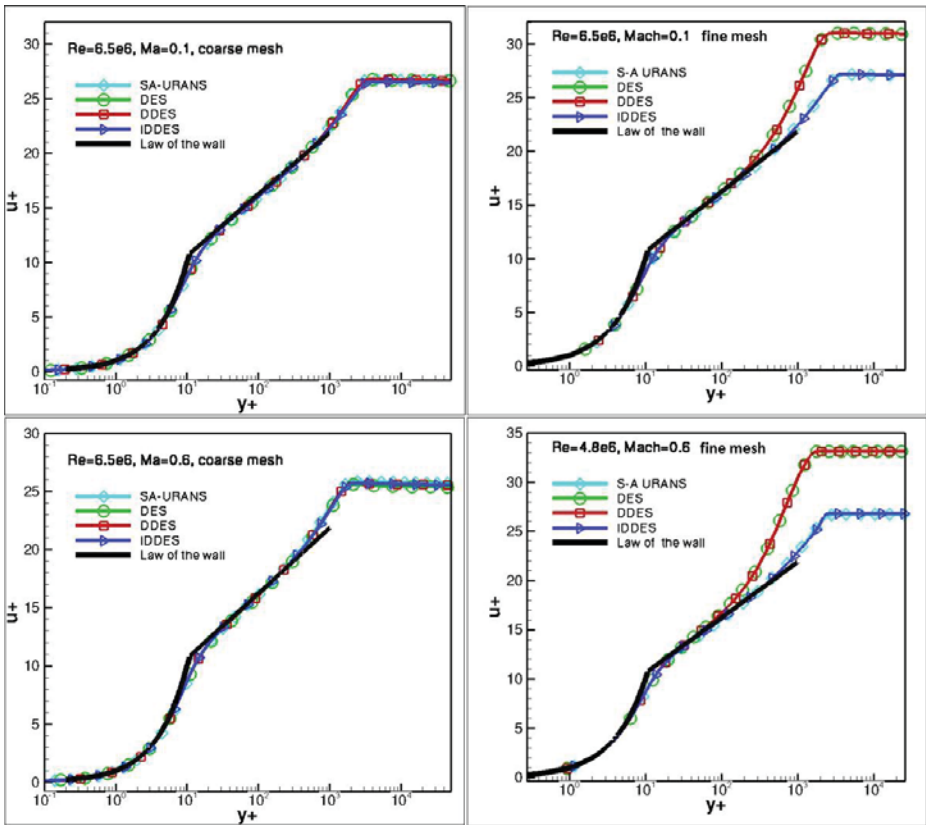

Figure 6.5: Mean velocity profiles calculated at Re=6500000, comparing to the law of the wall(Mach = 0.1(top figure), 0.6(bottom figure), coarse mesh(Left figure) and fine mesh(Right figure))

the DES97 and DDES. For the coarse mesh, both the velocity profiles predicted by DES97 and DDES agree well with the law of the wall.

At the highest Reynolds number of 20,000,000, the results are quite different for DES97 and DDES with the variation of Mach number. At Mach number of 0.1, DES97 and DDES obtain the velocity profiles that are deviated from the law of the wall in at the coarse mesh and fine mesh. At the high Mach number of 0.6, all the simulations agree well with the law of the wall. As always, the IDDES outperforms all the DES family models with an excellent prediction for all the cases.

In Fig. 6.8, the simulated velocity profile ratio ($\frac{u}{U_\infty}$), the dimensionless turbulent eddy viscosity($0.002\frac{\nu_t}{\nu}$), blending function f_d, and elevating function f_e are all

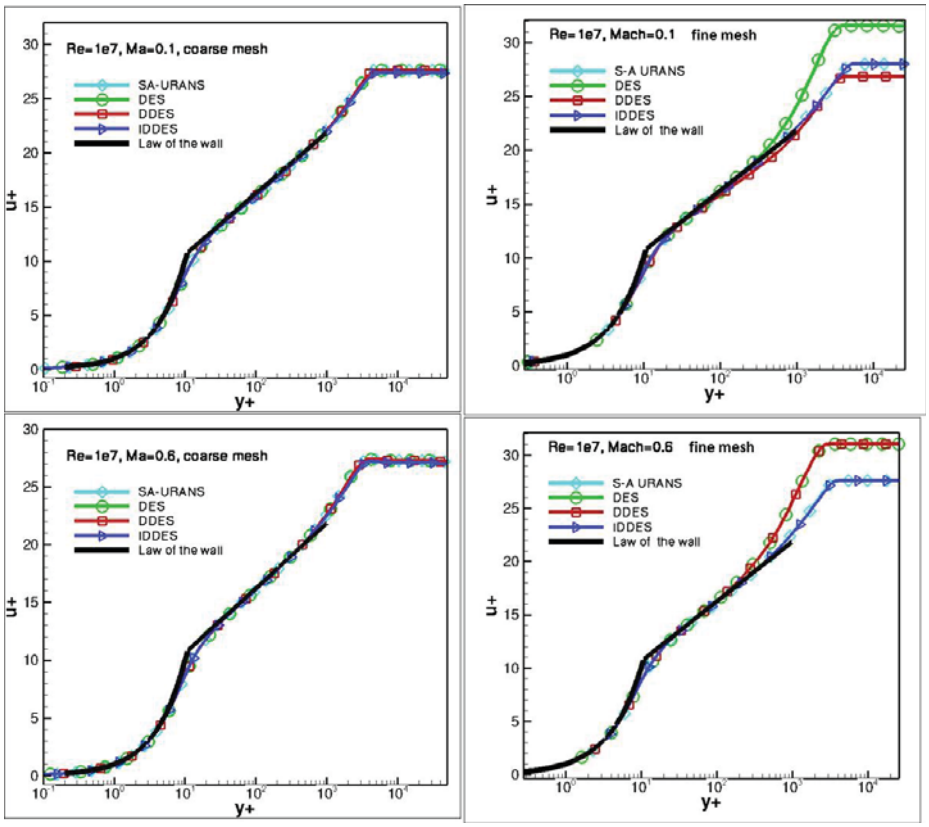

Figure 6.6: Mean velocity profiles calculated at Re=10000000, comparing to the law of the wall(Mach = 0.1(top figure), 0.6(bottom figure), coarse mesh(Left figure) and fine mesh(Right figure))

predicted well by IDDES. The turbulent eddy viscosity predicted by the IDDES is fully preserved inside the turbulent boundary layer. The turbulent eddy viscosity ν_t reaches the maximum value at the outer layer of boundary layer and decays rapidly when it approaches the wall and the edge of the boundary layer. The blending function f_d behaves as the expected transition in the buffer layer from near wall RANS scale to LES scale near the boundary layer edge. The elevating function reaches the maximum at $y/\delta = 0.3$.

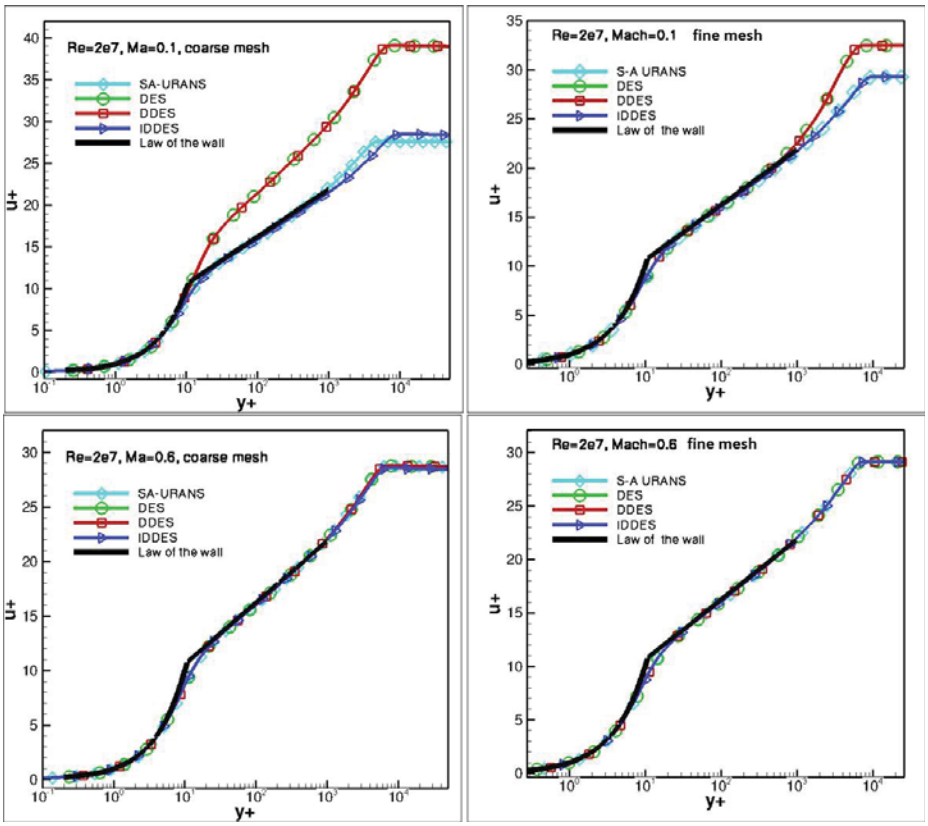

Figure 6.7: Mean velocity profiles calculated at Re=20000000, comparing to the law of the wall(Mach = 0.1(top figure), 0.6(bottom figure), coarse mesh(Left figure) and fine mesh(Right figure))

6.3 IDDES Investigation of the NACA0012 Airfoil Stalled Flows

Simulation of the NACA0012 airfoil stalled flows at four different angle of attack of $5°, 17°, 45°, 60°$ is carried out to investigate the capability of the IDDES for predicting flows with different large turbulent structures, including: a flow with minor separation near the trailing edge(AoA=5°), stall flow with large wake separations(AoA=17°) and stall flows with massive flow separation(AoA=$45°, 60°$).

For vortical flows, computational results of Q-criterion are used to represent vortices. The Q-criterion define vortices as areas where the vorticity magnitude is greater

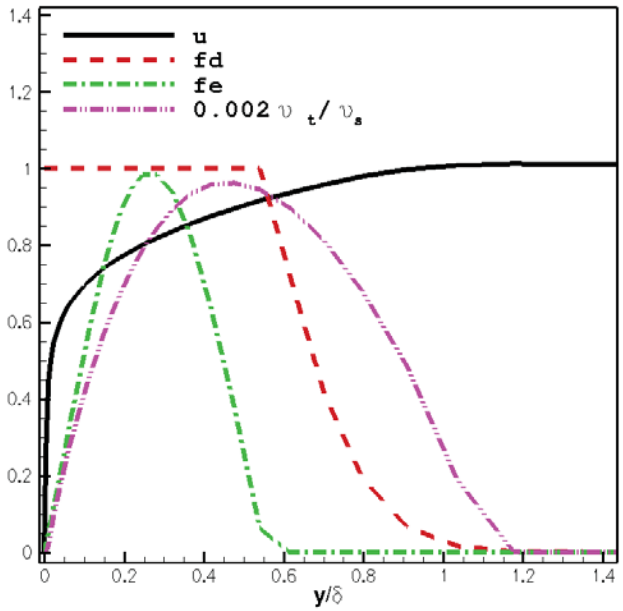

Figure 6.8: Distributions of $u/U_\infty, 0.002\frac{\nu_t}{\nu}, f_d, f_e$ in the flat plate boundary layer

than the magnitude of rate-of-strain [121]. Q=0 represents that the local balance between shear strain rate and vorticity magnitude. $Q = \frac{1}{2}(\left\|\overline{\Omega}\right\|^2 - \left\|\overline{S}\right\|^2)$ where, $\overline{S}$ is the rate-of-strain tensor, and $\overline{\Omega}$ is the vorticity tensor

The Reynolds number based on the airfoil chord (c) is 1.3×10^6 and Mach number based on the freestream velocity (U_∞) is 0.5. The experimental lift and drag coefficients at $R_e = 2 \times 10^6$ [122–124] are used for comparison, which is acceptable

Table 6.2: Simulation cases setup for NACA0012

#	AoA	Grid size	Δx^*	Δy_1	Δz	Δx^+	Δy_1^+	Δz^+
1	5	$192 \times 100 \times 30$	0.00020-0.02681	$1e^{-5}$	0.0344	10-1340	0-1	1720
2	5	$288 \times 100 \times 30$	0.00013-0.01788	$1e^{-5}$	0.0344	6.6-894	0-1	1720
3	17	$192 \times 100 \times 30$	0.00020-0.02681	$1e^{-5}$	0.0344	10-1340	0-1	1720
4	17	$288 \times 100 \times 30$	0.00013-0.01788	$1e^{-5}$	0.0344	6.6-894	0-1	1720
5	45	$192 \times 100 \times 30$	0.00020-0.02681	$1e^{-5}$	0.0344	10-1340	0-1	1720
6	45	$288 \times 100 \times 30$	0.00013-0.01788	$1e^{-5}$	0.0344	6.6-894	0-1	1720
7	60	$192 \times 100 \times 30$	0.00020-0.02681	$1e^{-5}$	0.0344	10-1340	0-1	1720
8	60	$288 \times 100 \times 30$	0.00013-0.01788	$1e^{-5}$	0.0344	6.6-894	0-1	1720

since the Reynolds number dependence is weak after stall at high Reynolds number greater than 1×10^5 [60, 122, 123]. Unsteady simulations are performed over 200-250 dimensionless time ($T = c/U_\infty$) with the implicit pseudo time step iterations. The CFL number in the current simulation is 1.0-5.0. The number of pseudo time steps within each physical time step is determined by having the residual reduced by at least three orders of magnitude, which is usually achieved within 20 iterations. The dimensionless physical time step of $0.02c/U_\infty$ is used.

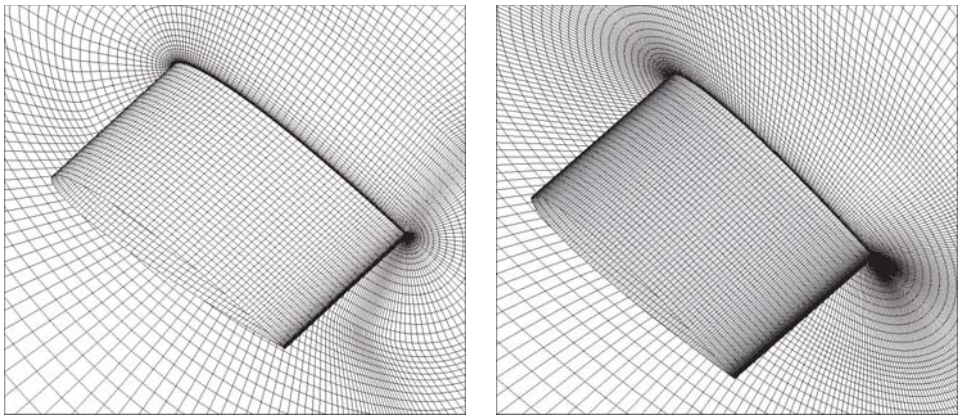

coarse mesh fine mesh

Figure 6.9: Computational meshes of NACA0012 computation

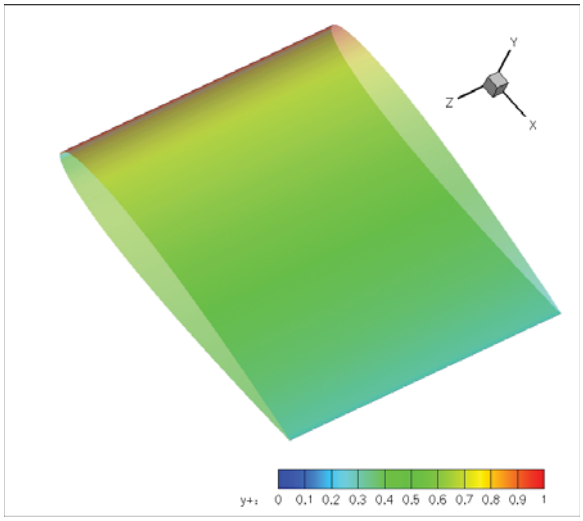

Figure 6.10: Calculated wall normal distance on the NACA 0012 airfoil surface.

Fig. 6.9 shows the 3D NACA0012 computational coarse and fine meshes topology. The coarse and fine computational meshes are constructed using an O-mesh topology with the mesh size of $192 \times 100 \times 30$ and $288 \times 100 \times 30$ in streamwise, normal to the wall and spanwise direction. The first grid spacing on airfoil surface yields y^+ less than unity. Calculated first wall normal mesh distance is shown in Fig.6.10. All the mesh parameters are summarized in table 6.2. The far field boundary is set about 80 times of the airfoil chord length. The span length used is the same as the chord. Periodic boundary conditions are employed in the spanwise direction. No-slip wall boundary conditions are enforced on the airfoil surface.

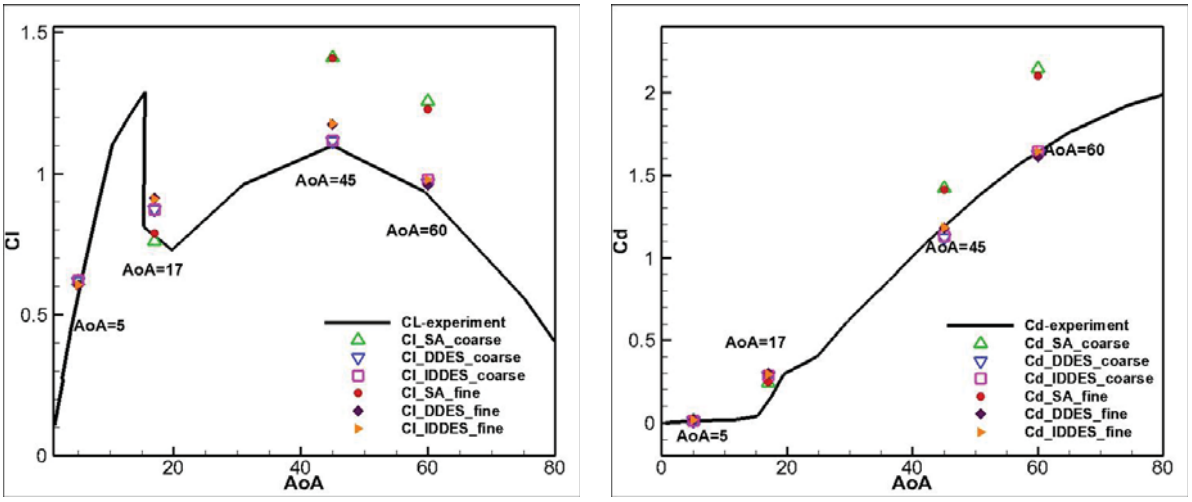

Figure 6.11: Time-averaged lift and drag coefficients of all NACA0012 computations and comparison with experimental data.

As shown in Fig. 6.11, the time-averaged lift and drag coefficient (C_l, C_d) at different AoAs are compared with the experimental data [60, 123]. At the AoA of 5°, all the S-A URANS, DDES, and IDDES calculated lift and drag coefficients agree well with the experiment. At the AoA of 17°, the S-A URANS predicted lift and drag coefficient agrees well with the experiment, whereas the DDES and IDDES predicted lift coefficients have small deviations. The URANS computation over-predicts the

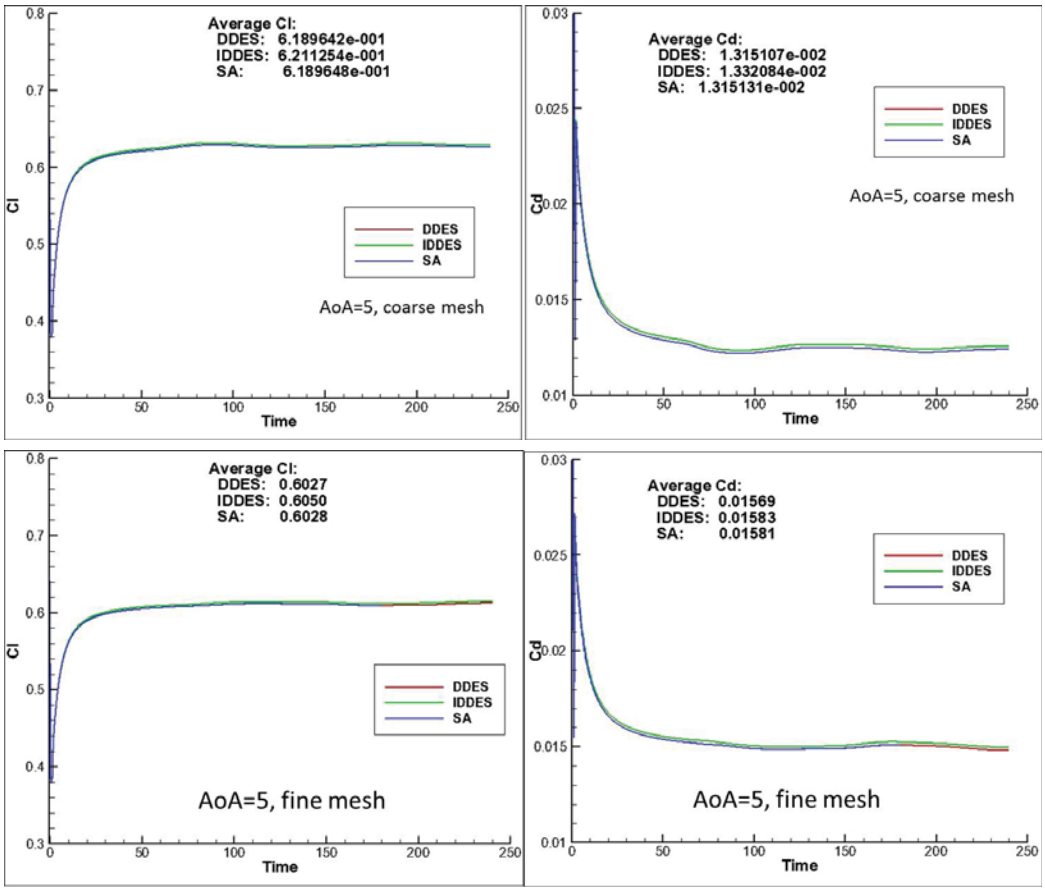

Figure 6.12: Lift and drag coefficient history at AoA = 5°.

lift and drag coefficient at AoA=45° and 60° by about 30%, whereas the DDES and IDDES accurately predict the lift and drag at these high AoA with massive flow separations.

Fig. 6.12 gives the lift and drag coefficient history at AoA=5°. Constant lift and drag coefficients are achieved from all unsteady CFD calculations. Time-averaged Mach number contours are presented in Fig. 6.13. Thicker boundary layer the trailing edge is observed. The instantaneous pressure and viscous drag coefficient components Cd_p and Cd_v are given in Fig. 6.14. The pressure and viscous forces are in the same order of magnitude. Both of them have a significant contribution to the resultant drag force.

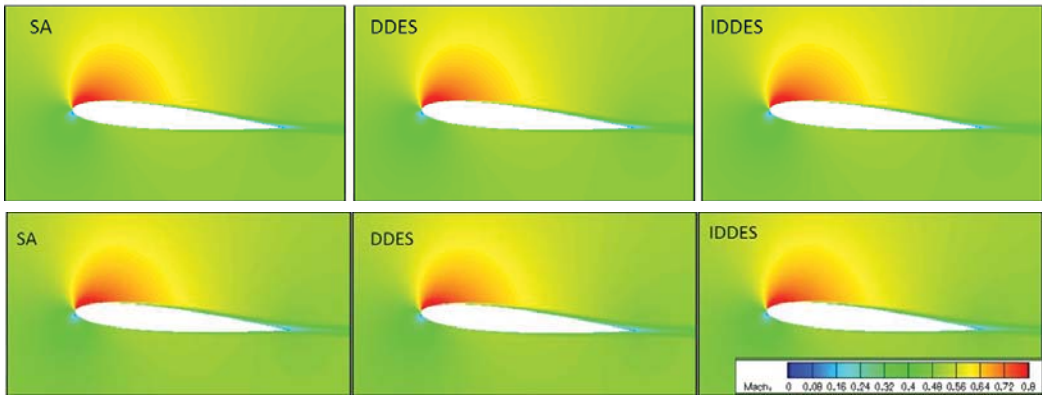

Figure 6.13: Time-averaged Mach contours at AoA = 5° in simulation with coarse(top) and fine(bottom) mesh.

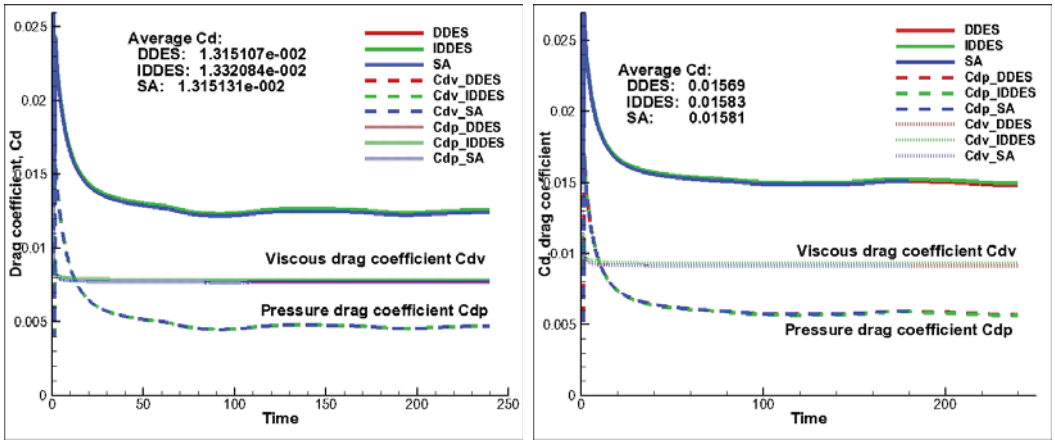

Figure 6.14: Viscous and pressure drag coefficient history at AoA = 5°.

Fig. 6.15 presents the instantaneous lift and drag coefficient at AoA=17°. IDDES and DDES obtain the lift and drag coefficient oscillating with time due to vortex shedding, whereas constant lift and drag coefficients are obtained by the URANS computation. This difference indicates that flow separation is phase-locked by the URANS model, which is inappropriate for real flow with large separations. From the C_L-AoA curve(see 6.11), the airfoil flow approaches dynamic stall region at near AoA=17° where the lift and drag coefficients have a dramatic drop. Fig. 6.16 presents the time-averaged Mach number contours at AoA=17°. The URANS simulated Mach number contours show little difference for coarse and fine mesh. Comparing the fine

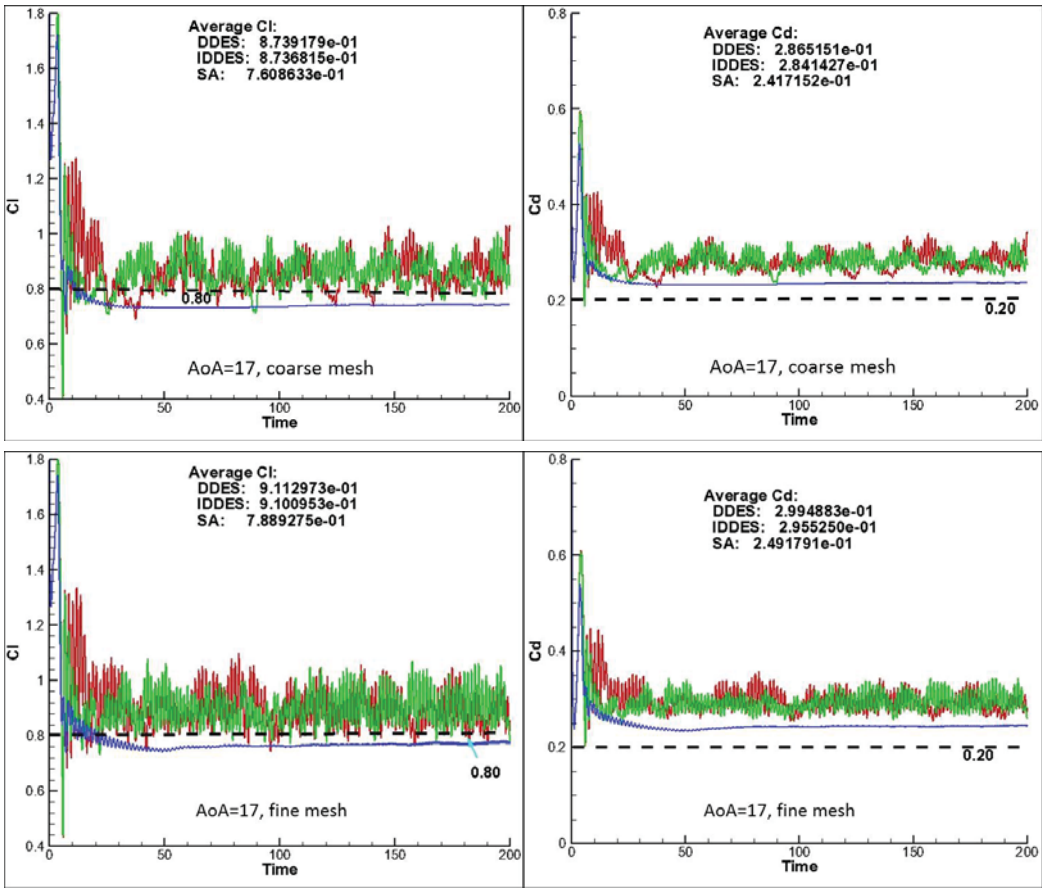

Figure 6.15: Lift and drag coefficient history at AoA = 17°.

mesh and coarse mesh simulation, DDES and IDDES predict large wake size than with the fine mesh. Fig. 6.17 presents the 3D iso-surfaces of Q-criterion=0 for S-A URANS, DDES, and IDDES computations using the fine mesh. The URANS simulates the vortical structures as two dimensional large organized harmonic vortex shedding. The vortical flow structures calculated by IDDES are three dimensional and chaotic with the streamwise, spanwise and transverse vortices.

Fig. 6.18 presents the lift and drag coefficients history at AoA of 45°. The URANS simulation obtains the harmonically oscillating lift and drag coefficients, whereas the lift and drag coefficients calculated by the DDES and IDDES oscillates without standard harmonics. The time-averaged Mach number contours are given in Fig.

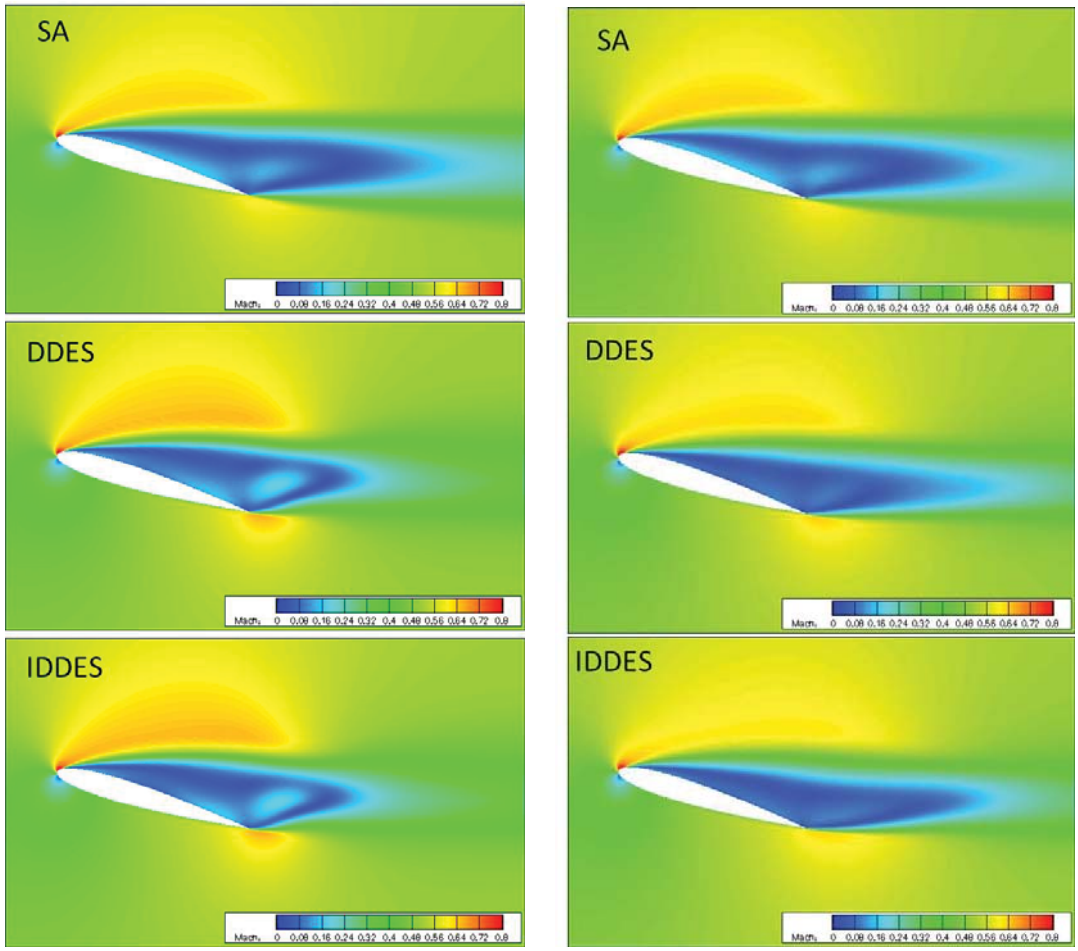

Figure 6.16: Time-averaged Mach contours at AoA = 17° in simulation with coarse(left) and fine(right) mesh.

6.19. Fig. 6.20 presents the 3D iso-surfaces of Q-criterion=0 for S-A URANS, DDES and IDDES computations using the fine mesh. Again, the URANS predicts large scale structured vortex shedding, whereas the DDES and IDDES achieve high chaotic large and small scale vortices. Both DDES and IDDES capture the massively separated flow with 3D streamwise, transverse, and spanwise vortical structures, while URANS obtains the vortex shedding that is dominant with spanwise vorticity. Such predicted vortical structures difference is believed to make the quantitative drag accuracy as reflected in Fig. 6.11.

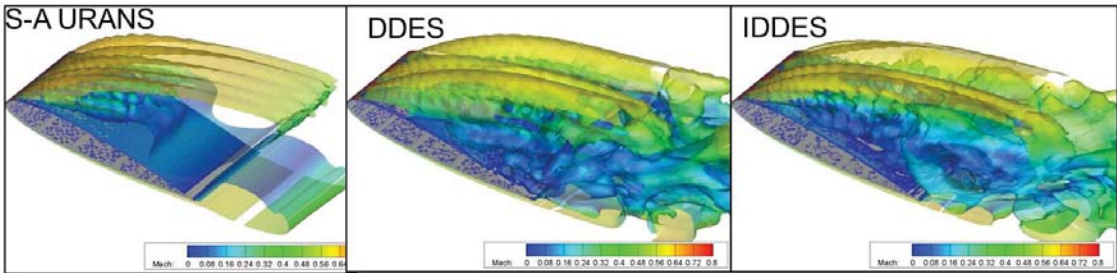

Figure 6.17: Iso-surfaces of the instantaneous Q-criterion=0, shown are the results of the S-A URANS, DDES and IDDES at AoA = 17°.

Fig. 6.21 presents the instantaneous Mach contours at three different span cross-sections predicted by URANS. Flow structures are organized vortex shedding at different span cross-sections. Fig. 6.22 presents the instantaneous Mach contours at different span cross-section predicted by IDDES. Vortical flow structure and spanwise flow structures are very different from those of the URANS and are more chaotic and disorganized. Fig. 6.23 shows the instantaneous vorticity of 10% span, 50% span and 90% span predicted by IDDES simulation. The present S-A URANS results capture the phase locked vortex shedding phenomena that usually occurs at low Reynolds number flows, whereas IDDES shows more realistic and turbulent vortical flow structures in the regions of massive separations.

Fig. 6.24 gives the lift and drag coefficients history at AoA of 60°. Similar trends are observed with periodic lift and drag coefficients variation using the URANS and irregularly oscillating lift and drag coefficients using the DDES and IDDES. The time-averaged Mach number contours are given in Fig. 6.25. The IDDES and DDES predict larger separation regions than the S-A URANS model. The 3D iso-surfaces of Q-criterion=0 for S-A URANS, DDES and IDDES are given in Fig. 6.26. Similar to the previous massive separation case, the large scale phase-locked vortex shedding is achieved using S-A URANS and three dimensional small scale vortices are captured

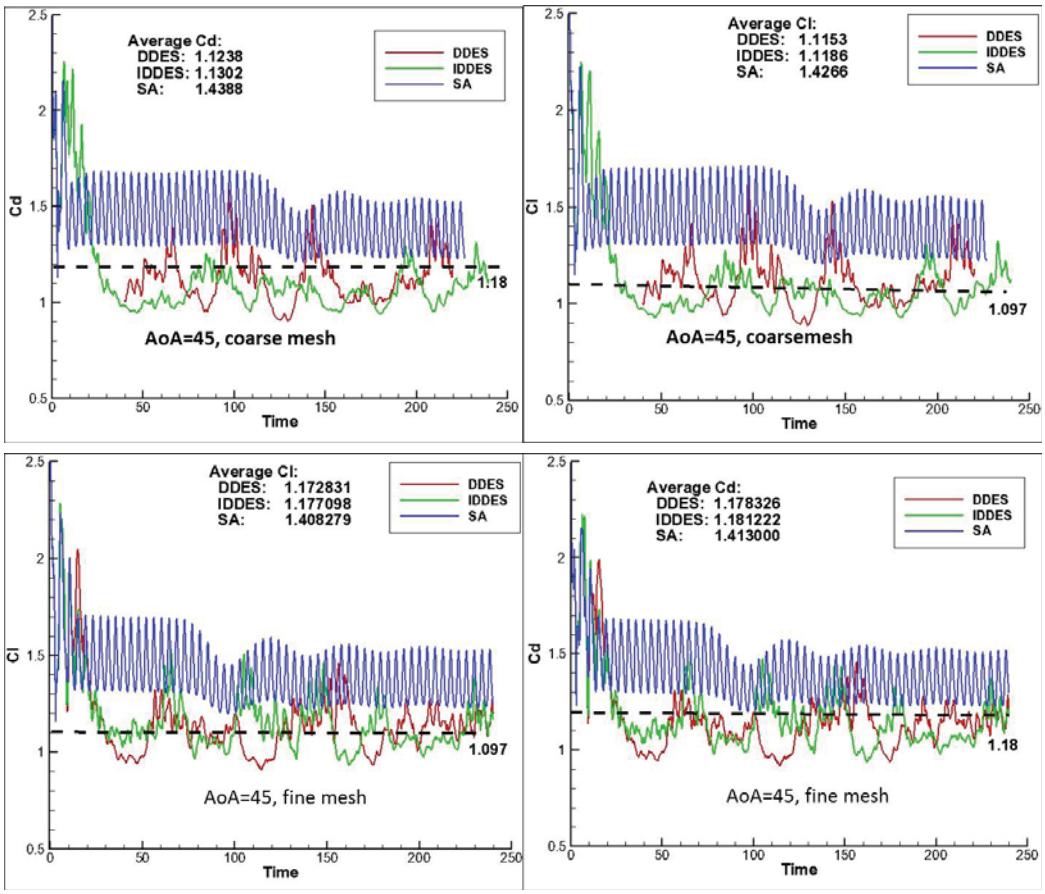

Figure 6.18: Lift and drag coefficient history at AoA = 45°.

using DDES and IDDES. The capacity to capture more realistic flow structures by DDES and IDDES, which determines the accuracy of drag prediction for massively separated flows.

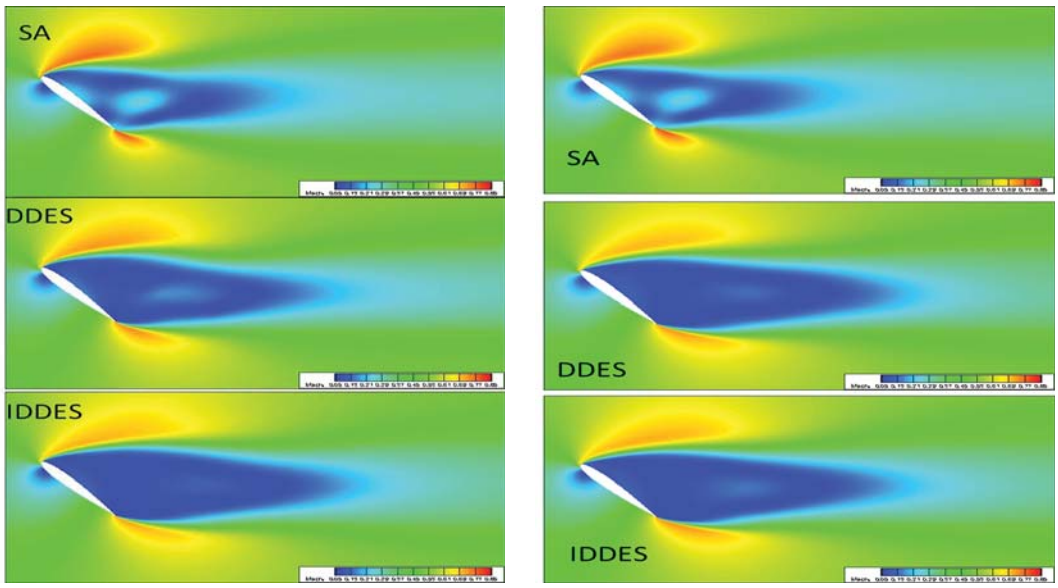

coarse mesh fine mesh

Figure 6.19: Time-averaged Mach contours at AoA = 45° in simulation with coarse(left) and fine(right) mesh.

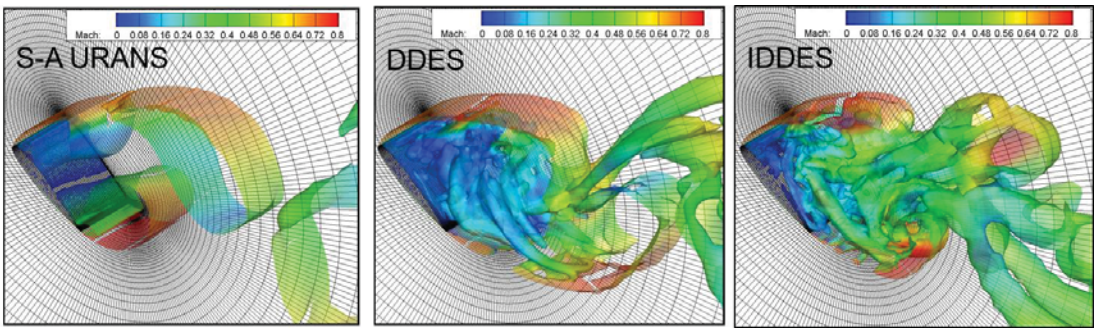

Figure 6.20: Iso-surfaces of the instantaneous Q-criterion=0, shown are the results of the S-A URANS, DDES and IDDES at AoA = 45°.

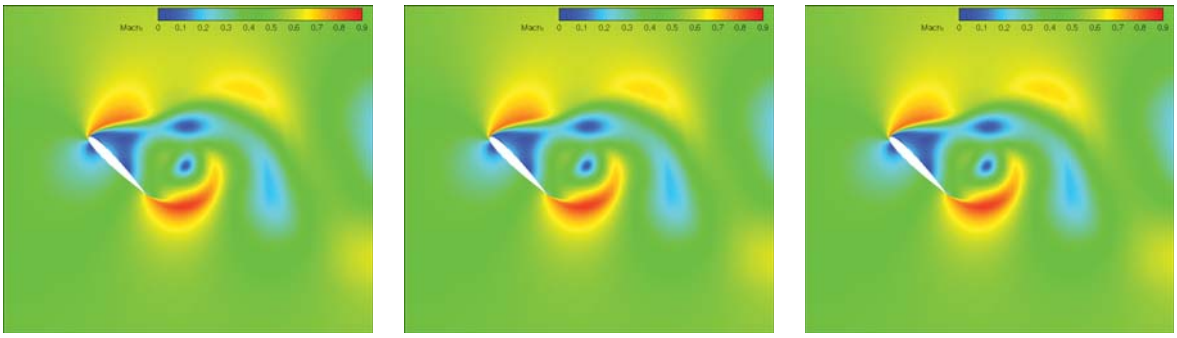

0.1Span 0.5Span 0.9Span

Figure 6.21: Mach contours at different spans in S-A URANS coarse mesh simulation at AoA = 45°

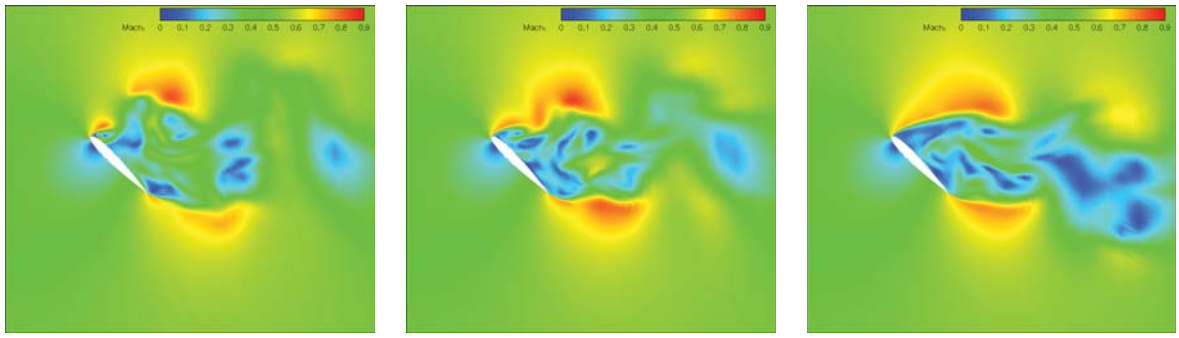

0.1Span 0.5Span 0.9Span

Figure 6.22: Mach number contours at three different spans in the IDDES coarse mesh simulation at AoA = 45°

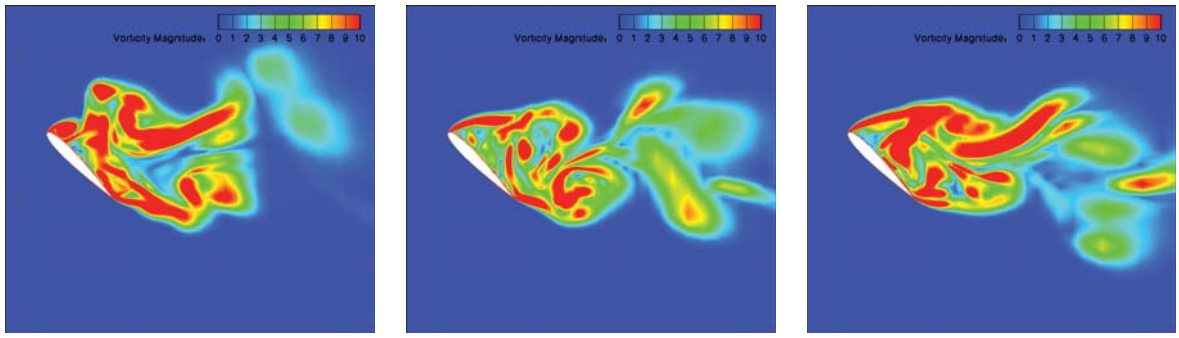

0.1Span 0.5Span 0.9Span

Figure 6.23: Vorticity contours at three different spans in the IDDES coarse mesh simulation at AoA = 45°

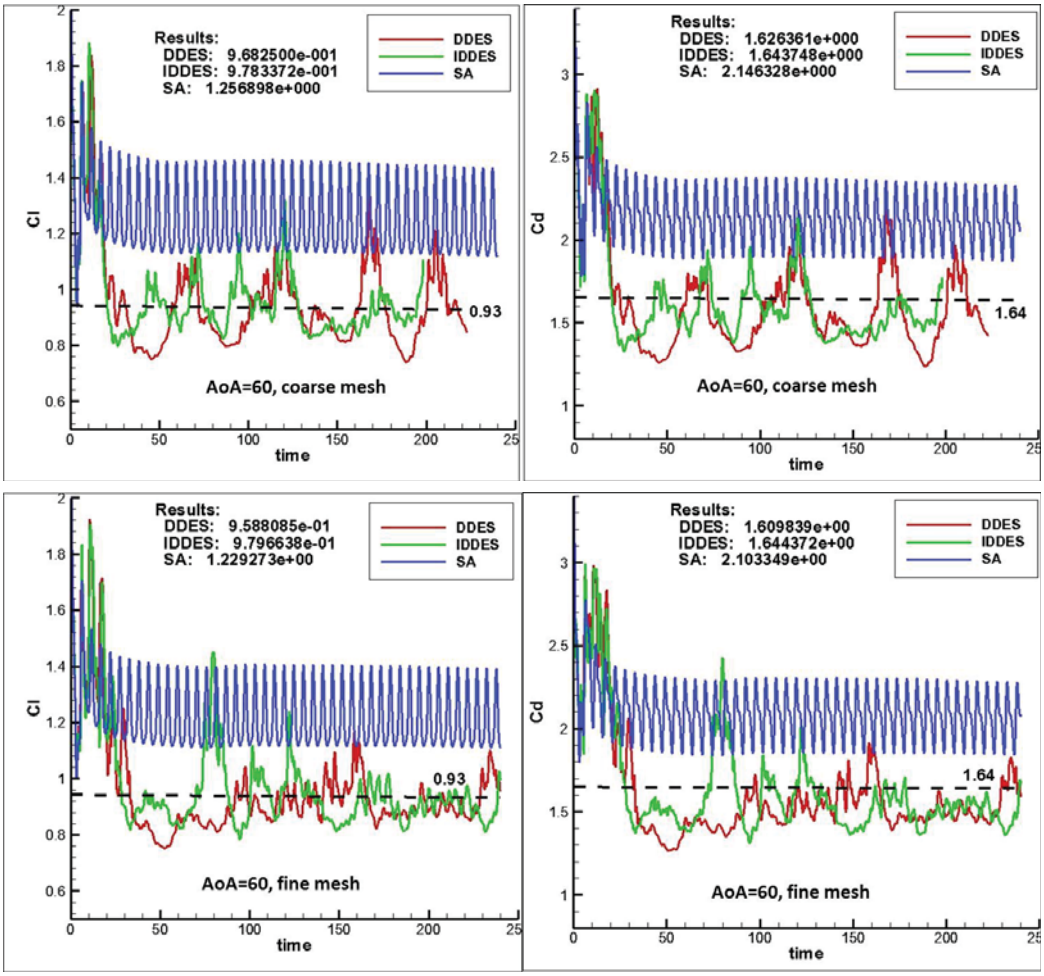

Figure 6.24: Lift and drag coefficient history at AoA = 60°.

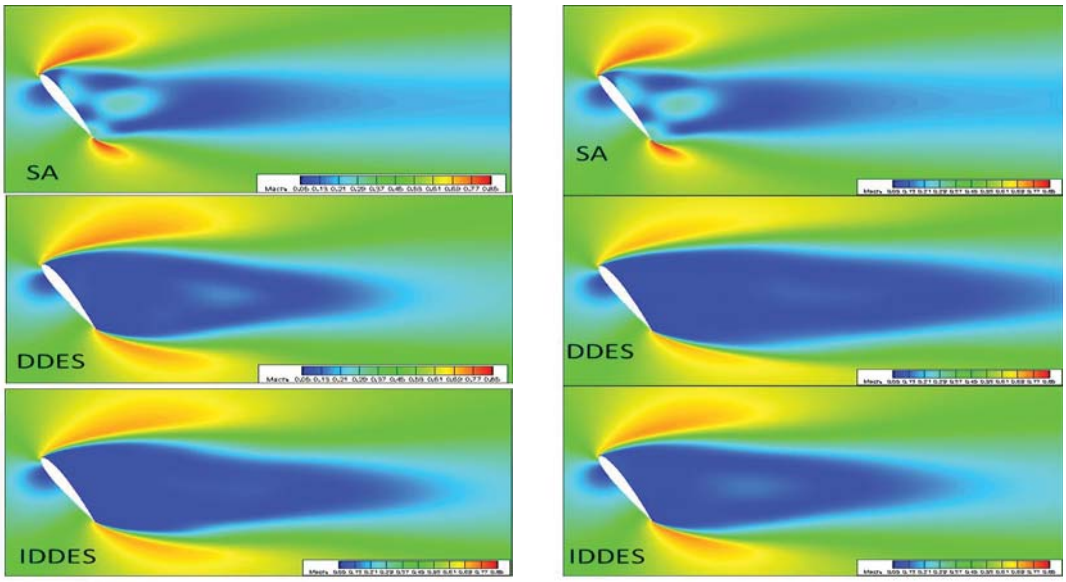

coarse mesh fine mesh

Figure 6.25: Time-averaged Mach contours at AoA = 60° in simulation with coarse(left) and fine(right) mesh.

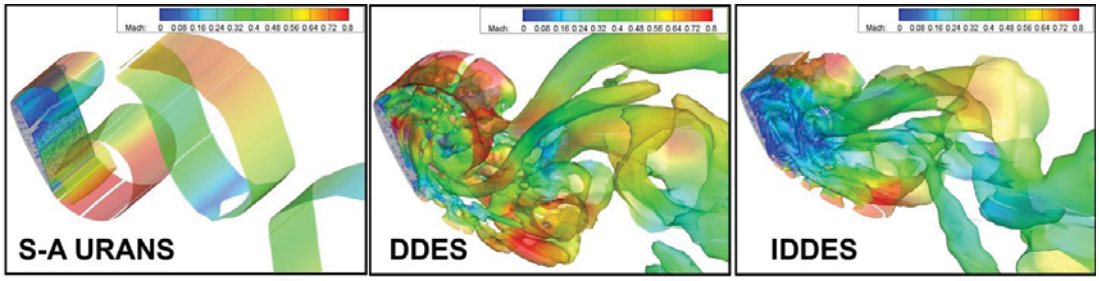

Figure 6.26: Iso-surfaces of the instantaneous Q-criterion=0, shown are the results of the S-A URANS, DDES and IDDES at AoA = 60°.

6.4 Conclusions

Comparative study of the S-A URANS, DDES and IDDES computation of the flat plate boundary layer and the stalled flow of the NACA0012 airfoil at different AoAs of 5°, 17°, 45°, and 60° . High order schemes are employed in the current study with the fifth order WENO reconstruction for the inviscid fluxes and 4th order central differencing for the viscous fluxes. Simulation of turbulent boundary layer indicates that the IDDES predicts the law of the wall accurately for different mesh sizes, Reynolds numbers, and Mach numbers, whereas the DES97 and DDES obtain the velocity profile in the boundary layer with model stress depletion and log layer mismatched at certain conditions. For the NACA0012 stalled flows, at low and medium AOAs(=5°, 17°), the URANS, DDES, and IDDES all predict the drag accurately. However, for the massively separated flows at high AoAs(=45°, 60°), the URANS over-predicts the drag coefficient significantly by about 30%, whereas the DDES and IDDES predict the drag coefficient accurately. The vortical flow structures obtained by the URANS are highly-regularized vortex shedding dominated by the spanwise vorticity. The IDDES can resolve more realistic flow structures, including smaller scale vortices that are chaotic and disorganized with streamwise, transverse and spanwise vortices.

CHAPTER 7

Super-Lift Coefficient of 2D CFJ Airfoil

7.1 Maximum Lift Coefficient

Maximum lift coefficient, C_{Lmax}, of an airfoil is a very important issue in aerodynamics theory and in engineering practice. In aerodynamics theory, Smith's [10] pioneering research in 1975 gives a limit below:

$$C_{Lmax} = 2\pi(1 + \frac{t}{c}) \tag{7.1}$$

which is based on inviscid potential flow model at an angle of attack(AoA) of 90°. Since it is potential flow with no boundary layer, the flow is treated that it will never get stalled. For a cylinder, since t is equal to c, the theoretical C_{Lmax} limit will be 4π=12.57. For the NACA 6421 airfoil studied in this paper, the theoretical limit C_{Lmax} will be 7.6. The derivation of the maximum lift coefficient for potential flow is provided in Chapter 2.

In practice, C_{Lmax} is extremely important to determine the takeoff/landing distance and noise. The higher the C_{Lmax}, the shorter the takeoff/landing distance, and the lower the airframe noise. Achieving high C_{Lmax} is hence critical to increase future airport capacity and reduce airport community noise. This is particular true

with the world economic growth that enables more people travel by air. According to FAA(2007), there are 22 major US airports that are predicted to suffer from capacity shortage for the next two decades. The extremely short takeoff/landing (ESTOL) [125, 126] and the Cruise-Efficient Short Takeoff and Landing (CESTOL) concepts [39] are strongly advocated to be introduced for future U.S. National Airspace System (NAS) civil aviation environment.

Smith's theory [10] provides the theoretical foundation for the multi-element flap high lift system. The more airfoil elements are used, the more the lifting surface meanline can approach a half circle. By observing the trend of the C_{Lmax} growing from 2 in 1935 to 3 in 1965, Smith [10] asked then "By 1995 will we have advanced to 4?". He did show a 7-element flap system that achieves a C_{Lmax} close to 4. However, flap high lift system is very complicated and expensive to make [127]. The airliner manufacturers are moving toward simpler high lift systems with less airfoil elements instead of the other way around [127]. Hence the answer to Smith's question is that today's high lift system and C_{Lmax} level is not much different from those 5 decades ago in 1965.

Aircraft design needs to consider the whole flight envelop including takeoff/landing and cruise. The C_{Lmax} matters for takeoff/landing, efficiency matters for the cruise to maximize range, pay load, and fuel consumption reduction. The ratio of lift to drag, or C_L/C_D, is usually used to represent the aircraft aerodynamic efficiency. In this paper, we introduce a productivity efficiency, C_L^2/C_D, to represent the aircraft cruise capability to move a gross weight by its maximum distance.

7.1.1 What is the C_{Lmax} Limit?

The numerical simulation conducted in this research achieves airfoil C_{Lmax} far greater than that defined by Eq. (1) using active flow control. We were puzzled by the results and were not fully sure if it is physically sound.

By surveying the literature, it is found that one of the earliest study to explore C_{Lmax} was done by Prandtl for his famous experiment to enhance lift by rotating the cylinder in a flow [128]. A spinning cylinder transfers its mechanical energy to the flow via viscosity with no-slip wall boundary condition. He argued that the maximum lift generated by a spinning cylinder in a uniform flow is limited to 4π ($\approx$12.57), which is consistent with the C_{Lmax} defined by Eq. (7.1) [129].

Tokumaru and Dimotakis (1993) [32] studied the mean lift acting on a rotating cylinder in a uniform flow. It is devised based on an inviscid point-vortex model. Their results for $Re = 3.8 \times 10^3$ show that Prandtl's limit on lift coefficient ($C_{L_{max}} = 4\pi$) can be exceeded, as shown in Fig. 10.4. They suggested that perhaps it is the unsteady effects that weaken Prandtl's hypothesis. And the three dimensional effects are responsible for the increase of the lift coefficient compared to a purely two-dimensional flow. Their results indicate that the faster the cylinder spins, the higher lift coefficient it can achieve, but the relation is not linear. Initially, the flow responds sensitively to the spinning speed of the cylinder with the lift coefficient increased about linearly with the spinning speed. However, when the cylinder spins too fast, the flow is not able to absorb more energy from the rotating cylinder and the lift increase becomes plateaued (see Fig. 10.4).

Another experiment on the circular cylinder lifting surface was conducted by Lockwood et al. (1960) [33] in NASA Langley to provide lift on takeoff and land-

ing by blowing on the circular fuselage of a hypersonic aircraft. As shown in Fig. 10.3, the maximum lift coefficient over $C_L \approx 20$ is measured at high $C_\mu \approx 5$ for a very low Reynolds number flow over an end-plated-cylinder with multiple injection slots [33], [130].

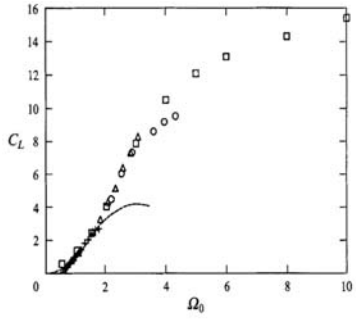

Figure 7.1: Lift coefficient C_L vs cylinder rotating speed in the rotating cylinder experiment. (Plot is adopted from [32])

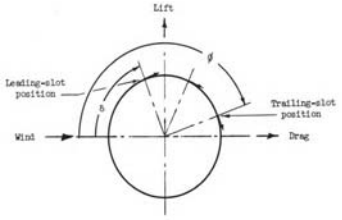

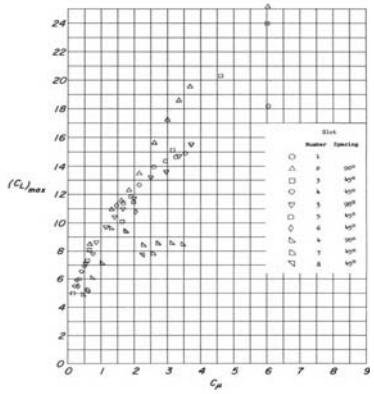

Figure 7.2: Lifting cylinder using tangential blowing from surface slots. (Plot is adopted from [33])

Above cylinder lift enhancement experiments indicate that the C_{Lmax} defined by Eq. (1) has been exceeded by adding energy to the flow using active flow control, such as rotating cylinder or jet injection. The C_{Lmax} limit from the potential flow is the result of imposing Kutta condition, which is necessary for potential flow, but not a true physical condition that realistic flows must satisfy.

Then the next question is "What is the limit?". The answer appears to be that there is no limit for C_{Lmax}. It depends on how much energy can be added to the flow. Depending on the active flow control method, the flow will not be able to absorb more energy at certain point, at which the C_{Lmax} will reach the limit. The present research supports this statement. So far, the lift coefficient breaking the theoretical limit is only seen for cylinder flows. No airfoil is shown to have such capability until the present study.

7.1.2 ESTOL Performance with Flow Control

The only large transport with ESTOL performance is the US military transport C-17 as shown in Fig. 7.3, which has a short takeoff/landing distance of 3000ft using the external blown flaps (EBF) flow control technology developed in mid-50s by NASA. As displayed in Fig. 7.3, EBF augments lift coefficient by directing the engine exhaust jets below the wings to flow through the highly deflected multi-element flap systems.

The aerodynamics principle of EBF is that the engine jets energize the wing suction surface boundary layer through the slots of the flap system and keep the flow attached with the highly cambered airfoil formed by the multi-element flaps. The EBF comes with a price of significantly increased drag. In addition, the heavy and costly titanium alloy must be used for the wing structure to resist the high temperature of the engine jets. For military transports, the engines hung beneath the wings for EBF also have the disadvantages of large radar cross sections.

The other possible lift enhancement technology using flow control is the internally blown flap (IBF), which introduces mass flow from the compressor (bleed) of the engine and blow the air on the suction surface leading edge (LE) and trailing edge (TE) of the wing. IBF augments lift based on the circulation control (CC) airfoil concept due to Coanda effect, which exists at the airfoil leading edge due to the LE suction and in the vicinity of a blunt trailing edge based on its low base pressure. Hence, a blunt TE is required to render the CC effective. However, a thick TE increases drag at cruise condition. To overcome the dependence on a blunt TE, a movable flap at the airfoil TE must be used [131]. But moving parts impose a weight penalty.

One considerable penalty of CC airfoil blowing is the dumped mass flow induced from the propulsion system bleed or other pumping systems. The mass flow rate of the engine bleed is directly proportional to the reduction of the thrust, i.e. the engine will suffer 1-2% thrust reduction for 1% blow rate used for wing flow control, and suffer 1-3% fuel consumption increase depending on whether the bleed is from the compressor front stage or back stage. Furthermore, a CC airfoil must include an extra drag, "equivalent" drag [62, 132] in addition to the measured drag in a wind tunnel. This is because a flow mass withdrawn from freestream is needed to supply the injection mass (mass conservation law). The withdraw of freestream mass flow will generate a ram drag, which can not be avoided, but is not measured in wind tunnel testing.

Figure 7.3: C-17 aircraft with STOL performance.

Figure 7.4: The double bubble concept

Figure 7.5: The SAX-40 concept aircraft

Future military and commercial transports are more and more evolved toward highly integrated airframe-propulsion system such as the "double-bubble" [133] and SAX [134]. A simple flapless high lift system without relying on engines is desirable.

The recent concept of co-flow jet (CFJ) flow control airfoil, developed by Zha et al. [35, 61–69] shows a great potential to fulfill the role of future flapless high lift system. The CFJ airfoil achieves a dramatically lift augmentation, drag reduction and stall margin increase at low energy expenditure. It can not only achieve ESTOL performance with ultra-high maximum lift coefficient, but also significantly enhance

cruise efficiency and cruise lift coefficient (wing loading) from subsonic to transonic conditions [35, 68, 69]. The CFJ airfoil has great potential to radically change the overall aircraft design philosophy from subsonic to transonic speeds.

The objective of this research is two folds: 1) to explore the maximum lift coefficient capability of the CFJ airfoil. It is our interest to see if this promising active flow control concept can break the theoretical inviscid limit. It is also our interest to study the C_{Lmax} relationship with the energy expenditure. 2) To demonstrate that the CFJ airfoil can also achieve high cruise lift coefficient and high efficiency when the flow is benign at low AoA.

7.2 CFD Simulation Setup

The 2D Reynolds averaged Navier-Stokes (RANS) equations with one-equation Spalart-Allmaras [101] turbulence model is used. A 5th order WENO scheme for the inviscid flux [102, 135–139] and a 4th order central differencing for the viscous terms [135,138] are employed to discretize the Navier-Stokes equations. The low diffusion E-CUSP scheme used as the approximate Riemann solver suggested by Zha et al [102] is utilized with the WENO scheme to evaluate the inviscid fluxes. Implicit time marching method using Gauss-Seidel line relaxation is used to achieve a fast convergence rate [140]. Parallel computing is implemented to save wall clock simulation time [141]. The RANS solver is validated for CFJ airfoil simulations [65, 68–70, 142, 143].

C_μ Iteration

To achieve zero net mass flux with the CFJ flow control, the mass flow exiting the injection slot must be equal to the mass flow entering the suction slot, i.e.

$\dot{m}_{inj} = \dot{m}_{suc}$. The prescribed jet momentum coefficient C_μ is achieved by adjusting the injection cavity total pressure. Total temperature is assumed constant during this process. The injection and suction mass flow rates are matched by adjusting the suction cavity static pressure. The iterative process is conducted throughout the simulation until the specified momentum coefficient is reached and the injection and suction mass flow match within the acceptable tolerance, which is 0.2% for the present study.

7.2.1 Boundary Conditions

The 3rd order accuracy no slip condition is enforced on the solid surface with the wall treatment suggested in [144] to achieve the flux conservation on the wall. Total pressure, total temperature and flow angles are specified as the inlet boundary conditions for the upstream portion of the farfield boundary and inside the injection cavity. Constant static pressure is used for the downstream farfield boundary and inside the suction cavity.

7.2.2 Mesh

The 2D structured meshes are constructed using the O-mesh topology in order to achieve high mesh quality within the airfoil boundary. A total of 1201 points are placed around airfoil, 601 points on suction surface, 601 points on the pressure surface and 151 points normal to the airfoil with an additional 41 points across the jet. The total mesh size is 205,600 cells, and is partitioned into 8 blocks for parallel computation. The farfield boundary is located 15 chords away from the airfoil. To

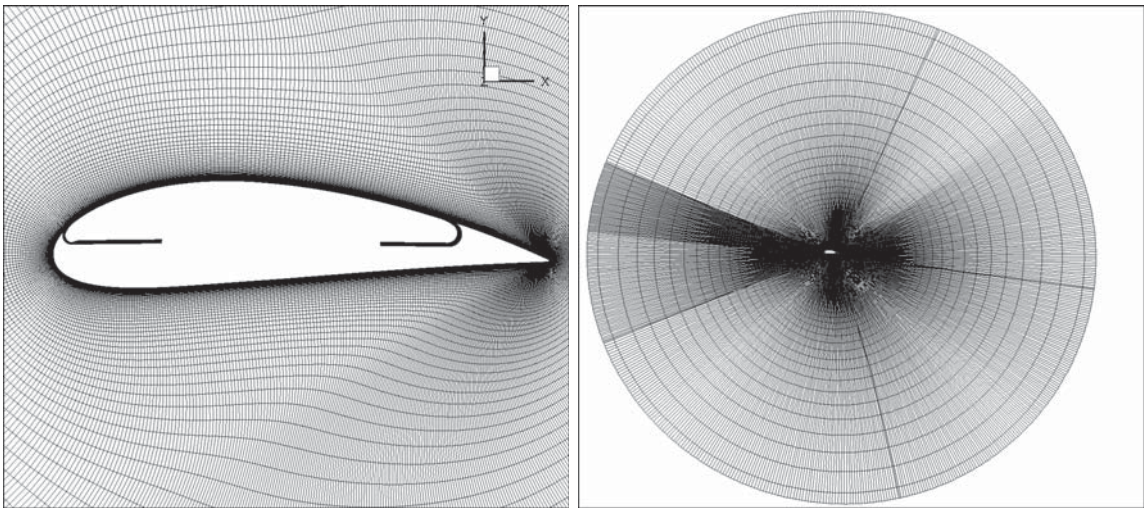

Figure 7.6: Computational mesh for CFJ calculation (AoA = 5°)

resolve the turbulent boundary layer, the first grid point is placed at $y^+ \approx 1$. The block definition is found in Table 10.2 and the mesh topology is shown in Fig. 10.8.

Table 7.1: Mesh for CFJ 6421 airfoil calculation

Block	ξ-Direction	η-Direction	Cell number	location
1-5	241	151	36000	around the airfoil
6	201	41	8000	Injection block
7	241	41	9600	Connection
8	201	41	8000	Suction block
Total mesh size			205600	

A mesh refinement study was performed for the baseline NACA6421 and CFJ6421 airfoil at M=0.063 and Re=3,030,000 by adjusting the mesh size in the chord-wise and wall-normal direction, as shown in Table 7.2 and 7.3. The mesh size of 601x151 is used for the baseline airfoil study. For the CFJ airfoil, the mesh size of 1201x151 is adopted. The C_L, C_D, C_M results are converged based on mesh size as shown in Table 7.2 and 7.3.

Table 7.2: Mesh independence study for the baseline NACA6421 airfoil at AoA=5°

Case	AoA	Grid size	C_L	C_D	C_M
1	5	601×151	1.011	0.020	-0.102
2	5	601×301	1.006	0.020	-0.100
3	5	1201×151	1.006	0.021	-0.103

Table 7.3: Mesh independence study for the CFJ6421 SST016-SUC053-INJ009 airfoil at AoA=70° and $C_\mu = 0.25$

Case	AoA	Grid size	C_L	C_D	C_M
1	5	601×151	8.873	0.065	-0.547
2	5	1201×151	8.275	0.314	-0.510
3	5	1201×301	8.222	0.324	-0.508
4	5	2401×151	8.249	0.327	-0.512

7.3 Results and Discussion

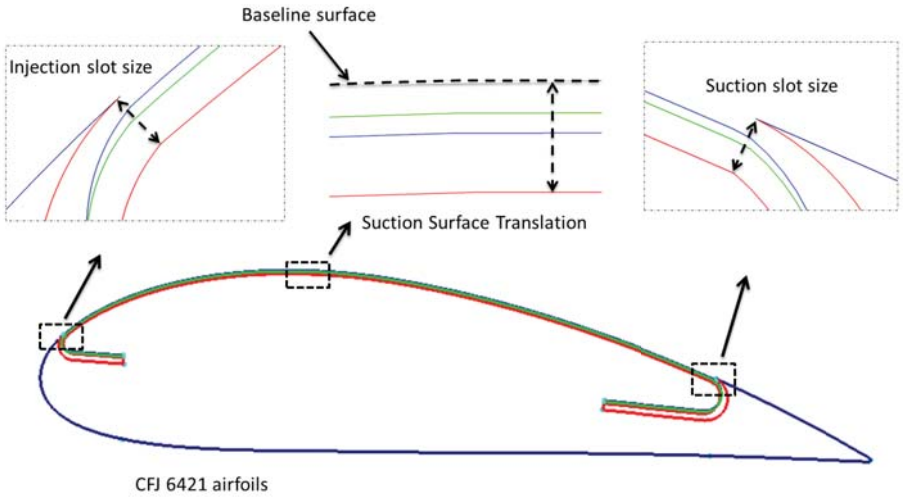

Figure 7.7: CFJ6421 airfoil geometry

The CFJ airfoil configurations are created from the baseline NACA 6421 airfoil by translating the suction surface downward, which is defined as the suction surface translation (SST). The CFJ injection and suction slot sizes are iterated with trade

study to obtain high lift coefficient for take-off and landing, and high aerodynamic efficiency for cruise condition. Fig. 7.7 shows several CFJ airfoil geometries with various SST, injection slot sizes and suction slot sizes in the trade study.

The CFJ airfoils are designed differently to achieve the max lift coefficient for takeoff/landing and to achieve maximum efficiency at cruise. In general, to have high C_{Lmax}, it is more effective to have smaller injection size with higher injection velocity, which will give higher injection jet momentum and lower mass flow rate if the C_μ is fixed. However, the power coefficient of the CFJ airfoil is also high with smaller injection size because the jet suffers high energy loss going through small holes. Thus for the cruise condition that a high efficiency is more important, a larger injection slot size with lower jet velocity and loss is more desirable. The results below are therefore presented in two separate sections, one for maximum lift coefficient at takeoff/landing with very high AoA and the other one for high efficiency at cruise condition with low AoA.

Table 7.4: CFJ6421 airfoil geometry parameters for takeoff/landing and cruise condition

Case	CFJ6421 airfoil	SST (%C)	INJ slot size (%C)	SUC slot size (%C)
Takeoff/Landing	SST016-SUC053-INJ009	0.16	0.09	0.53
Cruise	SST143-SUC133-INJ065	1.43	0.65	1.33

Table 11.1 gives the detailed parameters of the two CFJ airfoils designed for takeoff/landing and cruise condition, including the injection and suction slot size normalized by chord length(C), and the injection jet momentum coefficient used. The 3-digit number in the naming convention stands for the SST distance, injection slot size, and suction slot size normalized by the airfoil chord.

7.3.1 Maximum Lift Coefficient

This section is to investigate the maximum lift coefficient for the CFJ airfoil CFJ6421-SST016-SUC053-INJ009, which has a thin injection slot size of 0.09%C, suction slot size of 0.53%C, and the suction surface translation (SST) of 1.6%C. A comprehensive parametric study was conducted to obtain this CFJ airfoil geometry, which will be presented in another paper.

7.3.1.1 Airfoil Characteristics

For the low speed takeoff/landing simulation, the Mach number of 0.063 and Reynolds number of 3.03 million are used. The jet momentum coefficients $C\mu = 0.04, 0.15$, and 0.25 are simulated for the initial simulation to obtain the whole characteristics. The simulated AoAs vary from 0° to 74° with an increment of 4°. As the lift and drag coefficient shown in Fig. 7.8 and 7.9, the CFJ airfoil flow remains attached at AoA of 70°. To explore the maximum lift coefficient, higher momentum coefficient of 0.35, 0.4, 0.5 and 0.6 are simulated only at AoA of 70° as presented in the results.

Table 7.5: Takeoff/Landing simulation parameters

CFJ6421 airfoil	Mach number	Reynolds number	AoA	C_μ
SST016-SUC053-INJ009	0.063	3,030,000	2°-74°	0.04,0.15,0.25, 0.35,0.40,0.50,0.60

Fig. 7.8 shows the computed lift and drag coefficients at different momentum coefficients. The baseline NACA6421 airfoil is stalled at AoA=18° with the maximum lift coefficient of 1.42. The maximum lift coefficients for the CFJ airfoils are increased dramatically to 8.3 at $C_\mu = 0.25$ and the stall AoA is increased to AoA=70°. At AoA of 70°, the maximum lift coefficient continues to rise with increasing C_μ and reaches

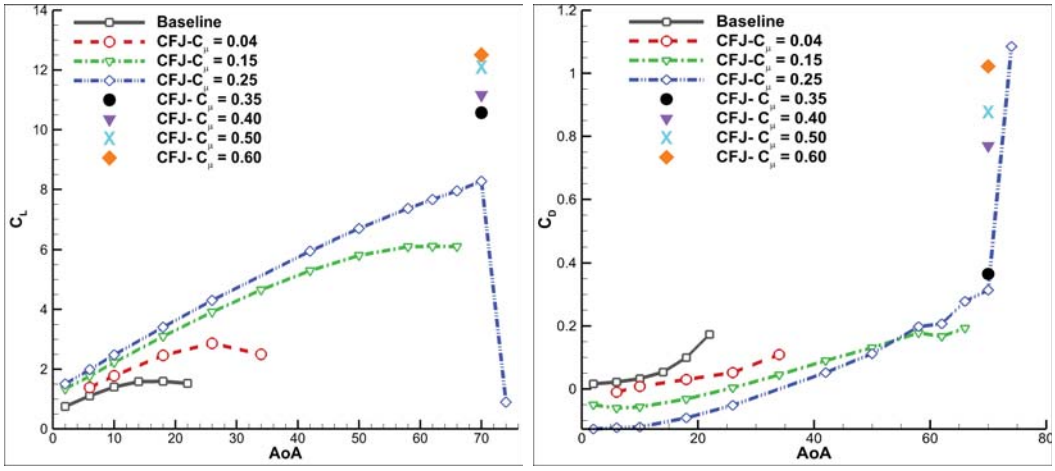

Figure 7.8: Lift and Drag coefficient vs AoA for the baseline and CFJ6421-SST016-SUC053-INJ009 airfoil.

a value of 12.60 at C_μ=0.60. This value is far greater than the C_{Lmax} of 7.6 defined for this airfoil based on Eq. (7.1). It also exceeds the maximum lift coefficient of 4π for all lifting devices based on the potential flow theory as indicated by Eq. (7.1). The lift coefficient greater than the maximum lift coefficient limit defined by potential flow is named as "Super-Lift Coefficient".

The drag coefficients of the CFJ airfoil are all reduced compared with that of the baseline NACA6421 airfoil. The negative drag coefficient is the thrust created by the CFJ. As the AoA increases, the drag coefficient is increased slowly until the flow is stalled when a massive flow separation occurs. At high momentum coefficient of $C_\mu > 0.25$ at high angle of attack such at AoA=70°, the ultra high lift also generates very high pressure drag as shown in Fig. 7.8.

For the pure aerodynamic ratio of L/D in Fig. 7.9, CFJ airfoil has extraordinarily high values because the drag can be so small or negative. The pure L/D will be used for a CFJ aircraft to decide its weight and propulsion systems. The negative drag will create negative L/D, which is a feature that the CFJ airfoil can be used as

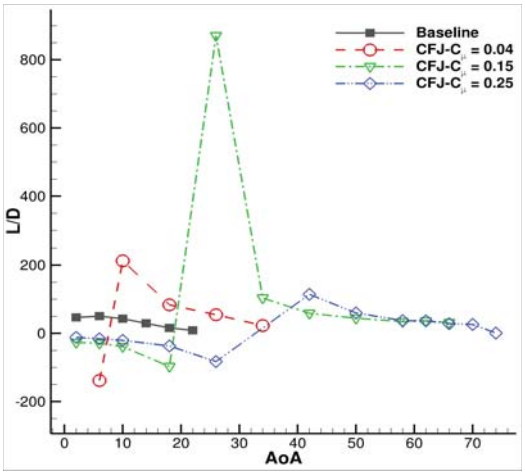

Figure 7.9: Aerodynamics efficiency L/D vs AoA for the baseline and CFJ6421-SST016-SUC053-INJ009 airfoil.

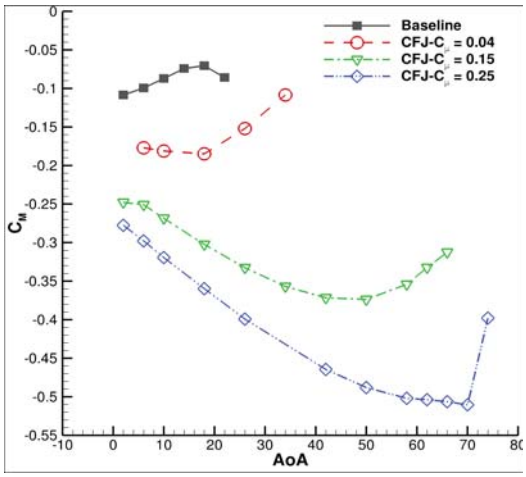

Figure 7.10: Moment coefficient C_M vs AoA for the baseline and CFJ6421-SST016-SUC053-INJ009 airfoil.

distributed thrust source. As shown in Fig. 13 for the C_μ from 0.04 to 0.25, the L/D are negative up to AoA about 30°. That means the CFJ airfoil will propel itself without a propulsion system. Even when the AoA is near 70° with C_L about 8, the L/D is at a high level of about 50. This means that the aircraft does not need a large engine and the system can be more optimized to favor cruise efficiency.

The pitching moment coefficient about the 1/4 chord point is shown in Fig. 7.10. The nose down moment coefficient C_M is significantly increased with the high C_μ and very high lift coefficient. For small injection momentum coefficient $C_\mu = 0.04$, the nose down moment coefficient is increased moderately. The high nose down moment may be better compensated by using canard as pitching moment control surface.

The corrected aerodynamic efficiency $(L/D)_c$ is plotted in Fig. 7.11. For the baseline airfoil, $(L/D)_c = (L/D)$ and the maximum $(L/D)_c$ of 50 occurs at AoA=6°. The maximum $(L/D)_c$ of 25 is obtained for this CFJ airfoil at AoA=22° and C_μ = 0.04. Since this CFJ airfoil is designed to achieve high maximum lift coefficient

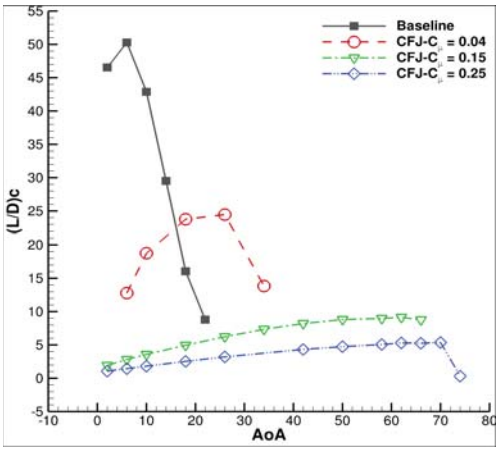

Figure 7.11: Corrected aerodynamic efficiency $(L/D)_c$ vs AoA for the baseline and CFJ6421-SST016-SUC053-INJ009 airfoil.

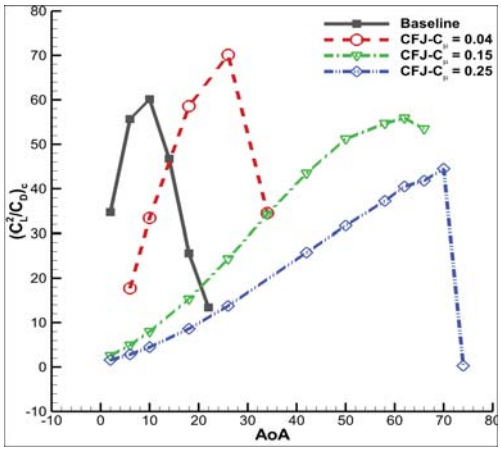

Figure 7.12: Corrected productivity efficiency $({C_L}^2/C_D)_c$ vs AoA for the baseline and CFJ6421-SST016-SUC053-INJ009 airfoil.

at takeoff/landing, not for high cruise efficiency, it is expected that the maximum $(L/D)_c$ is substantially lower than that of the baseline airfoil.

The productivity efficiency coefficient $({C_L}^2/C_D)_c$ is given in Fig. 7.12. The baseline maximum $({C_L}^2/C_D)$ is 60 at AoA=10°. For the CFJ airfoil, the maximum $({C_L}^2/C_D)_c = 70$ is obtained at AoA=26° and $C_\mu = 0.04$. Even though this airfoil is not designed for cruise efficiency, the maximum productivity efficiency is still better than the baseline airfoil due to its higher lift coefficient.

The power coefficients of the CFJ pumping are calculated based on Eq. (5.12) and (5.13) using a constant efficiency value of 100%. The results are shown in Fig. 7.13. The power coefficient decreases with the increase of AoA until the airfoil is stalled. Fig. 7.14 is the total pressure ratio PR. The pumping power is largely determined by the total pressure ratio PR between the injection and suction cavity. The total pressure ratio PR has a similar pattern to the power coefficient, which decreases with the increasing AoA until the airfoil is stalled. This is a typical behavior of CFJ airfoil [68], because when the AoA is increased, the static pressure of the main

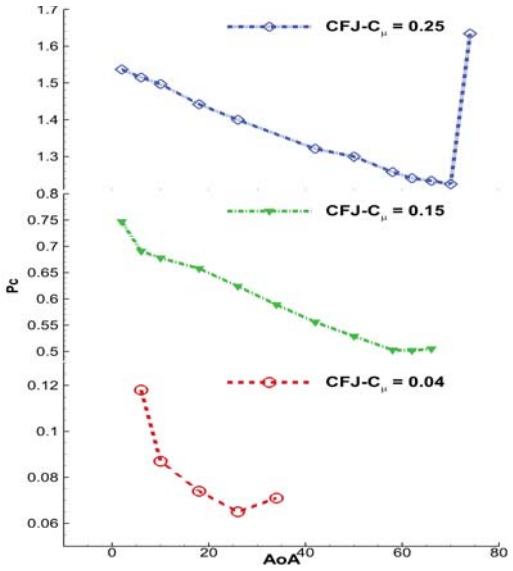

Figure 7.13: Power coefficient P_c for the CFJ6421-SST016-SUC053-INJ009 airfoil.

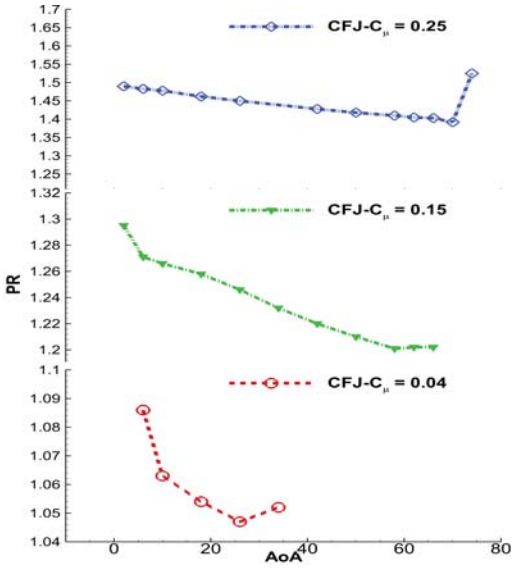

Figure 7.14: Total pressure ratio PR for the CFJ6421-SST016-SUC053-INJ009 airfoil.

flow at the injection region is decreased. The required injection total pressure is hence decreased accordingly to achieve the same C_μ. The total pressure ratio PR is reduced as well.

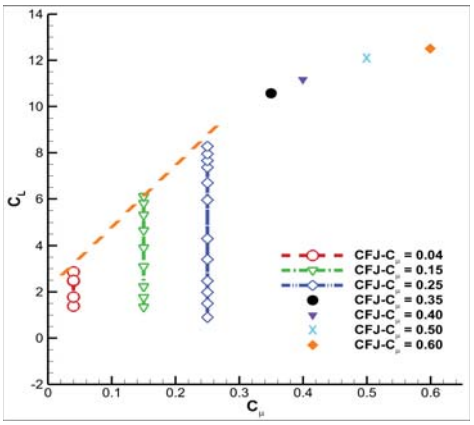

Figure 7.15: The lift coefficient C_L at different C_μ for the CFJ6421-SST016-SUC053-INJ009 airfoil.

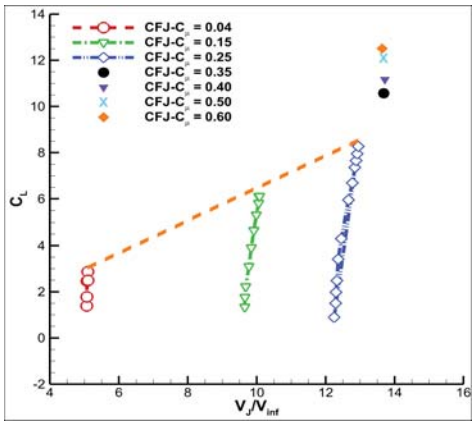

Figure 7.16: The jet velocity V_J/V_{inf} at different C_μ for the CFJ6421-SST016-SUC053-INJ009 airfoil.

Fig. 7.15 shows the relationship between the lift coefficient and momentum coefficient C_μ for the same airfoil. At low C_μ , the maximum lift coefficient C_{Lmax} linearly increases with the C_μ. As $C_\mu > 0.35$, the maximum lift coefficient becomes

plateaued. The relationship between the lift coefficient and CFJ jet velocity at different C_μ is shown on Fig. 7.16. For the same C_μ, it indicates that the injection jet velocity increases monotonically with increasing AoA. For $C_\mu < 0.25$, the maximum lift coefficient linearly grows with the jet velocity and momentum coefficient. For $C_\mu \geq 0.35$, the jet velocity becomes constant at choked condition in the injection slot.

7.3.1.2 C_{Lmax} Relationship with the CFJ Power Coefficient

It is important to understand what parameter can best correlate with the maximum lift coefficient to guide future engineering design. To achieve such a correlation, the results of all the different CFJ airfoils in the trade study are used, including the configurations to achieve high C_{Lmax} for takeoff/landing and high cruise efficiency with different SST and injection/suction size as listed in Table 11.1.

Fig. 7.17 is the variation of C_{Lmax} against C_μ. The linear growth of C_{Lmax} is observed at lower C_μ. The C_{Lmax} reaches a limit as the C_μ further increases. This observation matches to the variation of C_{Lmax} with the C_μ for a cylinder as reported by NASA [33]. However, the data are fairly scattered.

The relationship between C_{Lmax} and mass-averaged jet velocity at the injection slot is shown in Fig. 7.18. At lower jet velocity, the maximum lift coefficient grows linearly with the jet momentum. When the C_μ is greater than 0.35, the flow is choked at the jet injection, and the jet velocity becomes constant at about $V_J/V_{ref} \approx 14$ (Mach ≈ 0.9). The C_{Lmax} continues to increase after the flow is choked. The reason is that the increased injection total pressure P_{tinj} also increase the jet flow density,

hence the momentum coefficient. Similar to the relationship between C_{Lmax} and C_μ, the data are also fairly scattered.

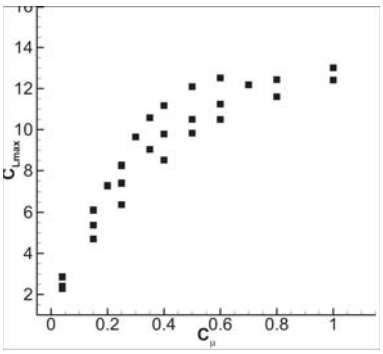

Figure 7.17: Variation of C_{Lmax} with C_μ for different CFJ airfoils.

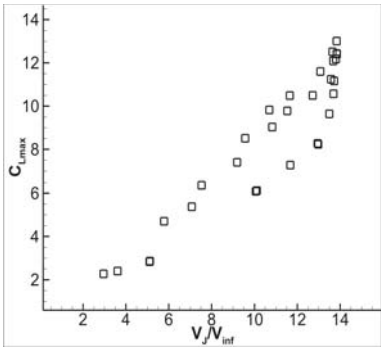

Figure 7.18: Variation of C_{Lmax} with V_J/V_{inf} for different CFJ airfoils.

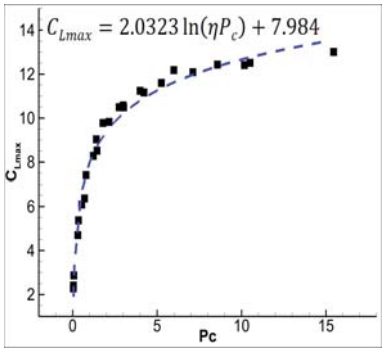

Figure 7.19: Variation of C_{Lmax} with P_c for different CFJ airfoils.

The relationship between the maximum lift coefficient C_{Lmax} and power coefficient P_c for different CFJ airfoils are shown in Fig. 7.19. The data collapse very well with the variation of P_c. It indicates that at a low power coefficient, the C_{Lmax} grows linearly with the increasing power coefficient P_c. The C_{Lmax} tends to reach a plateau of 14.0 as power coefficient P_c continues to increase. This is the same phenomenon as that observed by Tokumaru and Dimotakis [32] for their rotating cylinder result. When C_L is very high, it is beyond the capability of the flow control to add more energy to the main flow effectively due to very severe adverse pressure gradient. The lift coefficient increase hence becomes insensitive to the increasing P_c. To obtain the same C_{Lmax} increment, a much higher energy expenditure needs to be paid at a higher C_{Lmax} value than at a lower C_{Lmax} value. How to make an AFC to achieve the highest C_{Lmax} at the lowest energy expenditure is a very interesting and challenging research topic.

The natural logarithm function is used to fit the computational data.

$$C_{Lmax} = C_1 \ln(\eta P_c) + C_2 \tag{7.2}$$

where η is the CFJ pumping efficiency, C_1=2.0323 and C_2=7.984 for this airfoil. The correlation of Eq. (7.2) may only apply to this airfoil thickness of 21%, freestream Mach number of 0.063 and Reynolds number. In other words, the airfoil thickness, Mach number, Reynolds number and some other flow properties are expected to be a part of the parameters for a more general C_{Lmax} correlation.

7.3.1.3 Flow Field and Vortex Structures

Fig. 7.20 shows the computed airfoil surface pressure coefficient C_p for the baseline and the CFJ profile at their stall AoA of 18° and 70° at $C_\mu = 0.25$ and 0.35. A spike occurs at the injection slots as the C_p is measured on discontinuous wall surfaces. For the CFJ airfoil, a super-suction occurs at the airfoil leading edge with very low pressure value shown by the high peak value of 80 to 100 for the -C_p.

The airfoil surface isentropic Mach number distributions for the baseline and CFJ6421-SST016-SUC053-INJ009 airfoil at $C_\mu = 0.25$ and 0.35 are plotted in Fig. 7.21. The baseline airfoil accelerates the flow from freestream Mach number of 0.063 to the suction peak Mach number of 0.15, whereas the CFJ airfoil reaches the peak Mach number of near 0.8.

The static pressure contour is plotted in Fig. 7.59. The super-suction effect is displayed on the leading edge of the airfoil with a very low static pressure.

For the maximum lift of 8.2 and 10.6 at $C_\mu = 0.25$ and 0.35 respectively at AoA=70°, the Mach contours and streamlines are shown in Fig. 7.23. The upstream flow follows airfoil surface, turns around the LE for nearly 180°, and is nicely attached to the suction surface due to the strong induction effect from the high momentum co-flow jet.

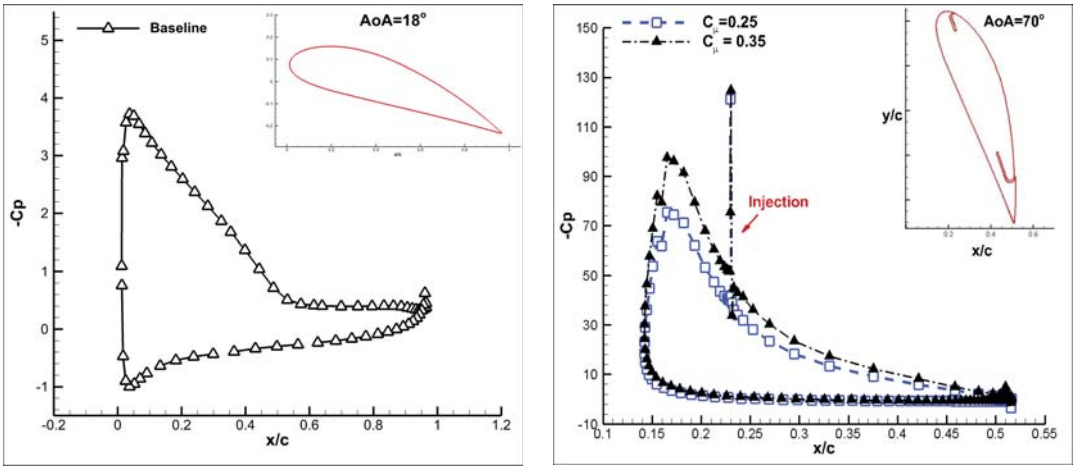

Figure 7.20: Surface pressure coefficient C_p distribution for the baseline airfoil at AoA=18° (left) and CFJ6421-SST016-SUC053-INJ009 airfoil at AoA=70°, C_μ = 0.25 and 0.35 (right).

The circulation generating the super-lift coefficient is so high that the stagnation point is detached from the airfoil as shown in Fig. 11.1 with C_μ=0.35. The very high velocity core occurs near the leading edge within the super suction region. The injection jet is choked at the slot, becomes supersonic within a small region immediately downstream of the injection slot, and turns to subsonic across a normal shock wave, as can be seen in the zoomed plot on the left upper plot in Fig. 11.1. The flow outside of the jet remains subsonic. This high momentum jet plays the major induction role to make the flow attached.

At the trailing edge, a large clock-wise vortex detaches the stagnation point from the airfoil surface as shown in the lower left plot of Fig. 11.1. The trailing edge vortex creates an extended virtual solid body to form a high pressure region due to the stagnant flow to support the airfoil with super-lift coefficient.

The vorticity contours at C_μ = 0.35 , C_L = 10.6, and AoA =70° is plotted in Fig. 11.2, which shows that there are four vortex layers starting from the airfoil leading edge. Fig. 7.26 gives a sketch to more clearly explain the vortex structures.

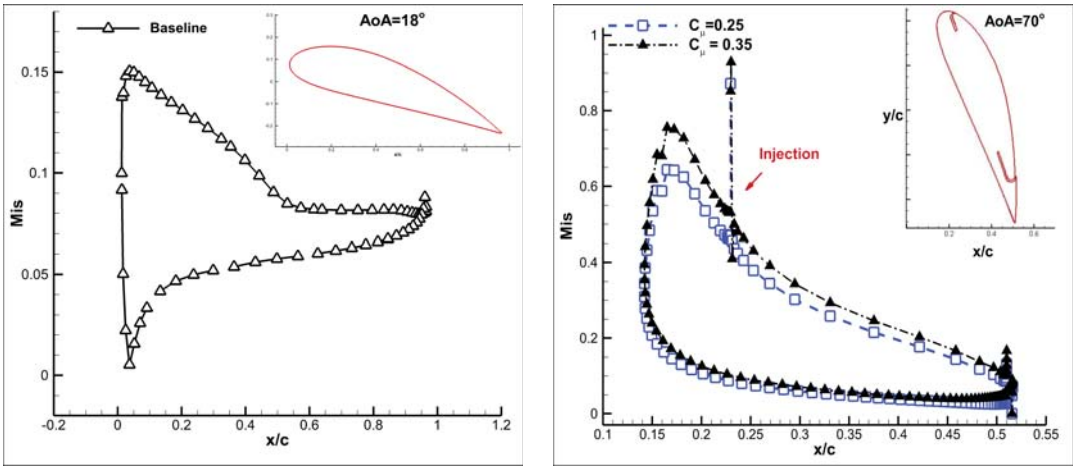

Figure 7.21: Surface isentropic Mach number M_{is} distribution for the baseline(left) and CFJ6421-SST016-SUC053-INJ009 airfoil(right).

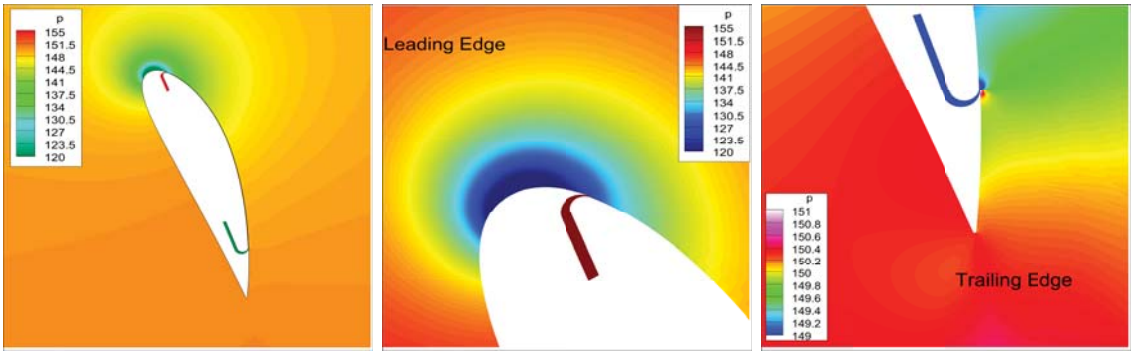

Figure 7.22: Static pressure distribution at $C_\mu = 0.35$ and AoA $= 70°$ for the CFJ6421-SST016-SUC053-INJ009 airfoil.

The near-wall surface region bounded by the non-slip wall boundary generates a clock-wise boundary layer vortex sheet. There is a mixing shear layer shed at the lip of the injection duct from the upstream leading edge boundary layer. Between the high momentum CFJ and the shear layer, a counter-clockwise CFJ vortex layer is generated downstream the CFJ injection slot. Next to the injection jet mixing layer is a clockwise vortex layer, which is induced by the CFJ via the mixing layer, named induced vortex layer. The induced vortex layer further induces a high speed jet turning around the leading edge, named as secondary induced jet, which can be

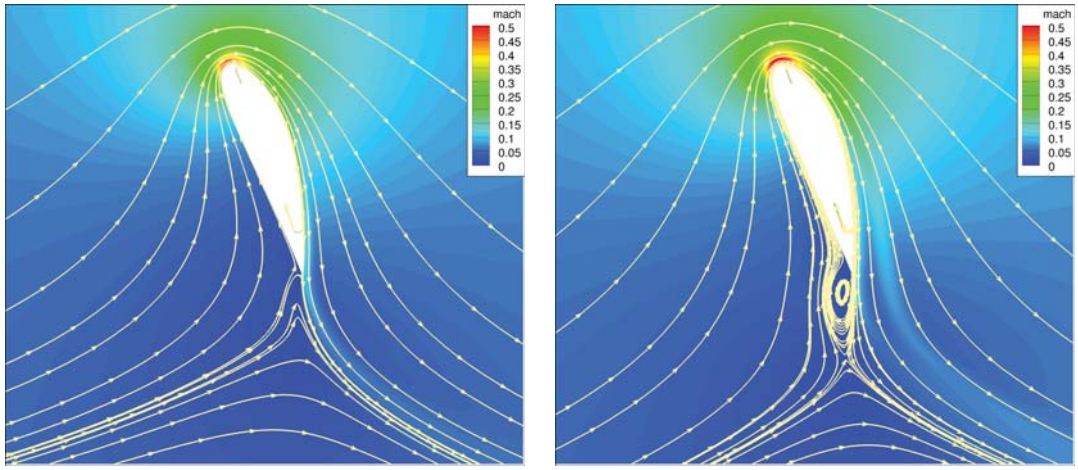

$C_\mu = 0.25$ $C_\mu = 0.35$

Figure 7.23: Mach number contours and streamlines at the momentum coefficient $C_\mu = 0.25$ (left) and 0.35 (right) and AoA=70° for the CFJ6421-SST016-SUC053-INJ009 airfoil.

clearly seen in Fig. 11.2 shown by the jet in green color next to the induced vortex layer. The high speed secondary induced jet creates a counter clockwise vortex layer to transit the velocity radially to the slower freestream velocity. The last vortex layer is hence named transitional vortex layer. These complex vortex structures appear to be very similar to the attached leading edge vortex structures of bird wing at powered downstroke, which also has very high angle of attack due to the relative flow direction and generates super-suction effect to provide lift and thrust for bird flight.

The C_{Lmax} appears to have no limit. The C_{Lmax} limit from the potential flow is the result of imposing Kutta condition, which is necessary for potential flow, but not a true physical condition that realistic flows must satisfy as shown in Fig. 11.1. In reality, C_{Lmax} depends on how much energy can be added to the flow, which varies with the active flow control method.

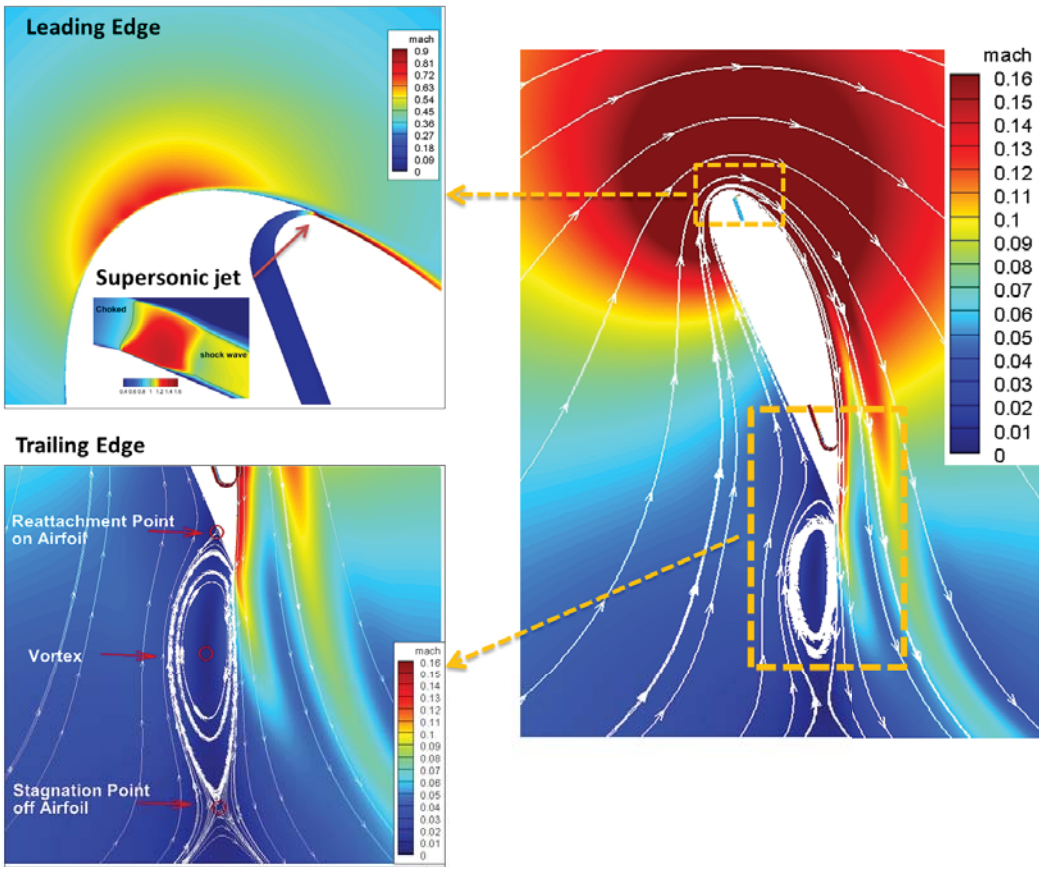

Figure 7.24: Mach number contours and streamlines at $C_\mu = 0.35$ and AoA =70° for the CFJ6421-SST016-SUC053-INJ009 airfoil.

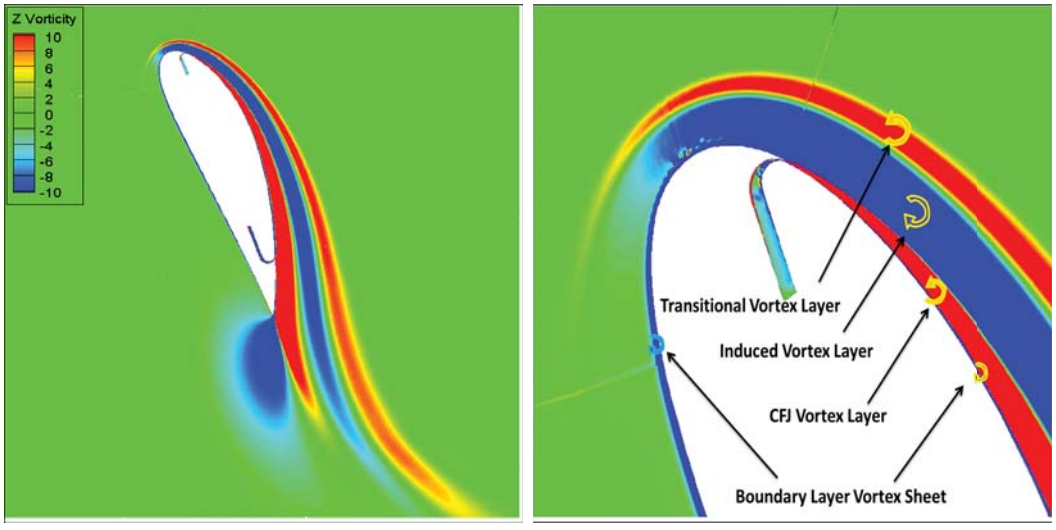

Figure 7.25: Vorticity contour at $C_\mu = 0.35$ and AoA =70° for the CFJ6421-SST016-SUC053-INJ009 airfoil.

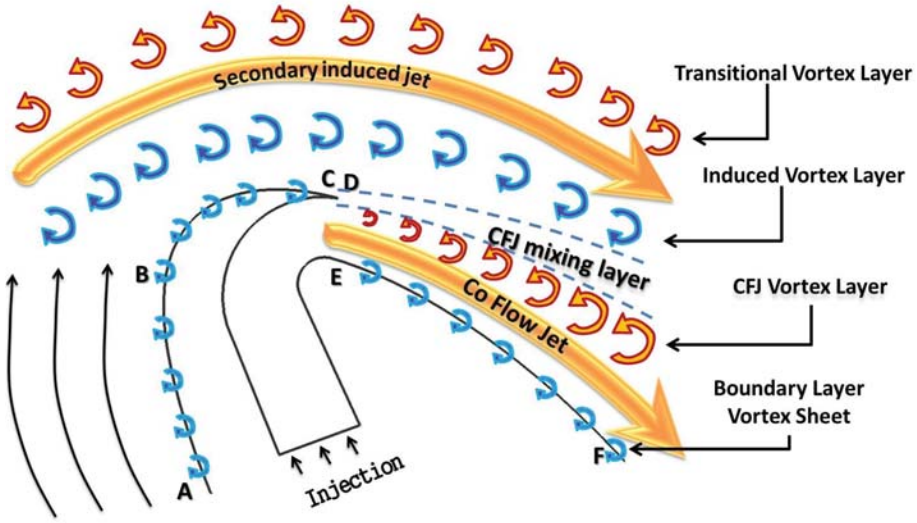

Figure 7.26: Sketch of the vortex distribution near the leading edge of CFJ airfoil at $C_\mu = 0.35$ and AoA =70°.

7.3.2 Cruise Efficiency

For transport aircraft, cruise efficiency is crucial. It is desirable to use the same set of airfoil with minimal geometry variation. This section is to present how the geometry variation can benefit the airfoil for high efficiency cruise condition. In general, at cruise condition, the injection slot size is larger and the C_μ is at low level such as 0.02 to 0.06, which minimizes the CFJ power consumption and maximizes the aerodynamic efficiency and productivity efficiency. For the cruise condition, the Mach number of 0.15 and Reynolds number of 2.6 million are used as the freestream conditions. A redesigned CFJ6421-SST143-SUC133-INJ065 airfoil based on NACA6421 airfoil with leading edge modification is used for the cruise configuration [145]. Compared with the previous airfoil CFJ6421-SST016-SUC053-INJ009 for maximum lift coefficient, this cruise airfoil has the SST increased from 0.16%C to 1.43%C, injection slot size increased form 0.09%C to 0.65%C, and suction slot size increased from 0.53%C to 1.33%C. The leading edge radius is slightly reduced to adjust the injection slot location where the lowest static pressure occurs to minimize the CFJ power consumption. All the simulation parameters are summarized in Table 7.6.

Table 7.6: Cruise simulation parameters

CFJ6421 airfoil	Mach number	Reynolds number	AoA	C_μ
SST143-SUC133-INJ065	0.15	2,600,000	2°-26°	0.02, 0.04, 0.06

The computed lift and drag coefficient is displayed in Fig. 7.27. Comparing to the previous design, for the same C_μ, the stall AoAs and maximum lift coefficient are lower because the larger injection slot size generates smaller jet velocity. For a very low C_μ such as 0.02, the stall AoA is smaller than the baseline NACA6421 airfoil. The drag coefficient of CFJ airfoil is also reduced. For a high C_μ of 0.06 at low AoA,

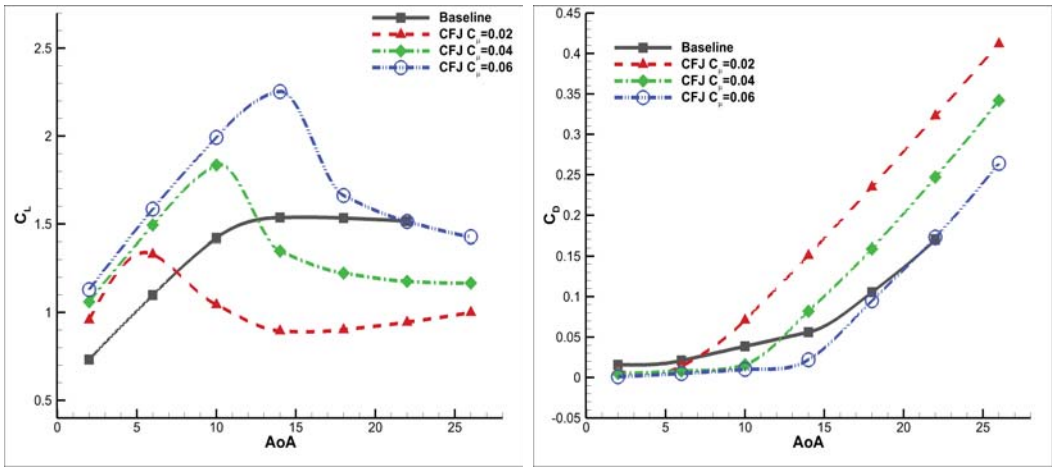

Figure 7.27: Lift and drag coefficient vs AoA at different C_μ for the baseline and CFJ6421-SST143-SUC133-INJ065 airfoil.

negative C_D (thrust generation) is obtained. The drag polar of C_L and C_D is plotted in Fig. 7.28. It shows that the CFJ airfoil can cruise at $C_L \geq 1.5$ with a near zero drag or a thrust. With such a lift coefficient, the baseline airfoil is already stalled.

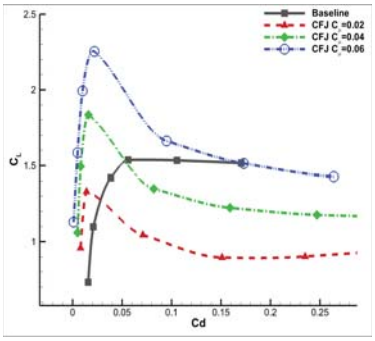

Figure 7.28: Drag polar at different C_μ for the baseline and CFJ6421-SST143-SUC133-INJ065 airfoil.

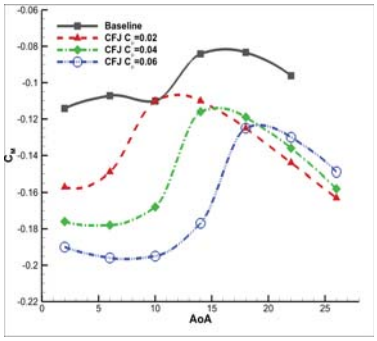

Figure 7.29: Moment coefficient C_M vs AoA at different C_μ for the baseline and CFJ6421-SST143-SUC133-INJ065 airfoil.

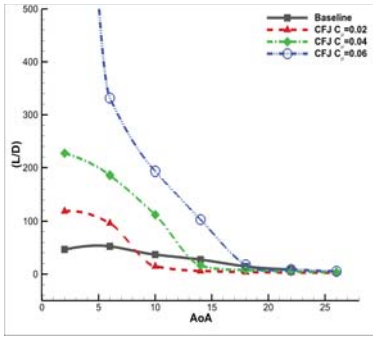

Figure 7.30: Aerodynamic efficiency (L/D) vs AoA at different C_μ for the baseline and CFJ6421-SST143-SUC133-INJ065 airfoil.

The moment coefficient is displayed in Fig. 7.29. The CFJ airfoil nose-down moment coefficient is higher than the baseline airfoil for all the C_μ, but is substantially reduced when the AoA is increased to near the AoA of C_{Lmax}.

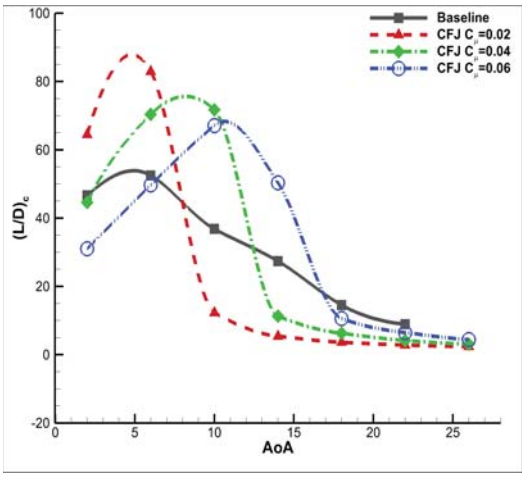

Figure 7.31: Corrected aerodynamic efficiency $(L/D)_c$ vs AoA at different C_μ for the baseline and CFJ6421-SST143-SUC133-INJ065 airfoil.

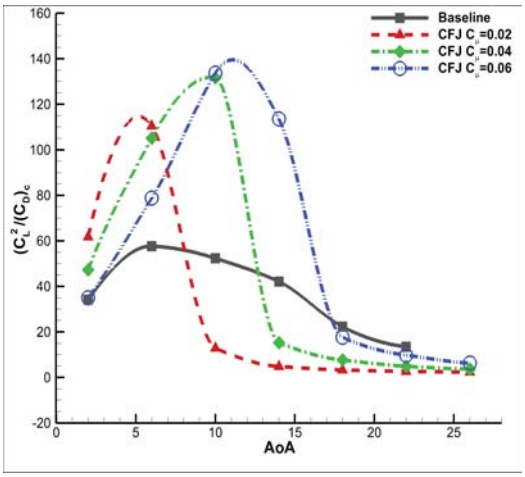

Figure 7.32: Corrected productivity efficiency $({C_L}^2/C_D)_c$ vs AoA at different C_μ for the baseline and CFJ6421-SST143-SUC133-INJ065 airfoil.

The ratio of lift to drag is shown in Fig. 7.30. The CFJ airfoil has extremely high L/D because the CFJ airfoil generates thrust. The corrected aerodynamic efficiency coefficient $(L/D)_c$ is plotted in Fig. 7.31. For the baseline airfoil, the maximum L/D is 53 at AoA=6°. For the CFJ airfoil at all the C_μ, the maximum $(L/D)_c$ is higher and up to 83 with an increase from 28% at $C_\mu = 0.06$ to 62% at $C_\mu = 0.02$. Compared with Fig. 7.11 for the takeoff/landing airfoil configuration with smaller injection size, the maximum $(L/D)_c$ is more than tripled.

The corrected productivity efficiency $({C_L}^2/C_D)_c$ for the CFJ and baseline airfoil is plotted in Fig. 7.32. Due to the high lift enhancement of CFJ, the productivity coefficient is much higher than that of the baseline airfoil, with an increase of 98% at $C_\mu = 0.02$ to 141% at $C_\mu = 0.06$. The substantially increased aerodynamic efficiency and productivity efficiency are all attributed to that the CFJ airfoil is able to achieve significant lift increase and drag reduction at low AoA with very low energy expenditure as shown in Fig. 7.33 and 7.34. This provides the CFJ airfoil a unique feature that it can be used for both high efficiency cruise and high lift takeoff/landing.

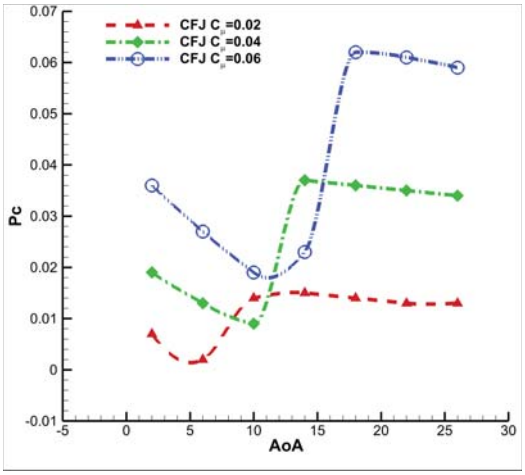

Figure 7.33: Power coefficient P_c vs AoA at different C_μ for the CFJ6421-SST143-SUC133-INJ065 airfoil.

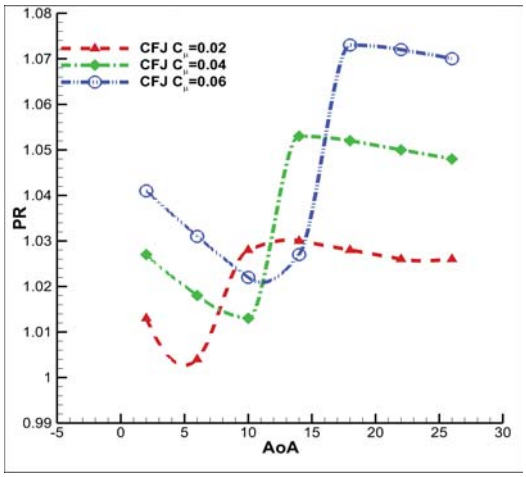

Figure 7.34: Total pressure ratio PR vs AoA at different C_μ for the CFJ6421-SST143-SUC133-INJ065 airfoil.

Table 7.7: Comparison of parameters for baseline and CFJ airfoils at the best aerodynamic efficiency point $(L/D)_{c_{max}}$. (CFJ pumping efficiency η =100%)

Airfoil	AoA	C_L	P_c	(L/D)	$(L/D)_{c_{max}}$	$(C_L^2/C_D)_{c_{max}}$	C_M
Baseline	6	1.098	-	52.496	52.496	57.672	-0.107
CFJ, C_μ=0.02	6	1.331	0.002	96.134	82.954	110.420	-0.149
CFJ, C_μ=0.04	10	1.835	0.009	112.057	71.744	131.629	-0.168
CFJ, C_μ=0.06	10	1.993	0.019	193.553	67.109	133.743	-0.195

Table 7.7 summarizes the comparison of aerodynamic efficiency performance obtained for the baseline and CFJ airfoils at different C_μ with the CFJ pumping efficiency assumed to be 100%. For the baseline airfoil, the most efficient point with the maximum $(L/D)_{max}$ of 52.496 is obtained at AoA=6°. At this condition, the lift coefficient is 1.098 and the moment coefficient is -0.107. For the CFJ airfoil at C_μ = 0.02, the maximum $(L/D)_{c_{max}}$ ratio of 82.954 is obtained at AoA=6°. The pure aerodynamic efficiency is enhanced to 96.134. The CFJ airfoil also achieves higher C_L of 1.331 and higher nose-down moment coefficient of C_M of -0.149. At higher C_μ of 0.04 and 0.06, the AoA of maximum $(L/D)_{c_{max}}$ ratio is shifted to 10°. The $(L/D)_{c_{max}}$

drops with the increase of C_μ. With the higher AoA and C_μ, the lift coefficient is increased. As a result of higher C_L, the maximum $(C_L^2/C_D)_{c_{max}}$ increases to 133.743. The moment coefficient C_M are higher at the higher C_μ.

Table 7.8: Comparison of parameters for CFJ airfoils at the best aerodynamic efficiency point $(L/D)_{c_{max}}$. (CFJ pumping efficiency η =80%)

Airfoil	AoA	C_L	P_c	(L/D)	$(L/D)_{c_{max}}$	$(C_L^2/C_D)_{c_{max}}$	C_M
Baseline	6	1.098	-	52.496	52.496	57.672	-0.107
CFJ, C_μ=0.02	6	1.331	0.0028	96.134	80.204	106.761	-0.149
CFJ, C_μ=0.04	10	1.835	0.0115	112.057	65.824	120.767	-0.168
CFJ, C_μ=0.06	10	1.993	0.0243	193.553	57.688	114.967	-0.195

To consider the realistic CFJ pumping energy loss, a CFJ pumping efficiency of 80% is used and the comparison of aerodynamic performance is given in Table 7.8. Based on Eq. (5.12), the required CFJ power consumption is higher for lower pumping efficiency. Even with the 80% CFJ pumping efficiency, the aerodynamic efficiency $(L/D)_{c_{max}}$ and productivity efficiency $(C_L^2/C_D)_{c_{max}}$ are still substantially higher than those of the baseline airfoil. The maximum aerodynamic efficiency $(L/D)_{c_{max}}$ is 80.204 at C_μ=0.02 , a 53% increase. More importantly, the productivity efficiency $(C_L^2/C_D)_{c_{max}}$ is 120.767 at C_μ=0.04, an increase of 109%. It means that the transportation capability of the CFJ airfoil is doubled with the same energy consumption.

Fig. 7.35 shows the computed surface pressure coefficient C_p and the isentropic Mach number M_{is} for the baseline and the CFJ airfoil at C_μ = 0.04 and AoA at 6° and 10°. The surface loading of the CFJ airfoil is significantly higher than the baseline airfoil, resulting a substantially higher lift coefficient.

Fig. 7.36 is the Mach number contours at AoA=10° for the baseline airfoil and CFJ airfoil at C_μ=0.04 and AoA = 6° and 10°. The trailing edge of the baseline airfoil has a small separation due to the high thickness of the airfoil. All the separation is

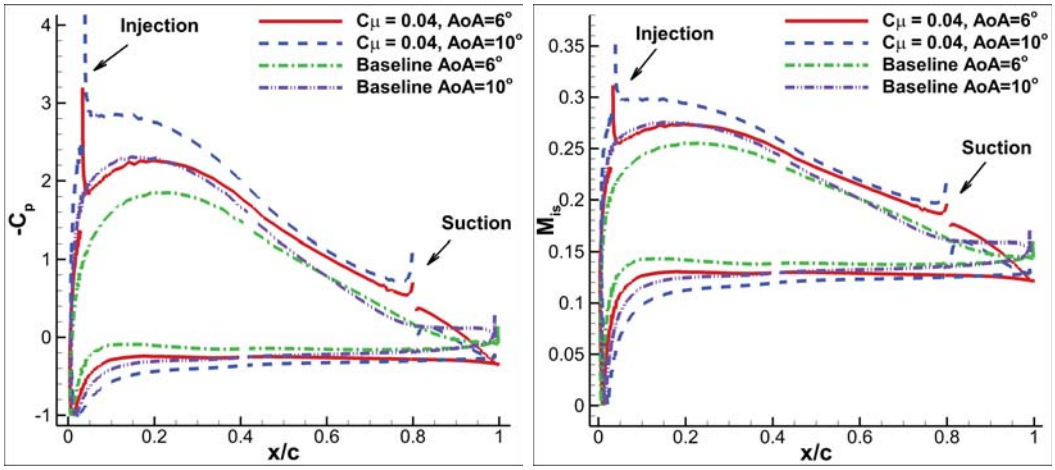

Figure 7.35: Surface pressure coefficient C_p (left) and isentropic Mach number M_{is} (right) distribution for the baseline and CFJ6421-SST143-SUC133-INJ065 airfoil at C_μ=0.04 and AoA = 6°, 10°.

removed by using the CFJ airfoil. And on the suction surface, the high velocity area and velocity magnitude are increased by the CFJ airfoil.

The pressure contours for the baseline and CFJ airfoil at C_μ=0.04, AoA=6°, 10° are shown in Fig. 7.37. Because of the higher acceleration on the suction surface of the CFJ airfoil, the low pressure area is larger.

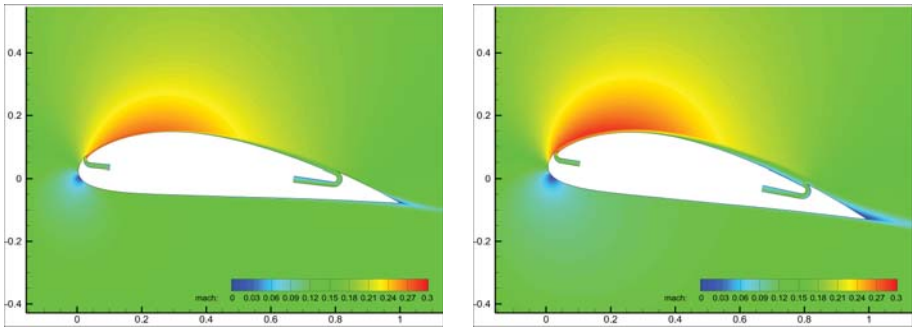

CFJ C_μ=0.04, AoA=6° CFJ C_μ=0.0, AoA=10°

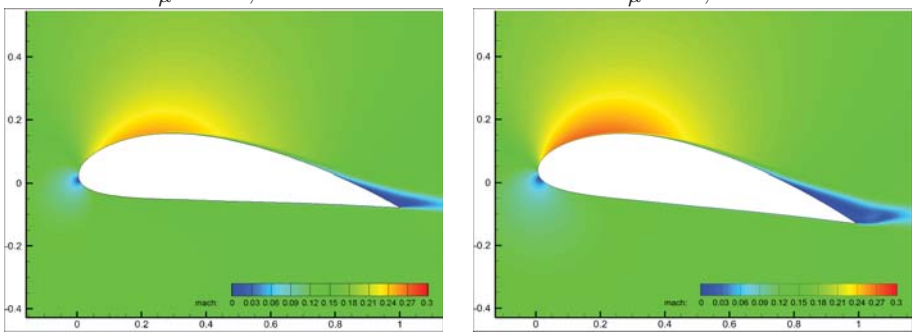

Baseline, AoA=6° Baseline, AoA=10°

Figure 7.36: Mach number contours at AoA = 6°, 10° for baseline(bottom) and CFJ6421-SST143-SUC133-INJ065 airfoil(top).

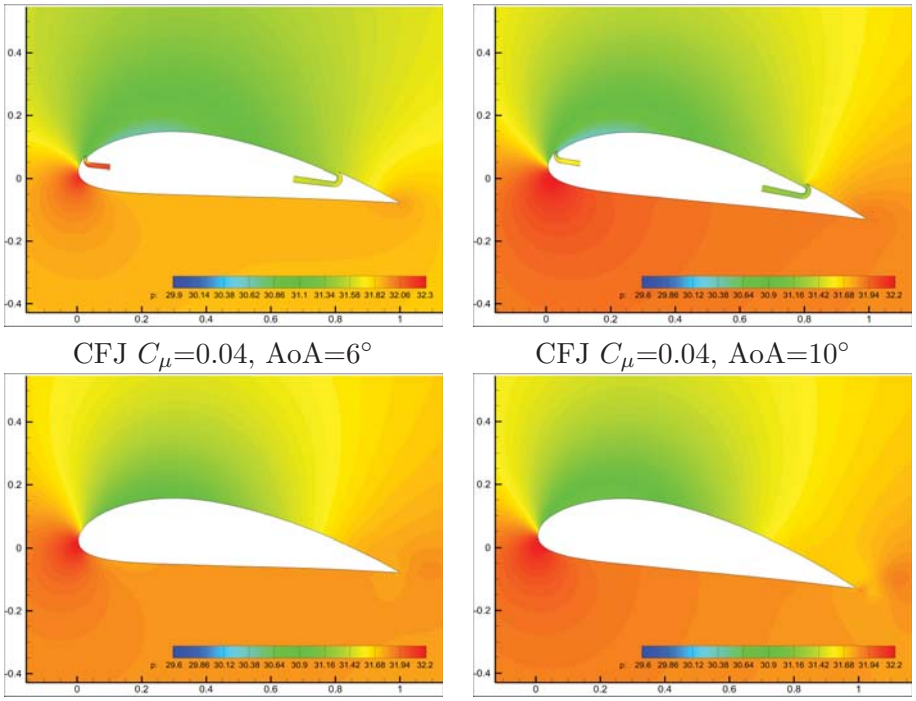

CFJ C_μ=0.04, AoA=6° CFJ C_μ=0.04, AoA=10°

Baseline, AoA=6° Baseline, AoA=10°

Figure 7.37: Static pressure contours at AoA = 6°, 10° for baseline(bottom) and CFJ6421-SST143-SUC133-INJ065 airfoil(top).

7.4 Parametric Study of Super-Lift CFJ Airfoil

This section present the parametric trade study of the CFJ geometry parameters,i.e. SST, injection and suction slot sizes on the lift enhancement performance for take-off and landing. Table 7.9 summarizes all the geometry parameters for CFJ airfoils with different SSTs, injection and suction slot sizes normalized by chord length (C), and the injection jet momentum coefficient used.

Table 7.9: CFJ airfoils geometry with various SST, injection and suction slot sizes

CFJ airfoil	SST (%C)	Injection slot size (%C)	Suction slot size (% C)	C_μ
SST016	0.16	0.09	0.18	0.04,0.15, 0.25,0.30,0.35
SST026	0.26	0.17	0.27	0.04,0.15,0.25
SST057	0.57	0.39	0.53	0.04,0.15,0.25
SST016-SUC036	0.16	0.09	0.36	0.04,0.15,0.25
SST016-SUC053	0.16	0.09	0.53	0.04,0.15,0.25
SST016-SUC053-INJ018	0.16	0.18	0.53	0.04,0.15,0.25
SST016-SUC053-INJ027	0.16	0.27	0.53	0.04,0.15,0.25
SST016-SUC053-INJ055	0.16	0.55	0.53	0.04,0.15,0.25

For the low speed takeoff/landing simulation, the jet momentum coefficients C_μ = 0.04, 0.15, and 0.25 are simulated for the lift variation with AoA. The simulated AoAs vary from 0° to 74° with an increment of 4°.

7.4.1 Effects of SST

Fig. 7.38 shows the computed lift coefficient with different SSTs (SST016, SST026, SST057). The lift coefficient of all the tested CFJ airfoils are increased drastically compared to the baseline NACA6421 airfoil. As the reference, the baseline NACA6421

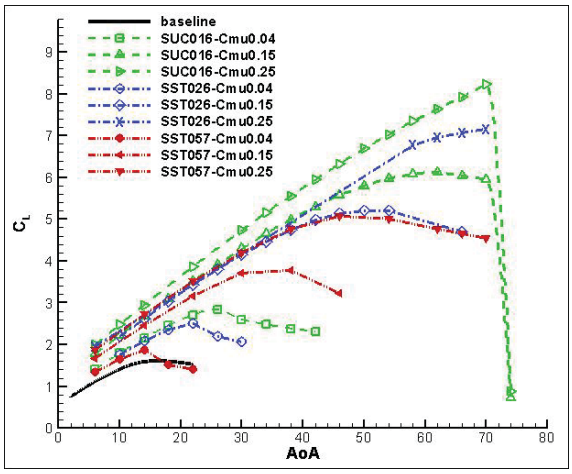

Figure 7.38: Lift coefficient vs AoA at different SSTs (SST016, SST026, SST057).

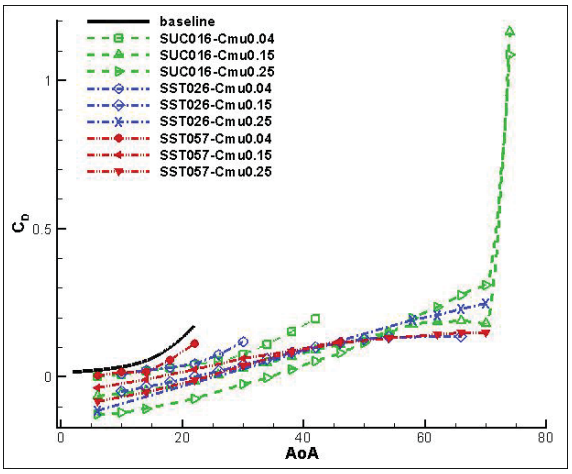

Figure 7.39: Drag coefficient vs AoA at different SSTs (SST016, SST026, SST057).

airfoil is stalled at AoA=18° with the maximum lift coefficient of 1.59. The maximum lift coefficient are increased to 8.3 for the SST016 airfoil at $C_\mu = 0.25$.

The CFJ airfoil with smaller SST achieves higher lift coefficient than the CFJ airfoils with larger SST at the same C_μ. For the same CFJ airfoil, the stall AoA is increased significantly with higher C_μ. At lower jet momentum coefficient of $C_\mu = 0.04$, the CFJ6421-SST016 airfoil flow is stalled at the AoA of 28°. At higher C_μ greater than 0.15, the stall AoA exceeds 50°. Overall, the general trend is that the CFJ airfoil using higher C_μ will achieve increased stall angle and massive lift enhancement.

Fig. 7.39 shows the computed drag coefficient for CFJ airfoil with various SSTs (SST016, SST026, SST057). The drag coefficients of all the CFJ airfoils are substantially reduced compared with the baseline airfoil. A tremendous amount of CFJ airfoil obtain negative drag coefficient. The negative drag is produced by higher jet momentum powered by the CFJ pump. The negative drag coefficients are achieved up until AoA=50° with $C_\mu \geq 0.04$ for the CFJ6421-SST016 airfoil. The enhanced lift and negative drag (thrust) is the result of the super-suction effect at leading edge.

The same effect also increase the nose down momentum.

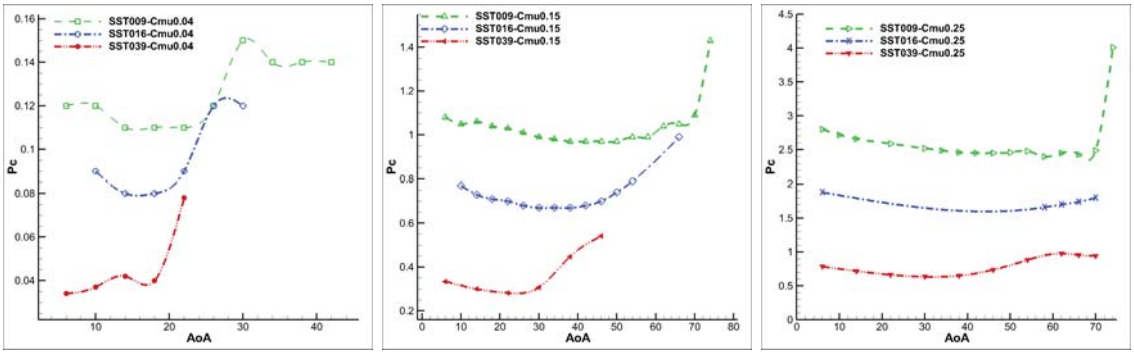

Figure 7.40: Power coefficient for CFJ6421 at different SSTs (SST016, SST026, SST057).

The power consumption coefficient computed by equation 5.13 is plotted in Fig. 7.40. For any fixed CFJ airfoil and at same C_μ, the minimum value of power consumption is achieved at the medium AoAs, which represent the most energy efficient point. The optimal AoA for different airfoils differs at different momentum coefficients. For C_μ=0.04, the minimum P_c is obtained at AoA≈18°. For higher jet momentum coefficient $C_\mu = 0.15$ and 0.25, the optimal P_c occurs at the AoA≈40°.

For the same airfoil comparing the P_c scale of three plot, higher momentum coefficient requires high Power coefficient to provide energy to sustain the attached flow. To achieve the same momentum coefficient, the CFJ airfoils with smaller SST requires high Pc, corresponding to high energy expenditure. The energy expenditure difference can be explained by the jet velocity. For the same C_μ, the power coefficient of the CFJ6421-SST057 always has lower power coefficient than the CFJ6421-SST016 airfoil due to less energy loss.

The normalized jet velocity for CFJ airfoils with different SSTs are plotted in Fig. 7.41. For a specifc CFJ airfoil configuration when the jet momentum coefficient C_μ is fixed, the jet velocity keeps unchanged for all AoAs before the flow gets detached. If

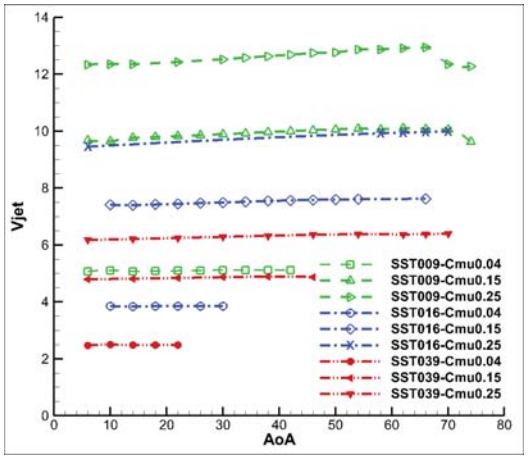

Figure 7.41: Normalized jet velocity for CFJ6421 at different SSTs (SST016, SST026, SST057).

we compare CFJ airfoils with different SSTs, at the same jet momentum coefficient C_μ, the jet velocity is higher for a CFJ airfoil with smaller SST, which corresponding to a high energy expenditure in Fig 7.40.

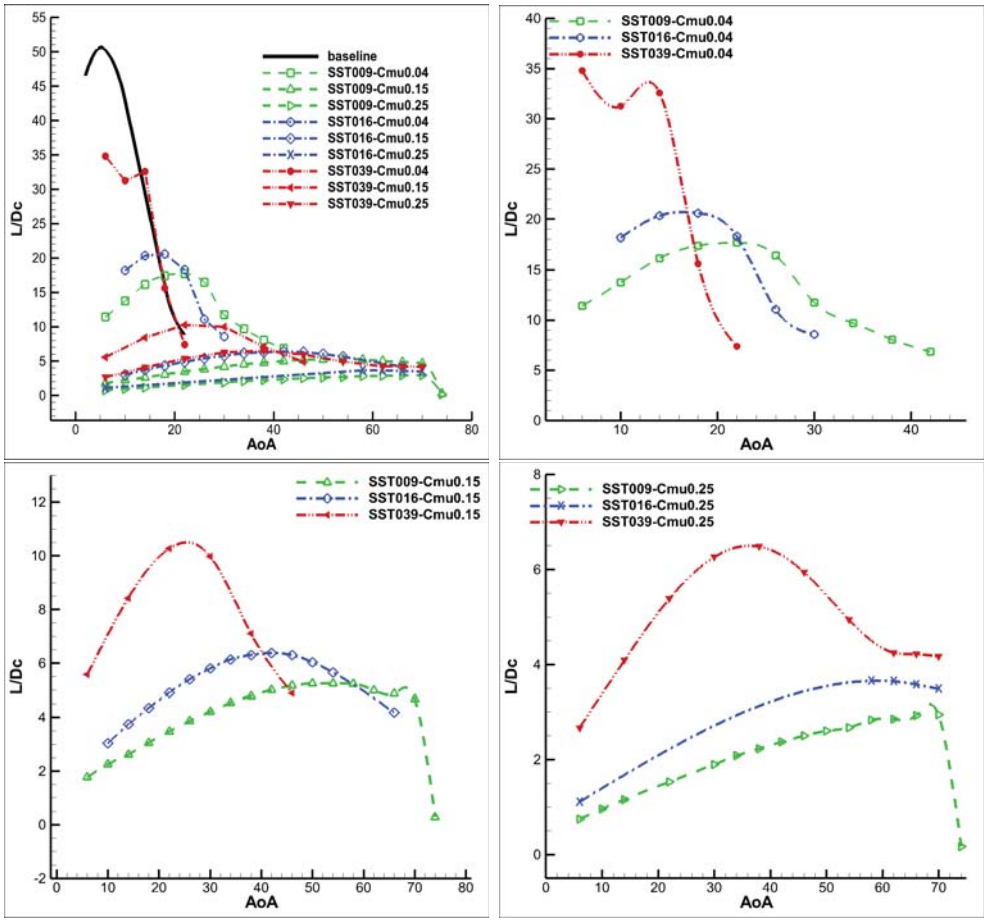

Figure 7.42: Corrected aerodynamic efficiency for CFJ6421 at different SSTs (SST016, SST026, SST057).

The corrected aerodynamic efficiency $(L/D)_c$ for the baseline airfoil and CFJ6421 airfoils with different SSTs are shown in Fig. 7.42. The maximum $(L/D)_c$ for SST016 is 18 at $C_\mu = 0.04$ and AoA $= 22°$. For SST057, the maximum $(L/D)_c$ achieves much higher value of $(L/D)_c = 33$ at $C_\mu = 0.04$ and AoA $= 14°$, where the lift coefficient is 1.8. This is because that the larger injection slot of CFJ6421-SST057 airfoil makes the energy loss smaller than the CFJ airfoil of SST016 with the smaller injection slot size. However, the baseline airfoil has the L/D=50 higher than all the CFJ airfoil with a significantly lower lift coefficient of 1.1.

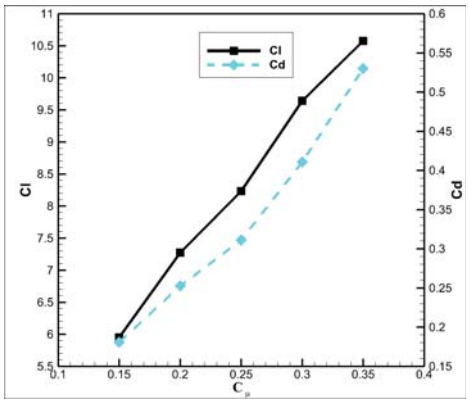

Figure 7.43: Lift and drag coefficient C_L , C_D vs C_μ at AoA = 70°.

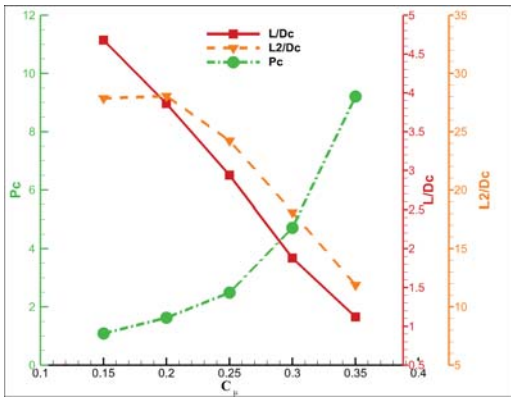

Figure 7.44: P_c, L/Dc, and C_L^2/C_{Dc} vs C_μ at AoA = 70°.

With the above study, the CFJ6421-SST016 airfoil with the most potential to go high AoA to achieve higher lift coefficient is selected for further study. The AoA is increased to 70° and the C_μ tested are 0.15, 0.2, 0.25, 0.3 and 0.35. All these C_μ are able to reach $AoA = 70°$ without being stalled. The higher the C_μ, the higher the C_{Lmax} as shown in Fig. 7.43. The maximum C_{Lmax} obtained at $C_\mu = 0.35$ is 10.6, 40% higher than the theoretical limit of 7.6. The calculated lift and drag coefficients are displayed in the left of Fig. 7.43. Both the lift and drag coefficient increase with the momentum coefficient C_μ. The suction mass flow rate cannot match the injection mass flow rate at further $C_\mu > 0.35$.

The power coefficient P_c, corrected aerodynamic efficiency $(L/D)_c$ and productivity efficiency C_L^2/C_{Dc} are plotted on the right of Fig. 7.44. The power coefficient P_c increases exponentially with the momentum coefficient C_μ. Both the aerodynamic efficiency $(L/D)_c$ and productivity efficiency C_L^2/C_{Dc} decreases linearly with the momentum coefficient C_μ.

To illustrate the flow filed, the Mach contours with streamlines for SST016 at $AoA = 70°$ with C_μ =0.2, 0.25, and 0.35 are displayed in Fig. 7.45. The circulation is so strong that the stagnation point is detached from the airfoil solid surface. In this

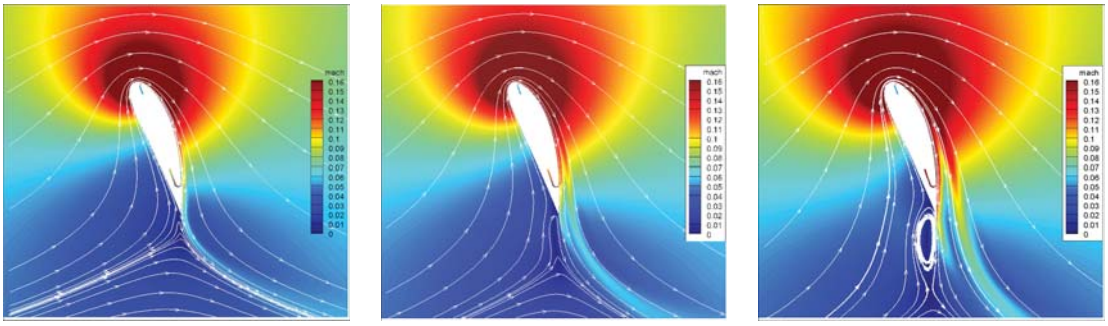

$C_\mu = 0.20$ $C_\mu = 0.25$ $C_\mu = 0.35$

Figure 7.45: Mach contours of for CFJ6421-SST016 airfoil with AoA=70° at different $C_\mu = 0.20, 0.25, 0.35$.

case, Kutta condition does not apply any more. This is because the trailing edge is not a wedge converging to a point, but is formed by a small circle.

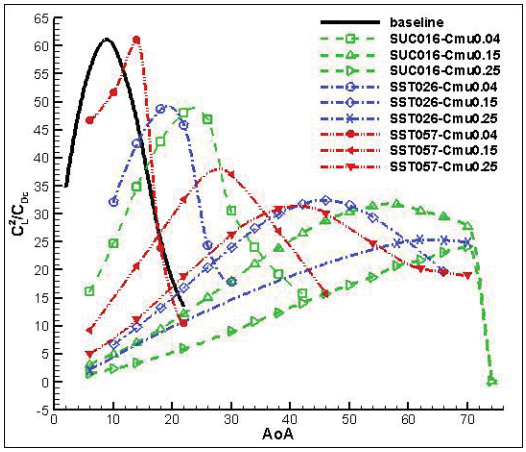

Figure 7.46: Productivity efficiency C_L^2/C_{Dc} vs AoA at different SSTs.

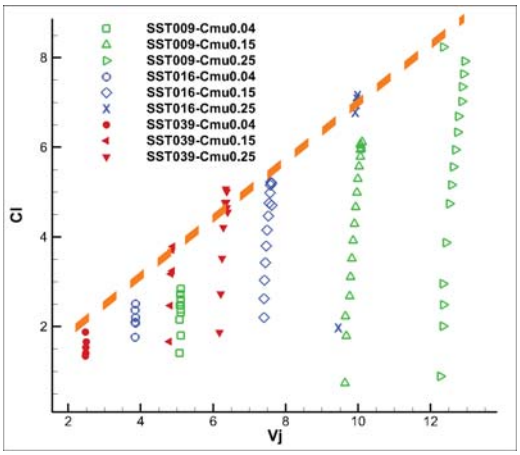

Figure 7.47: The correlation between the maximum lift coefficient and jet velocity.

The productivity efficiency C_L^2/C_{Dc} for CFJ6421 at different SSTs (SST016, SST026, SST057) is plotted in Fig. 7.46. For the baseline airfoil, the maximum productivity coefficient is 60 at AoA=14° with lift C_L=1.4. For the CFJ6421 airfoil family, the maximum productivity efficiency coefficient is 61 at the lift coefficient of C_L=1.9 at AoA=14°. Considering the same CFJ airfoil, the maximum productivity efficiency

C_L^2/C_{Dc} decreases with the CFJ momentum coefficient C_μ. For the CFJ airfoils with a series of SSTs, the larger SST achieves better maximum productivity efficiency coefficient than the smaller SST airfoils.

For all the cases mentioned above, the correlation between the lift coefficient C_L and jet velocity V_j is plotted in Fig. 7.47. It is observed that for specific airfoil, the maximum lift coefficient C_L grows linearly with the jet velocity V_j.

7.4.2 Effects of CFJ Suction Slot Size

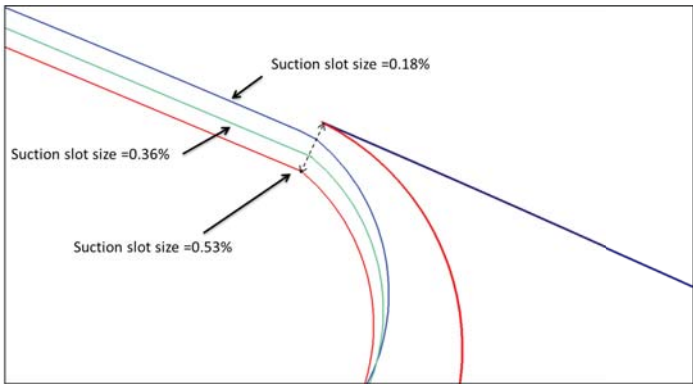

Figure 7.48: Modified suction slot size geometry from the CFJ6421-SST016 airfoil, (SUC018 (original), SUC036 (2×), SUC053 (3×)).

As discussed above, the flow is choked at the injection and suction slot for higher momentum coefficient of $C_\mu = 0.35$. Therefore, we will examine the effects of the CFJ injection and suction sizes on the super-lift coefficient performance of CFJ airfoils.

To remove the suction choked condition, the suction slot size is enlarged to allow more mass flow rate. The modified suction slot geometry is shown in Fig. 7.48. The enlarged slot size is twice and three times of the original. In this case, the suction surface transition is applied to enlarge the slot size.

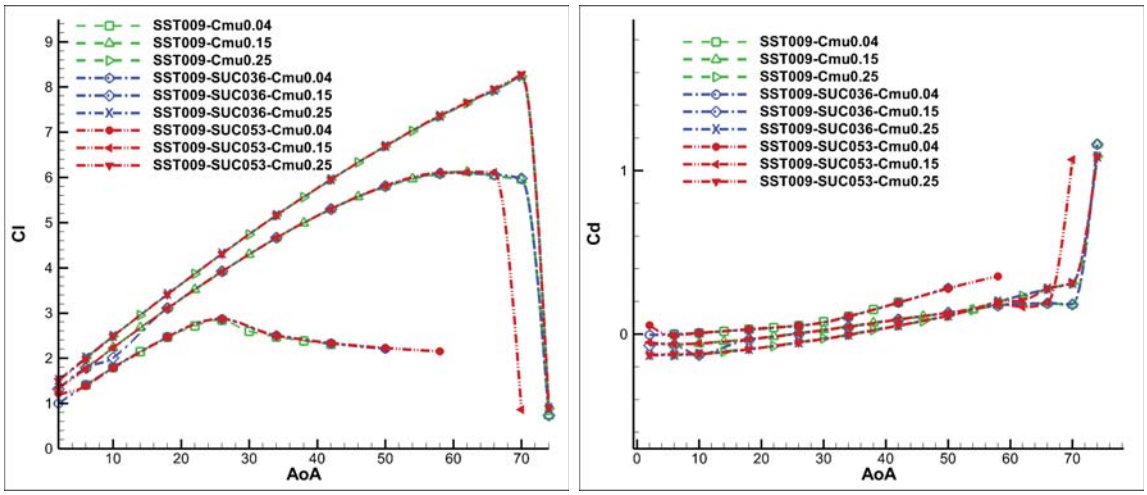

Figure 7.49: Lift and drag coefficient at different suction slot sizes CFJ airfoils (SUC018, SUC036, SUC053).

The computed lift and drag coefficient of modified suction slot size CFJ airfoils are displayed in Fig. 7.49. It is noticed that there is barely no change on the C_L and C_D curve comparing to the original airfoils. The only difference is the stall angle for SST016-SUC053 at $C_\mu = 0.15$ is 4° smaller.

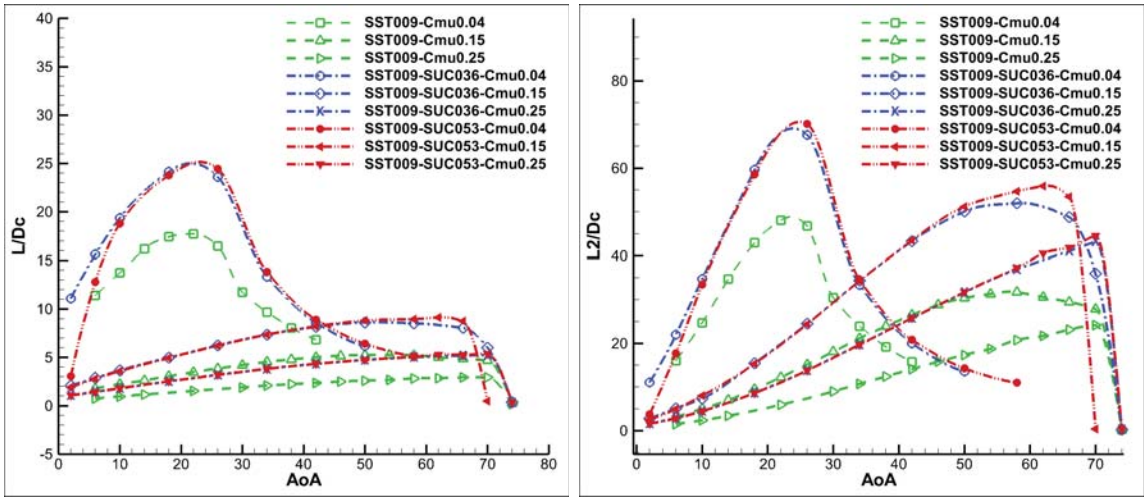

Figure 7.50: Aerodynamic efficiency $(L/D)_c$ (left) and productivity efficiency coefficient C_L^2/C_{Dc} (right) at different suction slot sizes CFJ airfoils (SUC018, SUC036, SUC053).

Fig. 7.50 shows the aerodynamic efficiency $(L/D)_c$ and productivity efficiency coefficient C_L^2/C_{Dc} of CFJ6421-SST016 at different suction slot sizes (SUC018, SUC036,

SUC053). With the enlarged suction slot size, the aerodynamic efficiency is enhanced tremendously. For the SST016-SUC053 airfoil at $C_\mu = 0.04$, the maximum aerodynamic efficiency $(L/D)_c$ is increased to 25, whereas the original SST016 airfoil achieves the maximum aerodynamic efficiency $(L/D)_c = 15$.

Similar pattern is obtained for the productivity efficiency C_L^2/C_{Dc}. The SST016-SUC053 achieve the maximum productivity efficiency $C_L^2/C_{Dc} = 70$, whereas the original SST016 obtains $C_L^2/C_{Dc} = 45$.

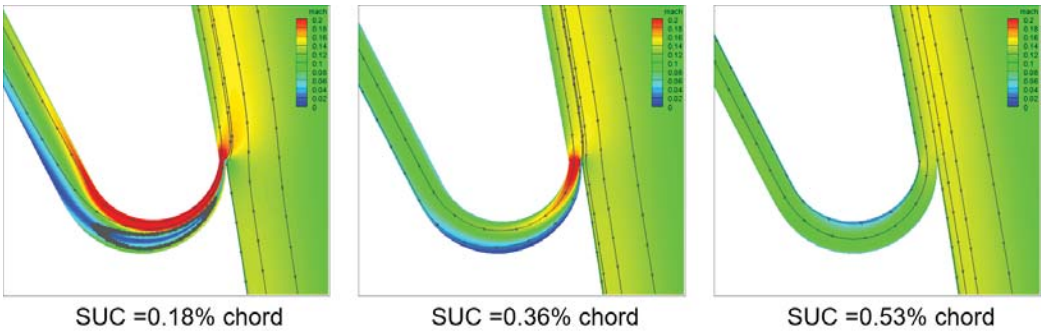

Figure 7.51: Mach contours and streamlines of suction slot at different suction slot sizes (SUC018, SUC036, SUC053) ($C_\mu = 0.25$, AoA=70°).

The enhancement of aerodynamic efficiency can be explained by the analysis of the flow field near the suction slot. The Mach contours and streamlines of suction slot is shown in Fig. 7.51. The enlarged suction slot (SUC053) obtains smooth flow field and totally removes the choked conditions, which significantly improve the flow conditions and thus the efficiency.

Aiming at achieving higher C_{Lmax}, higher C_μ is applied at the CFJ6421-SST016 airfoils with enlarged suction slot size (CFJ6421-SST016-SUC036, CFJ6421-SST016-SUC053). The maximum lift coefficient of $C_{Lmax} = 13.5$ is obtained for CFJ6421-SST016-SUC053 at $C_\mu = 0.75$ and AoA = 70°.

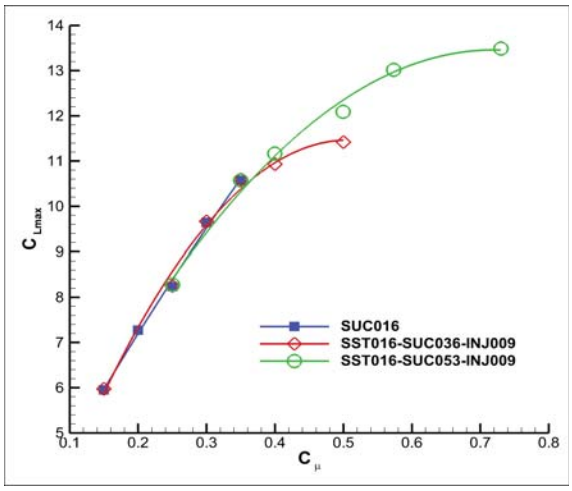

Figure 7.52: C_{Lmax} at different suction slot size with C_μ at AoA = 70°.

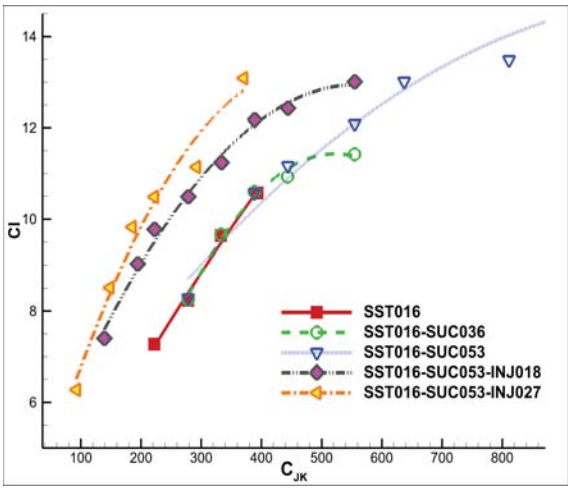

Figure 7.53: C_{Lmax} at different suction slot size with C_{JK} at AoA = 70°.

Therefore, we draw the conclusion that by enlarging the suction slot size, the maximum lift coefficient is increased by allowing more mass flow rate to match the higher injection momentum coefficient C_μ. Besides, increasing the suction slot size would significantly benefit the aerodynamic efficiency by removing the choked flow conditions.

7.4.3 Effects of CFJ Injection Slot Size

After comparing different suction slot size, it is observed that higher suction slot size is beneficial for the CFJ flow field. Therefore, we choose the CFJ6421-SST016-SUC053 to investigate the influence of the injection slot size (INJ).

Since previous results show the flow is fully choked at the injection for CFJ6421-SST016, the injection slot size is increased to increase the mass flow rate. The airfoil geometry near the injection slot is shown in Fig. 7.54. Three modified geometries are generated by increasing the injection slot size by twice, three times and six times (INJ018, INJ027, INJ055).

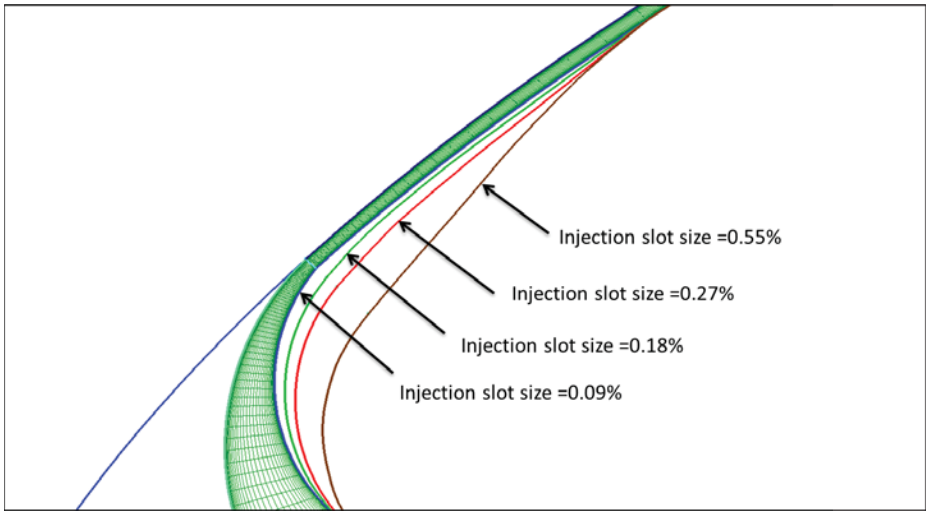

Figure 7.54: The modified CFJ6421-SST016-SUC053 airfoil geometry of enlarged injection slot sizes. (INJ009 (original), INJ018 (2×), INJ027 (3×), INJ055 (6×)).

Fig. 7.55 is the computed lift and drag coefficient for the three airfoils with modified injection slot size (INJ018, INJ027, INJ055). For the s CFJ6421-SST016-SUC053 airfoils with enlarged injection slot sizes, the lift coefficient is reduced significantly at the same momentum coefficient C_μ.

At $C_\mu = 0.25$, for the INJ018 ($S_{INJ} = 2 \times S_{INJ009}$), the airfoil stalled margin is elevated; however, the maximum lift coefficient is reduced from 8.3 to 7.5. For the INJ027 ($S_{INJ} = 3 \times S_{INJ009}$) and INJ055 ($S_{INJ} = 6 \times S_{INJ009}$), both the stall AoA and maximum lift coefficient are significantly reduced.

The aerodynamic efficiency $(L/D)_c$ and productivity efficiency coefficient $(C_L^2/C_D)_c$ are displayed in Fig. 7.56. It is observed that for all C_μ conditions, enlarged injection slot size can increase the aerodynamic efficiency $(L/D)_c$. The maximum $(L/D)_c = 34$ is obtained at AoA=14° for the INJ027 airfoil. The productivity efficiency improvement is similar to aerodynamic efficiency. The best productivity efficiency $(C_L^2/C_D)_c$ is obtained at AoA=18° for the INJ018 airfoil.

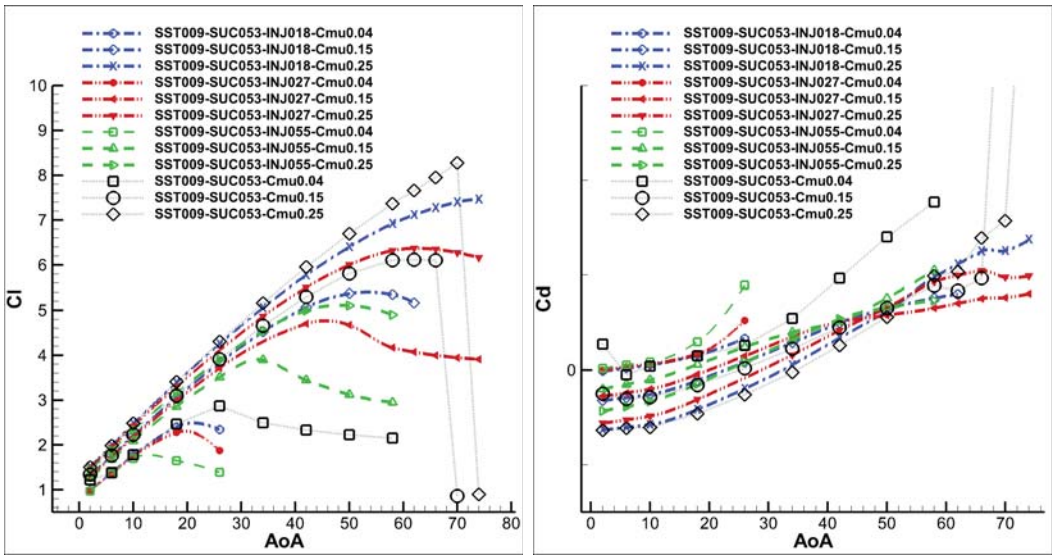

Figure 7.55: Lift and drag coefficient for the different CFJ airfoils with different injection slot sizes (INJ018, INJ027, INJ055).

Similar procedure is conducted for the INJ018, INJ027, and INJ055 airfoils by increasing the C_μ to explore the lift coefficient limit. The result is shown in Fig. 7.57. It is interesting that the maximum lift coefficient approximately approaches a limit at the C_L=13.5. The C_L increase is sensitive at low C_μ. As the momentum coefficient C_μ increases to a value, which is different for different airfoils, the final lift coefficient limit converges to a certain limit.

The C_μ limit, where the lift coefficient approaches its limit, is determined by the choked condition for different airfoils. For those airfoils with large injection slot sizes, the lift coefficient C_L limit is smaller and the C_μ limit is higher.

The normalized jet velocity for CFJ6421-SST016-SUC053 airfoils with different injection slot sizes (INJ009, INJ018, INJ027) are plotted in Fig. 7.58. For the same airfoil at the same momentum coefficient, the jet velocity is fixed for attached flows. For the same momentum coefficient, the airfoil with smaller SST has higher jet velocity, which corresponding to the high energy expenditure in Fig 7.40. All the V_j curves

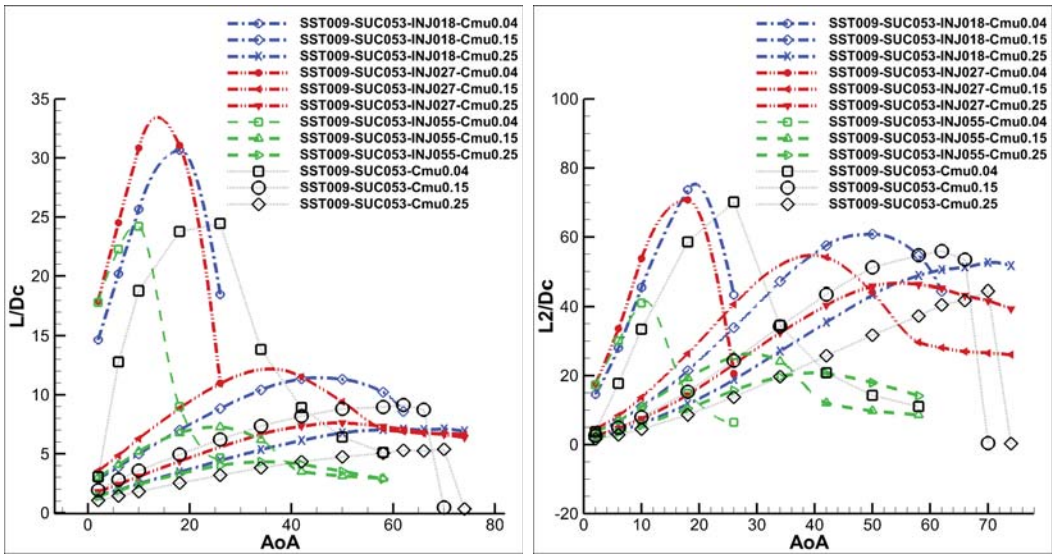

Figure 7.56: Aerodynamic efficiency $(C_L/C_D)_c$ (left) and productivity efficiency $(C_L^2/C_D)_c$ (right) at different injection slot sizes CFJ airfoils (INJ018, INJ027, INJ055).

converged to a fixed value ≈ 13.5, where the choked flow occurs. By comparing the C_L in Fig. 7.57 and V_j in Fig. 7.58 at the same $C_\mu = 0.40$, the jet velocity reaches the maximum limit, whereas the C_{Lmax} continues to grow. The reason for this is the by increasing the injection cavity total pressure P_{tINJ}, the jet density and jet momentum continue to increase although the jet velocity reaches the choke limit.

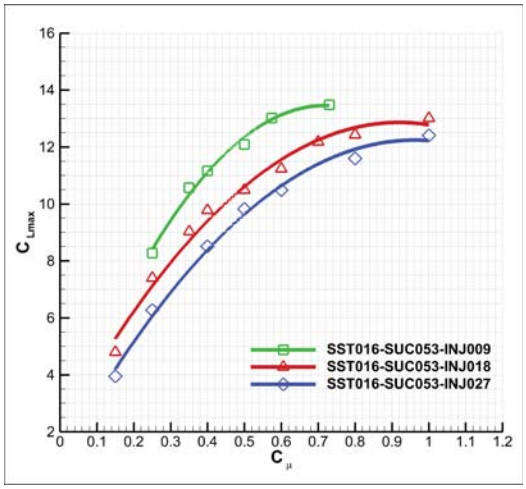

Figure 7.57: C_{Lmax} with different injection slot sizes. (INJ009, INJ018, INJ027)

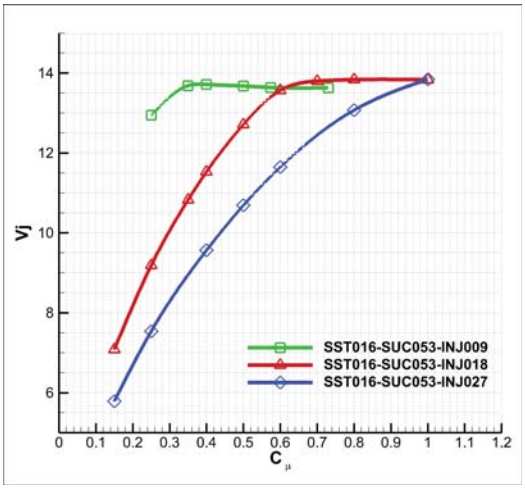

Figure 7.58: Normalized jet velocity with different injection slot sizes (INJ009, INJ018, INJ027).

7.4.4 Flow Field Analysis at Super-Lift Coefficient Conditions

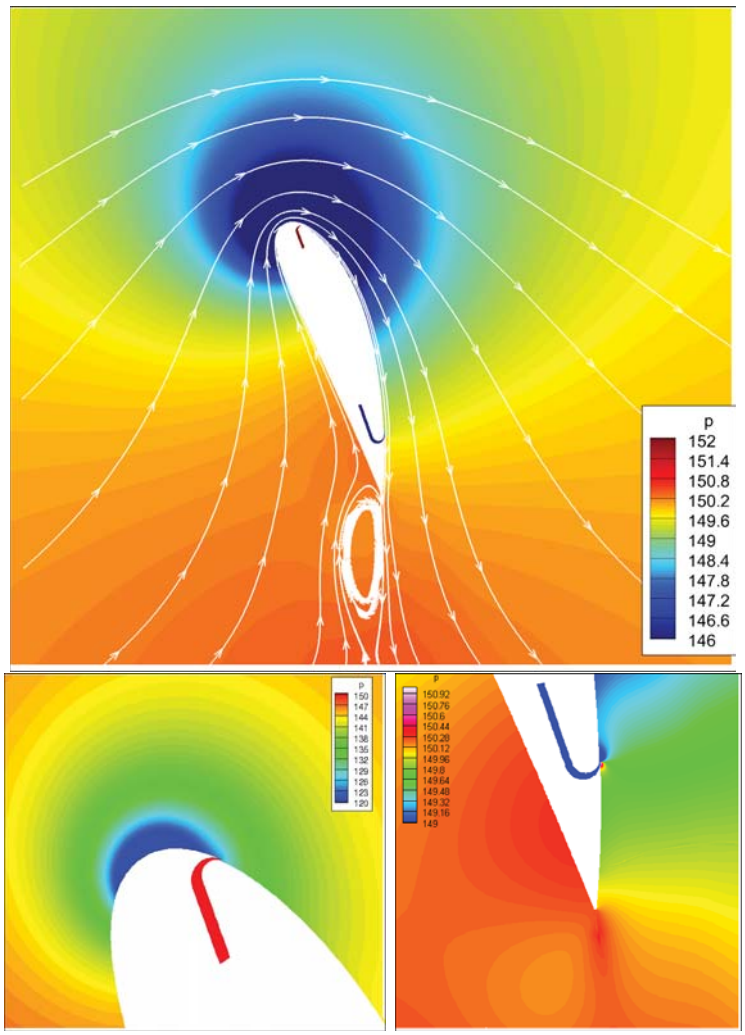

Figure 7.59: Static pressure contour and streamlines at $C_\mu = 0.35$.

To investigate the super lift generation of CFJ airfoils, the static pressure contour is plotted in Fig. 7.59. The super suction effect is displayed on the leading edge of the airfoil. The resulting high pressure difference is created to support super high lift coefficient of CFJ airfoils.

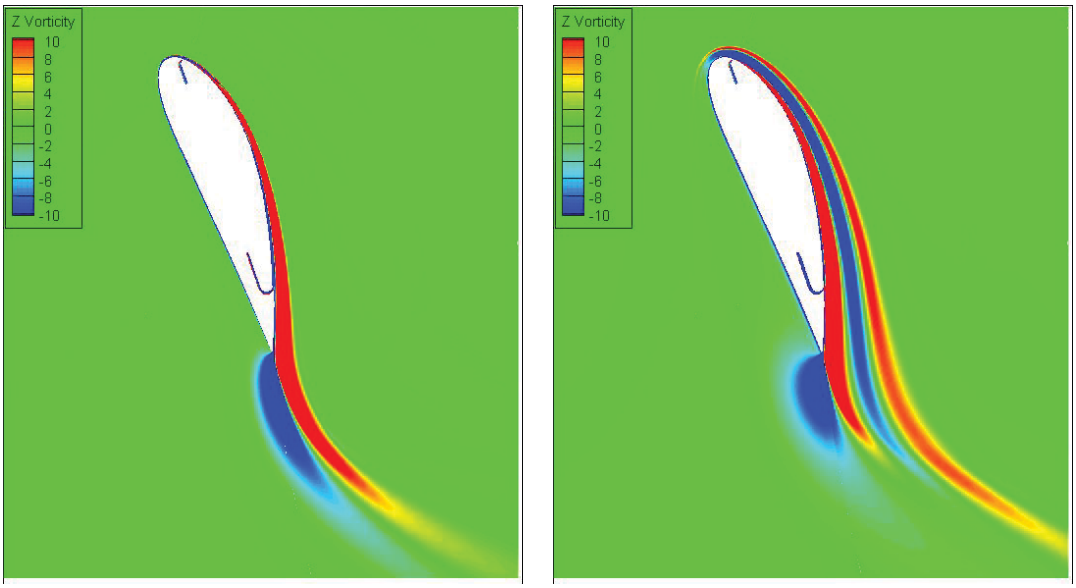

AoA =70°, $C_\mu = 0.25$ AoA =70°, $C_\mu = 0.35$

Figure 7.60: Vorticity contour at $C_\mu = 0.25$, 0.35 and AoA =70°.

Fig. 7.60 shows the spanwise vorticity distribution for $C_\mu = 0.25$ and 0.35 and AoA =70° for CFJ6421-SST016-SUC053-INJ009 airfoil. For different jet momentum coefficient, different flow structures are generated. For the lower C_μ of 0.25, near the suction surface, two distinct strong vortex layers are generated while four vortex layers are produced by the stronger C_μ of 0.35.

The vorticity contours for $C_\mu = 0.25$ and 0.35 and AoA =70° are plotted in Fig. 7.60. It is seen that the vortex layer are split into three different high vorticity regions, which correspond to the jet velocity contours. The near-wall region is bounded by the non-slipping wall surface boundary layer, which generate the clock-wise rotating vortex sheet (Boundary vortex sheet). Due to the high CFJ velocity and the wake velocity from the upstream wall boundary layer, the counter-clockwise CFJ vortex layer is generated downstream the CFJ injection slot. The high intensity CFJ vortex layer induce the clockwise vortex layer. Meanwhile, a mixing layer is generated by the CFJ vortex layer and induced vortex layer. The induced vortex layer travels

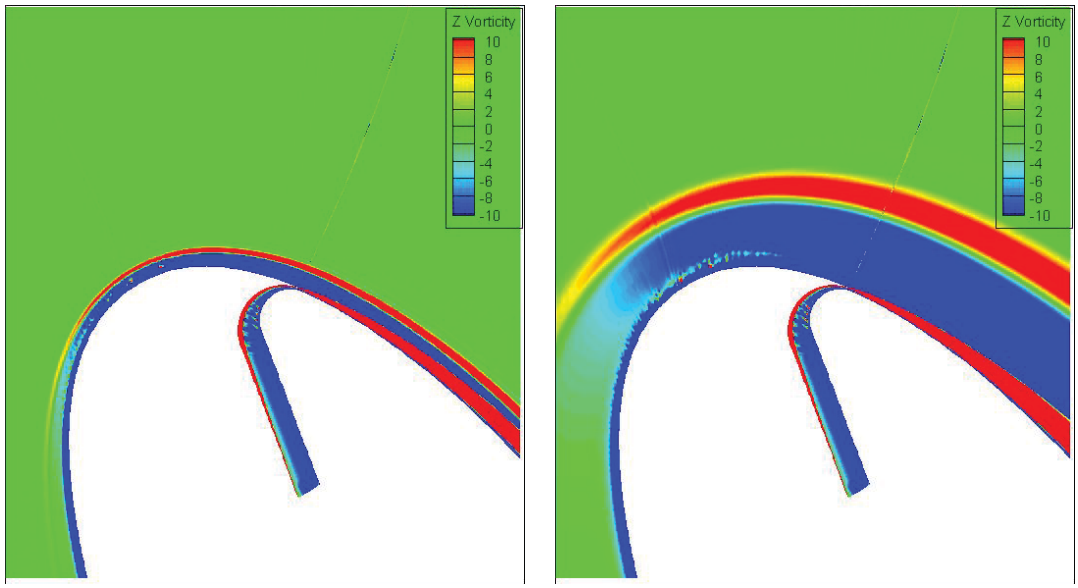

AoA =70°, $C_\mu = 0.25$ AoA =70°, $C_\mu = 0.35$

Figure 7.61: Vorticity contour at the LE for $C_\mu = 0.25$ and 0.35 and AoA =70°.

upstream and produces the high speed secondary induced jet to circulate around the whole airfoil from the stagnation point. Finally, the secondary induced jet decays and mixes with the free stream by generating a transitional vortex layer.

7.5 Conclusion

The present numerical study indicates that CFJ active flow control airfoil is able to achieve the maximum lift coefficient far exceeding the theoretical limit at a very high AoA up to 70°. At the same time, CFJ airfoil is also able to substantially increase the cruise aerodynamic efficiency and productivity efficiency at low AoA due to its increased lift, reduced drag, and very low energy expenditure.

Two CFJ airfoil configurations are created from the baseline NACA 6421 airfoil by translating the suction surface downward and adjusting the injection and suction slot sizes. One CFJ airfoil with smaller injection size is to achieve high C_{Lmax} for takeoff and landing. The other CFJ airfoil with larger injection size is to achieve high cruise efficiency. The first CFJ airfoil (CFJ6421-SST016-SUC053-INJ009) has the suction surface translation of 0.16% C, injection slot size of 0.09% C, and suction slot size of 0.53% C. The maximum lift coefficient of 12.6 is achieved at AoA=70°, M=0.063 and $C_\mu = 0.60$. It is 66% higher than the theoretical limit of 7.6 for a 21% thickness airfoil. The circulation achieved around the CFJ airfoil is so high that the stagnation point is detached from the airfoil solid body and the Kutta condition does not apply anymore. For the super-lift condition at AoA of 70°, the vortex structures in the CFJ injection region appear to include 4 vortex layers next to each other from the airfoil wall surface to the far field freestream : 1) clockwise boundary layer vortex sheet on the airfoil suction surface downstream of the injection slot; 2) counter clockwise CFJ vortex layer due to the high momentum jet and the shear layer shed from the upstream leading edge boundary layer; 3) clockwise induced vortex layer induced by the high momentum co-flow jet via the mixing shear layer. Next to the induced vortex layer is a high momentum secondary induced jet; 4) the last vortex layer is a counter

clockwise vortex layer, through which the secondary induced jet transits to the slower freestream velocity.

The C_{Lmax} appears to have no limit. The C_{Lmax} limit from the potential flow is the result of imposing Kutta condition, which is necessary for potential flow, but not a true physical condition that realistic flows must satisfy. In reality, C_{Lmax} depends on how much energy can be added to the flow, which varies with the active flow control method. This study indicates that the C_{Lmax} is correlated very well with the CFJ power coefficient. The C_{Lmax} increase is very sensitive to energy addition when the C_{Lmax} is at low level. There is almost a linear relationship between the C_{Lmax} increase and the CFJ power consumed at low C_{Lmax} level. The C_{Lmax} eventually becomes plateaued even with continuously increased consumption of CFJ power. This is because when the C_{Lmax} is very high, it is very difficult to add more energy to the flow due to the very severe adverse pressure gradient. How to make an AFC to achieve the highest C_{Lmax} at the lowest energy expenditure is a very interesting research topic.

A new parameter named productivity efficiency defined as C_L^2/C_D is introduced to measure the cruise transportation capability of aircraft to carry its total weight for maximum distance. The second CFJ airfoil (CFJ6421-SST143-SUC133-INJ065) is redesigned with slightly modified leading edge radius, and has the SST of 1.43%C, INJ of 0.65% C, and SUC of 1.33 % C. For the second CFJ airfoil with an assumed CFJ pumping efficiency of 80%, the peak aerodynamic efficiency $(L/D)_c$ is about 53% higher than that of the baseline airfoil. The productivity efficiency $(C_L^2/C_D)_c$ of the CFJ airfoil is 109% higher. The CFJ airfoil is demonstrated by validated numerical simulation to be able to achieve super-lift coefficient for ESTOL performance at

takeoff/landing at very high angle of attack and ultra-high efficiency for cruise at low angel of attack.

The parametric trade study is conducted to achieve the best performance CFJ airfoil. To improve the lift enhancement of CFJ airfoil, smaller injection slot size and smaller SST are desired to obtain high jet velocity near the leading edge. The suction slot size should be designed carefully, for the suction force should be strong attach the flow It is also important to avoid the choked condition and flow separation inside the suction slot. One CFJ airfoil with smaller injection size is to achieve high C_{Lmax} for takeoff and landing. The other CFJ airfoil with larger injection size is to achieve high cruise efficiency. On the other hand, to improve the cruise efficiency, the injection and suction slot sizes should be increased to reduce the power consumption, which is determined by the total pressure in the injection and suction cavity.

CHAPTER 8

IDDES Simulation of a Super-Lifting CFJ Airfoil

8.1 3D IDDES Simulation of Super-Lifting CFJ Airfoil

Chapter 7 gives a 2D RANS simulation of super-lifting CFJ airfoil. It indicates that a very high circulation detaches the stagnation point from the airfoil. The trailing edge vortex creates an extended virtual body to form a high-pressure region due to the stagnant flow to support the airfoil with a super-lift coefficient. The turbulent mixing and entrainment between the jet and main flow, energize the wall boundary-layer. It dramatically increases the circulation, augmenting lift, and reducing the total drag (or generates thrust) by filling the wake velocity deficit. The CFJ airfoil has a unique low energy expenditure mechanism because the jet gets injected at the leading edge suction peak location, where the main flow pressure is the lowest and makes it easy to eject the flow, and it gets sucked at near the trailing edge, where the main flow pressure is the highest and makes it easy to withdraw the flow.

Though 2D Reynolds-averaged Navier-Strokes (RANS) simulation reveals the steady state large flow structures, the three-dimensional turbulent vortex flow structures and

turbulent mixing process can not be well resolved by the RANS simulation due to its assumption of universal scale filtering. As an alternative, large eddy simulation (LES) is a more accurate approach to resolve the large turbulent flow structures and shear layer and reveal the flow mixing mechanisms. LES directly simulates the large eddies and models the small eddies that are more isotropic. However, LES requires very expensive computational resources. The hybrid RANS/LES approach is a promising compromise for engineering applications by taking the advantages of RANS's high efficiency within the wall boundary layers and LES's high accuracy with large flow structures outside of boundary layers [146]. Therefore, the improved delayed detached eddy simulation (IDDES) is employed in this study to investigate the baseline and super-lift CFJ flows at high angle of attacks.

The objective of this chapter is two folds: 1) to demonstrate the maximum lift coefficient capability of the CFJ airfoil using IDDES. 2) To investigate the vortical flow structures of the CFJ airfoil that sustains extremely severe adverse pressure gradient at high AoAs to obtain super-lift coefficient.

8.2 Results and Discussion

8.2.1 Computational Mesh and Flow Conditions

The 3D multiblock structured meshes are constructed using the O-mesh topology in order to achieve high mesh quality near airfoil wall surfaces. The total number of 2001 grid points are placed around the airfoil, 601 points on the lower surface, 1401 points on the upper surface, 181 points normal to the airfoil, and 51 points in the spanwise direction. For the CFJ flow domain, an additional 41 points across the jet

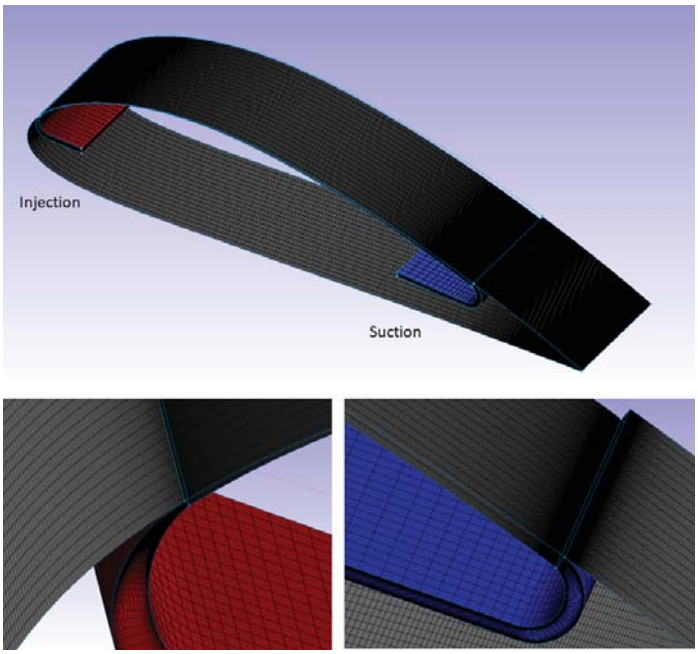

Figure 8.1: Computational mesh for IDDES calculation

is placed in the CFJ injection and suction slot. The total mesh size is 20,880,000 cells and is partitioned into 348 blocks for parallel computation. The far-field boundary is located 15 chords away from the airfoil. The CFJ wing span is 0.1 chord with the periodic boundary conditions applied in the spanwise direction. To resolve the turbulent boundary layer, the first grid point is placed at $y^+ \approx 1$. The mesh block information is available in Table 8.2 and the mesh topology is shown in Fig. 8.1.

Table 8.1: Computational parameters for IDDES study of CFJ6421 airfoil

cases	Mach	Re	Δx	Δy_1	Δz	Δx^+	Δy_1^+	Δz^+
baseline	0.028	$4.8e^5$	$1e^{-3}$	$5e^{-6}$	$2e^{-3}$	33.3	0.17	66.6
CFJ	0.028	$4.8e^5$	$1e^{-3}$	$5e^{-6}$	$2e^{-3}$	33.3	0.17	66.6

The CFJ airfoil configurations are created from the baseline NACA 6421 airfoil by translating the suction surface downward, which is defined as the suction surface translation (SST). The CFJ injection and suction slot sizes are obtained by 2D trade study to achieve high lift coefficient for take-off and landing and high cruise efficiency.

Table 8.2: Mesh details for CFJ6421 airfoil

Block	ξ-Direction	η-Direction	ζ-Direction	Cell number	location
1-300	20	60	50	60000	around the airfoil
301-304	20	60	50	60000	Injection block
305-344	20	60	50	60000	Connection
345-348	20	60	50	60000	Suction block
Total mesh size				20,880,000	

Fig. 7.7 shows the illustration of CFJ airfoil parameters, i.e., SSTs, injection slot sizes and suction slot sizes [147].

Table 8.3: CFJ-NACA6421 airfoil geometry parameters for takeoff/landing and cruise condition

Case	CFJ-NACA6421 airfoil	SST (%C)	INJ slot size (%C)	SUC slot size (%C)
Takeoff/Landing	SST016-SUC053-INJ009	0.16	0.09	0.53

Table 11.1 gives the detailed parameters of the CFJ airfoil designed for takeoff/landing including the injection and suction slot size normalized by chord length(C), and the injection jet momentum coefficient used. The 3-digit number in the naming convention stands for the SST distance, injection slot size, and suction slot size normalized by the airfoil chord.

For the IDDES simulation, the normalized physical time step of 0.02 and the CFL number of 5 is applied for the pseudo time are used. For the low-speed takeoff/landing simulation, the Mach number is 0.028 and Reynolds number is 4.8×10^5 based on the freestream velocity of 10 m/s. The jet momentum coefficients C_μ= 0.25, 0.35, and 0.50 are selected for the study to obtain the flow structures that can sustain the super-lift coefficient. The simulated angle of attack is set at 62°. The simulation parameters can be found in table 12.1.

8.2.2 CFJ wing at AoA = 62°

Table 8.4: Takeoff/Landing simulation parameters

CFJ NACA6421 airfoil	V_{inf}	Mach number	Reynolds number	AoA	C_μ
SST016-SUC053-INJ009	10m/s	0.028	480,000	62	0.25
SST016-SUC053-INJ009	10m/s	0.028	480,000	62	0.35
SST016-SUC053-INJ009	10m/s	0.028	480,000	62	0.50

Table 8.5: Time-averaged simulation results

CFJ6421 airfoil	AoA	C_μ	C_L	C_D
SST016-SUC053-INJ009	62	0.25	6.72	0.08
SST016-SUC053-INJ009	62	0.35	8.58	0.04
SST016-SUC053-INJ009	62	0.50	9.1	0.21

The lift and drag coefficient history for AoA=62° and C_μ= 0.5 is shown in Fig. 8.2. To obtain the desired C_μ, an iterative method is used to calculate the total pressure P_{tinj} at the injection cavity. The static pressure P_{ssuc} at the suction cavity is computed in the same way to maintain the mass conservation of the CFJ injection and suction. The lift and drag curve are gradually converged to a stable oscillation around the mean value of C_L and C_D after the characteristic time $\bar{t} \approx 200$. The time-averaged lift coefficient is 9.1 and the time-averaged drag coefficient is 0.21. Similar lift and drag coefficient history with physical time iteration is found for the other C_μ, the summarized time-averaged result is in table 8.5.

Fig. 8.3 is the streamlines for the CFJ airfoil at AoA = 62 ° and $C_\mu = 0.50$. The streamlines show that the flow is well attached to the airfoil, which indicates that the flow goes around the airfoil from the trailing edge towards the leading edge on the lower surface and turns back toward the trailing edge on the upper surface. Then the flow direction changes nearly 180° at the leading edge with suction peak velocity. The main flow then mixes with the high momentum CFJ jet and leaves the wing

surface near the trailing edge. The predicted 3D flow field is different from the 2D airfoil flow in that the spanwise vortical flow structures exist. Besides, the IDDES simulation indicates that flow is mildly separated near the trailing edge on the upper surface. Given the three-dimensional turbulent flow features, the exact location of the stagnation point can not be clearly identified as the 2D RANS simulation.

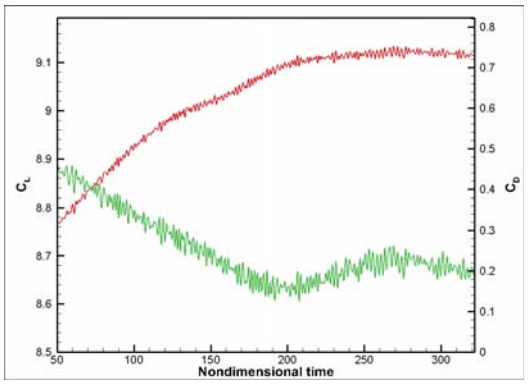

Figure 8.2: Lift and drag coefficient history at AoA = 62 ° and $C\mu = 0.5$.

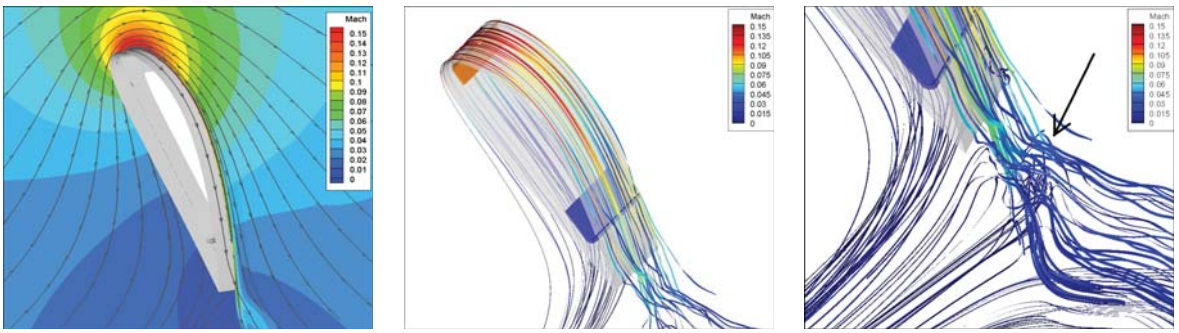

Time-averaged streamlines Instantaneous streamlines near trailing edge

Figure 8.3: The time-averaged and instantaneous streamlines and Mach number contours at AoA = 62 ° and $C_\mu = 0.5$.

The time-averaged and instantaneous Mach contours and streamlines of the CFJ wing at AoA = 62° and $C_\mu = 0.5$ are shown in Fig. 8.3. The time-averaged streamlines indicate that the flow is well attached to the surface throughout the airfoil surface. Therefore, the CFJ flow control can greatly enhance the maximum achievable lift by

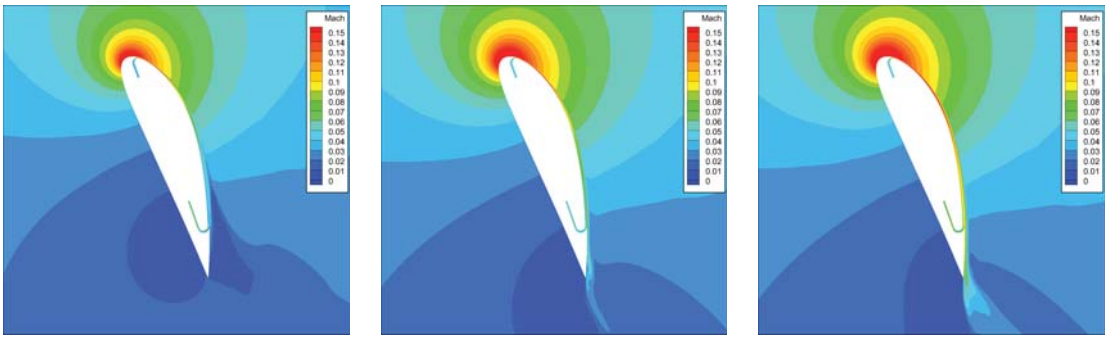

$C_\mu = 0.25$ $C_\mu = 0.35$ $C_\mu = 0.5$

Figure 8.4: Comparison of time-averaged Mach number distribution for different jet momentum coefficient C_μ.

making the flow attached to the wing. The high-speed velocity region is observed near the leading edge with the peak Mach number up to 0.15. The flow acceleration near the leading edge creates a very pressure region, which contributes to the high lift enhancement.

Fig. 8.4 shows the time-averaged Mach number contours of the CFJ wing at AoA = 62° and different C_μ of 0.25, 0.35, and 0.5. All the Mach number contours show that the high-speed flow field near the leading edge. This Mach is much higher than the free stream Mach number of 0.028. The local pressure field is significantly reduced due to the flow acceleration. The CFJ jet emanated from the injection slot creates the high-speed jet throughout the upper surface. For C_μ greater than 0.35, the high speed jet due to CFJ is maintained up to the trailing edge, whereas at C_μ=0.25, the high speed jet is terminated by a small flow separation at trailing edge.

The instantaneous turbulent flow structures represented by Lambda-2 vortex criterion at λ = -100 is shown in Fig. 8.5. Lambda-2 is a negative second eigenvalue of $S_{ik}S_{kj} + \Omega_{ik}\Omega_{kj}$, in which the strain tensor S_{ij} is defined as $0.5(du_i/dx_j + du_j/dx_i)$ and Ω_{ij} is the vorticity tensor defined as $0.5(du_i/dx_j - du_j/dx_i)$, respectively. S_{ij} represents the symmetric component of the velocity gradient tensor related to the

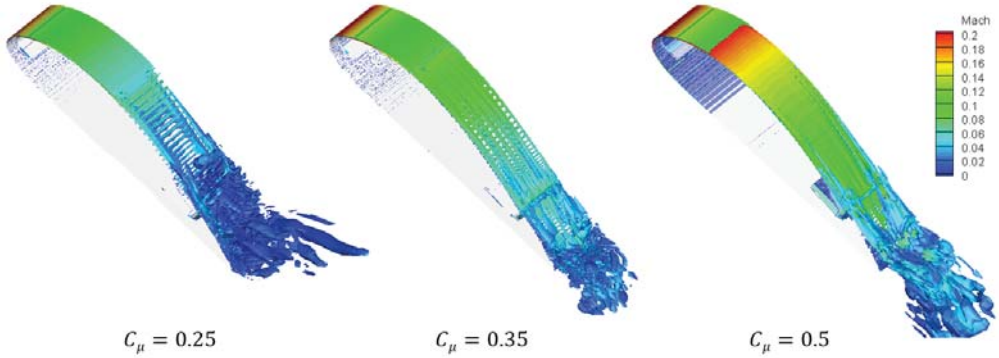

Figure 8.5: Turbulent flow structures of instantaneous flow field using iso-surface of Lambda-2 criterion colored by Mach number for the CFJ wing with different C_μ.

amount of stretching and folding that derives mixing to occur. Ω_{ij} represents the antisymmetric component of the velocity gradient tensor, which determines the vorticity motion. Lambda-2 is used to reflect various scales and structure of turbulent flow from a three-dimensional velocity field. This criterion had been employed by researchers for various cases such as in aerodynamics [148].

The turbulent flow field is obviously very chaotic with a large range of resolved scales of large eddies. The flow structures display different flow patterns for different C_μ. The comparison in Fig. 8.5 highlights the fact that the Lambda-2 vortex criterion clearly depicts the locations where the flow detaches from the surface at the lower C_μ of 0.25. At higher C_μ of 0.35 and 0.5, the flow is attached to the surfaces and leaves the trailing edge with shedding vortices. The large shedding vortices are considered the coherent vortical structure, which could provide the thrust and carry the extra jet energy.

The vortex layer near the injection is illustrated in Fig. 8.6, which is similar to the vortex structures observed in the 2D RANS simulation [147]. The near-wall surface region bounded by the non-slip wall boundary generates a clock-wise boundary layer vortex sheet in blue. The high momentum CFJ forms a counter-clockwise vortex layer

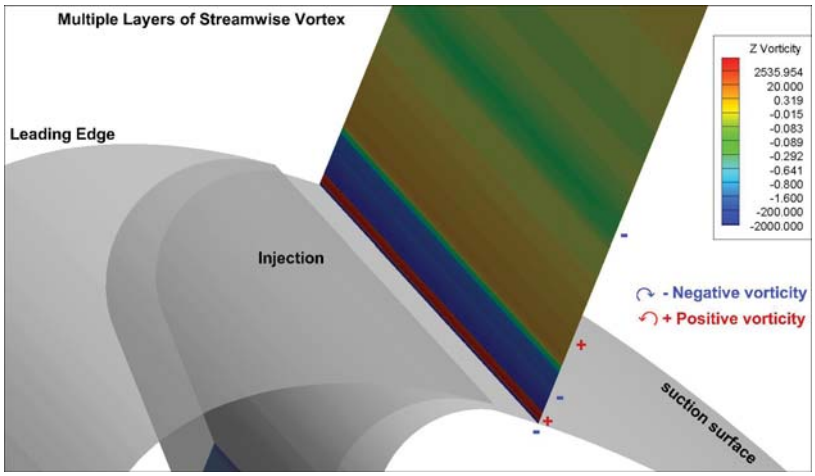

Figure 8.6: Multiple leading edge vortex layers at $C_\mu = 0.5$ and AoA = 62°

is generated downstream the CFJ injection slot. Next to the injection jet mixing layer is a clockwise vortex layer (in red), which is induced by the CFJ via the mixing layer, named induced vortex layer. The induced vortex layer further induces a high-speed jet turning around the leading edge, named as secondary induced jet. The high-speed secondary induced jet creates a counter-clockwise vortex layer to transit the velocity radially to the slower freestream velocity. The last vortex layer is hence named the transitional vortex layer. In general, the clockwise vortex layer contributes to lift generation, and the counter clockwise vortex layer contributes thrust generation.

8.2.3 CFJ-NACA6421 and baseline NACA6421 flows at AoA = 18°

As a comparison for reference, the flow of the baseline NACA6421 and CFJ-NACA6421 airfoil is also simulated by IDDES at the AoA = 18°. The lift and drag coefficient history with non-dimensional time is shown in Fig. 8.7. The time-averaged C_L of IDDES simulation is 1.416 and C_D is 0.149. The simulation results show excellent agreement with the experimental result of $C_L = 1.411$ and $C_D =$

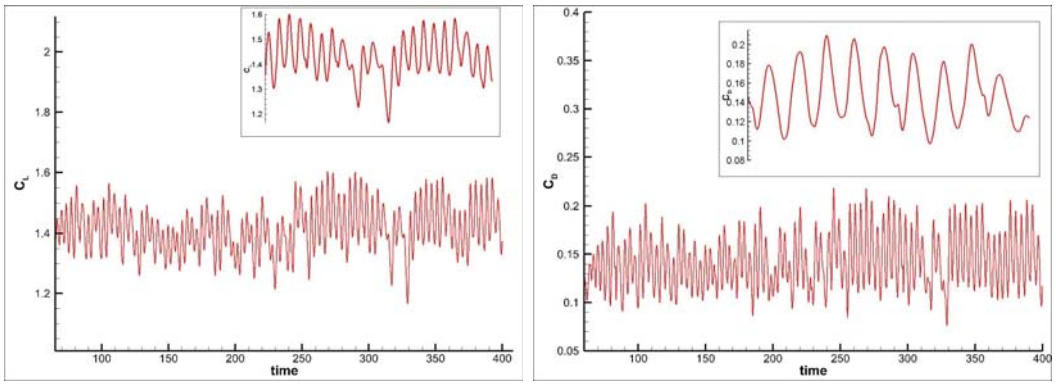

Figure 8.7: Lift and drag coefficient history for the baseline NACA6421 wing at AoA = 18°

0.162 [149]. The discrepancy of C_L is 0.3%. The IDDES simulation demonstrates its high accuracy against experimental results.

Table 8.6: Time-averaged simulation results of NACA6421 airfoil

airfoil	AoA	C_μ	C_L	C_D
NACA6421 Exp.*	17.5	-	1.411	0.149
NACA6421 Sim.	18	-	1.416	0.162
CFJ6421 Sim.	18	0.25	3.8	-0.12

* The experimental data is from NACA TECHNICAL NOTE NO. 392 [149].

Fig. 8.8 shows the instantaneous Mach number contours and streamlines for the turbulent flow of NACA6421 airfoil at AoA = 18°. It is seen that the boundary layer is at its inception of separation, resulting in a very weak recirculation region. Fig. 8.8 depicts the instantaneous turbulent flow structures using the Lambda-2 vortex identification criterion. Large vortical flow structure is created by the mildly separated flow from the upper surface. The boundary layer flow detachment takes place where both the pressure and velocity are relatively low.

To compare the CFJ airfoil flow at the same AoA with the same baseline airfoil, The flow structures of for CFJ-NACA6421 wing at AoA = 18° and C_μ = 0.25 are shown in Fig. 8.10 using the instantaneous Mach number contour and streamlines.

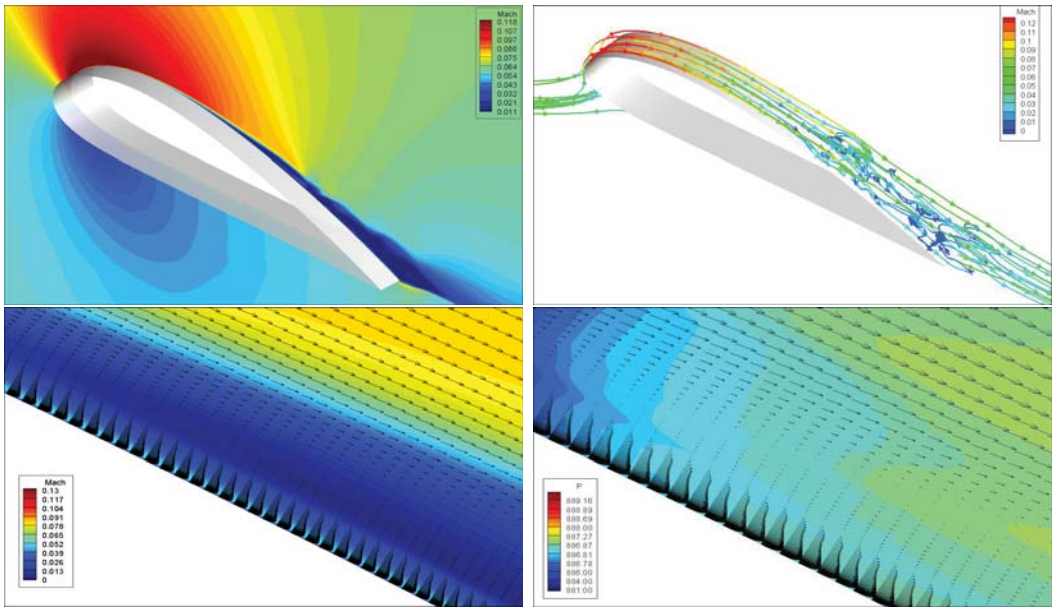

Figure 8.8: Instantaneous Mach number contour with streamlines and vorticity visualized by the Q=5 criterion for the baseline NACA6421 wing at AoA = 18°

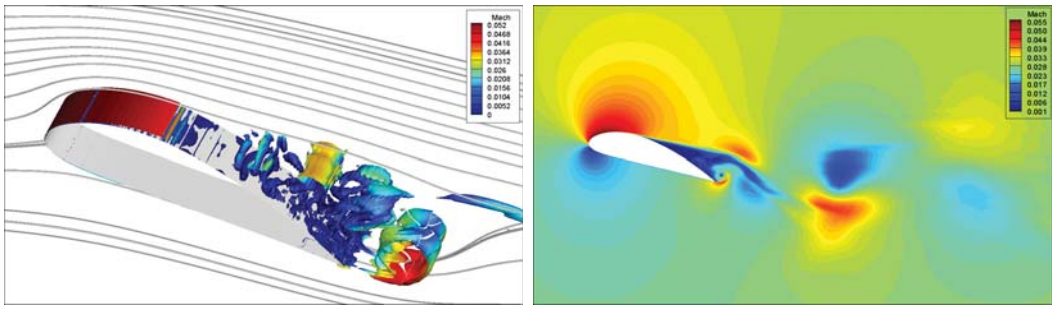

Figure 8.9: Instantaneous turbulent flow structures represented by Lambda-2 criterion λ_2=-100 colored by the Mach number

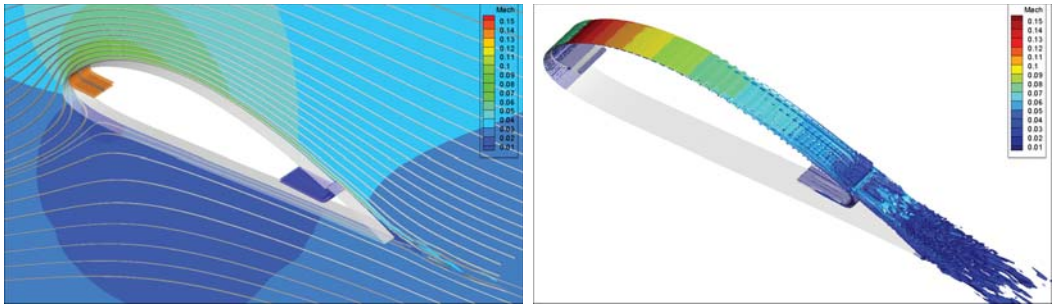

Figure 8.10: Mach number contour and streamlines for CFJ6421 wing at AoA = 18° and C_μ=0.25

The airfoil with CFJ flow control has the flow very well attached with various scale structures near the trailing edge.

8.3 Conclusion

The CFJ flow control airfoil is studied by using IDDES. The three-dimensional flow structures and vortices at high AoAs are investigated. Three different jet momentum coefficient from $C\mu = 0.25$ to $C\mu = 0.5$ simulated at the Mach number of 0.028 and the Reynolds number of 4.8×10^5. The present numerical study indicates that CFJ active flow control airfoil is able to achieve the super-lift coefficient exceeding the theoretical limit at a very high AoAs with attached flow. The super-lift coefficient is achieved by the three-dimensional IDDES study. The qualitative counter-rotating vortex structures at very high AoA and severe adverse pressure gradient is similar to those observed in 2D RANS simulation.

CHAPTER 9

Investigation of Ultra-High Lift CFJ Wing

9.1 3D Ultra-High Lift CFJ Wing

In Chapter 7, a systematic study of RANS simulation of 2D super-lifting CFJ airfoil has been conducted. The CFJ injection and suction slot sizes are iterated with trade study to obtain super lift coefficient for take-off and landing, and high aerodynamic efficiency for cruise condition. In , studied a 3D CFJ wing at cruise and takeoff/landing condition with a fixed configuration. The Lefebvre and Zha [70] studied the 3D flow field of a 3D CFJ wing configuration at takeoff/landing condition. The maximum lift coefficient achieved is 4.7. The super-lifting airfoil is firstly introduced by Yang and Zha [147]. It is beneficial to have larger injection slot size for high cruise efficiency, whereas to achieve Super-Lift coefficient for takeoff/landing, a reduced injection slot size with higher jet speed is more desirable. Based on this concept, a 3D super-lifting CFJ wing is created based on the configuration of 2D super-lifting airfoil. The 3D super-lifting CFJ wing does not use any flaps for lift enhancement. Therefore, one important advantage of CFJ wing is free of the complex and heavy-weight slat and flap system.

The objective of this chapter is to study the 3D super-lifting CFJ wing at different flow conditions. The 3D flow field including the tip-vortex effect on the super-lifting CFJ wing is of particular interest.It is critical to examine the capability of ultra-high lift coefficient generation at takeoff and landing. The study is hence focused only on the angle of attack of 25° and higher up to 70°.

9.2 Results and Discussion

Table 9.1: Computational parameters 3D CFJ wing

cases	Mach	Reynolds	AoA	C_μ
CFJ wing,AR=20	0.063	3,030,000	25°, 45°, 70°	0.15, 0.2, 0.25, 0.3

For the low speed takeoff/landing CFJ wing simulation, the Mach number of 0.063 and Reynolds number of 3.03 million are used. The jet momentum coefficients $C_\mu = 0.15, 0.2, 0.25$, and 0.3 are simulated at different AoAs of 25°, 45° and 70°. The results of the CFJ wing with aspect ratio of 20 is presented first. The 3D effect due to reduced aspect ratio to 10 and 5 are compared after. Table 9.1 summarizes the simulation parameters for the case of AR=20.

9.2.1 Mesh

The 3D structured meshes are constructed using the O-mesh topology in order to achieve high mesh quality within the airfoil boundary. For the wing with aspect ratio of 20, A total of 601 points are placed around the airfoil, 301 points on the upper surface, 301 points on the pressure surface and 121 points normal to the airfoil with an additional 41 points across the jet. The mesh consists of 10,112,000 cells and is partitioned into 216 blocks for parallel computation. The far-field boundary is

located 15 chords away from the airfoil. To resolve the turbulent boundary layer, the first grid point is placed at $y^+ \approx 1$. The block definition is found in Table 9.2 and the mesh topology is shown in Fig. 10.8.

Table 9.2: Mesh details for the CFJ Wing

Block	ξ-Direction	η-Direction	ζ-Direction	Cell number	location
1-180	60	20	40	48000	around the airfoil
181-192	50	24	40	48000	Wing Tip blocks
193-200	20	40	40	32000	Injection blocks
201-208	30	40	40	48000	Connection blocks
209-216	20	40	40	32000	Suction blocks
Total mesh size				10,112,000	

A mesh refinement study was performed for the CFJ6421 wing by adjusting the mesh size in the chord-wise and wall-normal direction, as shown in Table 9.3. The baseline mesh size of $601 \times 151 \times 81$ is placed on the CFJ wing surface. The C_L, C_D results are converged based on mesh size as shown in Table 9.3.

Table 9.3: Mesh independence study for the CFJ6421 wing at AoA=45° and C_μ=0.15.

Case	AoA	Grid size	C_L	C_D
1	45	$301 \times 121 \times 81$	6.18	1.54
2	45	$601 \times 61 \times 81$	4.88	0.47
3	45	$601 \times 121 \times 81$	4.92	0.46
4	45	$1201 \times 121 \times 81$	4.87	0.458

9.2.2 Lift and Drag Coefficient, AR=20

Table 9.4 shows the computed lift and drag coefficients at different AoAs and different jet momentum coefficients. For all the simulated cases, the lift coefficients for CFJ wings are substantially higher than the conventional wings. The lift coefficients

Table 9.4: Lift and drag coefficients at different angle of attacks

AoA	C_μ	C_L	C_D	P_c	L/D	C_L/C_{Dc}	C_L^2/C_D	C_L^2/C_{Dc}
25	0.15	3.392	0.173	0.972	19.6	2.96	66.50	10.048
	0.2	3.566	0.113	1.856	31.55	1.75	112.534	6.458
	0.25	3.74	0.144	2.6762	25.97	1.326	97.14	4.96
45	0.15	4.94	0.46	0.938	10.74	3.53	53.05	17.45
	0.25	5.54	0.497	2.695	11.14	1.735	61.75	9.615
70	0.25	7.26	1.05	2.818	6.91	1.88	50.20	13.65
	0.30	7.81	1.183	4.374	6.6	1.405	51.56	10.976

of 7.26 is obtained at AoA of 70° and $C_\mu = 0.25$. Note that for the 2D airfoil study at this condition, the lift coefficient of 8.3 is achieved. The lift coefficient along the wing span is attenuated toward the wing-tip due to the tip vortex of finite-span wing. Moreover, the drag coefficient is increased to $C_D = 1.05$ compared to the C_D=0.314 in the 2D airfoil simulation.

If we compare the aerodynamic efficiency parameter L/D, the maximum aerodynamic efficiency of 31.55 is achieved at the C_L of 7.26. The obtained aerodynamic efficiency is substantially higher than conventional wing at Takeoff/Landing conditions. As the angle of attack gets higher, the aerodynamic efficiency L/D decreases, since the drag coefficient increases faster than lift coefficient.

Table 9.4 also gives the power efficiency coefficient of the CFJ wing. For takeoff and landing, the aerodynamic efficiency is reduced because of higher drag. Considering the CFJ pumping power, the best corrected aerodynamic efficiency C_L/C_{Dc} of 10.739 is obtained at AoA = 45° and $C_\mu = 0.15$, where the maximum corrected productivity efficiency C_L^2/C_{Dc} of 17.45 is obtained. The reason of the higher efficiency at this condition is that the lift is relatively high, and the power consumption is fairly low. Therefore, the best efficiency point is at AoA=45° and $C_\mu = 0.15$.

Fig. 9.2 shows the comparison of the lift and drag coefficients for 3D wing and 2D airfoil simulation at different $C_\mu = 0.15$ and 0.25. The lift coefficient of the 3D wing with AR of 20 is decreased by 12% compared to the 2D airfoil. The drag coefficient of 3D wing is increased by 234%-244% compared to the 2D airfoil at the jet momentum condition of $C_\mu = 0.25$. As shown in Table 9.4 and Fig. 9.2, the lift coefficient reaches 7.81 at C_μ of 0.3 and AoA of 70°. This coefficient is greater than 7.6, which is the theoretical limit of the 2D airfoil used to form the 3D wing.

9.2.3 High Lift CFJ Wing Flow Structures, AR=20

The CFJ wing streamlines are plotted in Fig. 9.3 at the AoA of 45° and C_μ of 0.25. It indicates that in the inner part of CFJ wing the flow is well aligned with the main flow. The wing tip flow is affected by downwash generated by the roll-up flow from the lower surface to the upper surface. A circulating flow pattern is observed downstream of the wingtip.

Figs. 9.4, 9.5 and 9.6 show the Mach number contours at different spans across the wing at the AoA of $25°, 45°, 70°$ for the wing with AR of 20. The flow is accelerated near the leading edge and is very well attached. The attached flow is induced by the high momentum jet across the wing span except for the wing tip region. Comparing the Mach number contours on the suction surface for three AoAs, the higher the AoAs and C_μs, the higher the peak Mach number near leading edge. It means that the main flow is strongly induced by the mixing effect of the very high-velocity jet. Moreover, considering the wing tip, there exists a region of flow separation induced by the tip vortex. As the AoA increases, the separation region tends to become larger. Because of the roll-up of wingtip vortex, the rotating wingtip flow interacts with the

high-speed jet flow, created the strong interaction and large separation at the wingtip region. The wingtip separated flow could explain the high drag coefficient at high AoA of 70°.

9.2.4 High Lift CFJ Wing Pressure Distribution, AR=20

Figs.9.7, 9.8 and 9.9 shows the pressure contours at different spans across the wing at different AoAs. The pressure on the upper surface of the CFJ wing is substantially lower than conventional wing. The lower pressure region is created by the strong flow acceleration induced by the Co-Flow Jet. The lowest pressure region is observed at near the leading edge, which corresponds to the super-suction effect of the leading edge.

At the wingtip region, the flow is formed by the high-speed co-flow jet and the rolling-up wingtip vortex. The rolling-up flow at the wingtip is enhanced by the very large pressure difference. The air flow rolls up from the lower surface to the upper surface and created the flow separation on the upper surface, thus generating a low-pressure region near the trailing edge. As the AoA gets higher, the separation point becomes closer to the leading edge, and the separation region grows larger. This large low-pressure region on the upper surface accounts for the large drag at high AoA.

To better visualize the flow field, the pressure contours with streamlines at AoA = 45° are plotted in Fig. 9.10. For the streamlines near the tip, due to the extremely high-pressure difference between the upper surface and lower surface, the strong tip vortex is generated in a way that the secondary flow is migrated from the lower surface to the upper surface through the wing-tip region. The tip vortex affects the flow structures on the upper surface and reduce the lift.

The pressure contours on the wing surfaces are shown in Fig. 9.11. For all the CFJ wing simulation, the pressure at the leading edge is very low due to the super-suction effect induced by the CFJ. It contributes to the high lift generated by CFJ wing.

The local lift loading can be seen from the pressure coefficient (C_p) and isentropic Mach number plots M_{is} shown in Figs. 9.12 and 9.13. The spikes at 3% and 80% chord correspond to the injection and suction slot location respectively, where the wing upper surface is discontinuous.

All C_p plots show that the peak pressure coefficient $C_{p_{max}}$ is much higher than the conventional wings with no flow control. For AoA of 70°, the maximum pressure coefficient $C_{p_{max}}$ at the leading edge is greater than 70 with the peak Mach number of 0.65, 10 times higher than the freestream Mach number. The high suction peak near the LE contributes to lift increase and pressure drag reduction. Also, all C_p plots show that the lift loading is fairly uniform in the inner 75% wingspan, while the outer 25% span loading near the wingtip is reduced by the strong wingtip vortex.

To investigate whether the lowest pressure region is located at the leading edge of the wing or inside the tip vortex core, the normalized iso-pressure surfaces with the values of 146, 147, 148, and 149 are plotted in Fig. 9.14 at the AoA of 70° near the tip region. Fig. 9.14 indicates that the lowest pressure is obtained at the wing leading edge.

9.2.5 Induced Drag and Tip Vortex Structures

The vorticity magnitude $|\omega|$ at different crosssection distribution is shown in Fig. 9.15. The vorticity field is formed by the interaction of the CFJ flow and wingtip

flow field. At the plane immediately behind the CFJ wing at $x/c = 1$, the wingtip vortices core is observed. The wingtip flow is majorly composed by the circulating flow in the streamwise vortex as shown in the spiral streamlines in Fig. 9.10. The wingtip vortex core gradually expands and dissipates as flow proceeds downstream. The wingtip vortices spins at very high speed and are regions of very low pressure, as shown in Fig. 9.16.

The wingtip vorticity is connected with the inner vorticity field behind the CFJ wing. The inner CFJ wing vorticity is similar to the 2D CFJ airfoil, which indicates that the inner CFJ is not influenced by the wingtip vortex. Besides, the inner CFJ vorticity is majorly contributed by the spanwise vorticity ω_z.

The streamlines and spanwise vorticity distribution are plotted on Fig. 9.17. The wingtip flow streamlines from the lower surface get across the wingtip and mix with the jet flow and upper surface mainstream.

On the upper surface at the different location, the wingtip streamlines generate different vortices. At the location close to the leading edge, the streamlines mix with the jet and created negative vorticity. The streamlines from near the trailing edge mix with the mainstream flow. The mixed flow rotates and created a counter-directional flow on the upper surface near the trailing edge. Therefore, the vorticity near the trailing edge is positive.

9.2.6 Oswald Efficiency

To investigate the induced drag effect due to the ultra-lift coefficient of the CFJ wing, the Oswald efficiency of the wing is studied with the aspect ratio of 20, 10 and 5. The Oswald efficiency represents the induced drag increase due to lift of a three-

Table 9.5: The zero-lift drag coefficient C_{D0} at different C_μ.

C_μ	AoA	C_{D0}
0.15	-9.5°	-0.056
0.25	-10.5°	-0.106

dimensional wing, as compared with an ideal wing having the same aspect ratio and an elliptical lift distribution. The Oswald efficiency e_0 is defined by the drag polar equation:

$$C_D = C_{D0} + \frac{C_L^2}{\pi e_0 AR} \tag{9.1}$$

where C_D is the total drag coefficient, C_{D0} is the zero lift drag coefficient of the wing. The induced drag coefficient is

$$C_{Di} = \frac{C_L^2}{\pi e_0 AR} \tag{9.2}$$

For conventional fixed-wing with moderate aspect ratio and sweep, Oswald efficiency is typically between 0.7 and 0.85.

The zero-lift drag coefficient C_{D0} varies with the jet momentum coefficient C_μ. In this paper, C_{D0} is calculated by 2D RANS simulation at zero lift with the same C_μ of the 3D CFJ wing. A 2D airfoil naturally does not have induced drag. A comparison conducted in our group for the zero lift drag coefficient of 2D airfoil and 3D wing indicates that the difference is small. Table 9.5 gives the values of C_{D0} and its AoA at different C_μ.

The correlation between the induced drag coefficient C_{Di} and C_L^2 is shown in Fig. 9.18. The induced drag coefficient linearly grows with the square of lift coefficient as shown in Eq. (9.2). The linear correlation between C_{Di} and C_L^2 is observed at different aspect ratio. The slope of linear correlation is decreased with the AR decreased from

Table 9.6: Oswald efficiency e_0 calculated for the finite CFJ wing

C_μ	AR	AoA	C_L	C_D	C_{D0}	Oswald efficiency e_0
0.15	5	25	2.52	0.39	-0.056	0.899
0.15	5	45	3.64	0.92	-0.056	0.865
0.15	10	25	3.03	0.29	-0.056	0.854
0.15	10	45	4.42	0.72	-0.056	0.802
0.15	20	25	3.39	0.17	-0.056	0.800
0.15	20	45	4.94	0.46	-0.056	0.753
0.25	5	25	2.75	0.39	-0.106	0.967
0.25	5	45	3.96	1.07	-0.106	0.849
0.25	10	25	3.32	0.27	-0.106	0.929
0.25	10	45	4.85	0.79	-0.106	0.839
0.25	20	25	3.74	0.14	-0.106	0.890
0.25	20	45	5.54	0.50	-0.106	0.810
0.25	20	70	7.26	1.05	-0.106	0.726

20 to 5. The right plot shows that the at the same C_μ and AoA, the induced drag is smaller for the CFJ wing with higher AR .

Following the equation (9.1), the Oswald efficiency e_0 are calculated for different aspect ratio and C_μ as shown in Table 9.6 and Fig. 9.19. Interestingly, the Oswald efficiency is increased with the AR decreased from 20 to 5 at the same AoA and C_μ. It achieves the value as high as 0.967 for AR of 5, C_μ of 0.25 and AoA of 25°. This value is substantially higher than the Oswald efficiency of conventional wing. If it is proved to be true, it means that the penalty of induced drag for 3D CFJ wing is smaller than the conventional wing even though the total induced drag coefficient is still increased with decreasing AR. The lowest value of the Oswald efficiency is 0.726 occurring at aspect ratio =20 with $C_\mu = 0.25$ and AoA = 70°.

9.3 Conclusion

This chapter conducts three-dimensional RANS simulation of Co-Flow Jet wings with different aspect ratios at higher angle of attack and jet momentum C_μ in order to investigate the ultra-high lift performance without using any flaps. The 3D RANS CFD solver employs the Spalart-Allmaras (S-A) one-equation turbulence model, 5th order WENO scheme for the inviscid fluxes, and 4th order central differencing for the viscous terms. The study indicates that CFJ active flow control wing is able to achieve the maximum lift coefficient of 7.8 without flaps at a very high AoA of 70° with fairly good aerodynamic efficiency. For high AoAs, the outer 25% wingspan is affected most by the wingtip vortex contributing the lift reduction and drag increase. The Oswald efficiency is increased with the AR decreased from 20 to 5 at the same AoA and C_μ. It achieves the value as high as 0.967 for AR of 5, C_μ of 0.25 and AoA of 25°, indicating that the penalty of induced drag for 3D CFJ wing is small with decreased aspect ratio even though very high lift coefficient is obtained. The lowest value of the Oswald efficiency is 0.726 occurring at AR of 20, C_μ of 0.25, and AoA of 70°.

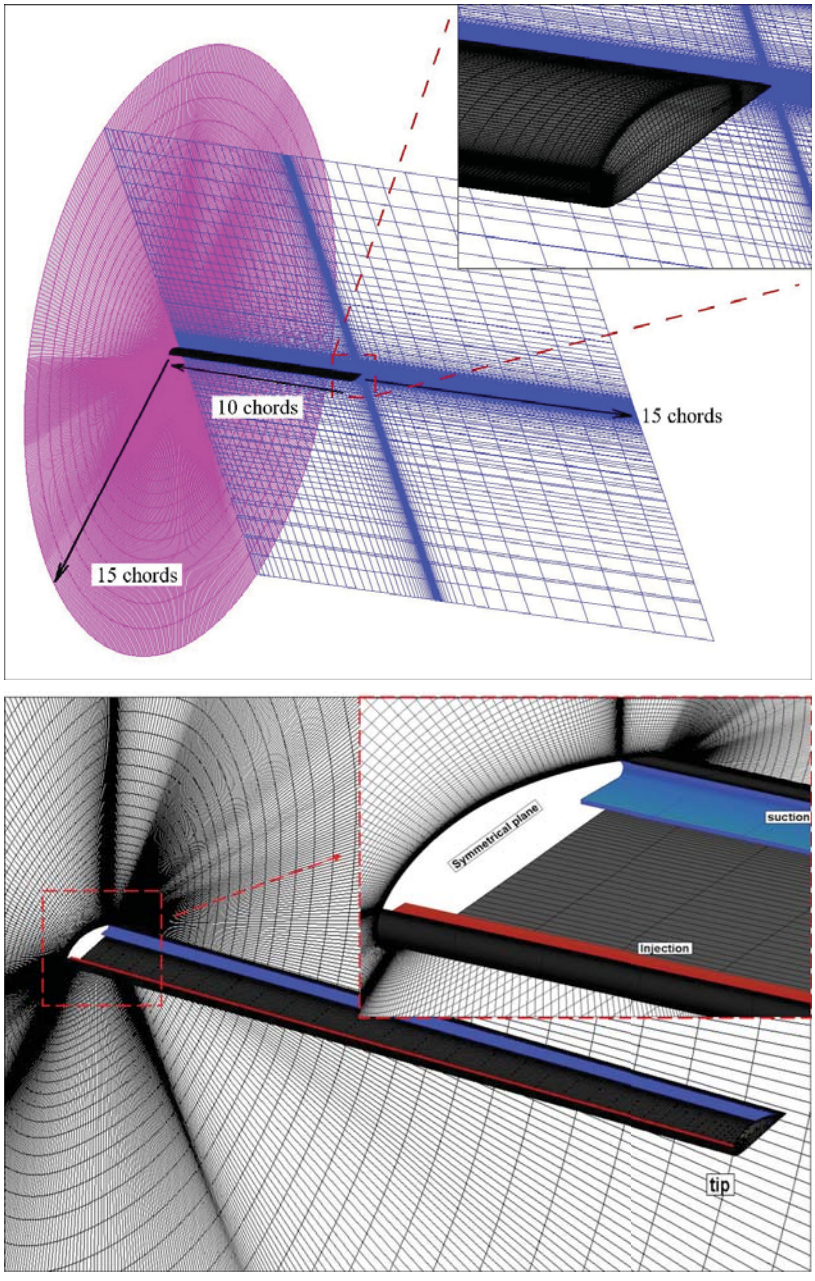

Figure 9.1: Computational mesh

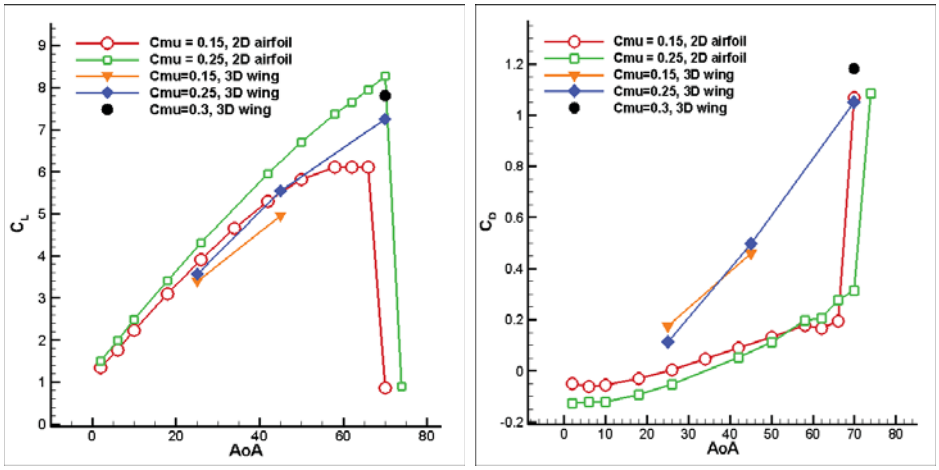

Figure 9.2: Lift and drag coefficient of 3D CFJ wing and 2D airfoil

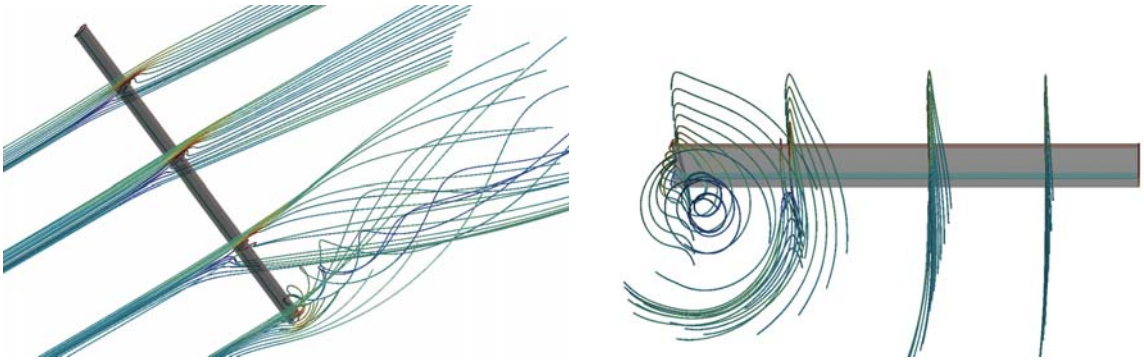

3D streamlines from the top view 3D streamlines from the rear view

Figure 9.3: Three-dimensional streamlines on CFJ wing with finite span

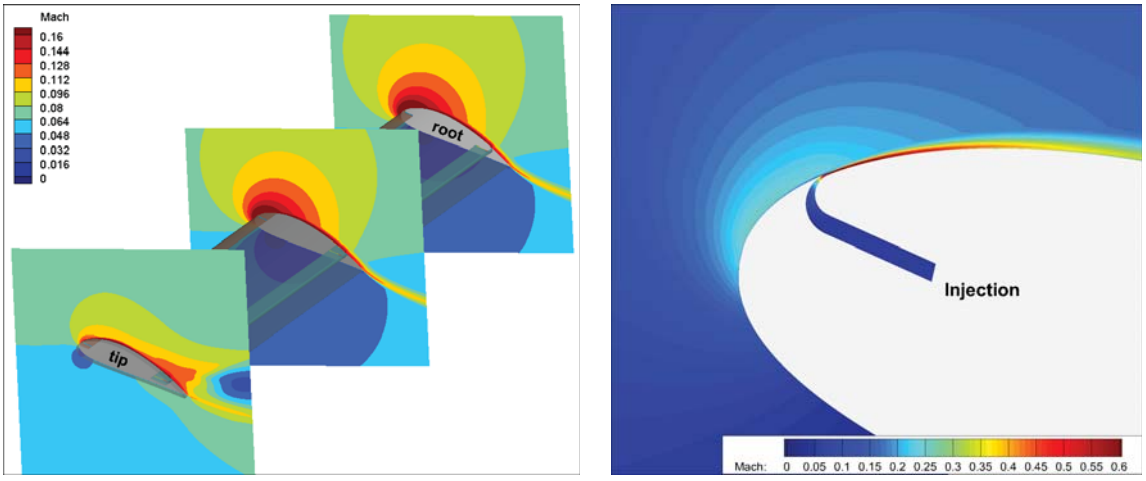

spanwise location: z/s = 0.0, 0.5, 0.99 z/s = 0.5

Figure 9.4: Mach number contours at AoA=25° and C_μ=0.25

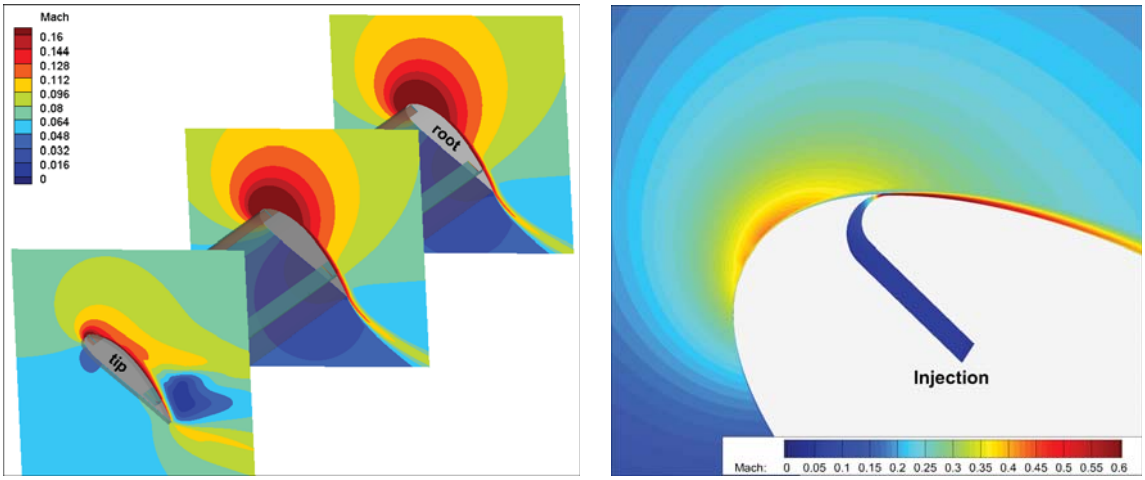

spanwise location: z/s = 0.0, 0.5, 0.99 z/s = 0.5

Figure 9.5: Mach number contours at AoA=45° and C_μ=0.25

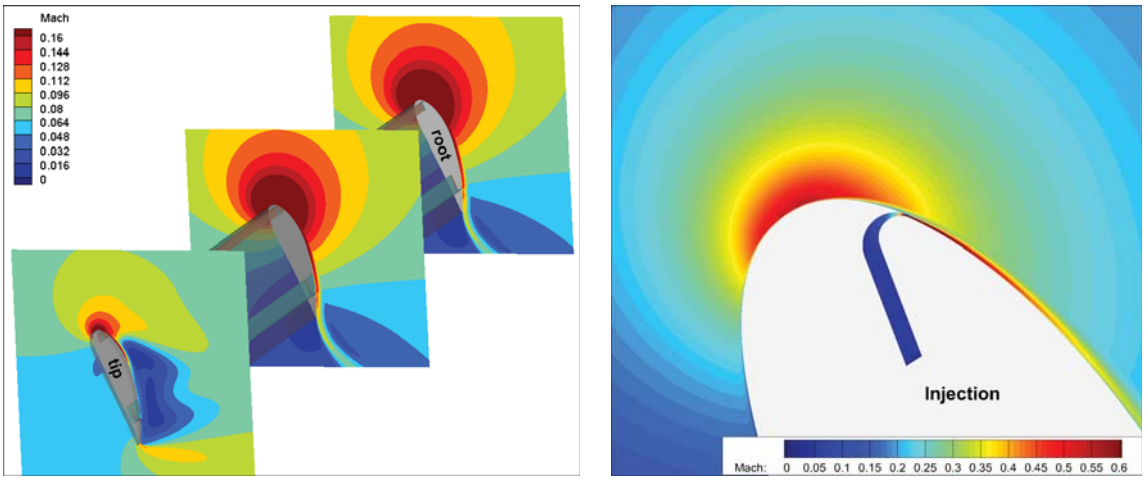

spanwise location: z/s = 0.0, 0.5, 0.99 z/s = 0.5

Figure 9.6: Mach number contours at AoA=70°

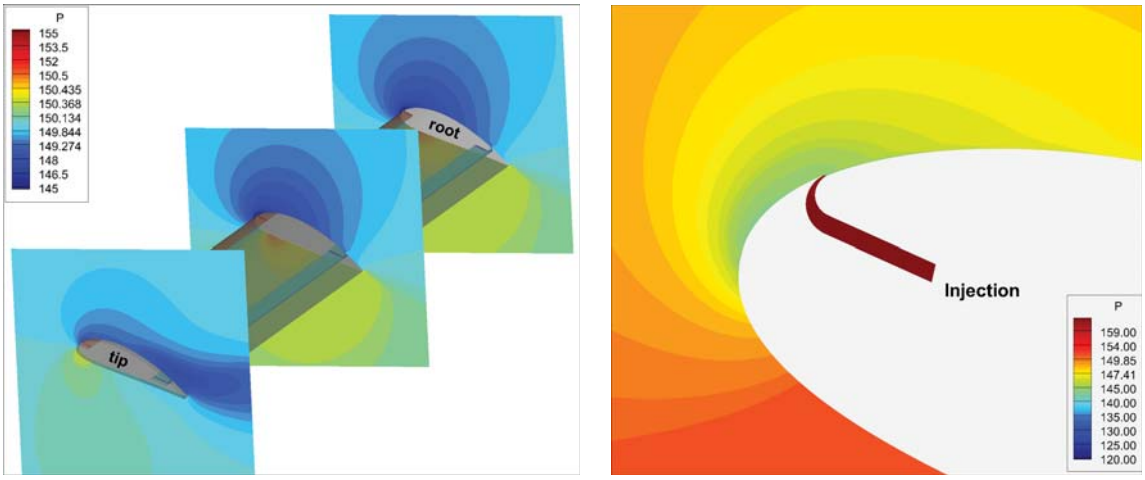

spanwise location: z/s = 0.0, 0.5, 0.99 z/s = 0.5

Figure 9.7: Pressure contours of different spanwise crosssection at AoA=25° and C_μ=0.25

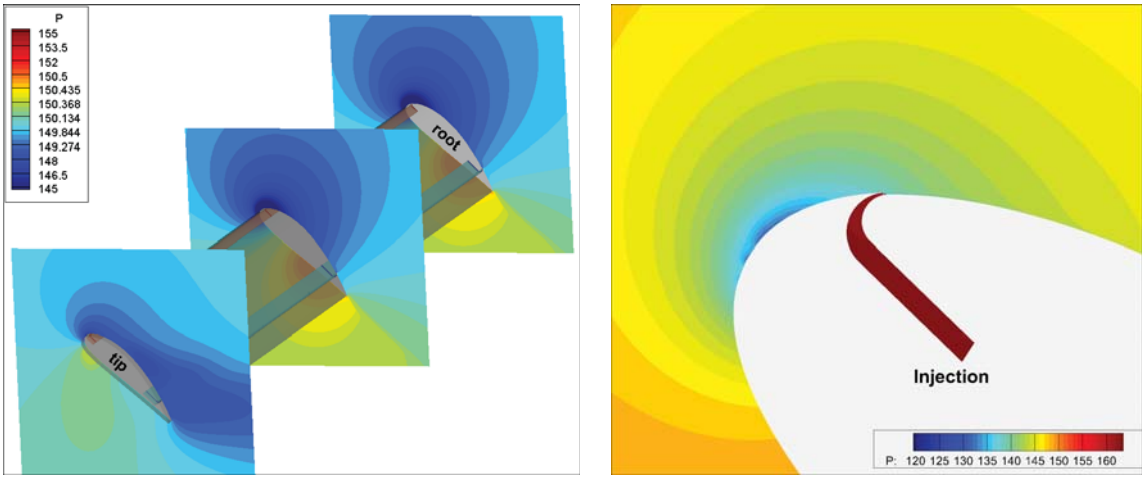

spanwise location: z/s = 0.0, 0.5, 0.99 z/s = 0.5

Figure 9.8: Pressure contours of different spanwise crosssection at AoA=45° and C_μ=0.25

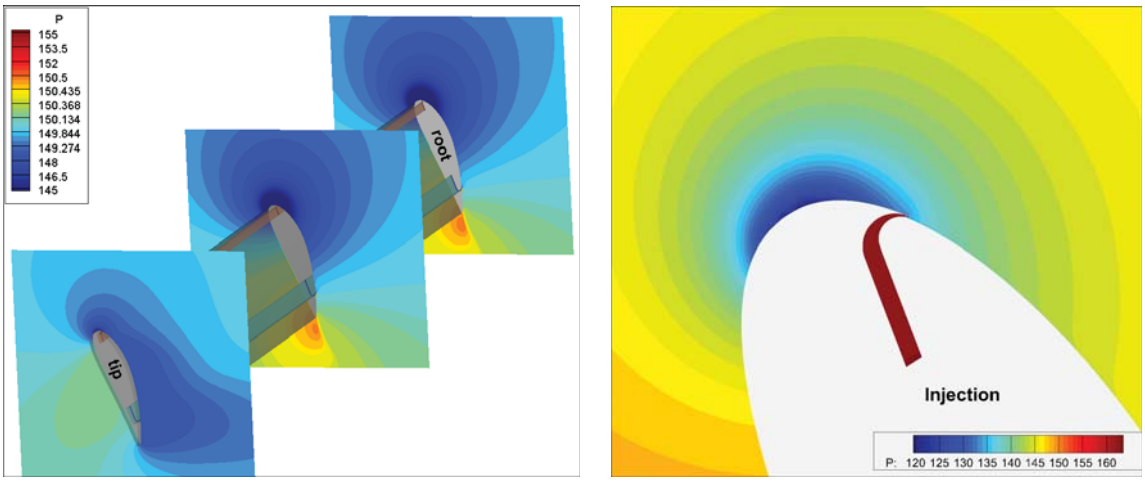

spanwise location: z/s = 0.0, 0.5, 0.99 z/s = 0.5

Figure 9.9: Pressure contours of different spanwise crosssection at AoA=70° and C_μ=0.25

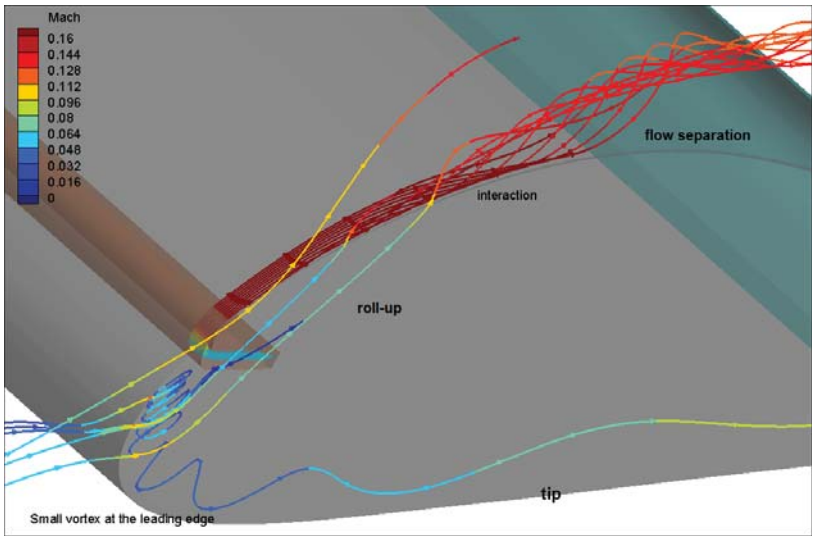

Figure 9.10: streamlines near the wing tip showing the interaction of CFJ and tip vortex

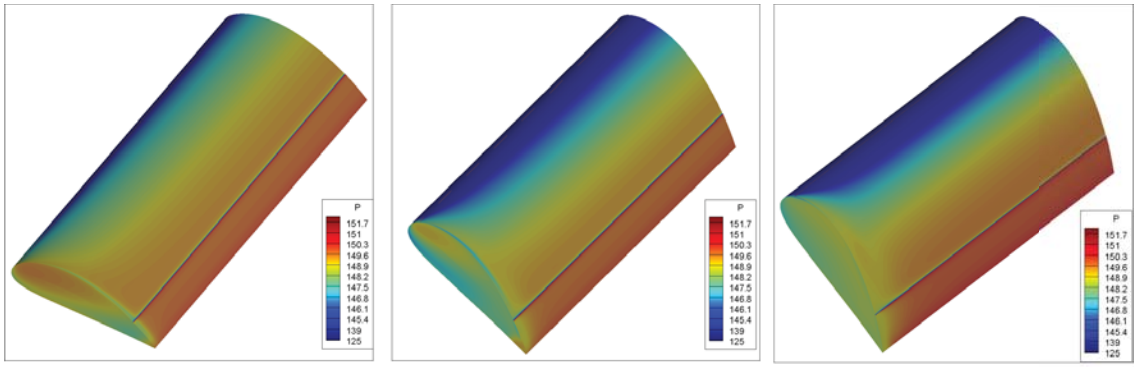

Figure 9.11: Pressure distribution on the wing surface at 3 angles of attack.

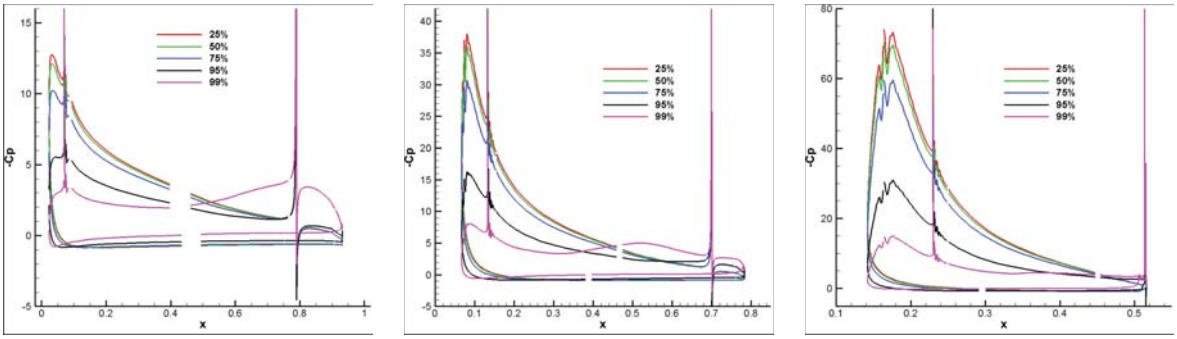

AoA=25 ° AoA=45 ° AoA=70 °

Figure 9.12: Pressure coefficient C_p at different span at the AoA of 25 °, 45 °, and 70 °.

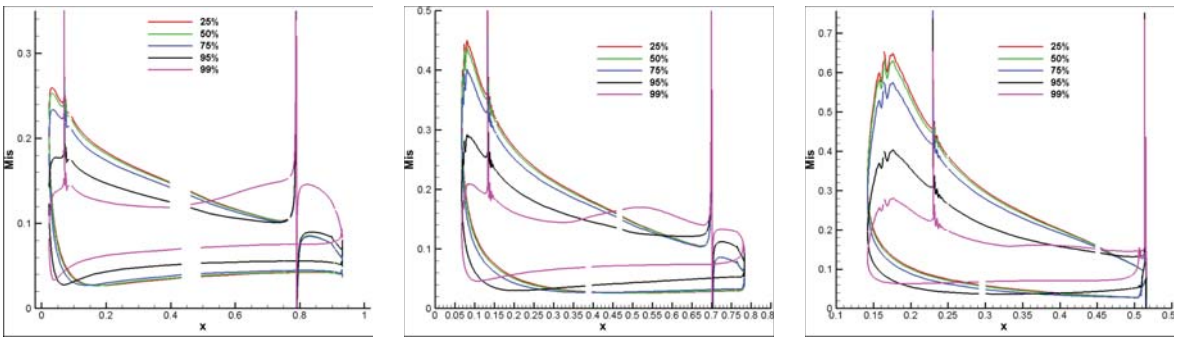

AoA=25 ° AoA=45 ° AoA=70 °

Figure 9.13: Isentropic Mach number M_{is} at different span at the AoA of 25 °, 45 °, and 70 °

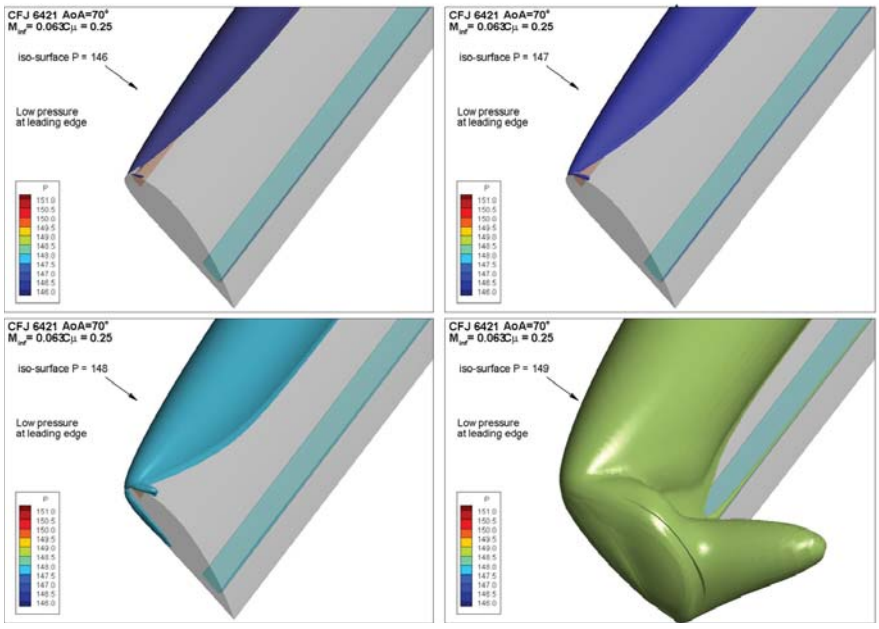

Figure 9.14: Iso-pressure surfaces at the wing-tip

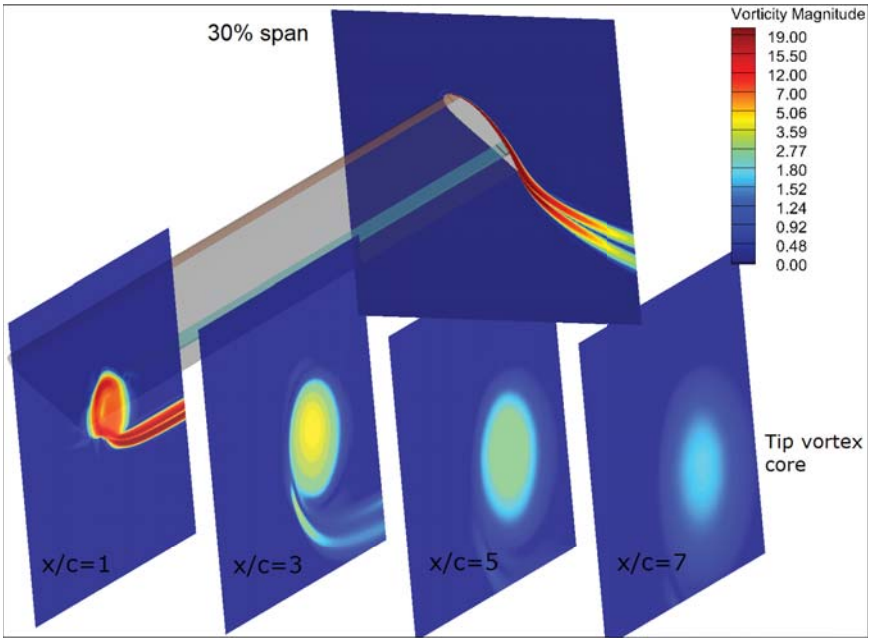

Figure 9.15: Vorticity magnitude distribution at different location of x/chord = 1, 3, 5, and 7.

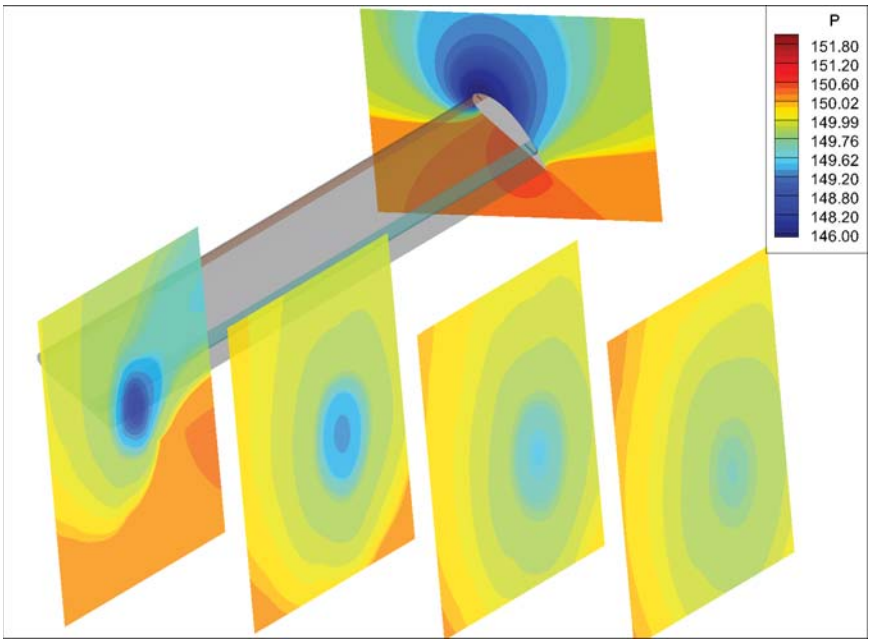

Figure 9.16: Pressure distribution at different crosssection of x/chord = 1, 3, 5, and 7.

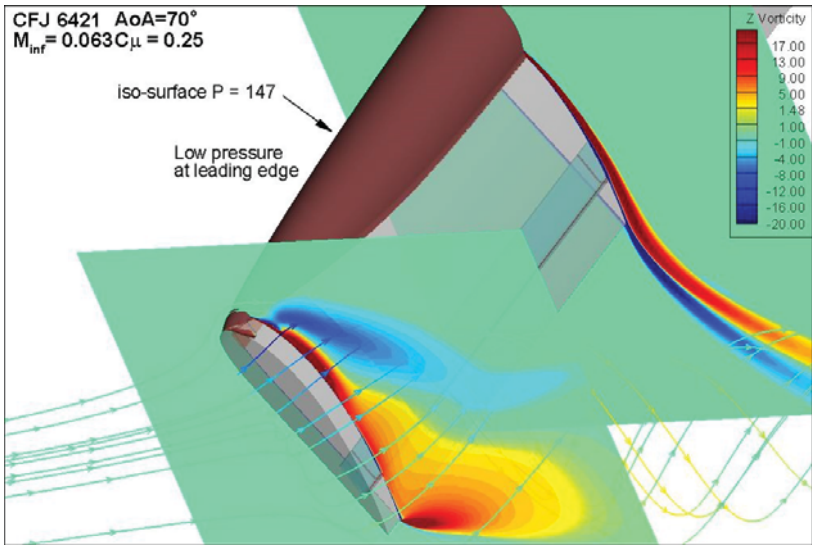

Figure 9.17: Spanwise vorticity ω_z and streamlines at the wingtip

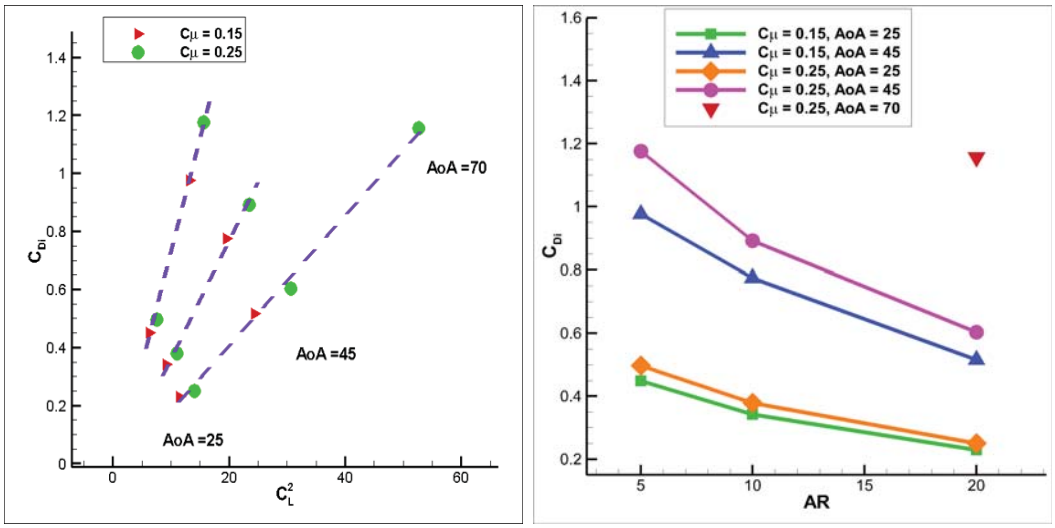

Figure 9.18: Induced drag coefficient C_{Di} vesus C_L^2 (left) and vesus AR (right).

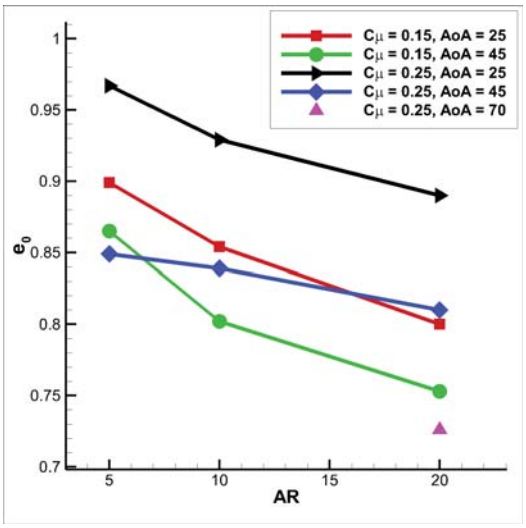

Figure 9.19: Oswald efficiency e_0 vesus aspect ratio AR.

CHAPTER 10

Investigation of CFJ Cylinder

10.1 Maximum Lift Coefficient of a Circular Cylinder

The flow around a circular cylinder has been studied for fundamental fluid mechanics. The investigation of cylinder flows is of great importance in aerodynamics and engineering applications. Prandtl first studied the lift enhancement by rotating cylinder and concluded that the maximum lift coefficient is 4π from his experiment in 1925 (see Fig. 10.1) [128]. A rotating cylinder transfers its mechanical energy to the surrounding flow via viscosity with no-slip wall boundary condition. In the early 1920's, the Flettner rotorship was experimented and tested to generate thrust and improve ship efficiency by the Magnus effect. Those pioneering explorations provide some applications of rotating in the cylinder flows.

In classical aerodynamics, the lifting flow over circular cylinder is obtained by superimposing a uniform flow, a doublet and a vortex, which provide the fundamental of lift generation theorem. The flow field is associated with the ratio of rotating speed, which determines the circulation introduced as shown in Fig. 10.1. The rotating cylinder can be considered the earliest effort of active flow control (AFC) method to

achieve lift enhancement. Researchers studied the fluid dynamics and lift and drag coefficient of rotating cylinder [32, 129, 150, 151]. Many researchers applied rotating cylinders in aeronautics [21, 34, 152–154].

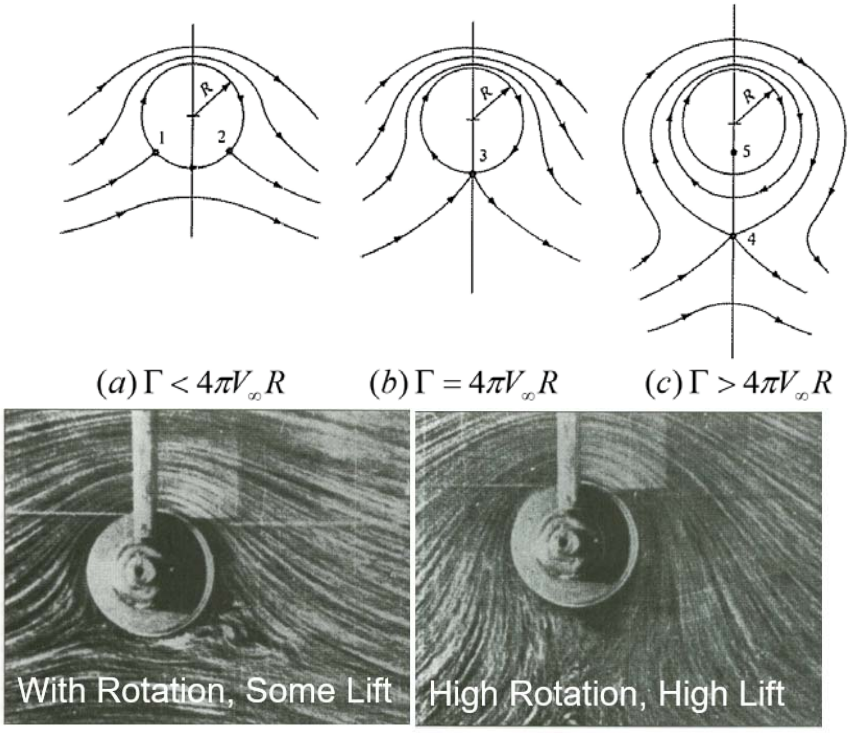

Figure 10.1: Flow field around a rotating cylinder. (Figures are adapted from reference [11]

.

Even though Prandtl suggested that the maximum lift coefficient of 4π is the limit for a rotating cylinder if the Kutta condition must be satisfied. Researchers obtained the lift coefficient that exceeds this limit [32, 129]. In 1960s, Lockwood [33] from NASA Langley conducted experiment of a circular cylinder using tangential blowing and achieved the maximum lift coefficient of $C_L \approx 20$ at high blowing jet of $C_\mu \approx 5$ for a very low Reynolds number flow over an end-plated-cylinder with multiple injection slots (See Fig. 10.4). Tokumaru and Dimotakis in 1993 [32] re-visited the rotating cylinder experiment and obtained the lift coefficient greater than 15 (see Fig. 10.3).

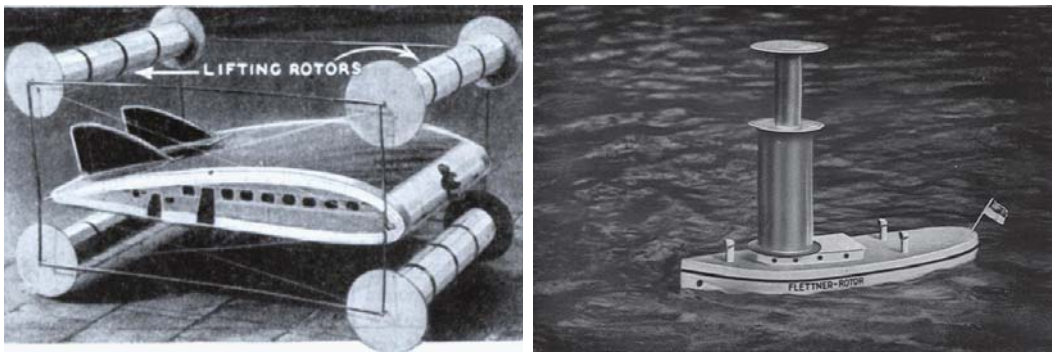

Figure 10.2: Rotating cylinder application examples, rotor airplane concept(left) and sailing boat(right).(Figures are adapted from [34])

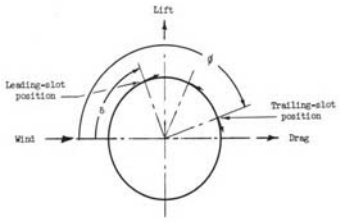

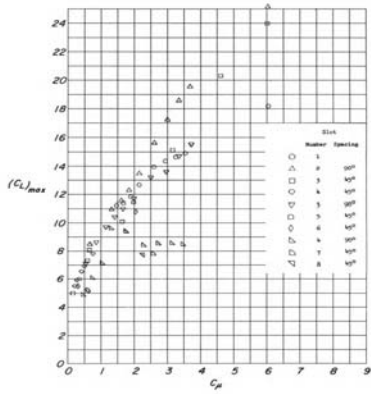

Figure 10.3: Lifting cylinder using tangential blowing from surface slots. (Plot is adopted from [33])

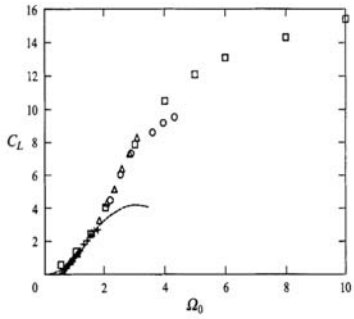

Figure 10.4: Lift coefficient C_L vs cylinder rotating speed in the rotating cylinder experiment. (Plot is adopted from [32])

The rotating cylinder may not be the most effective flow control method to achieve high-lift enhancement, because it requires very large auxiliary energy to rotate a solid cylinder and it is not efficient to transfer the mechanical energy to the flow. Overall, the rotating cylinder and the aforementioned tangential blowing are shown to have very high energy expenditure.

The recent concept of co-flow jet (CFJ) flow control method, developed by Zha et al. [35, 61–69, 147] shows a great potential to exceed the lift coefficient limit with high energy efficiency. The CFJ airfoil achieves a dramatically lift augmentation, drag reduction and stall margin increase at low energy expenditure. The purpose of this paper is to apply the CFJ flow control to circular cylinders in order to enhance

the lift coefficient at low energy cost. In addition, a cylinder flow can be used as a simple example to study the fundamental fluid mechanics associated with the CFJ flow control.

10.1.1 The Co-Flow Jet Concept

The CFJ concept was originated for airfoil flow control. The implementation is to open an injection slot near the leading edge(LE) and a suction slot near the trailing edge(TE) on the airfoil suction surface as sketched in Fig. 10.5. A small amount of mass flow is withdrawn into the airfoil near the TE, pressurized and energized by a pumping system inside the airfoil, and then injected near the LE in the direction tangent to the main flow. The whole process does not add any mass flow to the system and hence is a zero-net mass-flux (ZNMF) flow control. It is a self-contained high lift system with no moving parts.

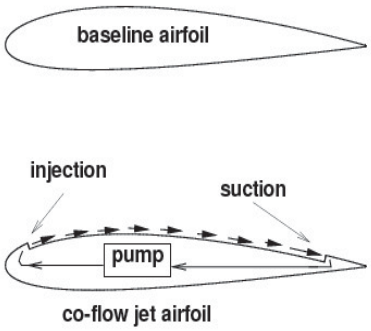

Figure 10.5: Baseline airfoil and CFJ airfoil.

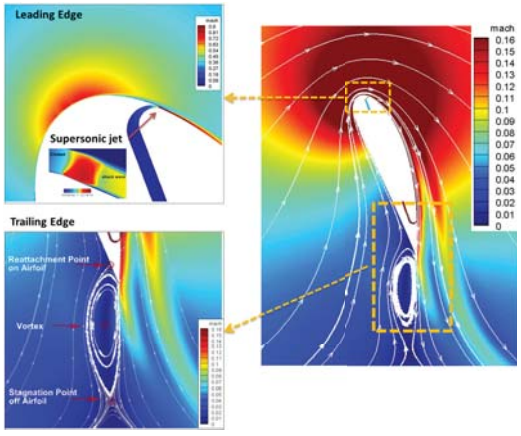

Figure 10.6: Mach number contours and streamlines at $C_\mu = 0.35$ and AoA =70° for the CFJ6421-SST016-SUC053-INJ009 airfoil.

The fundamental mechanism of the CFJ airfoil is that the turbulent mixing between the jet and main flow energizes the wall boundary-layer, which dramatically increases the circulation, augmenting lift, and reducing the total drag(or generates thrust) by filling the wake velocity deficit. The CFJ airfoil has a unique low energy expenditure mechanism because the jet gets injected at the leading edge suction peak location, where the main flow pressure is the lowest and makes it easy to eject the flow, and it gets sucked at near the trailing edge, where the main flow pressure is the highest and makes it easy to withdraw the flow.

Fig. 11.1 from [147] shows the computed flow field of CFJ-NACA6421 airfoil at the AoA of 70° and C_μ of 0.35. The lift coefficient is 10.6, which is greater than the lift limit of 7.6 calculated by Equation (1). The circulation generating the super-lift coefficient is so high that the stagnation point is detached from the airfoil by a large clock-wise vortex beneath the trailing edge. This high momentum jet induction makes the flow attached.

The objective of this paper is two folds: 1) to explore the maximum lift coefficient capability of the CFJ flow control on circular cylinder. It is also our interest to study the energy expenditure as compared to the rotating cylinder technique. 2) To conduct parametric study for the CFJ flow control on circular cylinder to identify the optimal injection and suction geometry and jet momentum coefficient

10.1.2 Geometry and Mesh

From the potential flow theory, to achieve the super-lift coefficient, the flow stagnation point should be detached from the surface as shown in flow field in Fig. 10.7. However, for a circular cylinder, the vortex shedding usually starts near the very top

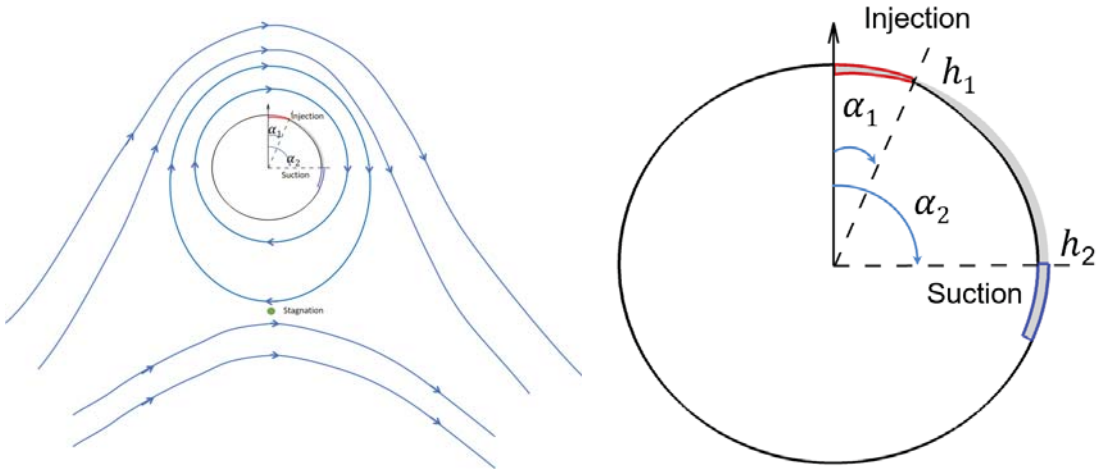

Figure 10.7: CFJ flow control illustration on circular cylinder

and bottom points and forms a large wake behind the cylinder. The intuition is thus to apply the CFJ on the downstream side of the cylinder near the very top and bottom point to remove flow separation by energizing the wake flow. The geometry parameters for CFJ flow control on cylinder are hence defined as injection slot location α_1 and slot size h_1 and suction slot location α_2 and slot size h_2 as illustrate in Fig. 10.7. Please note that the slot location angle is measured from y-axis. If $\alpha_1 = 0$, it means the injection slot is located at the very top position. Table 11.1 shows several CFJ cylinder geometries with varied geometry parameters for trade study. The injection and suction slot size is normalized by the cylinder diameter.

The 2D structured meshes are constructed using the O-mesh topology in order to achieve high mesh quality on cylinder surface. A total of 1601 grid points are placed around the cylinder and 121 points normal to the wall surface with an additional 41 grid points across the jet slot. The total mesh size is 216,000 cells, and is partitioned into 7 blocks for parallel computation. The farfield boundary is located about 60 reference length (diameter) away from the cylinder. To resolve the turbulent boundary

Table 10.1: Geometry parameters for the CFJ cylinder.

Cases	Injection slot location $\alpha_1(^\circ)$	Injection slot size (%)	Suction slot location $\alpha_2(^\circ)$	Suction slot size (%)
1	0	0.125	90	1
2	0	0.125	135	1
3	0	0.125	180	1
4	15	0.125	135	1
5	-15	0.125	135	1
6	0	0.25	135	1
7	0	0.5	135	1
8	0	0.125	135	0.5
9	0	0.125	135	2

layer, the first grid point is placed at $y^+ \approx 1$. The block information is found in Table 10.2 and the mesh topology is shown in Fig. 10.8.

Table 10.2: Grid size distribution CFJ cylinder

Block	ξ-Direction	η-Direction	Cell number	location
1-4	401	121	48000	around the cylinder
5	101	41	4000	Injection block
6	401	41	16000	Connection
7	101	41	4000	Suction block
Total mesh size			216000	

10.2 Results and Discussion

The numerical investigation of stationary circular cylinder at the Reynolds number of $Re = 3.03 \times 10^6$ is conducted to validate the computational code. The pressure coefficient C_p are plotted with the azimuth angle in Fig. 10.9. The relevant experimental results are available at Re near 1×10^6. The steady RANS simulation predicted results agrees well with the experiment with some deviation. The deviation is due to

the intrinsic feature of RANS simulation, which filters unsteady and turbulent flow energy. The streamlines are given in Fig. 10.10.

10.2.1 CFJ Cylinder Trade Study

In this section, a parametric trade study is conducted to evaluate the influence of the CFJ airfoil geometry parameters, including the suction slot size h_2, suction location α_1, injection slot size h_1, and injection location α_1. The flow simulation parameters are as listed in table 10.3. For the CFD simulation, the Mach number of 0.063 and Reynolds number of 3.03 million are used.

Table 10.3: Simulation parameters for CFJ cylinder

Mach number	Reynolds number	C_μ
0.063	3,030,000	0.2-0.8

10.2.1.1 Suction Location

Three suction slot locations are used, 90°, 135°, and 180°. The jet momentum coefficients C_μ varies from 0.2 to 0.8. The case 1, 2 and 3 in Table 11.1 are described in this section with the injection slot fixed at 0° location.

Fig. 10.11 shows the computed lift and drag coefficients with different jet momentum coefficients. The lift coefficient increases with C_μ for all three configurations with different suction slot locations. For the same C_μ, the lift coefficient is higher for the suction location of $\alpha_2 = 135°$. For all the three configurations, the lift coefficient is greater than 15.0 when C_μ is greater than 0.7. When C_μ is 0.8, both the suction location at 90° and 135° reach the C_L of 28. The suction location at 180° has the C_L slightly lower with the value of 27. The maximum lift coefficients for the CFJ

cylinder at $\alpha_2 = 135°$ are increased dramatically to 28 at $C_\mu = 0.8$. Obviously, the lift coefficient of CFJ cylinder easily exceeds the theoretical limit of $4\pi = 12.56$ by far.

The drag coefficients of the CFJ cylinder are largely varied with the suction slot location. The negative drag coefficient is the thrust created by the CFJ power introduction. For the suction slot location at $\alpha_2 = 180°$, a very large thrust (negative drag) is generated attributed to the horizontal placement of the suction slot, which generates all the suction impulse in the thrust direction as shown in Eq. (1). Since the injection slot is located at the 0° location for all the cases studied in this section, the injection jet has all the impulse always in the thrust direction.

For the corrected aerodynamic efficiency C_L/C_{Dc} in Fig. 10.12, a CFJ cylinder has comparatively high values for such high lift coefficients. The maximum value of $C_L/C_{Dc} = 6.0$ is obtained at $C_\mu = 0.4$ with the suction slot location of $\alpha_2 = 135°$. The lift coefficient of 19.5 is obtained at the best efficiency point. At high C_μ, since the flow can not absorb more energy and the flow in the suction slot becomes choked, the higher C_μ will decrease the aerodynamic efficiency. The high lift contribution to the productivity efficiency is reflected by C_L^2/C_D in Fig. 10.13. The maximum productivity efficiency of about 155 is obtained by the suction location at 135° and C_μ of 0.3.

The power coefficients of the CFJ pumping are calculated based on Eq. (5.12) and (5.13) using a constant pumping efficiency value of 100%. The results are shown in Fig. 10.14. The power coefficient increase rapidly with C_μ. Fig. 10.15 is the total pressure ratio PR calculated by the ratio of the total pressures at the injection and suction cavity. The CFJ pumping power is largely determined by the total pressure

ratio PR between the injection and suction cavity. The total pressure ratio PR has a similar variation trend to the power coefficient with the injection jet momentum coefficient.

Flow Structures

Fig. 10.16 displays a qualitative comparison of the streamlines and Mach number contours at different jet momentum coefficient C_μ at the suction location of $\alpha_2 = 135°$. At the lower jet momentum coefficient $C_\mu = 0.2$, there are two stagnation points attached on the solid surface (see Fig. 10.16(a)). Both the upstream and downstream stagnation points are located at the lower surface of cylinder. The flow pattern represents the small circulation introduced in the flow. The downstream stagnation point is observed near the suction slot, where the flow from the lower surface and the upper surface collides. The flow direction is changed drastically around the second stagnation point with the reversed flow from the lower surface near the suction slot (see Fig. 10.16(b)). As the jet momentum coefficient is increased and the jet becomes larger, the two stagnation points are merged and form the single stagnation point detached from the solid surface (see Fig. 10.16(c-d)). . Increasing the jet momentum coefficient drives the stagnation point further away from the cylinder.

For all three suction configurations of Case 1, 2, and 3 at $C_\mu = 0.3$, the Mach contours and streamlines are shown in Fig. 10.17. With the CFJ jet flow mixing, the flow field is fully attached to the surface and creates very large circulation around the cylinder surface. The stagnation point is far detached from the solid surface. The upstream incoming flow follows front cylinder surface, turns around the top surface by 180°, and is nicely attached to the rear surface due to the strong induction effect from the high momentum co-flow jet. Note that the stagnation point location is a little

different for three different suction slot locations. For $\alpha_2 = 135°$, the stagnation point is located exactly on the y-axis below the cylinder at the length of 1.5 diameter and $x_{stagnation} = 0$ (the middle plot of Fig. 10.17). When the suction slot is located at the lowest point of the cylinder at $\alpha_2 = 180°$, the stagnation point is shifted upstream to $x_{stagnation} = -0.15$. For the suction slot located at $\alpha_2 = 90°$, the stagnation point shifts downstream to $x_{stagnation} = 0.15$ (the right plot of Fig. 10.17). This flow stagnation point is driven by the suction slot location by its suction effect. For $\alpha_2 = 180°$, higher suction force is required to make the flow turn 180°. Therefore, the resulting flow field will shift the stagnation point upstream.

Fig. 10.18 shows the computed static pressure contour for the CFJ cylinder at different suction locations. At the top of the cylinder, the super-suction effect is generated with a very low static pressure. Near the bottom of the cylinder, the high pressure regions are obtained by the stagnation areas. The pressure field is almost symmetric about the y-axis for the suction slot located at 135°, which provides slightly highest lift coefficient at $C_\mu = 0.3$ as shown in Fig. 11.

10.2.1.2 Suction Slot Size

Fig. 10.19 is the comparison of lift and drag coefficients among the different suction slot sizes of CFJ flow control cylinder. The baseline CFJ cylinder has a suction size of 2%. The increased suction slot size has a negative effect of lift enhancement at higher $C_\mu > 0.3$. At the lower value of C_μ, the lift coefficient is higher for larger suction slot size. For the drag coefficient, the 4% slot size has a large variation with negative drag at low C_μ and a rapid increase to large positive drag at high C_μ. The 2% slot size is fairly stable with a positive drag at different C_μ.

10.2.1.3 Injection Location

Fig. 10.20 presents the lift and drag coefficients with different injection slot locations. It is obvious that when we move the injection slot away from the very top location, the lift coefficient is reduced, and the drag coefficient is increased.

10.2.1.4 Injection Slot Size

Fig. 10.21 is the simulation results of different injection slot size. It is shown that when the injection slot size is decreased, the lift coefficient is increased at lower C_μ. At higher C_μ, reducing the injection slot size will decrease the lift coefficient. The increased slot size has substantially lower drag.

10.3 Conclusion

This paper investigates the maximum lift coefficient for Co-Flow Jet flow control on cylinder flows. The numerical study indicates that CFJ flow control is able to achieve the maximum lift coefficient far exceeding the theoretical limit. Several CFJ cylinder configurations are created for parametric trade study. The best lift coefficient with highest efficiency is obtained at the suction slot location at and injection slot location at 0°. The injection slot location of 0° appears to be the optimum for all the aerodynamic and efficiency performance. The maximum lift coefficient of C_L=28 is achieved at $C_\mu = 0.8$.

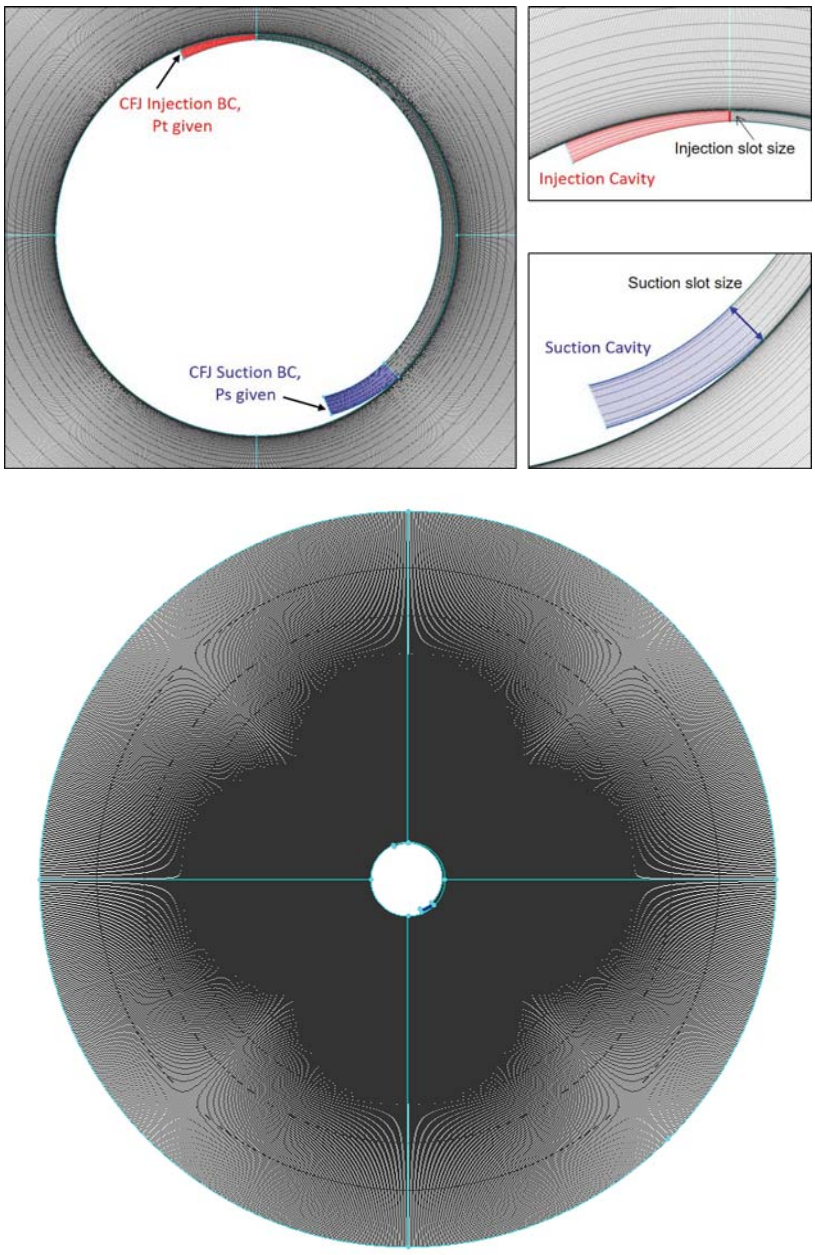

Figure 10.8: Computational mesh for CFJ cylinder calculation.

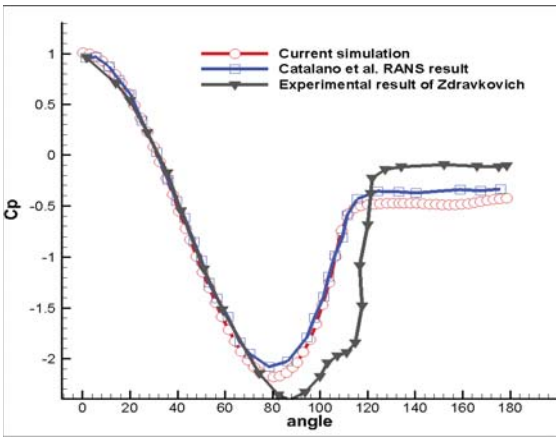

Figure 10.9: Pressure coefficient plotted as a function of the azimuth angle for one semi-circle of the cylinder's surface

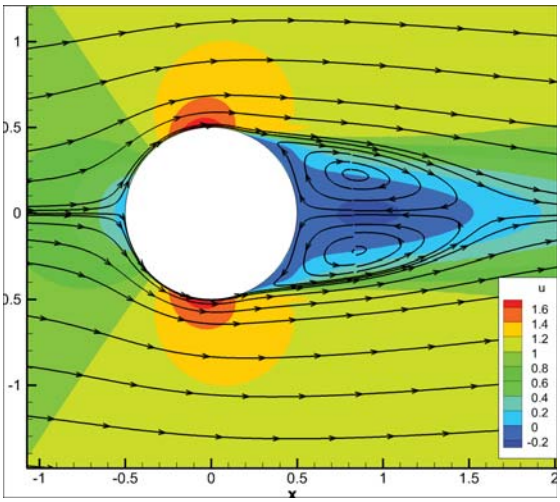

Figure 10.10: streamlines of steady state RANS results for the stationary cylinder flow

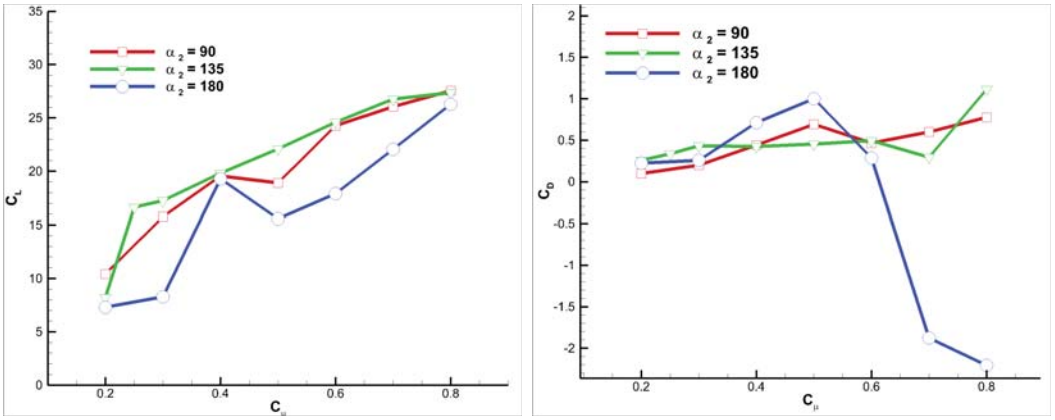

Figure 10.11: Lift and drag coefficient vs C_μ for the cylinder with CFJ flow control at different suction locations.

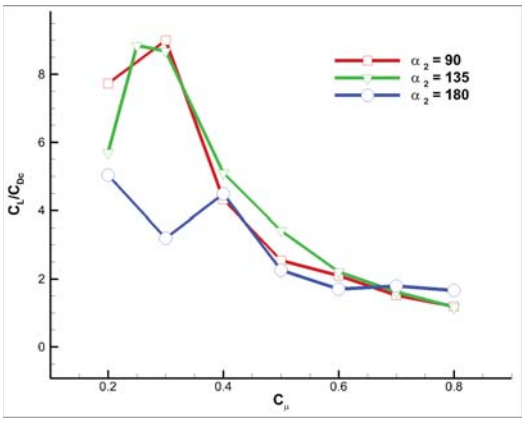

Figure 10.12: Aerodynamic efficiency C_L/C_{Dc} vesus C_μ

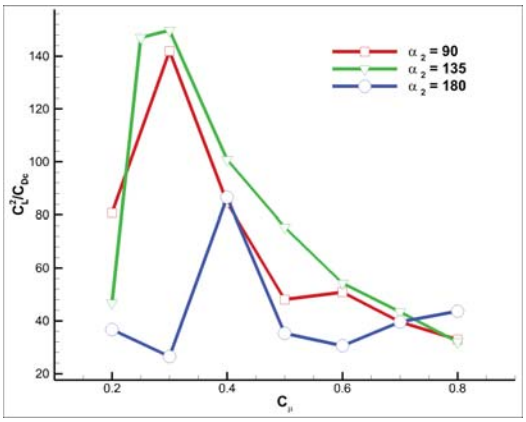

Figure 10.13: Productivity efficiency C_L^2/C_{Dc} vesus C_μ

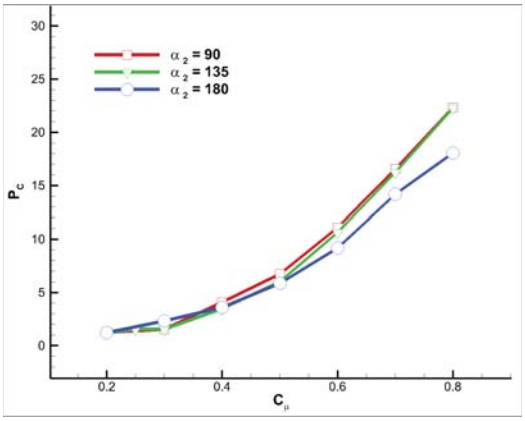

Figure 10.14: Power coefficient C_L vs C_μ

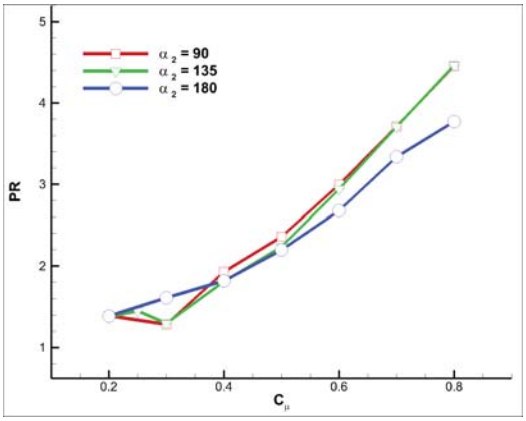

Figure 10.15: Pressure ratio PR vs C_μ

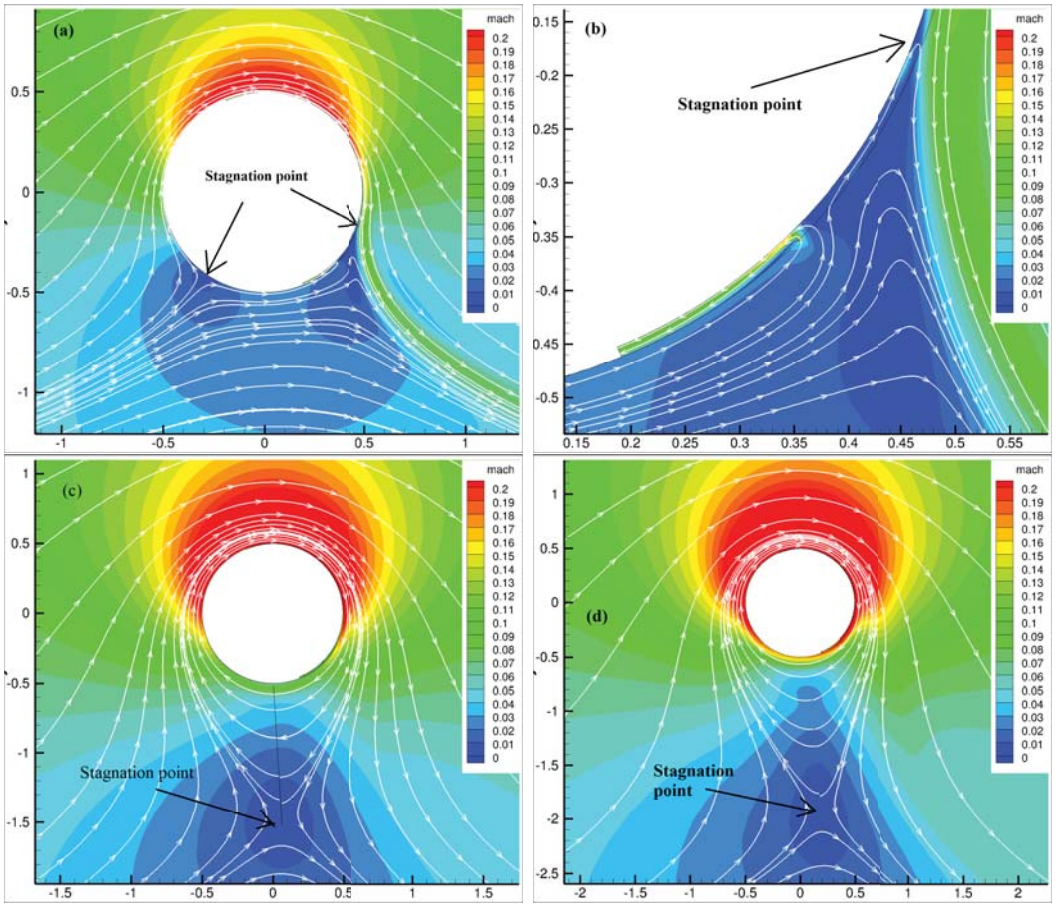

Figure 10.16: The Mach number and streamlines at the jet momentum coefficient C_μ of 0.2, 0.3 and 0.5

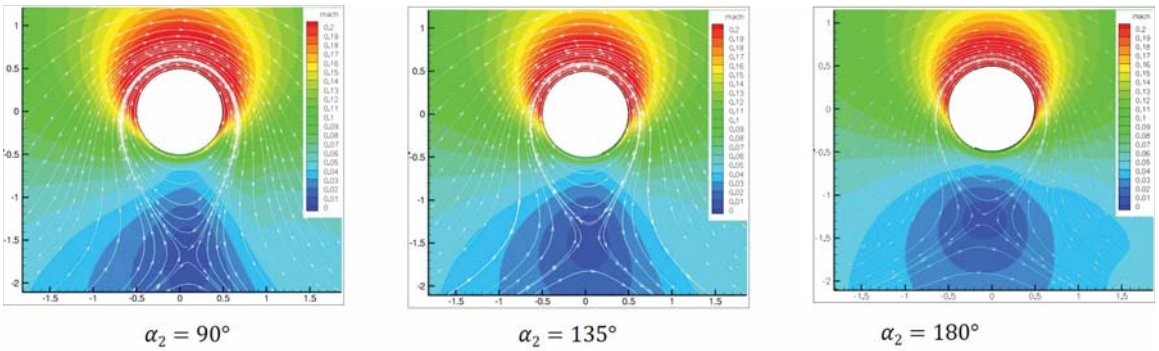

Figure 10.17: Mach contours and streamlines at $C_\mu = 0.6$

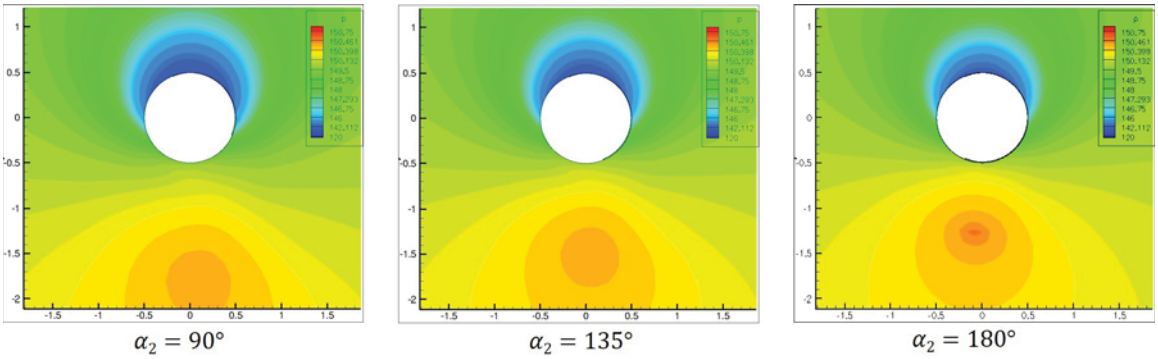

Figure 10.18: Pressure distribution at different suction configurations

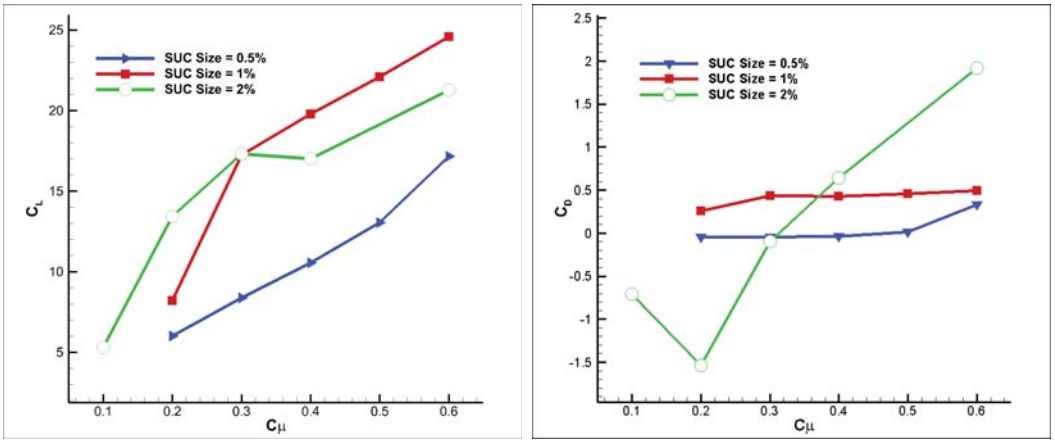

Figure 10.19: Lift and drag coefficient with different suction slot sizes

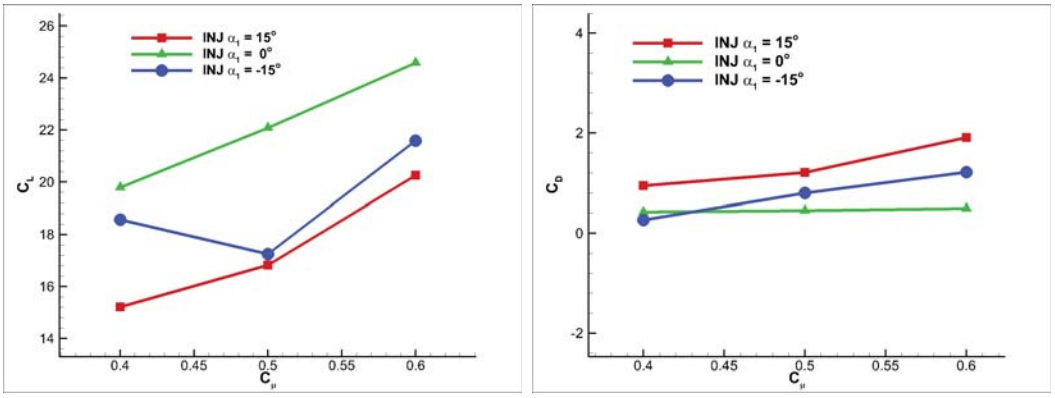

Figure 10.20: Lift and drag coefficient with different injection location

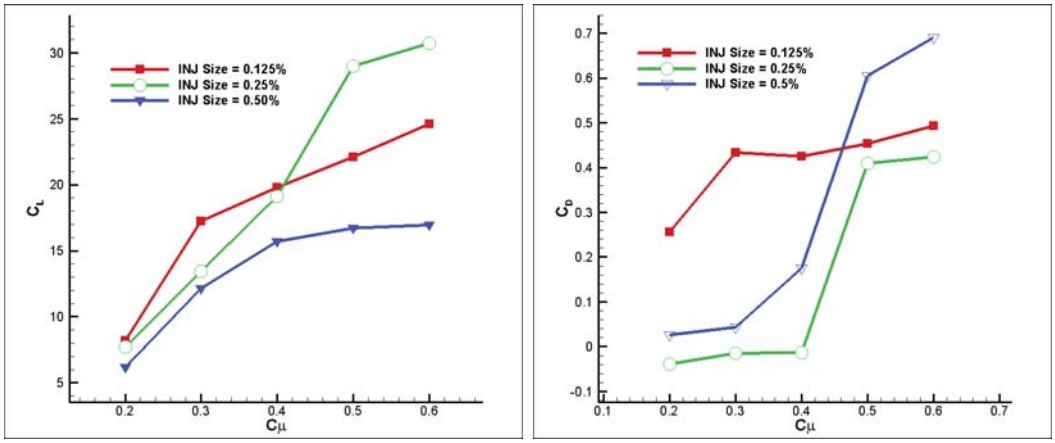

Figure 10.21: Lift and drag coefficients with different injection slot sizes

CHAPTER 11

Wind Tunnel Testing of Super-Lifting and Thrusting CFJ Airfoil Actuated by Micro-Compressors

11.1 Motivation

Maximum lift coefficient, C_{Lmax}, is very important to determine an airplane's takeoff/landing distance and noise level. The higher the C_{Lmax}, the shorter the take-off/landing distance, and the lower the airframe noise due to smaller stall velocity. Achieving high C_{Lmax} is hence critical to increase future airport capacity and reduce airport community noise. In aerodynamics theory, Smith's [10] pioneered the research of high lift aerodynamics and defined the C_{Lmax} limit as $C_{Lmax} = 2\pi(1 + \frac{t}{c})$. For the NACA 6421 airfoil studied in this paper, the theoretical limit C_{Lmax} will be 7.6.

One important condition to achieve the solution of Eq. (7.1) is that the airfoil or cylinder must satisfy the Kutta condition at the trailing edge. To make cylinder flow satisfy Kutta condition, a small "tail" is added to the cylinder to make the mathematical solution well posted [10]. The potential flow theory achieves the C_{Lmax} limit at the condition when the stagnation point is at the trailing edge, the lowest possible point that allows the potential flow to have a solution. In other words, the

Kutta condition is a mathematical condition based on simplified potential flow theory, it is not necessarily a physical condition. However, the Kutta condition does agree excellently with physics as long as the lift coefficient is lower than the limit defined in Eq. (7.1).

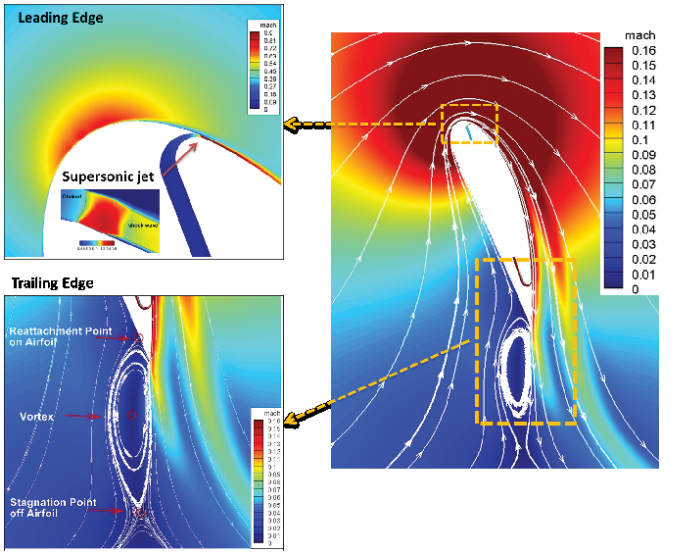

Figure 11.1: Mach number contours and streamlines at C_μ = 0.35 and AoA =70° for the CFJ-NACA6421 airfoil.

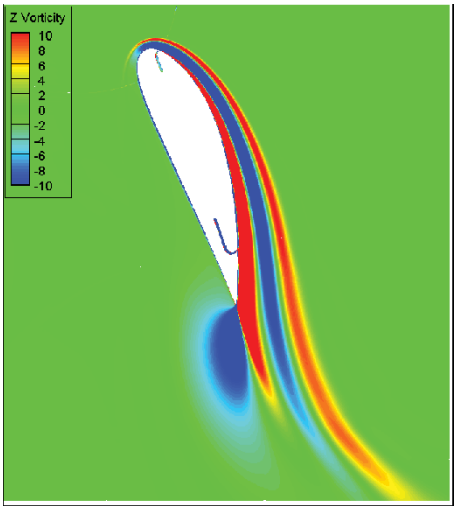

Figure 11.2: Vorticity contour at C_μ = 0.35 and AoA =70° for the CFJ-NACA6421 airfoil.

The C_{Lmax} limit of potential flow theory is so high that it has never been challenged in the past one and half century since George Cayley first observed the airfoil shape from dolphin. Based on the potential flow theory, the more airfoil elements are used, the more the lifting surface meanline can approach a half circle to maximize the lift coefficient. By observing the trend of the C_{Lmax} growing from 2 in 1935 to 3 in 1965, Smith [10] asked then "By 1995 will we have advanced to 4?". He did show a 7-element flap system that achieves a C_{Lmax} close to 4. However, flap high lift system is very complicated and expensive to make [127]. The airliner manufacturers are moving toward simpler high lift systems with less airfoil elements instead of the

other way around [127]. Hence the answer to Smith's question is that today's high lift system and C_{Lmax} level is not much different from those 5 decades ago in 1965.

If the Kutta condition limiting the C_{Lmax} is not necessarily a physical condition, it is then possible that an airfoil lift coefficient may break the limit under certain physical conditions. Yang and Zha [147] obtained a SLC that is far greater than the theoretical limit by using CFJ flow control [35, 61–69, 147] based on CFD simulation. The CFD results indicate that when a SLC occurs, the circulation is so high that the stagnation point is detached from the airfoil as shown in Fig. 11.1 with C_μ=0.35 and C_{Lmax}=10.6. The vorticity structures also reveal some unseen phenomena with 4 layers of counter-rotating vortices emanating from leading edge and trailing to the wake of the airfoil as shown in Fig. 11.2.

The Super-lift coefficient phenomenon is very important. However, without experimental proof, it will remain as a hypothesis. The purpose of this chapter is to conduct wind tunnel experiment to prove the super-lift coefficient phenomenon quantitatively. This is the important first step to explore this new area of aerodynamics.

11.2 The CFJ Airfoils

Two CFJ airfoil configurations are tested in this study, one for takeoff/landing to maximize the lift coefficient, one for cruise to maximize the aerodynamic and productivity efficiency. Both airfoils are numerically studied in Chapter 7. In general, to have high C_{Lmax}, it is more effective to have smaller injection size with higher injection velocity, which will give higher injection jet momentum and lower mass flow rate if the C_μ is fixed. However, the power coefficient of the CFJ airfoil is also high with smaller injection size because the jet suffers high energy loss going through small

holes. Thus for the cruise condition that a high efficiency is more important, a larger injection slot size with lower jet velocity and loss is more desirable.

Table 11.1 gives the detailed parameters of the two CFJ airfoils designed for takeoff/landing and cruise condition, including the injection and suction slot size normalized by chord length(C), and the injection jet momentum coefficient used. The 3-digit number in the naming convention stands for the SST distance, injection slot size, and suction slot size normalized by the airfoil chord.

Table 11.1: CFJ6421 airfoil geometry parameters for takeoff/landing and cruise condition

Case	CFJ6421 airfoil	SST (%C)	INJ slot size (%C)	SUC slot size (%C)
Takeoff/Landing	SST016-SUC053-INJ009	0.16	0.09	0.53
Cruise	SST143-SUC133-INJ065	1.43	0.65	1.33

11.2.1 Subsonic Wind Tunnel at TAMU

The Texas A&M Oran W. Nicks Low Speed Wind Tunnel (LSWT) is used for the wind tunnel testing of this research. The LSWT is a large-scale, closed-circuit wind tunnel located at Easterwood Airport in College Station, Texas. A schematic of the facility is given in Fig. 11.3. The test section is housed in a two-story building that includes model preparation areas, data acquisition and computer equipment, an instrumentation lab and a model receiving area with appropriate hoists and support equipment for model transport and installation. An extensive CNC machine shop housed in an adjacent building. Office space is available for customer representatives.

The circuit length of the wind tunnel at the centerline is 398 feet. The cross section is circular from the fan to the entrance of the contraction section with a maximum diameter of 30 feet occurring in the settling chamber. Each turn in the

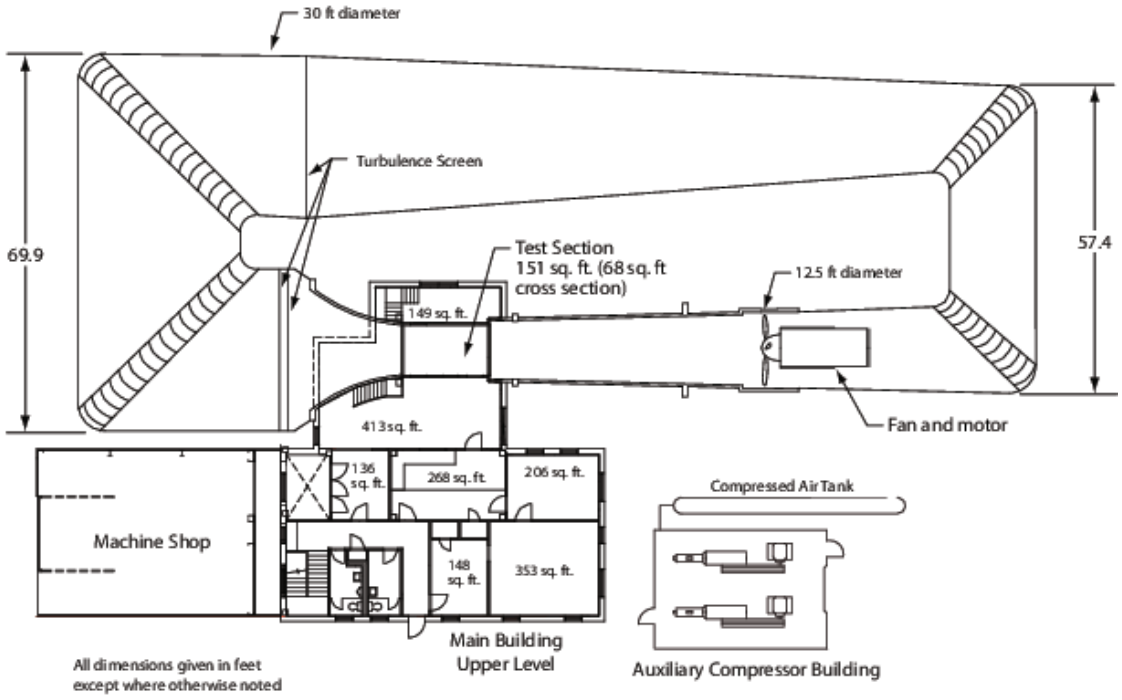

Figure 11.3: Schematic view of the LSWT at TAMU.

circuit contains a set of turning vanes to help guide the flow. A double screen is located between the settling chamber and contraction section to minimize turbulence and provide uniform flow into the test section. A 30-foot long contraction segment then changes the cross section from circular to rectangular with a 10.4 contraction ratio. The rectangular test section is 7 feet tall, 10 feet wide, and 12 feet in length. The test section contains one-foot chamfers in all four corners that reduce the overall cross sectional area to 68 square feet. The walls diverge two inches in the horizontal direction over the length of the test section to account for boundary layer growth and minimize stream-wise buoyancy. Two vertical vent slots allow the tunnel to maintain a static pressure in the test section near ambient.

A 46-foot-long diffuser, located downstream of the test section, changes the cross sectional shape from rectangular, back to circular at the fan. The horizontal and

vertical angles of the diffuser are 1.43 and 3.38 degrees, respectively. The fan is a Curtiss Electric four-blade, B-29 propeller with a diameter of 12.5 feet. Each blade is cut 18 inches from the tip in order to properly fit them to the diameter of the tunnel. The blade tips are inset into the tunnel wall to minimize tip effects. A 24-volt direct current motor and planetary gear system, housed in the propeller assembly, allow for the variable pitch capabilities. The motor is a 3,000 horsepower, induction motor that was recently built by TECO-Westinghouse and installed at the LSWT in May of 2012. The induction motor combined with a variable frequency drive allows for adjustable revolutions per minute (RPM) capabilities. The maximum setting is 1,200 RPM. However, the motor can force the tunnel to reach the current top allowable wind speed of 200 miles per hour (MPH) at 60 percent of its maximum speed, 720 RPM.

The test section can be outfitted with a three axis traversing mechanism. This can be used to position hotwires or pressure probes with repeatability accuracy of 0.01 inches. The traverse moves in the plane normal to the flow, while the probes are mounted to an extension arm that is set manually. The LSWT is equipped to read pressure data with a Measurement Specialties System 8400. The system can read up to 16 64-port pressure scanners. The facility is currently outfitted with 10 inH_20 and 20 inH_20 scanners, as well as one-psi and five-psi scanners. The System 8400 is capable of scanning the pressure measurements at a maximum 40 Hz. Standard procedure is to recalibrate the scanners, via the on board calibration unit, every two hours. The data acquisition system is housed within the Signal Conditioning Extensible Interface (SCXI) unit built by National Instruments. SCXI contains an internal multiplexer that is connected to an M-series PCI 6289, 18-bit analog to digital board with signal

conditioning capabilities. The unit has a maximum aggregate sampling rate of 300 kHz. The SCXI unit can be used in conjunction with up to 24 different voltage channels.

The tunnel is controlled using the calculated dynamic pressure of the airflow at the center of the test section. Two static pressure rings, consisting of four ports each, are used to measure the average static pressure in the tunnel at the end of the settling chamber and five feet in front of the test section. The difference of these static pressure measurements is a pseudo dynamic pressure called q_{set}. The measurement of q_{set} is used to calibrate the actual dynamic pressure in the center of the empty test section, q_{act}, with the use of a Pitot tube. A calibration curve is created and used to calculate q_{act} from set when the Pitot tube is not installed in the test section. While the tunnel is in operation, q_{set} is constantly measured and used to calculate q_{act}.

The temperature inside the tunnel is measured with a thermocouple that is located on the wall at the beginning of the test section. The barometric pressure is recorded in the balance room, beneath the test section. These measurements allow the velocity in the test section, based on tunnel conditions, to be calculated in real-time. The total and static pressure in the tunnel are also measured during a test, with use with a Pitot tube located on the far wall.

LSWT is equipped with a six component, pyramidal electromechanical, external balance system located beneath the test section. The external balance measures three force components and three moments in a wind-oriented coordinate system. The origin of the coordinate system is the geometric center of the test section, 42 inches above the floor. The measurements are sent to the data acquisition system using optical encoders. Lift force can be measured from -1000 lbf to +3000 lbf, while

drag and side force can be measured from ±1000 lbf. Pitching and rolling moments can be measured to ±2000 ft-lbf, while yaw can be measured to ±1000 ft-lbf. Force and moments are accurate to 0.1% of the applied load or moment, with a minimum accuracy of 0.1 lbf or ft-lbf, respectively. The external balance is isolated from the upper turntable. The turntable can rotate to any yaw angle (ψ) orientation within -120° to +190°. LSWT can also be equipped with an internal balance system for other tests.

11.3 Results and Discussion

Table 11.2 is the wind tunnel testing conditions with the dynamic pressure varied from 0.3Q to 3Q. The Q has the dynamic pressure equal to 1psf. The velocity is varied from 4.84 m/s to 16.26 m/s and the Reynolds number is from 208588 to 691126. The CFJ airfoil has 5 micro-compressors embedded inside along the span as shown in 11.4.

Table 11.2: Wind Tunnel Testing Conditions

Case	Velocity(m/s)	Reynolds number
0.3Q	4.84	208,588
0.5Q	6.25	269,078
1Q	9.39	399,022
2Q	13.27	564,217
3Q	16.26	691,126

The micro-compressor has an outer diameter of 84mm and length of 124mm. It is a compressor mixed with centrifugal and axial compressor design. The mass flow rate is from about 20g/s to 80g/s with the pressure ratio varying from 1.05 to 1.4. The maximum power of the compressor is 2kw. The micro-compressor is customer designed based on our CFD design and simulation of the CFJ airfoil matching the wind tunnel conditions. The aerodynamic design of the micro-compressor was conducted

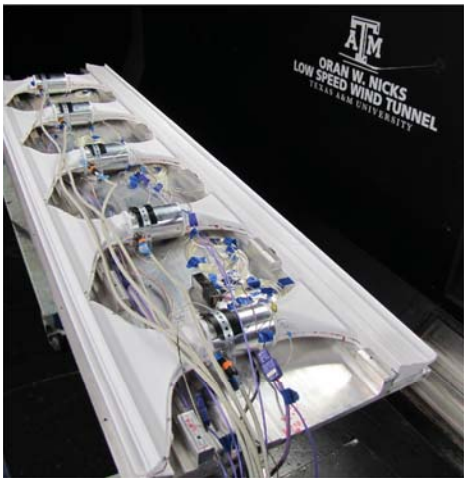

Figure 11.4: Photo of the tested CFJ-NACA-6421 airfoil with 5 micro-compressors embedded.

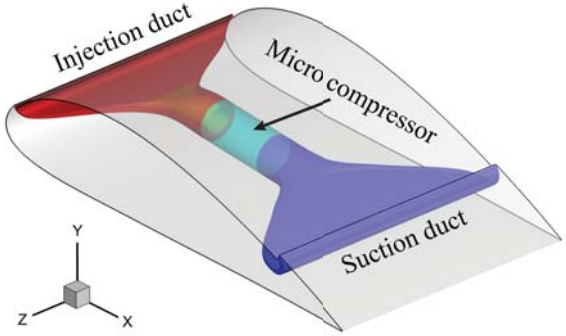

Figure 11.5: Sketch of the CFJ airfoil with the micro-compressor and the suction and injection duct.

by PCA Limited in England [155]. The mechanical design and manufacturing of the micro-compressors are done by Celeroton, a company in Switzerland [156]. Manufacturing such a small and high power compressor is very challenging. There will be a separated paper focusing on the design and manufacturing of the micro-compressors.

The micro-compressors were tested in Celeroton before being delivered to the University of Miami. They come with a compressor characteristics map showing the performance of the range of mass flow, pressure ratio, power consumption, and efficiency of the compressor at different RPM. For the CFJ airfoil at cruise and takeoff/landing, the slot sizes are different. The injection slot size is largely varied. The micro-compressors hence experience the throttling effect similar to jet engines. Since CFJ airfoil generates very high thrust, the CFJ wing with embedded micro-compressors is a tightly integrated distributed propulsion system. The power consumed by CFJ enhances the lift and generates thrust simultaneously. This is different from a conventional propulsion system with the sole function to generate thrust.

Since each compressor covers a span length of 0.42m as shown in Fig. 11.6. The ratio of the span width to the compressor inner diameter is 6.46. The duct has a shape of rectangle at the CFJ airfoil injection and suction slots, and then transits to a circular shape to match the compressor inlet and outlet interface. This brings a lot of challenges to design the injection and suction ducts with no flow separation.

To save airfoil manufacturing cost, the two CFJ airfoil configurations for cruise and takeoff/landing share many common parts. Between the two configurations, the upper surface of the airfoil is translated by different amount to match the injection and suction slot size optimized by CFD. To match the injection duct contours, two leading edge parts are designed and manufactured respectively for the cruise and takeoff airfoils. There are a lot of detailed mechanical design and manufacturing to integrate the micro-compressors with the CFJ airfoil.

At the wind tunnel testing, each micro-compressor has a total pressure and static pressure probes at the compressor inlet and outlet. Three of the five compressors also have the temperature sensors at the inlet and out let. The intent is to help to determine the mass flow rate and pressure ratio of the compressor. However, since the flow has high swirl at the outlet, the total pressure measurement has very large uncertainty and is not very useful. The static pressure measurement is then used to have some rough idea of the pressure ratio. Accurate measurement of the pressure ratio requires multiple pressure probes distributed circumferentially. So is for the temperature measurement. In the wind tunnel testing, the micro-compressors are controlled by different RPM to obtain different mass flow rate and pressure ratio. But accurate measurement of moment coefficient C_μ is not available. This will be left as future work.

The following are some direct measurement of the CFJ airfoil aerodynamic performance. More detailed analysis will be presented in the final paper.

Fig. 11.6 is the CFJ airfoil vertically mounted in the wind tunnel. The injection and suction slots are visible. Fig. 11.7 is the baseline airfoil tested for comparison. Since the injection slot is very small with the size less than 0.1% of the chord, the baseline airfoil is restored by simply sealing the injection slot with aluminum tape. The suction slot has a larger size. A contoured wedge is 3D printed, inserted to the suction slot, and is merged with the suction surface. To ensure smoothness, the wedge is also taped as shown in Fig. 11.7. The treatment of the baseline airfoil is to save cost. Thus the baseline airfoil does not represent the exact NACA 6421 airfoil. It has some small deviation. However, it is sufficient to be used as a reference for uncontrolled airfoil.

Fig. 11.8 to 11.10 are the coefficient of lift, drag and pitching moment of the cruise CFJ airfoil at 1Q condition compared with the baseline airfoil. The RPM is varied from 75k to 145k. The baseline airfoil has the maximum lift coefficient of 1.3 with fairly delayed stall angle of attack, which may be due to the trip effect of the tape sealing the injection slot. At the lowest RPM of 75k, the CFJ airfoil reaches the C_{Lmax} of 2, a 54% increase. At the RPM of 145k, the C_{Lmax} is 3.8, a 292% increase. Fig. 11.9 indicates that the CFJ airfoil achieves thrust for all the RPM at low AoA. The maximum thrust coefficient is about 0.18. For the high RPM of 145k, the thrust is maintained up to AoA of 28°. Fig. 11.10 shows that the nose down pitching moment is greater than that of the baseline airfoil. However, with the increase AoA and lift, the nose down pitching moment is decreased and approaches that of the baseline airfoil.

Figure 11.6: Photo of the CFJ-NACA-6421 airfoil tested.

Figure 11.7: Photo of the baseline NACA 6421 airfoil tested.

Fig. 11.11 to 11.13 are the coefficient of lift, drag and pitching moment of the high lift configuration of the CFJ airfoil for takeoff/landing (TOL) at 1Q freestream condition. The maximum lift coefficient is increased to 5, a 385% improvement. The thrust coefficient is also increased to 0.32.

Fig. 11.14 to 11.16 are the coefficient of lift, drag and pitching moment of the CFJ airfoil achieving super-lift coefficient. The CFJ airfoil configuration is the same as the one for takeoff/landing. The purpose of this test is to prove the CFD predicted super-lift coefficient phenomenon, that is the lift coefficient exceeding the theoretical

limit of 7.6. Since the micro-compressors are not powerful enough to achieve sufficient injection momentum coefficient at 1Q freestream condition, the freestream condition is reduced to 0.5Q and 0.3Q, which correspond to the freestream velocity of 6.25m/s and 4.84m/s. In the morning when the tunnel air is cooler, the C_{Lmax} reaches 9 at AoA of 30deg and freestream of 0.3Q. In the afternoon when the tunnel is hot, the compressors are less powerful and the repeated tests obtained the C_{Lmax} of 8.6. They are all substantially higher than the limit of 7.6. This is the first time in history than an airfoil achieves the lift coefficient beyond the theoretical limit. It is almost certain that the C_{Lmax} can go even higher with more powerful micro-compressors. The maximum thrust coefficient is very large up to 1.0. The pitching moment behaves similarly to the previous cases with nose down moment increased.

11.4 Conclusion

The wind tunnel testing of CFJ airfoil with embedded compressors proves experimentally for the first time that an airfoil can achieve a lift coefficient exceeding the potential flow theoretical limit by using coflow jet (CFJ) active flow control. The CFJ airfoil is also able to generate a very high thrust coefficient. Both the high lift and thrust are attributed to the super-suction effect with very low pressure at the airfoil leading edge induced by the injection jet. The CFJ airfoil appears to be the only man made airfoil that can generate ultra-high lift and thrust simultaneously without flapping. The CFJ airfoil in the experiment is actuated by micro-compressors embedded inside the airfoil with zero-net-mass-flux (ZNMF). The C_{Lmax} achieved in the experiment varies from 8.0 to 8.6, substantially exceeding the theoretical limit of 7.6. A very large thrust coefficient (negative drag) of 1.0 is achieved at low angle of attack

(AoA). A thrust is maintained up to the angle of attack of 40deg when the airfoil is about to get stalled. This study indicates that the perceived airfoil lift coefficient limit in the past 5 decades is artificial due to enforcing the Kutta condition, which is a mathematical condition necessary for airfoil potential flow, not a physical condition. This study may expand classical fluid mechanics to new territory and foster industrial applications very different from the current technologies.

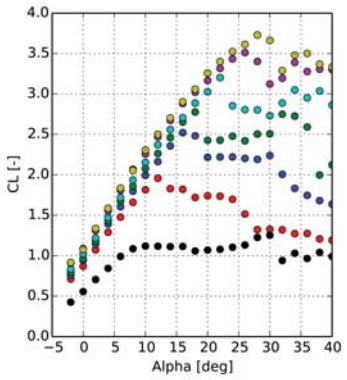

Figure 11.8: Lift coefficient of the cruise CFJ and baseline airfoil vs AoA.

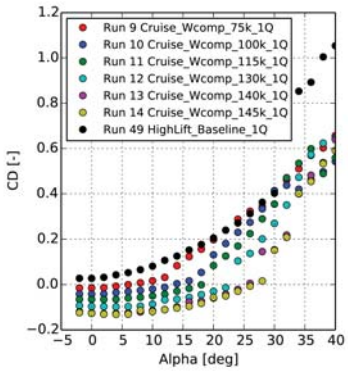

Figure 11.9: Drag coefficient of the cruise CFJ and baseline airfoil vs AoA.

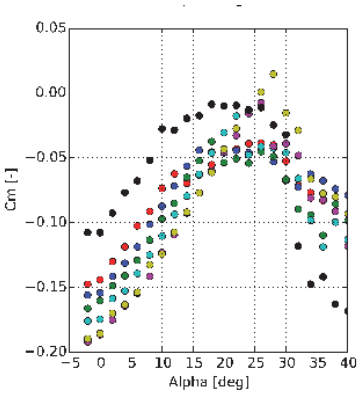

Figure 11.10: Pitching Moment coefficient of the cruise CFJ and baseline airfoil vs AoA.

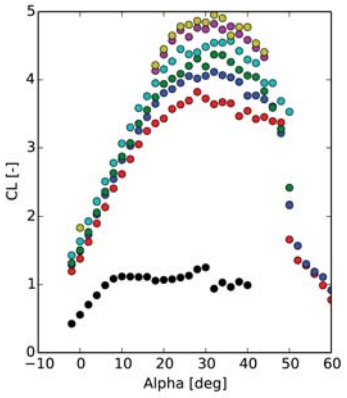

Figure 11.11: Lift coefficient of the TOL CFJ and baseline airfoil vs AoA.

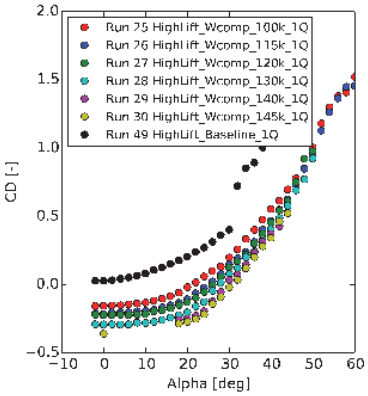

Figure 11.12: Drag coefficient of the TOL CFJ and baseline airfoil vs AoA.

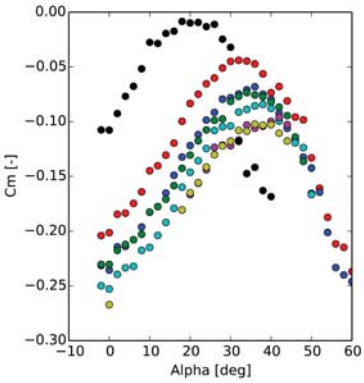

Figure 11.13: Pitching Moment coefficient of the TOL CFJ and baseline airfoil vs AoA.

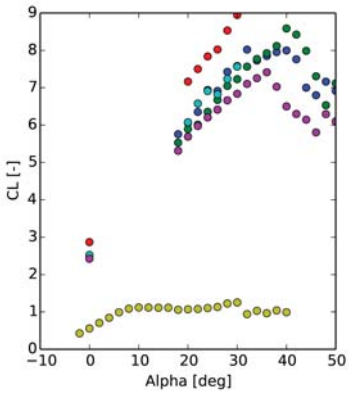

Figure 11.14: Lift coefficient of the Super-Lift CFJ airfoil and baseline airfoil vs AoA.

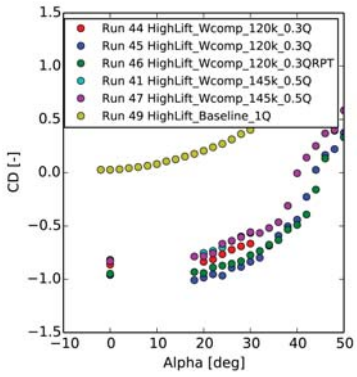

Figure 11.15: Drag coefficient vs AoA.

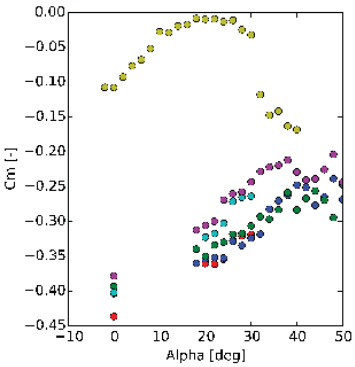

Figure 11.16: Pitching Moment coefficient vs AoA.

CHAPTER 12

Performance Improvement of CFJ Electric Airplane

12.1 CFJ Electric Airplane

A conceptual design of general aviation aircraft utilizing CFJ flow control and electric propulsion is designed by Lefebvre and Zha [35]. The sketch and dimensions are shown in Fig. 12.1. The mission of CFJ-EA airplane is to carry 4 passengers for the range of 300 nm with the cruise Mach number of 0.15. Ah high wing loading and a compact size is obtained for CFJ-EA to increase battery storage and reach a longer range. At cruise, the designed lift coefficient is 1.3 at the Mach number of 1.5 with the wing AoA of 5° and CFJ C_μ of 0.04. The CFJ-EA cruise aerodynamic efficiency L/D is 36. Considering the CFJ pumping power, the corrected aerodynamic efficiency $(L/D)_c$ is 24. For the cruise performance improvement, a modified CFJ-NACA6421 airfoil is utilized to achieve higher efficiency.

Regarding the takeoff/landing (TOL) performance of CFJ-EA, the takeoff velocity of 24.6 m/s with reasonable takeoff and landing distances are achieved. The lift coefficient is C_L is 4.8 at the AoA of 25° and C_μ of 0.28. To improve the ESTOL performance of CFJ-EA, the super-lifting CFJ airfoil configuration with smaller in-

jection and suction slot sizes is utilized to achieve higher maximum lift coefficient C_{Lmax}.

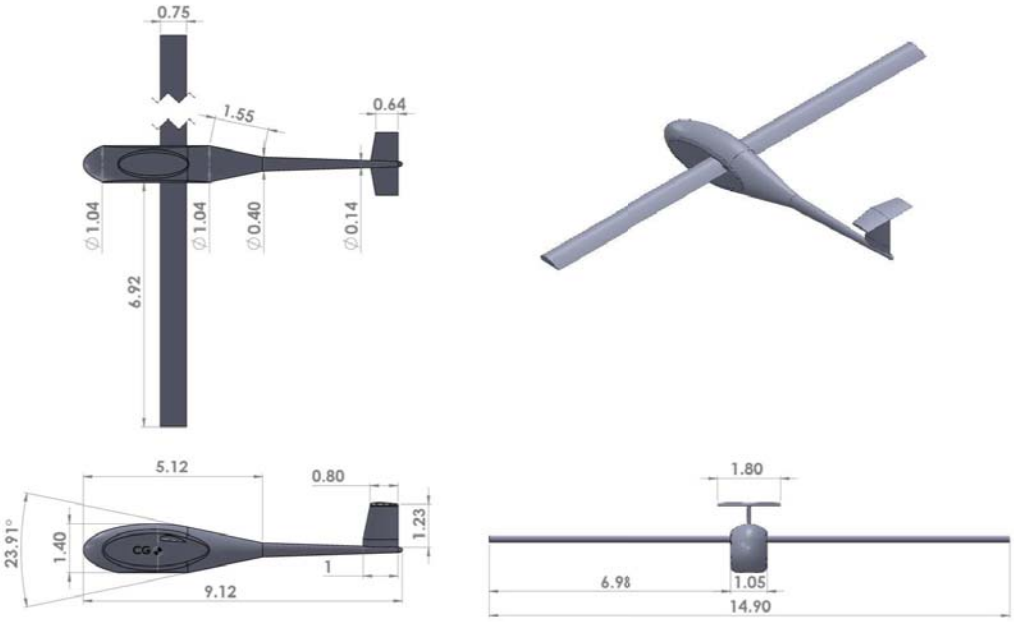

Figure 12.1: The original design of CFJ-EA isometric view [35].

12.2 Super-Lifting Performance at Takeoff/Landing

12.2.1 Super-lifting CFJ Wing Geometry for Takeoff/Landing

Since super-lifting CFJ airfoils can generate ultra-high lift coefficient with attached flows at ultra high AoAs, the CFJ-EA wing is desirable to pivot around the gravity center of the CFJ wing. At takeoff, the CFJ-EA wings fix high AoA up to 50° to maximum the achievable lift coefficient . At cruise, the CFJ-EA wings cruise at a lower AoA with smaller C_μ to achieve maximum cruise efficiency. Three different angles of rotation of the CFJ-EA wings are studied at AoA of 30°, 40°, 50° as shown

in Fig 12.2. The present CFJ airfoil geometry with injection and suction slot sizes is based on the result of a trade study conducted [147] as shown in table 7.9. Higher C_μs are used in the range of 0.2-0.6.

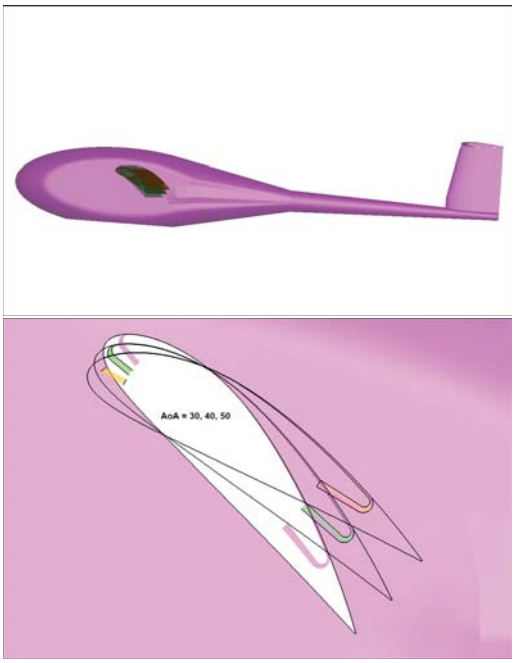

Figure 12.2: CFJ-EA with rotatable wing

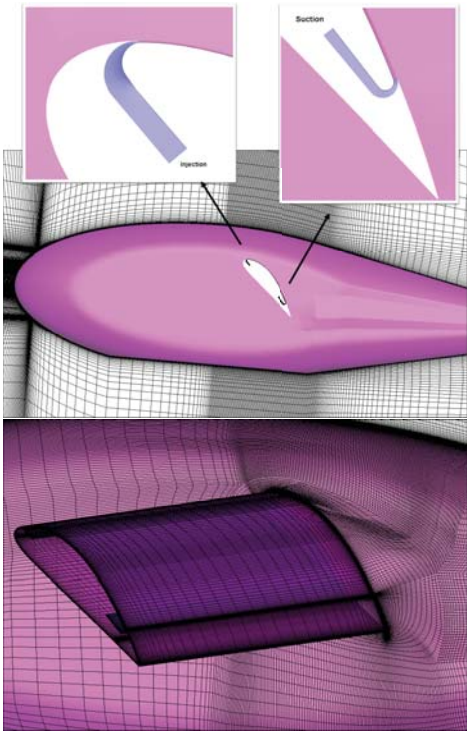

Figure 12.3: Mesh topology at AoA = 50°

Table 12.1: Takeoff/Landing simulation parameters

Case	Mach	Re	AoA	C_μ
CFJ-EA	0.063	3,030,000	30°, 40°, 50°	0.2-0.6

Table 12.2 summarizes the simulation results of the super-lifting CFJ-EA aircraft at different AoAs and different jet momentum coefficients C_μ. For all the simulated cases, the lift coefficients for CFJ-EA aircraft are substantially higher than the conventional aircraft. The maximum lift coefficient of 6.93 is achieved at AoA of 50° and C_μ of 0.6. The optimum productivity efficiency is obtained at AoA of 50° and C_μ of 0.2.

Table 12.2: Simulation results for CFJ-EA at the takeoff condition

AoA	C_μ	C_L	C_D	P_c	L/D	C_L/C_{Dc}	C_L^2/C_D	C_L^2/C_{Dc}
30	0.2	4.05	0.280	0.92	14.47	3.38	58.62	13.68
	0.3	4.37	0.275	1.90	15.88	2.01	69.45	8.79
	0.4	4.50	0.276	3.57	16.30	1.17	73.37	5.27
40	0.2	4.16	0.498	0.95	8.353	2.88	34.75	11.99
	0.3	4.63	0.463	1.958	10.00	1.91	46.30	8.85
	0.4	4.78	0.476	3.633	10.04	1.16	48.00	5.56
50	0.2	5.44	0.710	0.94	7.66	3.28	41.75	17.91
	0.3	5.90	0.713	2.078	8.26	2.11	48.75	12.46
	0.4	6.15	0.7	4.441	8.79	1.19	54.12	7.369
	0.5	6.19	0.660	8.754	9.38	0.65	58.11	4.073
	0.6	6.93	0.668	12.1	10.38	0.54	71.98	3.768

12.2.2 Flow Structures

The simulated CFJ-EA flow structures are discussed in this section. Fig. 12.4 is the streamlines over the CFJ-EA wing-body across the wingspan at AoA = 50° and C_μ of 0.5. With the entrainment effect of CFJ, the flow over the wing is attached on the upper surface for most of the wingspan. The wingtip flow is affected by the downwash produced from the wingtip vortex. The wingtip vortex has an impact of the CFJ distribution on the upper surface. The flow attachment near the wingtip is affected by the tip vortex. It is also worth noting that a small flow separation occurs at the fuselage and wing conjecture. The flow from the fuselage detaches a small amount of flow at the interaction region. The affected region is very limited to a small percentage near the wing root.

The Mach number contours at different span section is displayed in Fig. 12.5.

The local lift loading can be seen from the pressure coefficient (C_p). Fig. 12.6 is the pressure coefficient C_p at different wingspans The C_p distribution shows the two spikes at the injection and suction slot locations, where the wing upper surface is open. The C_p profiles shows that the suction peak achieves a much higher value

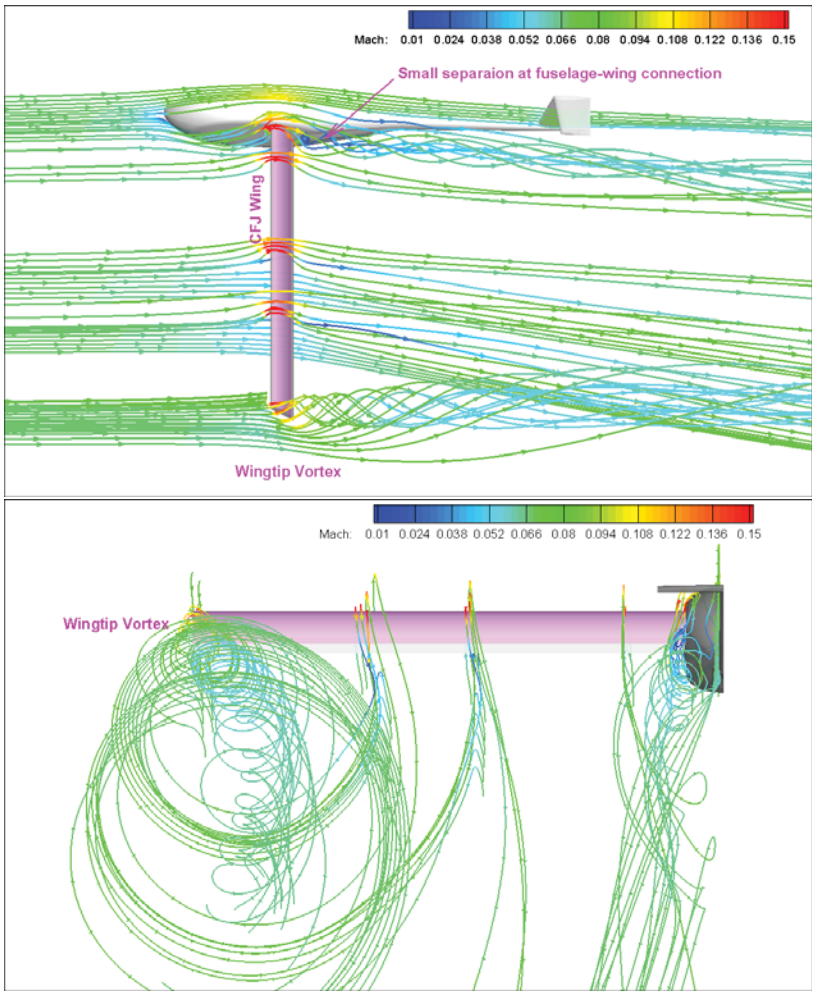

Figure 12.4: The streamlines of CFJ-EA at AoA = 50° and C_μ of 0.5

than traditional wings with no flow control. The maximum C_p exceeds 45 across the wingspan from the root to the middle. The super-suction effect is achieved with such low leading edge pressure. From 75% span to the wingtip, the leading edge C_p value is reduced due to the interaction effect of the wingtip vortex. However, the high lift is generated even at the 99% section of the wing with the C_p distribution on the upper surface is 10. Therefore, the lift generation is tremendously enhanced by the CFJ wing throughout the whole wingspan. The ultra-high loading CFJ wing enable the ESTOL performance of CFJ-EA aircraft.

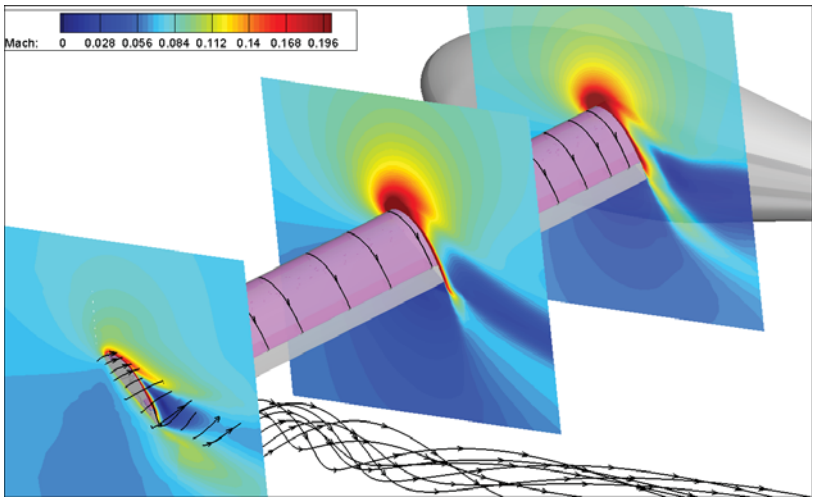

Figure 12.5: Mach number contours with streamlines

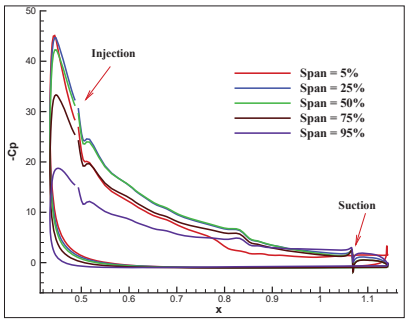

Figure 12.6: Pressure coefficient C_p distribution at different wingspan for the AoA of 50° and C_μ of 0.50.

Fig.12.7 presents the Mach number distribution at different wingspan. It is seen that the flow is attached on the surface at the AoA of 50°.

Fig. 12.8 shows the pressure distribution on the surfaces of the wing, fuselage, and tail. It is clear that the pressure at the leading edge on the upper surface is significantly lower than that of the trailing edge due to the supersuction effect of CFJ.

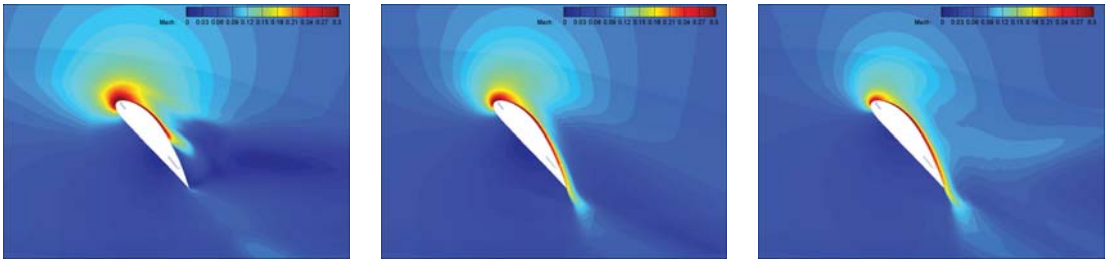

wing root mid-span wing tip

Figure 12.7: The pressure contour at the wing root between the fuselage and CFJ wing

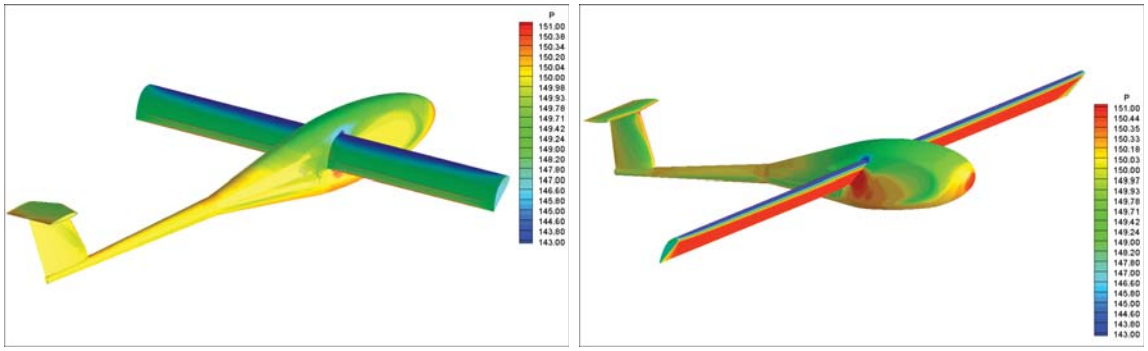

Figure 12.8: Pressure distribution on the surface of CFJ wing and fuselage

12.3 Cruise Efficiency Improvement

The original CFJ-EA design [35] has a large efficiency improvement compared with the state of the art electric aircraft. The CFJ-EA has a payload of 4 passengers at a cruise Mach number of 0.15 with a range of about 314 nm. The cruise lift coefficient of CFJ-EA is 1.3, with a wing loading of 182.3 kg/m^2. At cruise, the angle of attack of the CFJ wing is 5° with the CFJ jet momentum coefficient C_μ of 0.04. The corrected aerodynamic efficiency with the power consumption of the CFJ power $(L/D)_c$ is 24.

To further improve the cruise performance, a modified CFJ-NACA6421-INJ012-SUC015 airfoil is used. The airfoil geometry modification is displayed in Fig. 12.9. The same aspect ratio of 20 is used in CFJ-EA2. The calculated cruise lift coefficient of CFJ-EA2 wing is 1.59 and the drag coefficient is 0.037 at the same C_μ of 0.04. The cruise aerodynamic efficiency C_L/C_{D_c} is 31 and productivity efficiency C_L^2/C_{D_c} is 50. The wing loading of CFJ-EA2 is increased to 214.24 kg/m^2. More batteries can be carried in the CFJ-EA2 to achieve the maximum range of 531 nm. The design parameters for CFJ-EA2 are summarized in Table 12.3. The parameters for the modified CFJ wing are shown in Table 12.4.

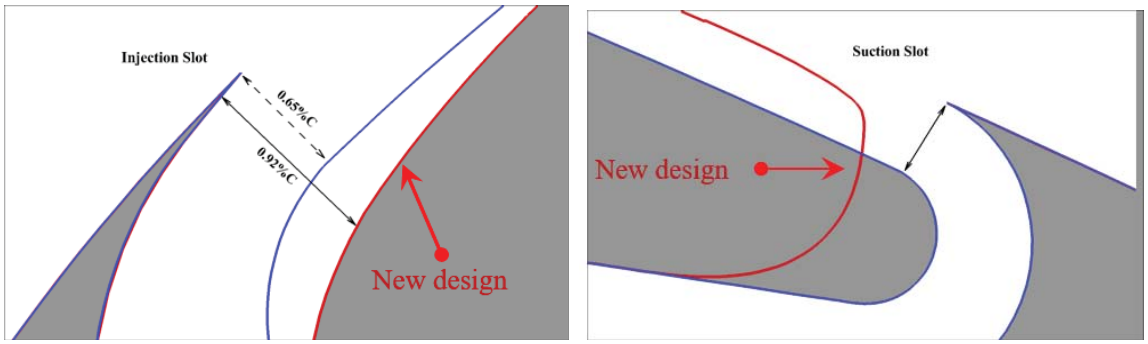

Figure 12.9: The modified design of the CFJ-EA2 cruise airfoil.

Table 12.3: Design parameters for the CFJ-EA2.

Range (nm)	500
Cruise Mach number	0.15
Passengers	4
MTOW(kg)	2200
Propulsion	Electrically powered

12.3.1 CFJ Wing Geometry for Cruise

Table 12.4: CFJ-EA2 wing design.

Wing span (m)	14.96
Wing area (m^2)	10.40
Aspect ratio	21.5
Length (m)	9.12
Cruise C_L	1.59
Cruise C_D	0.037
Cruise C_μ	0.04
Cruise P_c	0.014
Cruise C_L/C_{D_c}	31
Cruise C_L^2/C_{D_c}	50

The overall performance of CFJ-EA2 is shown in table 12.5. The range of CFJ-EA2 is 521 nm with the maximum take off weight of 2289 kg. The carried battery weight is 980 kg.

Table 12.5: CFJ-EA2 overall performance.

MTOW(kg)	2289
Range(nm)	531
Battery weight (kg)	980
Payload (kg)	416
Wing loading (kg/m^2)	214.24
Wing area (m^2)	10.40

A comparative investigations of modified CFJ airfoil is performed. Fig. 12.10 shows that lift, drag and power coefficient of the baseline, CFJ-EA, and CFJ-EA2 at cruise condition. It is obvious that during cruise the lift coefficient is increased

significantly for the CFJ-EA2 aircraft. The cruise lift coefficient for CFJ-EA2 is 1.59 while C_L is 1.32 for the CFJ-EA cruise. With the higher lift coefficient, the wing loading is increased from 182.3 kg/m^2 to 214.24 kg/m^2. The drag coefficients for CFJ-EA and CFJ-EA2 remain at the same level, 0.037. A significant improvement for the modified CFJ airfoil is the reduced power consumption for the CFJ pumping. Therefore, taking all of the above into consideration, for the sake of high cruise efficiency of the aircraft, the modified CFJ wing are preferable.

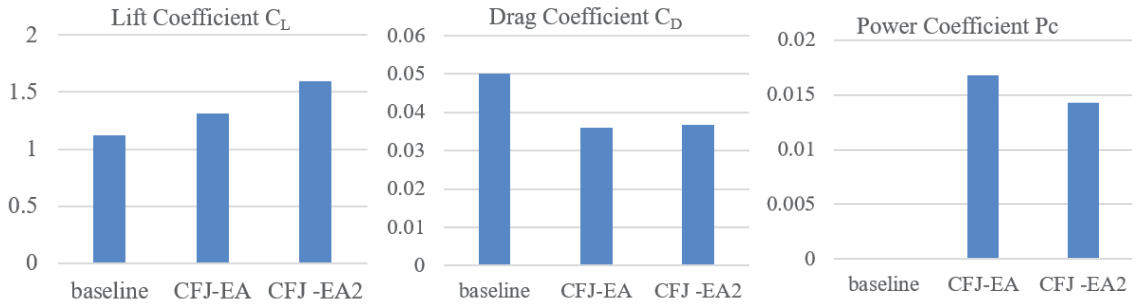

Figure 12.10: Lift, drag and power coefficient of the baseline, CFJ-EA, CFJ-EA2 at cruise.

The comparison of corrected aerodynamic efficiency and productivity efficiency is presented in Fig. 12.11. At cruise for CFJ-EA2 airplane, the aerodynamic efficiency C_L/C_{D_c} is increased by 25% and the productivity efficiency $C_L^2/C_{D_c}$is enhanced by 51%.

12.3.2 Flow Structures for Cruise Condition

The Mach number contours for the 2D CFJ-EA and CFJ-EA2 airfoils are given in Fig. 12.12. The high speed flow region (red color) is expanded throughout the upper surface from injection slot to suction slot. The accelerated flow produces lower pressure on the upper surface. The pressure distribution comparison is given in Fig.

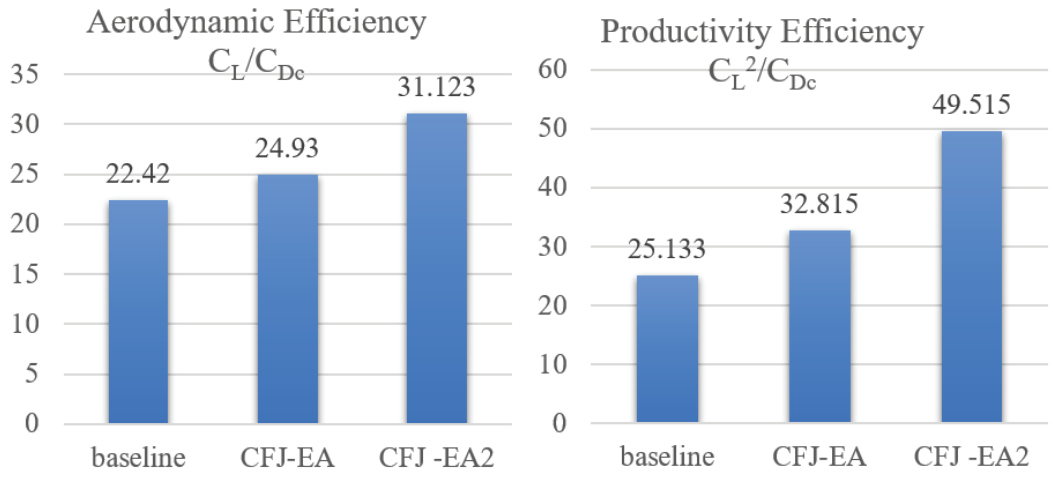

Figure 12.11: Aerodynamic and Productivity efficiency of the baseline, CFJ-EA, CFJ-EA2 at cruise.

12.13. Therefore, the modified CFJ-EA2 airfoil has the better performance with higher lift coefficient.

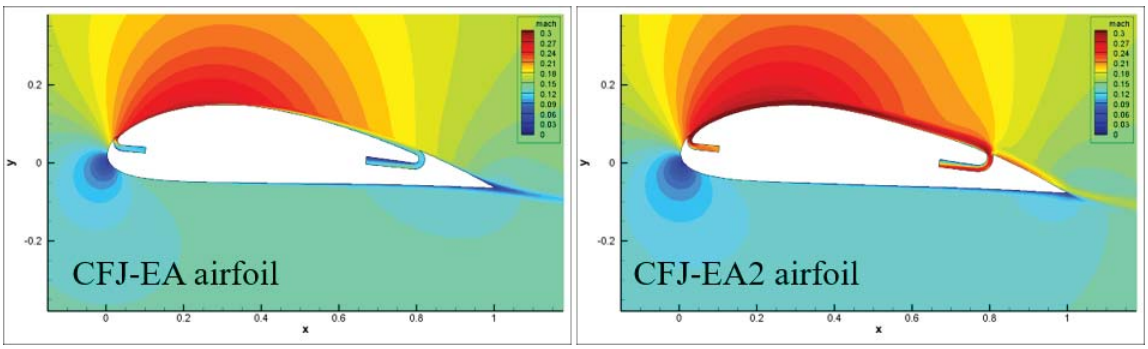

Figure 12.12: Mach number contours for the CFJ-EA and CFJ-EA2 airfoils

The pressure coefficient distribution C_p along the wing is given in Fig. 12.14. The Mach number and pressure contours at different cross-sections of the CFJ-EA2 wing is displayed in Fig. 12.15. The flow is attached on the CFJ wing to the wingtip. The low pressure region is well developed on the upper surface of CFJ wing to provide higher lift.

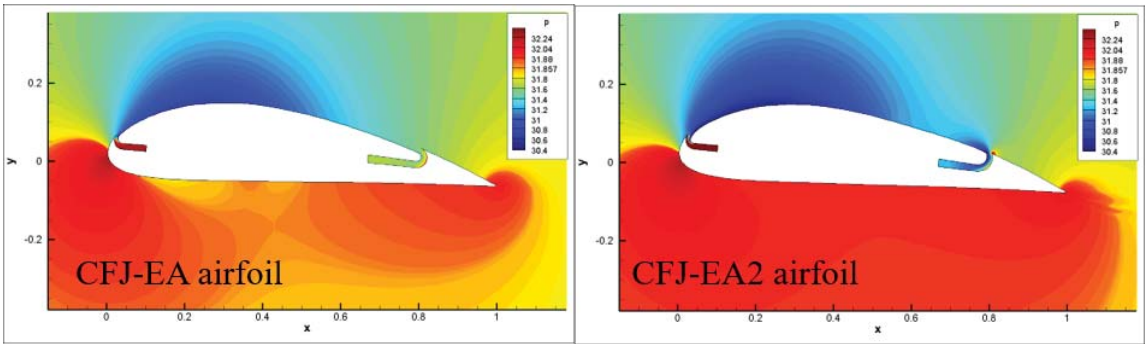

Figure 12.13: Pressure contours for the CFJ-EA and CFJ-EA2 airfoils

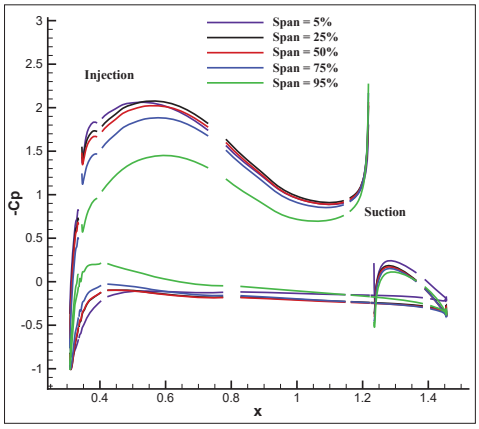

Figure 12.14: C_p distribution at different wingspan for the AoA of 5° and C_μ of 0.04.

12.4 Conclusion

This Chapter presents the numerical investigation of the improved CFJ-EA2 aircraft at take-off condition. The takeoff performance of CFJ-EA2 is substantially improved using the super-lifting CFJ wing configuration to achieve ultra-high maximum lift coefficient. And the CFJ wing is designed to be rotatable to achieve ultra-high lift coefficient at high AoA. The 3D RANS simulation of CFJ-EA with the AoA of 30°, 40°, and 50° is performed using the C_μ from 0.2 to 0.6. The simulation results indicate that using the super-lift CFJ airfoil, the CFJ-EA can achieve the maximum lift coefficient of 6.9 at the incidence of 50° and C_μ of 0.6. The improved cruise performance of CFJ-EA2 airplane is also achieved with a higher wing loading, cruise

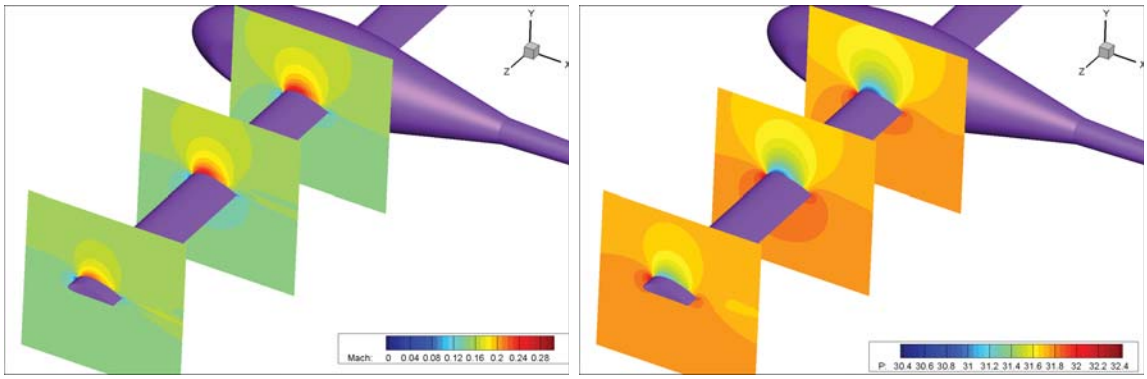

Figure 12.15: Mach number and pressure distributions along the CFJ-EA2 wing.

productivity efficiency, and range. The cruise lift coefficient is 1.59 and the drag coefficient is 0.037. The CFJ-EA2 airplane has a range of 531 nm with the gross weight of 2289 kg. The wing loading is increased to 214.24 kg/m^2.

CHAPTER 13

Conceptual Design of CFJ Regional Aircraft with Hybrid Electric Propulsion

13.1 Overview

The electric-based propulsion has attracted more and more interests in the aviation industry. Full electric propulsion relies on batteries as the sole energy source. Hybrid electric propulsion (HEP) is defined more broadly as described in Chapter 1, which is a fusion of combustion and electric propulsion system. It may or may not use a large amount of batteries as the only energy source.

The advantages of fully electric/hybrid electric propulsion techniques include less Carbon and NOx emissions, lower noise, and high efficiencies, etc. The justification for efficiency gains for electric propulsion is illustrated in . Despite their great potentials, the development of fully electric and hybrid electric propulsion in aviation is still in its embryonic stage.

The bottleneck for full electric propulsion is the lower energy and power density, which requires aircraft to carry a large amount of battery and the range is still quite limited if a full electric propulsion system is adopted. The hybrid electric propulsion provides an alternative approach, which may not carry massive amount of batteries.

For the hybrid electric propulsion system, the fuel engines always operate at its best efficiency point to achieve maximum efficiency and lowest running cost. The installed battery serves as a supplementary component, which is used to balance the power provided by the engine and the power required to sustain the aircraft.

The objective of this Chapter is to conduct a conceptual design of a CFJ regional airplane with hybrid electric propulsion. It will demonstrate the advantage of the CFJ wing as a crucial part of the high-efficiency distributed propulsion system.

13.2 Conceptual Design Method

13.2.1 Conventional Propulsion

For conventional aircraft, the propulsion is generated by combustion of jet fuel of internal combustion engines (ICE) or gas turbine engines. Jet fuel has a high specific energy value of 11.9 kWh/kg [157]. The total weight of energy storage is much lower compared with full electric propulsion. During the flight, the weight fraction of jet fuel is decreased. However, the thermodynamic process of engines has low efficiency of no greater than 40% to convert the chemical energy to mechanical energy. The fuel combustion exhausts CO_2 and NOx causes various environmental pollution.

13.2.1.1 Range Equations for Conventional Propulsion

For the steady, level cruise, the range of aircraft is determined by the Breguet range equation [15]:

For jet engines,

$$R = \frac{V}{C}\,\frac{L}{D}\,\ln(\frac{W_i}{W_f}) \tag{13.1}$$

For reciprocating propeller engines,

$$R = \frac{\eta}{C} \frac{L}{D} \ln(\frac{W_i}{W_f}) \tag{13.2}$$

where, V is the cruise velocity, L/D is the lift-to-drag ratio, C is the thrust specific fuel consumption (TSFC) for turbo-jet propulsion, or power specific fuel consumption (SFC) for propeller propulsion, η is the overall efficiency for propeller propulsion, W_i is the initial fuel weight, and W_f is the final fuel weight.

13.2.2 Full Electric Propulsion

13.2.2.1 Battery Technologies

The full electric propulsion uses battery based system to supply the required power and energy. Various types of battery systems have been developed for electric propulsion including Lithium-Ion (Li-Ion) battery, Lithium-Oxygen(Lithium-Air) battery, and Lithium-Sulfur (Li-S) battery. The Li-Ion battery is the most widely used energy storage system for electric powered vehicles including automobiles and aircraft. The specific energy of current Li-Ion battery is 0.1 - 0.265 kWh/kg. The Li-S and Li-Air are the promising technologies that attract considerable research interest due to their potential of high energy density. The gravimetric energy densities of Li-S and Li-Air are much higher than the Li-Ion battery. Although they have great potentials for the future energy storage technology significant problems remain unresolved, including poor cycle stability and low rate capability for practical applications [158]. However, practical applications of these technologies are not feasible yet.

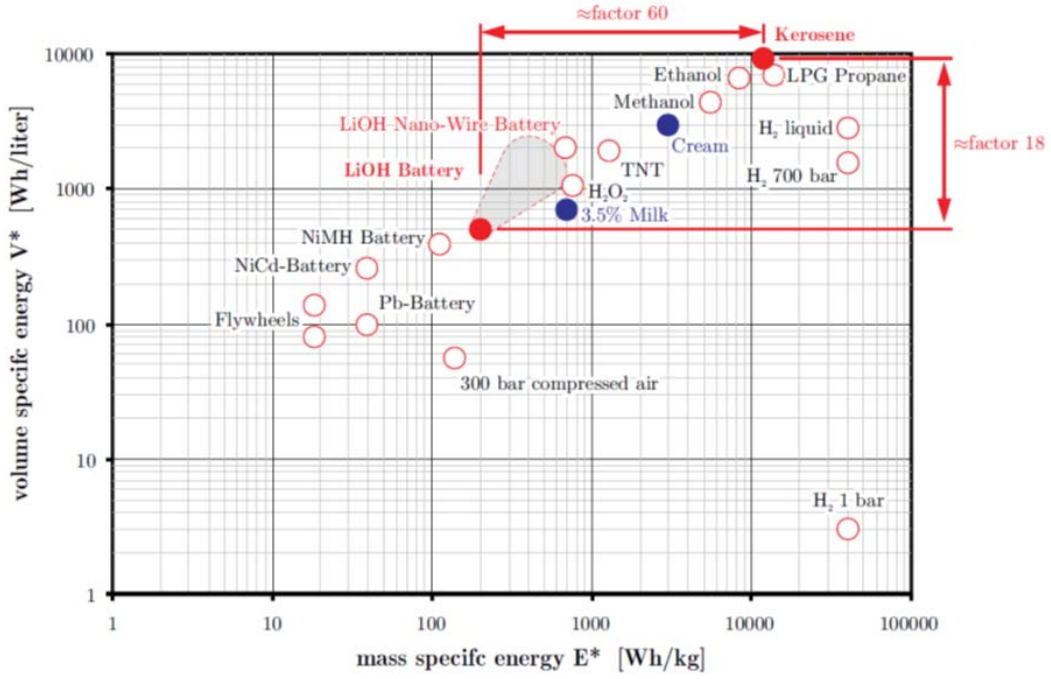

Figure 13.1: Volume and mass specific energy characteristics of different energy storage systems [36]

13.2.2.2 Electric Motor and Power Management System

For electric aircraft, the electric motors convert the electric power into the shaft power to drive propellers or fan propulsor. Therefore, selection and sizing of electric motors for aircraft propulsion are crucial. The electric motor system is desired to have high power density to reduce the aircraft weight and high efficiency to improve the system efficiency [159]. The typical gravimetric power densities of electric motors are between 2-10 kW/kg [157].

A power management system is required to maintain the voltage and current level for the electric motors, power distribution across the electric powertrain, and aircraft subsystems. The overall powertrain architecture provides sufficient safety redundancy for the aircraft propulsion system [159]. The power management and distribution system is required to ensure the operation of electric system, including the inverters,

converters and cables [157]. Besides, a converter/inverter module to control the motor power and speed is required to connect the motor to the DC distribution system. The specific power density of motor converters is 11 kW/kg [159]. A nickel-plated aluminum cable in [157] has the density of 0.00325 Kg/A/meter with an efficiency of 98.5%.

13.2.2.3 Range Equation for the Full Electric Propulsion

For all electric aircraft, the range depends on the maximum energy carried in the batteries. Assuming that the weight of propulsion system keeps constant during flight path. Consider an airplane in steady, level flight with the gross weight m_a and battery weight m_b. The propulsive power drawn from the battery through the drivetrain is determined by an overall efficiency, $\eta_{total} = \eta_{elec} \times \eta_{motor} \times \eta_{prop}$.

The maximum cruise time is limited by the energy carried in the battery. The range equation is described as,

$$R = e_b^* \, \eta_{total} \, \frac{L}{D} \, \frac{1}{g} \, \frac{m_b}{m_{aircraft}} \tag{13.3}$$

The aircraft range is determined by the battery specific energy, lift to drag ratio, the ratio of battery weight to the total aircraft weight, and overall efficiency. For a more rigorous derivation, see Appendix. A.

13.2.2.4 Comparison between Electric and Conventional Propulsion Systems

Various kinds of energy conversion systems are investigated by Hepperle [36] including Hydrogen/Kerosene fuel cell, Kerosene I/C engine generator hybrid system, a

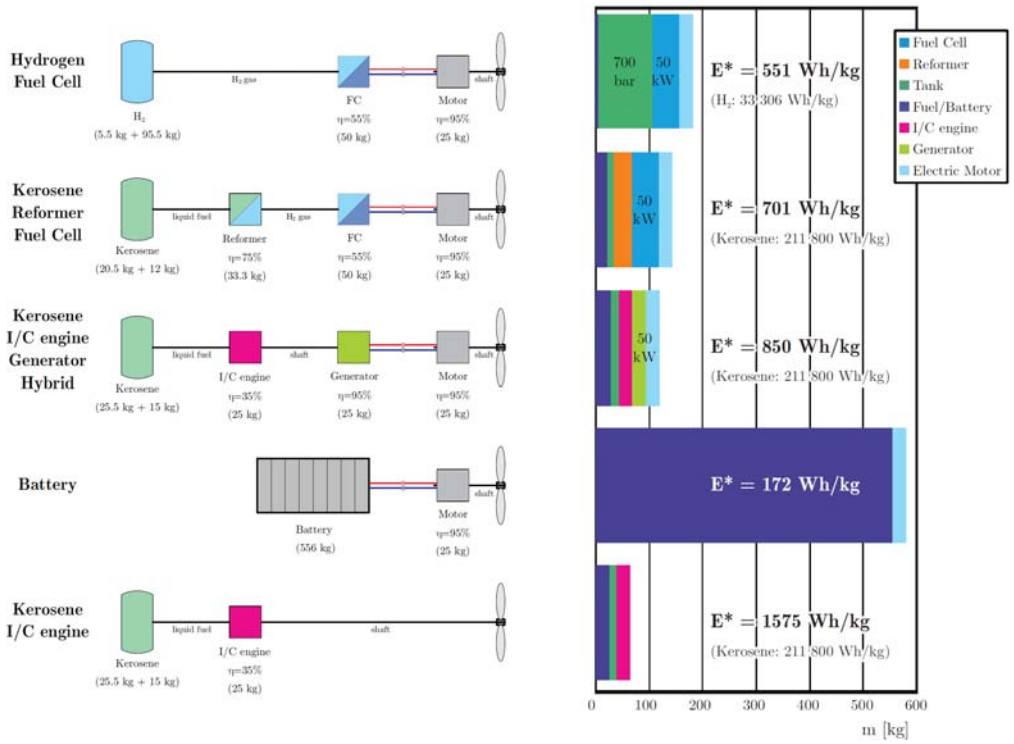

Figure 13.2: The Mass and equivalent energy density of propulsion systems providing a shaft power of 50 kW for 2 hours [36]. (E*: the equivalent energy density)

battery motor system, and a traditional Kerosene I/C engine system as shown in Fig. 13.2. The mass and equivalent energy density (E*) of the propulsion system is illustrated. The comparison shows that the battery system has a higher weight penalty despite its high energy conversion efficiency. The conventional internal combustion engine has the highest equivalent specific energy than other propulsion methods. The hybrid electric system based on IC engine introduces the generator and motor with some extra weight.

The comparison of energy conversion efficiency chains of turboprop, turbofan, battery, and fuel cell system are conducted by Hepperle [36] as illustrated in Fig. 13.3. The turboprop system has higher overall efficiency of 39% than the turbofan system with fan and nozzles. The battery electric systems has a much higher overall energy

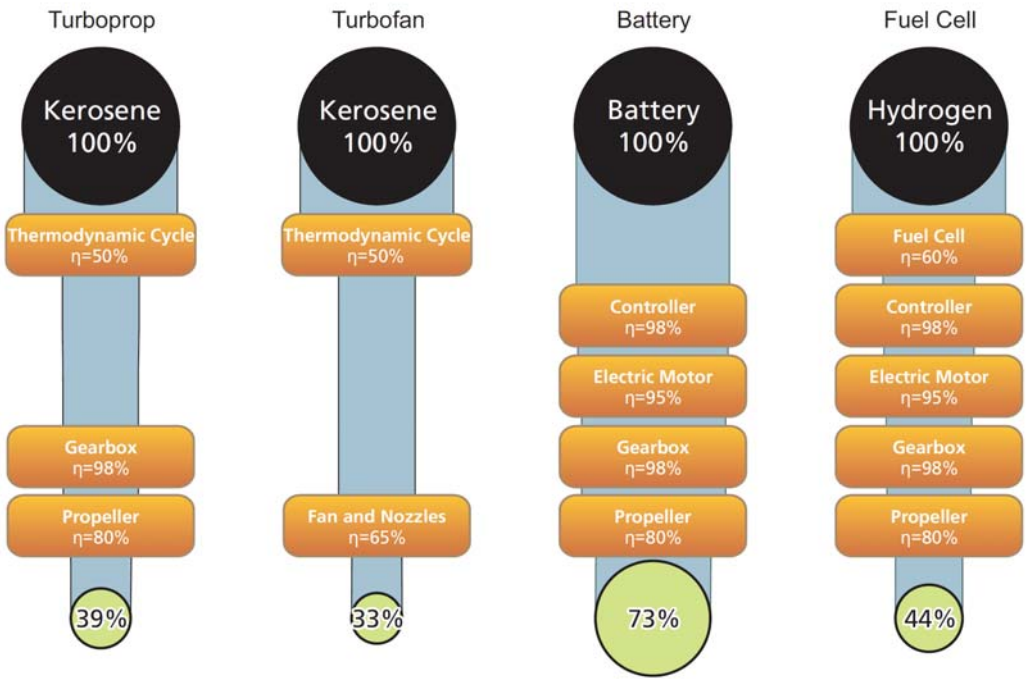

Figure 13.3: Typical on-board conversion chains with typical component efficiencies and total chain efficiency [36].

conversion efficiency. The overall battery system with controller, motor, gearbox, and propeller has a efficiency of 73%.

13.2.3 Hybrid Electric Propulsion

13.2.3.1 Hybrid Electric Propulsion Strategy

The hybrid electric propulsion strategy is defined as the power and energy storage combined by the conventional fuel and electric components. The electric propulsion has a high energy conversion efficiency but it has a penalty of heavy weight of batteries. The conventional propulsion has a high energy density of jet fuel and light-weight components but a lower energy conversion efficiency. The hybrid strategy takes advantages of the high efficiency of electric propulsion and high specific energy

of conventional aircraft engine. The hybrid propulsion strategy has been growing rapidly in the past decade.

As indicated in Chapter 1, two major types of hybrid strategies are commonly applied: series and parallel. In the series hybrid configuration, the chemical energy in jet fuel is converted to the electricity to charge the battery or to drive the motor. The series drivetrain is considered as the simplest configuration. The combustion engine can be downsized because power demands requirement for the engine is reduced. Moreover, the electrical power is easily distributed to multiple fans/propulsors for the purpose of distributed propulsion. Therefore, in this study, the series hybrid drivetrain is selected to design the CFJ distributed electric propulsion aircraft.

13.2.3.2 Range Equation for the Series Hybrid Electric Propulsion

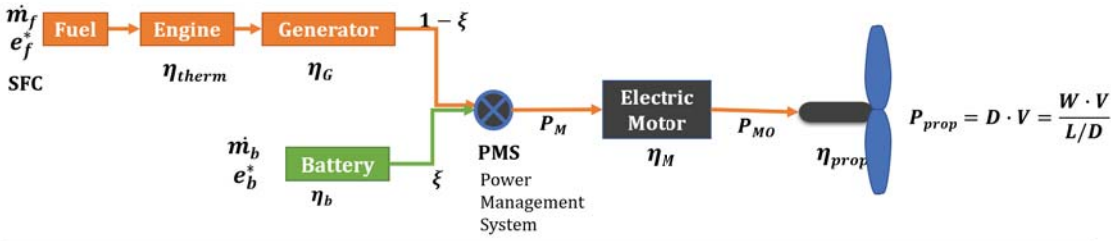

E_{total} : Total installed energy, (kWh)		η_{therm} :	Efficiency of the combustion engine;
E_b :	Battery installed energy, (kWh)	η_b :	Battery charging and discharging efficiency;
m_b :	Battery weight, (kg)	η_M :	Efficiency of the electric motor;
m_f :	Fuel weight, (kg)	η_{prop} :	Propeller efficiency;
e_b^* :	Battery Specific energy, (kWh/kg)	**SFC**:	Specific Fuel Consumption, SFC = $\frac{\dot{m}_f}{P_{turb}}$
e_f^* :	Fuel Specific energy, (kWh/kg)	P_M :	Electrical input power of the motor
ξ :	DoH in power, $\xi = \frac{P_b}{P_{total}}$	P_{MO}:	Output power of the motor, $P_{MO} = \eta_M \cdot P_M$
ψ :	DoH in energy, $\psi = \frac{E_b}{E_{total}} = \frac{m_b \cdot e_b^*}{m_f \cdot e_f^* + mb \cdot e_b^*}$	P_{prop}:	Propeller power, $P_{prop} = \eta_{prop} \cdot P_{shf}$

Figure 13.4: Diagram of series hybrid electric propulsion

The range equation is calculated by the integral of cruise velocity over time,

$$R = \int_{t_i}^{t_f} V_\infty \cdot dt \tag{13.4}$$

The total installed energy variation over time is the combination of battery energy variation and fuel energy variation.

$$\frac{dE_{total}}{dt} = \frac{dE_f}{dt} + \frac{dE_b}{dt} \tag{13.5}$$

where, E_{total} is the total energy installed (kWh); E_f and E_b stand for the energy stored in fuel and batteries (kWh) respectively.

Fuel Energy Change

The rate of fuel energy variation with time is determined by the fuel weight change.

$$\frac{dE_f}{dt} = \frac{dm_f \times e_f^*}{dt} = e_f^* \frac{dm_f}{dt} = e_f^* \, \dot{m}_f \tag{13.6}$$

where, e_f^* represents the fuel specific energy density (kWh/kg) and $\dot{m}_f$ is the mass flow rate of fuel consumption (kg/s).

The efficiency of a combustion engine can be represented by the Specific Fuel Consumption (SFC). SFC is the mass flow of fuel consumed to provide shaft power. It is defined by dividing the fuel mass flow rate (kg/s) to the shaft output power (kW), SFC $= \dot{m}_f / P_{shf}$.

The rate of fuel energy variation hence can be also described as:

$$\frac{dE_f}{dt} = \frac{SFC \cdot P_{MG} \cdot e_f^*}{\eta_G} \tag{13.7}$$

where, P_{MG} is the power input from engine generator to the motor; η_G is the energy conversion efficiency of the generator from the input shaft power to electric power output.

Battery Energy Change

The second term in Eq. 13.5 represents the variation of battery energy with time $\frac{dE_b}{dt}$; it can be calculated by the discharging rate. The batter weight is kept constant during flight.

Degree-of-Hybridization (DoH) for Power

The electrical power transmitted to the motor P_M has two sources: batteries and electric generator, $P_M = P_{Mb} + P_{MG}$ as illustrated in Fig. 13.4. For a hybrid-electric propulsion, the ratio of electric power to the total installed power is declared as the parameter ξ, also called the Degree-of-Hybridization (DoH) for power [5]. It represents the percentage of maximum installed power in the total maximum installed power (motor, and fuel engine).

$$\xi = \frac{P_{Mb}}{P_M} \tag{13.8}$$

Combine Eq. 13.6 and 13.7 together with the DoH parameter ξ, we get

$$\frac{dE}{dt} = \mathbf{A} \cdot P_M \tag{13.9}$$

where, $\mathbf{A} = \left(\frac{e_f^* \cdot SFC \cdot (1-\xi)}{\eta_G} + \frac{\xi}{\eta_b} \right)$, represents the combined energy conversion efficiency with the consumption of fuel and battery power.

For a steady and level cruise flight with the velocity of V_∞, $L = W$, $T = D$. The propulsive power required by the aircraft is calculated by $P_{prop} = \frac{W \cdot V_\infty}{L/D}$. The propulsive power is obtained from the motor output power with the propulsive efficiency $\eta_{prop} = \frac{P_{prop}}{P_{MO}}$; the motor output power is the product of total motor input power P_M and motor efficiency $\eta_M = \frac{P_{MO}}{P_M}$. Therefore, the motor input power can be obtained using the propulsive efficiency η_{prop} and motor efficiency η_M.

$$P_M = \frac{P_{MO}}{\eta_M} = \frac{P_{prop}}{\eta_M \cdot \eta_{prop}} = \frac{W \cdot V_\infty}{(L/D) \cdot \eta_{prop} \cdot \eta_M} \tag{13.10}$$

Therefore,

$$R = \int_{t_i}^{t_f} V_\infty dt = \int_{E_i}^{E_f} \frac{V_\infty}{\mathbf{A} \cdot P_M} \cdot dE = \frac{\eta_{prop} \cdot \eta_M}{\mathbf{A}} \cdot \frac{L}{D} \int_{E_i}^{E_f} \frac{1}{W}\, dE \tag{13.11}$$

Degree-of-Hybridization (DoH) for Energy

The ratio of stored electric energy to the total stored energy of the whole propulsion system is to describe the Degree-of-Hybridization (DoH) for energy [5],

$$\psi = \frac{E_b}{E} \tag{13.12}$$

where, the total energy is $E = E_f + E_b$.

Using above definition of DoH parameter ψ, the gross weight change is thus correlated with the total energy change,

$$dW = \frac{\psi e_f^* + (1-\psi) e_b^*}{e_f^*\, e_b^*}\, g\, dE = \frac{g}{\mathbf{B}}\, dE \tag{13.13}$$

where, $\mathbf{B} = \dfrac{e_f^*\, e_b^*}{\psi e_f^* + (1-\psi) e_b^*}$; it can be interpreted as an equivalent specific energy for the whole energy storage system.

Insert Eq. 13.13 into Eq. 13.11 and integrate this equation, we obtain the range equation for hybrid electric propulsion,

$$R = \frac{\mathbf{B} \cdot \eta_{prop} \cdot \eta_M}{\mathbf{A} \cdot g} \cdot \frac{L}{D} \cdot \ln\left(\frac{W_i}{W_f}\right) \tag{13.14}$$

13.3 CFJ Hybrid Electric Regional Airplane

Since there is a growing demand for short-haul airline market, this chapter choose to design a short-haul regional airplane as the example to demonstrate the advantage of CFJ aircraft with hybrid electric propulsion. Some hybrid electric aircraft

has aimed at the short haul airline market, such as the E-Fan X by Airbus, Rolls-Royce, and Siemens. The ATR72 families produced in France and Italy by aircraft manufacturer ATR widely are recognized as one of the most cost-effective regional aircraft for the past several decades. The ATR 72 is a short-haul regional airliner with twin turbo-prop engines made to carry 72 passengers. The ATR 72-500 has a high wing configuration equipped with twin P&W 127F/M turbo-prop engines, designed for efficiency and operational flexibility. The isometric view and dimension of ATR72 airliner is shown in Fig. 13.5. As a reference, the ATR72-500 is selected as the baseline short-haul airplane to compare the performance of the CFJ regional airplane with hybrid propulsion.

The goal of the conceptual design of the CFJ regional airplane is to use the advanced CFJ aircraft concept with hybrid electric propulsion to achieve high cruise efficiency and CO_2 emission reduction.

13.3.0.1 Design Requirement

The design of the CFJ regional airplane includes the major aircraft components: sizing, CFJ wing design, and turboelectric propulsion. The original empennage and landing gear are employed the same with the ATR72 aircraft. The sizing of fuselage is based on the original ATR72 scaled with the increased payload and passenger numbers.

An iterative procedure to determine the maximum takeoff weight of the CFJ-HERA aircraft based on Eqn. (31) is developed. The mission parameters of the CFJ-HERA are shown in Table 13.1. The major advantage of CFJ aircraft is its ultra-high productivity efficiency with high cruise lift coefficient. The present CFJ

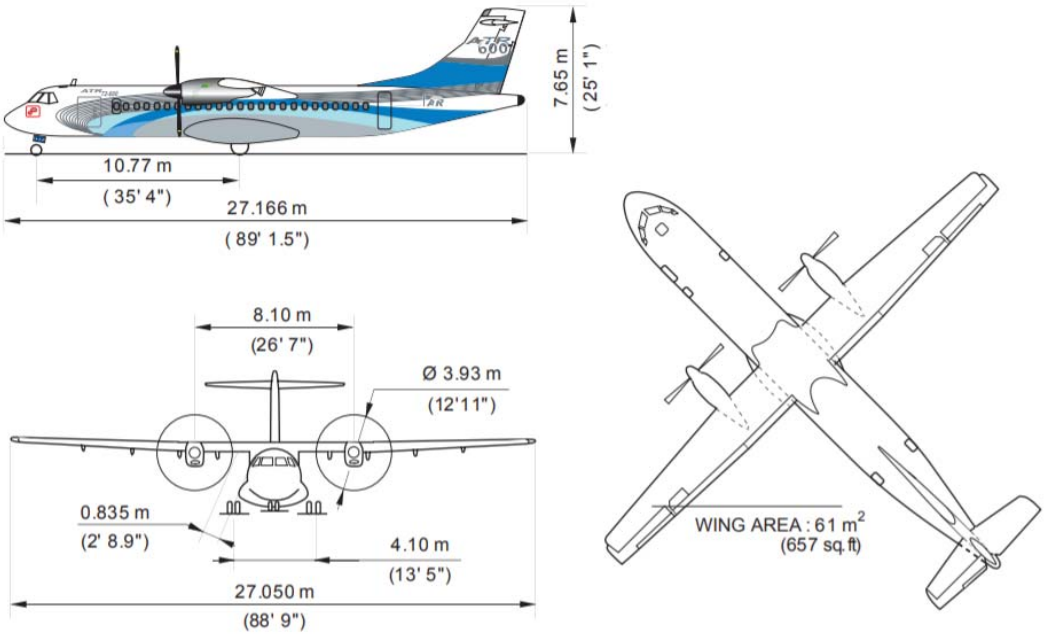

Figure 13.5: The isometric view and dimension of ATR72 regional airliner [37].

regional airliner has a productivity efficiency of 27, substantially higher than the estimated productivity efficiency of 15 for ATR72-500. The area and aspect ratio of the CFJ wing of the regional aircraft are kept the same as those of ATR72-500. The maximum takeoff weight and wing loading are substantially increased. The fuel capacity is increased to 14200 kg with the battery weight of 6200 kg. The CFJ-HERA regional airliner is depicted in Fig. 13.6.

The weight decomposition of the conventional turboprop airliner and CFJ hybrid electric airliner is illustrated in Fig. 13.7. With reference to the maximum takeoff weight (MTOW) of the conventional airliner, the total weight of a CFJ aircraft is substantially increased because of the high lift coefficient and wing loading of the CFJ wing. The hybrid electric airliner will carry a certain amount of battery for energy storage and distribution. The turbo engines always operates in the optimal

Figure 13.6: CFJ-HERA regional airliner.

efficiency point to provide energy to the propulsor and charge the battery during cruise. A certain amount of extra weight is also introduced by the powertrain system. The energy distribution of fuel and battery is controlled by the energy split factor ψ = 0.01 and power split factor $\xi = 0.01$. It means that during the entire cruise phase, the energy stored in the batteries ψ is 1%. The range of the hybrid electric airliner can be obtained using Eq. 31.

13.3.0.2 Propulsion System

The major difference of a hybrid electric propulsion system from a conventional one is the components associated with electric power transmission. Unlike the conventional aircraft that have integrated engines and propulsors with chemical energy directly converted to mechanical energy. the gas combustor, turbines, generators,

Table 13.1: Comparison of ATR72-500 and CFJ-HERA regional turboprop airliner mission performance

	ATR72-500	CFJ-HERA-72	Unit
Maximum Take-off Weight	22800	39500	kg
Range	890	2500	nm
Maximum payload weight	7200	7200	kg
Maximum fuel weight	5000	14200	kg
Battery weight	-	6200	kg
Passengers	72	72	-
Wing surface	61	61	m2
Wing span	27.05	27.05	m
Aspect ratio	12	12	-
Wing loading	369	660	m/s
Cruise Mach	0.46	0.46	-
Wing aerodynamic efficiency	23.91	23.2	-
Productivity efficiency	15.27	26.87	-

and electric motors are separated components for a hybrid electric propulsion system. For a serial hybrid electric propulsion, the first step is to convert chemical energy of kerosene into electricity. The combustor, turbine, and generator are required for this process. A power management system (PMS) is needed to control the electricity source, storage, distribution, and consumption. It also ensures safe operation by controlling the voltage and current level. The electric motor converts the electric energy into the shaft power, and drive the propeller.

13.3.0.3 CFJ Wing Design

The CFJ-NACA6421-INJ13-SUC20 airfoil is based on a trade study conducted by Yang Wang in our group at the University of Miami. The detailed trade study of the CFJ airfoil will be published in 2019 AIAA conference. The current CFJ airfoil

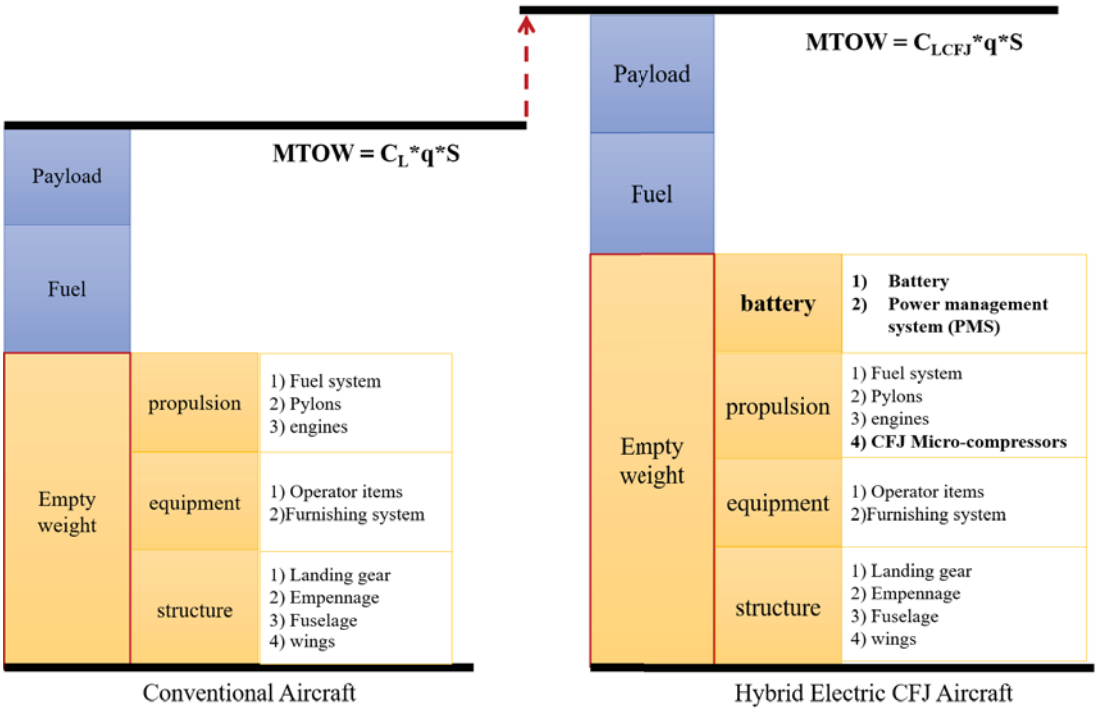

Figure 13.7: The weight decomposition of a conventional and CFJ airliner with hybrid electric propulsion

has an enlarged injection slot size and suction slot size compared with the one used in [35]. And the suction slot angle is adjusted to achieve drag reduction. The CFJ wing has a wing area of 61 m^2 and aspect ratio of 12. The CFJ-HERA wing with micro-compressors is shown in Fig. 13.8.

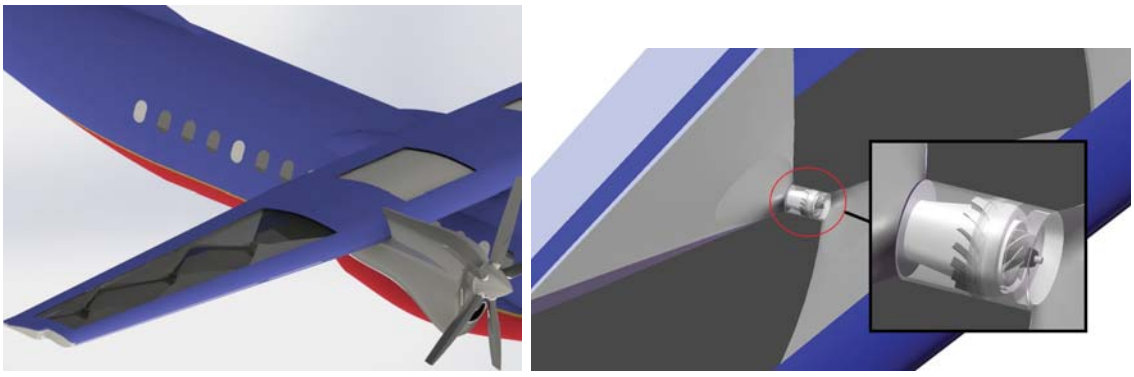

Figure 13.8: CFJ-HERA wing with Micro-compressors

Table 13.2: Weight decomposition of CFJ regional aircraft electric propulsion

Components	Gravimetric Densities	unit	Efficiencies	Weight(kg)
Electric motor	15	kW/kg	95%	175.0211
Inverter/converter	20	kW/kg	98%	131.2658
Electric cable	20	KW/kg	98.50%	131.2658
CFJ compressor	2	KW/kg	70%	256.1284
Total		kg		693.6811

	Specific Energy(kWh/kg)	Efficiencies	Weight(kg)
Fuel	11.6	35%	14200
Battery	0.26	95%	6200

* DoH for power = 0.01 and DoH for energy = 0.01

Table 13.3: The cruise parameters for CFJ Regional Aircraft

Airfoil	AoA	C_μ	C_L	C_D	P_c	C_L/C_D	C_L/C_{Dc}	C_L^2/C_{Dc}
CFJ-NACA6421	4	0.02	1.158	0.042	0.0079	27.57	23.2	26.87

13.3.0.4 Cruise Condition

The CFJ regional airliner cruises at the speed of Mach number of 0.46 at the altitude of 7600 m. A RANS study of the 3D CFJ wing is performed at the Mach number of 0.46 and Reynolds number of 3.0 million. The simulation predicts the lift coefficient of 1.158 and drag coefficient of 0.042 at the AoA of 4° and C_μ of 0.02. The corrected aerodynamic efficiency of 23.2 and productivity efficiency of 26.87 is achieved.

13.3.0.5 Takeoff/Landing Condition

To evaluate the takeoff/landing performance, the simulation of CFJ-HERA at high AoA and high C_μ is performed. For the CFJ-HERA, the takeoff speed is at Mach number of 0.15. At takeoff condition, the CFJ-HERA wing has the AoA of 30°

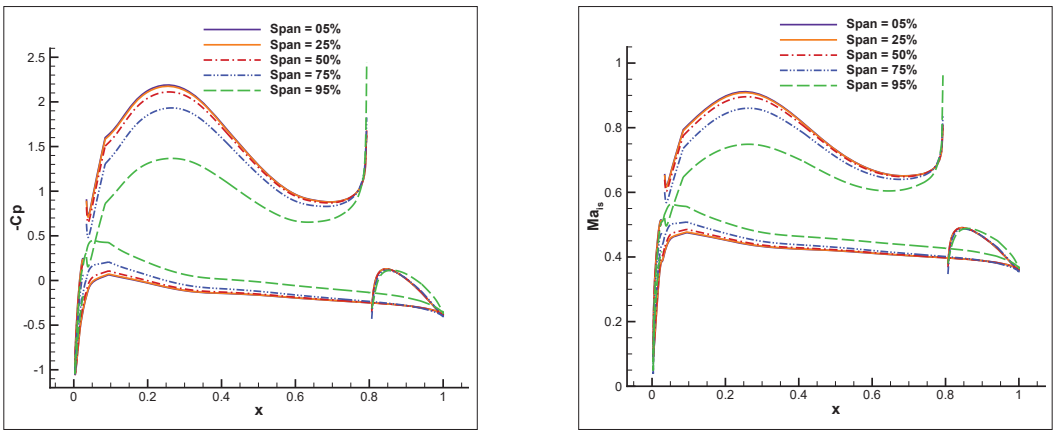

Figure 13.9: Pressure coefficient C_p and isentropic Mach number Ma_{is} of the CFJ-HERA wing at AoA of 4° and C_μ of 0.02.

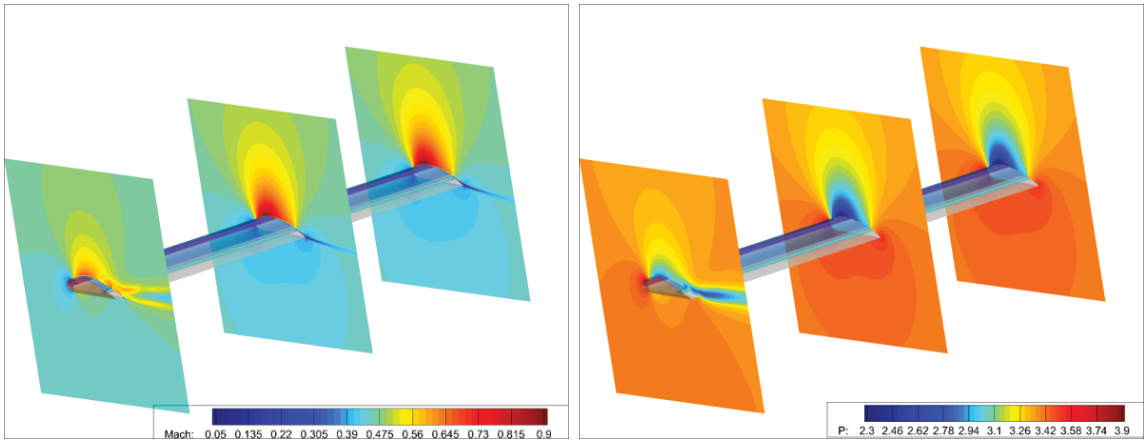

Figure 13.10: The Mach number and pressure contour of the CFJ-HERA wing

and C_μ of 0.4. The lift coefficient of 4.05 and drag coefficient of 0.425 are obtained. The power coefficient for CFJ Micro-compressors is 0.36. The local lift loading can be seen on the pressure coefficient (C_p) and isentropic Mach number (Ma_{is}) plots shown in Fig. 13.11. The suction peak is obtained near the LE of CFJ wing. The LE suction effect contributes to the lift increase and the pressure drag decrease. The lowest Cp and isentropic Mach number achieved are -17 and 0.6 respectively. The Mach and pressure contours are plotted for the takeoff condition at different spanwise locations in Fig.13.12.

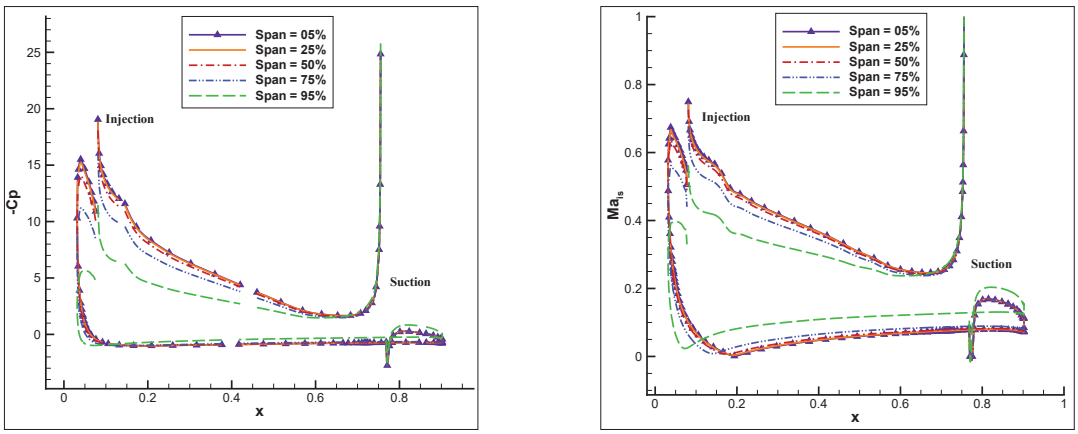

Figure 13.11: Pressure coefficient C_p and isentropic Mach number Ma_{is} of the CFJ-HERA wing at AoA of 30° and C_μ of 0.4.

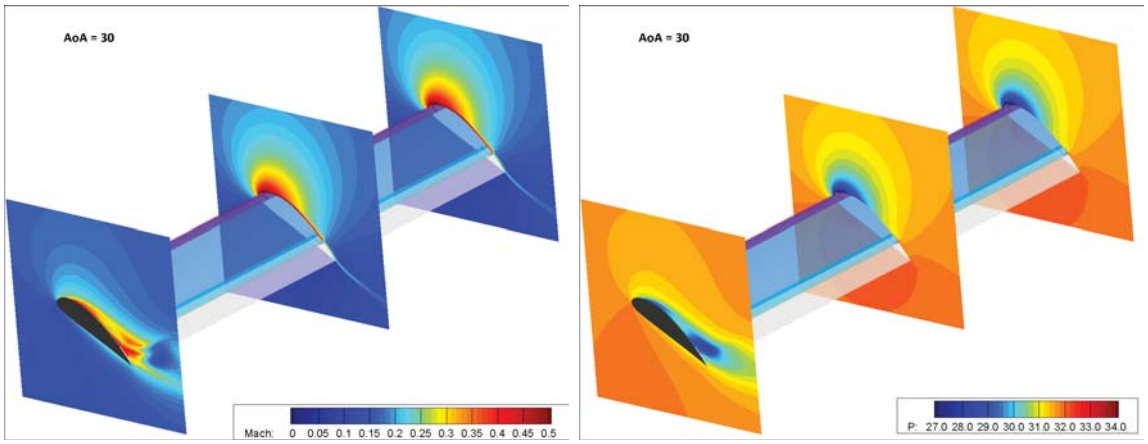

Figure 13.12: The Mach number and pressure contours of the CFJ-HERA wing at the takeoff condition

13.4 Conclusion

This Chapter presents a conceptual design of the novel CFJ aircraft with electric and hybrid electric propulsion. The range equations for electric and hybrid electric propulsion are derived for the design purpose. A CFJ hybrid electric regional airplane (CFJ-HERA) is designed. The CFJ regional aircraft cruises at Mach number of 0.46 with a range of 2500 nm. The aspect ratio of CFJ wing is 12 based on the CFJ-NACA6421-INJ13-SUC20 airfoil. The lift coefficient of 1.158 is achieved at the AoA

of 4 ° and C_μ of 0.02. Due to the high lift cruise coefficient of CFJ wing, the CFJ regional aircraft has a wing loading of 660 kg/m^2. The MTOW is increased to 39500 kg. The hybrid propulsion system is analyzed with various components including electric motor, inverter/converter, electric cable, and CFJ micro-compressors.

CHAPTER 14

Conclusions

14.1 Summary

In this dissertation, the investigation of super-lifting Co-Flow Jet flow control airfoil and its application to electric aircraft is conducted using computational fluid dynamics simulation and experimental testing. A high order CFD method with improved delayed detached eddy simulation (IDDES) is developed and applied to study the complex flow structures and energy transferring mechanism of the super-lifting CFJ airfoils and wings. The high fidelity IDDES method is validated using the turbulent flows over the flat plate and the separated flow over a NACA0012 airfoil at high angles of attack. The super-lift coefficient is discovered on a 2D airfoil for the first time using the CFJ flow control at a low energy expenditure. The C_{Lmax} of 12.6 is achieved, far greater than the theoretical limit of 7.6. The experimental testing on the CFJ-NACA6421 airfoil embedded with Micro-compressors proves that CFJ flow control is able to achieve super-lifting and thrusting coefficient simultaneously. Further numerical simulations are conducted on a 3D super-lifting CFJ wing with a variety of aspect ratios, angles of attack, and jet momentum coefficients. The 3D super-lifting CFJ wing can generate an ultra-high lift coefficient of 7.8 at AoA of 70°

with attached flow at a C_μ of 0.35. Then, the super-lifting CFJ airfoil is applied on a CFJ-EA airplane to improve its ESTOL performance. The cruise performance of the CFJ-EA airplane is also enhanced using a modified cruise-efficient CFJ airfoil. Lastly, using the hybrid electric propulsion and Co-Flow Jet flow control wings, a CFJ hybrid electric regional aircraft is designed to achieve high payload, high efficiency, and long range.

14.2 Conclusions

14.2.1 IDDES

First, the Improved Delayed Detached Eddy Simulation (IDDES) model is implemented in the in-house CFD code, FASIP and validated with the comparative study of the S-A URANS, DES, DDES and IDDES computation of the flat plate boundary layer and the stalled flow of the NACA0012 airfoil at different AoAs of 5°, 17°, 45°, and 60°. High order schemes are employed with the fifth order WENO reconstruction for the inviscid fluxes and 4th order central differencing for the viscous fluxes. For the flat plate turbulent boundary layer flow, the simulation results indicate that the IDDES predicts the law of the wall accurately for different mesh sizes, Reynolds numbers, and Mach numbers, whereas the DES and DDES obtain the velocity profile in the boundary layer with model stress depletion and log layer mismatched at certain conditions. For the NACA0012 stalled flows simulation, at low and medium AoAs(=5°, 17°), the URANS, DDES, and IDDES all predict the drag accurately. However, for the massive separated flows at high AoAs (=45°, 60°), the URANS over-predicts the drag coefficient significantly by about 30%, whereas the DDES and

IDDES predict the drag coefficient accurately. The vortical flow structures obtained by the URANS are highly-regularized vortex shedding dominated by the spanwise vorticity. The IDDES method can resolve more realistic flow structures, including smaller scale vortices that are chaotic and disorganized with streamwise, transverse and spanwise vortices.

14.2.2 Super-Lift Coefficient

The 2D RANS simulation has been performed on the CFJ flow control on the CFJ6421 airfoil, which indicates that CFJ airfoil is able to achieve the maximum lift coefficient far exceeding the theoretical limit at a very high AoA up to 70°. In addition to Super-Lift coefficient, CFJ airfoil can also substantially increase the cruise aerodynamic efficiency and productivity efficiency at low AoAs due to its increased lift, reduced drag, and very low energy expenditure. Two CFJ airfoil configurations have been created from the baseline NACA 6421 airfoil by translating the suction surface downward and adjusting the injection and suction slot sizes. One CFJ airfoil with smaller injection size is to achieve high C_{Lmax} for takeoff and landing. The other CFJ airfoil with larger injection size is to achieve high cruise efficiency. The first CFJ airfoil (CFJ6421-SST016-SUC053-INJ009) has the suction surface translation of 0.16% C, injection slot size of 0.09% C, and suction slot size of 0.53% C. The maximum lift coefficient of 12.6 is achieved at AoA=70°, Ma=0.063 and $C_{\mu} = 0.60$. It is 66% higher than the theoretical limit of 7.6 for a 21% thickness airfoil. The circulation achieved around the CFJ airfoil is so high that the stagnation point is detached from the airfoil solid body and the Kutta condition does not apply anymore. For the super-lift condition at AoA of 70°, the vortex structures in the CFJ injection region appear

to include 4 vortex layers next to each other from the airfoil wall surface to the far field freestream : 1) clockwise boundary layer vortex sheet on the airfoil suction surface downstream of the injection slot; 2) counter clockwise CFJ vortex layer due to the high momentum jet and the shear layer shed from the upstream leading edge boundary layer; 3) clockwise induced vortex layer induced by the high momentum co-flow jet via the mixing shear layer. Next to the induced vortex layer is a high momentum secondary induced jet; 4) the last vortex layer is a counter clockwise vortex layer, through which the secondary induced jet transits to the slower freestream velocity.

The 2D simulation indicates that the C_{Lmax} appears to have no limit. The C_{Lmax} limit from the potential flow is the result of imposing Kutta condition, which is necessary for potential flow, but not a true physical condition that realistic flows must satisfy. In reality, C_{Lmax} depends on how much energy can be added to the flow, which varies with the active flow control method. It indicates that the C_{Lmax} is correlated very well with the CFJ power coefficient. The C_{Lmax} increase is very sensitive to energy addition when the C_{Lmax} is at low level. There is almost a linear relationship between the C_{Lmax} increase and the CFJ power consumed at low C_{Lmax} level. The C_{Lmax} eventually becomes plateaued even with continuously increased consumption of CFJ power. This is because when the C_{Lmax} is very high, it is very difficult to add more energy to the flow due to the very severe adverse pressure gradient. How to make an AFC to achieve the highest C_{Lmax} at the lowest energy expenditure is a very interesting research topic.

A new parameter named productivity efficiency defined as C_L^2/C_D is introduced to measure the cruise transportation capability of aircraft to carry its total weight for maximum distance. The second CFJ airfoil (CFJ6421-SST143-SUC133-INJ065)

is redesigned with slightly modified leading edge radius, and has the SST of 1.43%C, INJ of 0.65% C, and SUC of 1.33 % C. For the second CFJ airfoil with an assumed CFJ pumping efficiency of 80%, the peak aerodynamic efficiency $(L/D)_c$ is about 53% higher than that of the baseline airfoil. The productivity efficiency $(C_L^2/C_D)_c$ of the CFJ airfoil is 109% higher. The CFJ airfoil is demonstrated by validated numerical simulation to be able to achieve super-lift coefficient for ESTOL performance at takeoff/landing at very high angle of attack and ultra-high efficiency for cruise at low angel of attack.

14.2.3 IDDES Investigation of CFJ Super-Lift Coefficient

The validated IDDES method is employed to study the CFJ6421 airfoil with the span length of 10% chord. The three-dimensional flow structures and vortices at high AoAs are investigated. Three different jet momentum coefficient from $C_\mu = 0.25$ to $C_\mu = 0.5$ simulated at the Mach number of 0.028 and the Reynolds number of 4.8×10^5. The IDDES study indicates that CFJ active flow control airfoil is able to achieve the super-lift coefficient exceeding the theoretical limit at a very high AoAs with attached flow. The super-lift coefficient is also achieved by the three-dimensional IDDES study. The qualitative counter-rotating vortex structures at very high AoA and severe adverse pressure gradient is similar to those observed in 2D RANS simulation.

14.2.4 Study of 3D High Lift CFJ Wings

The finite-span super-lifting CFJ wings with different aspect ratios are investigated using 3D steady RANS simulation. The simulation is conducted at high angle

of attack of 25°-70° and C_μ of (0.15-0.35) aiming at the ultra-high lift conditions. The RANS simulation results indicate that CFJ wing is able to achieve the maximum lift coefficient of 7.8 without any flaps at a very high AoA of 70° with fairly good aerodynamic efficiency. For high AoAs, the outer 25% wingspan is affected most by the wingtip vortex contributing the lift reduction and drag increase. The Oswald efficiency is increased with the AR decreased from 20 to 5 at the same AoA and C_μ. It achieves the value as high as 0.967 for AR of 5, C_μ of 0.25 and AoA of 25°, indicating that the penalty of induced drag for 3D CFJ wing is small with decreased aspect ratio even though very high lift coefficient is obtained. The lowest value of the Oswald efficiency is 0.726 occurring at AR of 20, C_μ of 0.25, and AoA of 70°.

14.2.5 CFJ Cylinder

The CFJ flow control on circular cylinder has also been investigated to achieve the ultra-high maximum lift coefficient at a considerably low energy expenditure. The 2D RANS study indicates that CFJ flow control is able to achieve the maximum lift coefficient far exceeding the potential limit with Kutta condition applied on the cylinder. Various CFJ cylinder configurations are created for parametric trade study. The best lift coefficient with highest efficiency is obtained at the suction slot location at and injection slot location at 0°. The injection slot location of 0° appears to be the optimum for all the aerodynamic and efficiency performance. The maximum lift coefficient of C_L=28 is achieved at $C_\mu = 0.8$.

14.2.6 Wind Tunnel Experimental Study of CFJ Airfoil

The wind tunnel testing of CFJ airfoil with embedded compressors proves experimentally for the first time that an airfoil can achieve a lift coefficient exceeding the potential flow theoretical limit by using Co-Flow Jet active flow control. The CFJ airfoil is also able to generate a very high thrust coefficient. Both the high lift and thrust are attributed to the super-suction effect with very low pressure at the airfoil leading edge induced by the injection jet. The CFJ airfoil appears to be the only man made airfoil that can generate ultra-high lift and thrust simultaneously without flapping. The CFJ airfoil in the experiment is actuated by micro-compressors embedded inside the airfoil. The C_{Lmax} achieved in the experiment varies from 8.0 to 8.6, substantially exceeding the theoretical limit of 7.6. A very large thrust coefficient (negative drag) of 1.0 is achieved at low angle of attack (AoA). A thrust is maintained up to the angle of attack of 40° when the airfoil is about to get stalled. This study indicates that the perceived airfoil lift coefficient limit in the past 5 decades is artificial due to enforcing the Kutta condition, which is a mathematical condition necessary for airfoil potential flow, not a physical condition. This study may expand classical fluid mechanics to new territory and foster industrial applications very different from the current technologies.

14.2.7 Full CFJ Electric Aircraft

The super-lifting CFJ airfoil is applied on the CFJ-EA aircraft to improve its takeoff performance. And the CFJ-EA2 wings are designed to be pivotable to achieve an ultra-high lift coefficient at a high AoA. The 3D steady RANS simulation of CFJ-EA2 with the AoA of 30°, 40°, and 50° is performed using the C_μ from 0.2 to 0.6. The

simulation results indicate that using the super-lift wing configuration, the CFJ-EA can achieve the maximum lift coefficient of 6.9 at a very high AoA of 50° with a good aerodynamic efficiency. For high AoAs, the wing tip flow field is slightly affected by the tip vortex. The improved cruise performance of CFJ-EA2 wings is also achieved with a higher wing loading, cruise productivity efficiency, and range. The cruise lift coefficient is 1.59 and the drag coefficient is 0.037. The CFJ-EA2 airplane has a range of 531 nm with the gross weight of 2289 kg. The wing loading is increased to 214.24 kg/m^2.

14.2.8 Hybrid Electric CFJ Aircraft

A conceptual design of the novel CFJ hybrid electric propulsion airliner(CFJ-HERA) is investigated. The range equation for electric and hybrid electric propulsion are derived for a design with a series hybrid propulsion, which has the batteries pre-charged before takeoff and no battery charge during the flight. The CFJ-HERA cruises at Mach number of 0.46 with a range of 2500 nm. The CFJ wing has an aspect ratio of 12 based on the CFJ-NACA6421-INJ13-SUC20 airfoil. The lift coefficient of 1.158 is achieved at the AoA of 4 ° and C_μ of 0.02. Due to the high lift cruise coefficient of CFJ wing, the CFJ regional aircraft has a wing loading of 660 kg/m^2. The MTOW is increased to 39500 kg.

14.3 Summary of Contributions

The main contributions achieved in this dissertation include:

- The improved delayed detached eddy simulation with high order schemes has been validated on the turbulent boundary layer flow and massively separated flow over NACA0012 airfoil.

- Super Lift coefficient is discovered for 2D CFJ airfoil flows, which has the lift coefficient exceeding the potential flow lift coefficient limit. Numerical simulation indicates that the C_{Lmax} appears to have no limit depending on how much energy can be added into the flow by a flow control method.

- The 2D CFJ airfoil can achieve super-lift coefficient with a maximum lift coefficient of 12.6 at AoA=70°, M=0.063 and $C\mu = 0.60$. The circulation achieved around the CFJ airfoil is so high that the stagnation point is detached from the airfoil solid body and the Kutta condition does not apply anymore.

- The CFJ cylinder is investigated to achieve a ultra-high maximum lift coefficient of 28 at $C_\mu = 0.8$ with a considerably low energy expenditure than conventional rotating cylinder flow control method.

- The 3D flow structures and vortices for CFJ6421 airfoil at high AoAs are investigated using validated IDDES method with the super-lift coefficient achieved.

- The 3D finite span CFJ wing is able to achieve the maximum lift coefficient of 7.8 without any flaps at a very high AoA of 70° with fairly good aerodynamic efficiency.

- The wind tunnel testing of CFJ airfoil with embedded compressors proved experimentally for the first time the super-lifting thrusting phenomenon. The C_{Lmax} achieved in the experiment varies from 8.0 to 8.6, substantially exceed-

ing the theoretical limit of 7.6. A very large thrust coefficient (negative drag) of 1.0 is achieved at low angle of attack.

- The CFJ electric aircraft with super-lift CFJ configuration achieves the maximum lift coefficient of 6.9 at a very high AoA of 50°.

- The conceptual design methodology of CFJ hybrid electric airliner is developed. A CFJ regional aircraft with hybrid electric propulsion is designed with a range of 2500 nm and MTOW of 39500 kg.

14.4 Future Work

14.4.1 CFJ Development on Transonic and Supersonic Flows

The CFJ flow control has shown its tremendous advantages on super-high lift coefficient for extremely short takeoff and landings. The CFJ flow control method has great potential to transform the commercial transonic airliners with both ESTOL and ultra-high cruise efficiency. For transonic and supersonic flows, due to the existence of shock wave, the drag reduction mechanism is different than the low-speed general aviation aircraft. Therefore, the implementation of CFJ flow control needs to be explored for good energy efficiency for future transonic and supersonic aircraft.

14.4.2 Validation of CFJ Cylinder using LES/IDDES and Wind Tunnel Testing

The 2D investigation of CFJ cylinder has achieved super-high lift coefficient with very lower energy cost compared to the rotating cylinder. However, due to universal

filtering of RANS method, the lift and drag coefficient are overestimated by 2D RANS simulation. Therefore, the LES or IDDES methods are more appropriate to simulate the complex flow structures and study the energy transferring mechanism.

The wind tunnel testing is desirable to prove that the CFJ concept on cylinder can achieve super-lift coefficient with much lower energy expenditure than the rotating cylinder flow control.

APPENDIX

Range Equation for Hybrid Electric Propulsion

A1. Range Equation for Full Electric Propulsion

For all electric aircraft, the range depends on the maximum energy carried in the batteries. The weight of propulsion system keeps constant during flight path. Considering an airplane in steady, level flight with the gross weight m_a and battery weight m_b. The maximum cruise time is limited by the energy carried in the battery.

$$t = \frac{m_b \times e_b^*}{P_b} \tag{1}$$

Then the range is R $= V_\infty \times t$. The power drawn from the battery is related to the propulsive power through the drivetrain with an overall efficiency $\eta_{total} = \eta_{elec} \times \eta_{motor} \times \eta_{prop}$,

$$P_b = \frac{P_{aircraft}}{\eta_{total}} \tag{2}$$

The power drives the aircraft is determined by the lift to drag ratio, flight speed, and weight.

$$P_{aircraft} = D \times V_\infty = L \times \frac{D}{L} \times V_\infty = \frac{W_{aircraft}}{L/D}\, V_\infty \tag{3}$$

Therefore,

$$P_{battery} = \frac{W_{aircraft}}{L/D\ \eta_{total}}\, v_\infty \tag{4}$$

Finally, insert the P_b into the Range equation,

$$\mathrm{R} = e_b^*\, \eta_{total}\, \frac{L}{D}\, \frac{1}{g}\, \frac{m_b}{m_{aircraft}} \tag{5}$$

A2. Range Equation for Hybrid Electric Propulsion

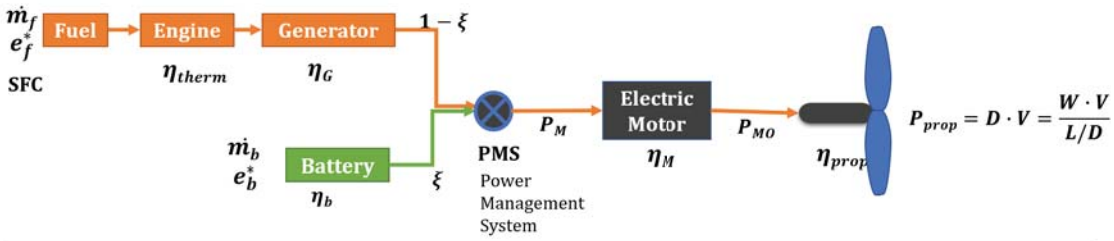

E_{total} : Total installed energy, (kWh)		η_{therm} :	Efficiency of the combustion engine;
E_b :	Battery installed energy, (kWh)	η_b :	Battery charging and discharging efficiency;
m_b :	Battery weight, (kg)	η_M :	Efficiency of the electric motor;
m_f :	Fuel weight, (kg)	η_{prop} :	Propeller efficiency;
e_b^* :	Battery Specific energy, (kWh/kg)	SFC:	Specific Fuel Consumption, SFC = $\frac{\dot{m}_f}{P_{turb}}$
e_f^* :	Fuel Specific energy, (kWh/kg)	P_M :	Electrical input power of the motor
ξ :	DoH in power, $\xi = \frac{P_b}{P_{total}}$	P_{MO}:	Output power of the motor, $P_{MO} = \eta_M \cdot P_M$
ψ :	DoH in energy, $\psi = \frac{E_b}{E_{total}} = \frac{m_b \cdot e_b^*}{m_f \cdot e_f^* + mb \cdot e_b^*}$	P_{prop}:	Propeller power, $P_{prop} = \eta_{prop} \cdot P_{shf}$

Figure 1: Diagram of series hybrid electric propulsion

The range equation is calculated by the integral of cruise velocity over time,

$$R = \int_{t_i}^{t_f} V_\infty dt \tag{6}$$

The total installed energy variation over time is the combination of battery energy variation and fuel energy variation.

$$\frac{dE_{total}}{dt} = \frac{dE_f + dE_b}{dt} = \frac{dE_f}{dt} + \frac{dE_b}{dt} \tag{7}$$

where, E_{total} is the total energy installed (kWh); E_f and E_b represent the energy stored in fuel form and in batteries (kWh) respectively.

Fuel Energy Variation

The rate of fuel energy over time is determined by the fuel weight variation.

$$\frac{dE_f}{dt} = \frac{dm_f \times e_f^*}{dt} = e_f^* \frac{dm_f}{dt} = e_f^* \, \dot{m}_f \tag{8}$$

where, e^* represents specific energy density (kWh/kg) and $\dot{m}_f$ is the mass flow rate of fuel consumption (kg/s).

The fuel efficiency of an engine can be represented by the Specific Fuel Consumption (SFC). SFC is the mass flow of fuel needed to provide the net thrust or shaft power. It is defined by dividing the fuel mass flow rate (kg/s) to the shaft output power (kW),

$$\text{SFC} = \frac{\dot{m}_f}{P_{shf}} \tag{9}$$

Insert SFC definition into the dE_f Eqn. 8,

$$\frac{dE_f}{dt} = \text{SFC} \cdot P_{shf} \cdot e_f^* \tag{10}$$

$\frac{dE_f}{dt}$ can also be described using the energy conversion efficiency chains,

$$P_{shf} = e_f^* \cdot \dot{m}_f \cdot \eta_t \tag{11}$$

where, η_{therm} is the thermal efficiency of the engine.

Then, the power output from the generator can be described as

$$P_{MG} = P_{shf} \cdot \eta_G \tag{12}$$

where, η_G is the energy conversion efficiency of the generator from the input shaft power to electric power output.

Therefore, the rate of fuel energy variation rate derived as,

$$\frac{dE_f}{dt} = \frac{SFC \cdot P_{MG} \cdot e_f^*}{\eta_G} \tag{13}$$

Battery Energy Variation

The second term in Eq. 7 represents the change of battery energy with time $\frac{dE_b}{dt}$; it can be calculated by

$$\frac{dE_b}{dt} = \text{const} \tag{14}$$

Here, we assume that the battery discharge rate is constant. The weight of battery remains basically unchanging.

Electrical Power

The electrical power transmitted to the motor P_M has two sources: batteries and electric generator,

$$P_M = P_{Mb} + P_{MG} \tag{15}$$

For a hybrid-electric propulsion, the ratio of electric power to the total installed power is declared as the parameter ξ, also called as the Degree-of-Hybridization (DoH) for power [5]. It represents the percentage of maximum installed electric power in the total maximum installed power (motor, and fuel engine).

$$\xi = \frac{P_{Mb}}{P_M} \tag{16}$$

Then, the rate of variation of battery installed energy is represented as,

$$\frac{dE_b}{dt} = \frac{P_{Mb}}{\eta_b} = \frac{P_M \ \xi}{\eta_b} \tag{17}$$

where η_b is the battery energy conversion efficiency.

Combine Eq. (10) and (17), we get

$$\frac{dE}{dt} = SFC \cdot P_{MG} \cdot e_f^* + \frac{P_{Mb}}{\eta_b} = P_M \left(\frac{e_f^* \cdot SFC \cdot (1-\xi)}{\eta_G} + \frac{\xi}{\eta_b} \right) \tag{18}$$

To simplify the above formula,

$$\frac{dE}{dt} = \mathbf{A} \cdot P_M \tag{19}$$

where, $\mathbf{A} = \left(\frac{e_f^* \cdot SFC \cdot (1-\xi)}{\eta_G} + \frac{\xi}{\eta_b} \right)$, represents the combined energy conversion efficiency with the consumption of fuel and battery power.

$$dt = \frac{dE}{\mathbf{A} \cdot P_M} \tag{20}$$

For a steady and level cruise flight with the velocity of V_∞, $L = W$, $T = D$. The propulsive power required by the aircraft is calculated by

$$P_{prop} = T \cdot V_\infty = D \cdot V_\infty = \frac{W \cdot V_\infty}{L/D} \tag{21}$$

The propulsive power is obtained from the motor output power with the propulsive efficiency $\eta_{prop} = \frac{P_{prop}}{P_{MO}}$; the motor output power is the product of total motor input power P_M and motor efficiency $\eta_M = \frac{P_{MO}}{P_M}$. Therefore, the motor input power can be obtained using the propulsive efficiency η_{prop} and motor efficiency η_M.

$$P_M = \frac{P_{MO}}{\eta_M} = \frac{P_{prop}}{\eta_M \cdot \eta_{prop}} = \frac{W \cdot V_\infty}{(L/D) \cdot \eta_{prop} \cdot \eta_M} \tag{22}$$

Therefore,

$$R = \int_{t_i}^{t_f} V_\infty dt = \int_{E_i}^{E_f} \frac{V_\infty}{\mathbf{A} \cdot P_M} \cdot dE = \int_{E_i}^{E_f} \frac{\eta_{prop} \cdot \eta_M}{\mathbf{A} \cdot W} \cdot \frac{L}{D}\, dE \tag{23}$$

$$R = \frac{\eta_{prop} \cdot \eta_M}{\mathbf{A}} \cdot \frac{L}{D} \int_{E_i}^{E_f} \frac{1}{W}\, dE \tag{24}$$

The overall aircraft weight consists of the four contributions: empty weight, payload weight, fuel weight, and battery weight,

$$W = W_{empty} + W_{payload} + W_f + W_b \tag{25}$$

The total stored energy of the whole propulsion system E is the sum of electric energy and fuel energy,

$$E = E_f + E_b = e_f^* \, m_f + e_b^* \, m_b \tag{26}$$

The ratio of stored electric energy to the total stored energy of the whole propulsion system is to describe the Degree-of-Hybridization (DoH) for energy [5],

$$\psi = \frac{E_b}{E} = \frac{e_b^* \, m_b}{e_f^* \, m_f + e_b^* \, m_b} \tag{27}$$

$$W_f + W_b = (m_f + m_b)g = (\frac{E(1-\psi)}{e_f^*} + \frac{E\psi}{e_b^*})g = \frac{\psi e_f^* + (1-\psi)e_b^*}{e_f^* \, e_b^*} gE \tag{28}$$

$$W = \frac{\psi e_f^* + (1-\psi)e_b^*}{e_f^* \, e_b^*} gE + W_{structure} + W_{payload} \tag{29}$$

The change of aircraft gross weight is thus correlated with the total energy change,

$$dW = \frac{\psi e_f^* + (1-\psi)e_b^*}{e_f^* \, e_b^*} \, g \, dE = \frac{g}{\mathbf{B}} \, dE \tag{30}$$

where, $\mathbf{B} = \dfrac{e_f^* \, e_b^*}{\psi e_f^* + (1-\psi)e_b^*}$, it can be interpreted as an equivalent specific energy for the whole energy storage system.

Insert Eq. 30 into Eq. 24 and integrate this equation, we obtain the range equation for hybrid electric propulsion,

$$R = \frac{\mathbf{B} \cdot \eta_{prop} \cdot \eta_M}{\mathbf{A} \cdot g} \cdot \frac{L}{D} \cdot \ln\left(\frac{W_i}{W_f}\right) \tag{31}$$

For the pure fuel case, If $\psi = 0$, then $\mathbf{B} = e_f^*$; If $\xi = 0$, then $\mathbf{A} = \frac{e_f^* \cdot SFC}{\eta_g}$, If we assume that $\eta_G = 100\%$, $\eta_M = 100\%$. the range equation is reduced to

$$R = \frac{\eta_{prop}}{SFC \cdot g} \cdot \frac{L}{D} \cdot \ln\left(\frac{W_i}{W_f}\right) \tag{32}$$

which is exactly the same as Bregruet range equation.

Bibliography

[1] NASA, "New Aviation Horizons Initiative and Complementary Investments." NASA Aeronautics 10-Year Plan, https://www.nasa.gov/sites/default/files/atoms/files/ nasa-aero-10-yr-plan-508-reduced.pdf, 2016. accessed 12/27/2017.

[2] P. Okonkwo and H. Smith, "Review of Evolving Trends in Blended Wing Body Aircraft Design," *Progress in Aerospace Sciences*, vol. 82, pp. 1–23, 2016.

[3] B. Blumenthal, A. A. Elmiligui, K. Geiselhart, R. L. Campbell, M. D. Maughmer, and S. Schmitz., "Computational Investigation of a Boundary Layer Ingestion Propulsion System for the Common Research Model." 46th AIAA Fluid Dynamics Conference, AIAA Aviation Forum (AIAA 2016-3812), 2007.

[4] A. S. Gohardani, G. Doulgeris, and R. Singh, "Challenges of Future Aircraft Propulsion: a Review of Distributed Propulsion Technology and Its Potential Application for the All Electric Commercial Aircraft," *Progress in Aerospace Sciences*, vol. 47, no. 5, pp. 369–391, 2011.

[5] C. Pornet and A. Isikveren, "Conceptual Design of Hybrid-electric Transport Aircraft," *Progress in Aerospace Sciences*, vol. 79, no. Supplement C, pp. 114 – 135, 2015.

[6] R. DelRosario, "A Future With Hybrid Electric Propulsion Systems: a NASA Perspective." Turbine Engine Technology Symposium Oral/Visual Presentation, 2014.

[7] W.-C. Sun, K. Broichhausen, J. Seifert, and B. Luftfahrt eV, "Promissing Future Aircraft Concepts - ESTOL." 26th Congress of the international council of the aeronautical sciences, 2008.

[8] A. Lefebvre, B. Dano, W. Bartow, M. Fronzo, and G. Zha, "Performance and Energy Expenditure of Co-flow Jet Airfoil With Variation of Mach Number," *Journal of Aircraft*, vol. 53, no. 6, pp. 1757–1767, 2016.

[9] S. G. Anders, W. L. Sellers, and A. E. Washburn, "Active Flow Control Activities at NASA Langley." 2nd AIAA Flow Control Conference, Fluid Dynamics and Co-located Conferences, 2004.

[10] A. O. Smith, "High-lift Aerodynamics," *Journal of Aircraft*, vol. 12, no. 6, pp. 501–530, 1975.

[11] J. D. Anderson Jr, *Fundamentals of Aerodynamics*. Tata McGraw-Hill Education, 2010.

[12] J. Chattot and M. Hafez, "Theoretical and Applied Aerodynamics," *Theoretical and Applied Aerodynamics: and Related Numerical Methods*, 2015.

[13] G. E. Erickson, "High Angle-of-attack Aerodynamics," *Annual review of fluid mechanics*, vol. 27, no. 1, pp. 45–88, 1995.

[14] J. D. Anderson, *Aircraft Performance and Design*. McGraw-Hill Science Engineering Math, 1999.

[15] T. C. Corke, *Design of Aircraft*. Pearson College Division, 2003.

[16] V. Ciobaca and J. Wild, "An Overview of Recent DLR Contributions on Active Flow-separation Control Studies for High-lift Configurations," *AerospaceLab*, no. 6, pp. 1–12, 2013.

[17] R. Radespiel, M. Burnazzi, M. Casper, and P. Scholz, "Active Flow Control for High Lift With Steady Blowing," *The Aeronautical Journal*, vol. 120, no. 1223, pp. 171–200, 2016.

[18] J. C. Lin, E. A. Whalen, J. L. Eppink, E. J. Siochi, M. G. Alexander, and M. Y. Andino, "Innovative Flow Control Concepts for Drag Reduction." 54th AIAA Aerospace Sciences Meeting, AIAA SciTech Forum, (AIAA 2016-0864), 2016.

[19] J. C. Lin, M. Y. Andino, M. G. Alexander, E. A. Whalen, M. A. Spoor, J. T. Tran, and I. J. Wygnanski, "An Overview of Active Flow Control Enhanced Vertical Tail Technology Development." 54th AIAA Aerospace Sciences Meeting, 2016.

[20] T. Murugan, M. Deyashi, S. Dey, S. C. Rana, and P. Chatterjee, "Recent Developments on Synthetic Jets," *Defence Science Journal*, vol. 66, no. 5, pp. 489–498, 2016.

[21] V. Modi, "Moving Surface Boundary-layer Control: a Review," *Journal of Fluids and Structures*, vol. 11, no. 6, pp. 627–663, 1997.

[22] G. S. Jones, J. C. Lin, B. G. Allan, W. E. Milholen, C. L. Rumsey, and R. Swanson, "Overview of CFD Validation Experiments for Circulation Control Applications at NASA." 2008 International Powered Lift Conference, 2008.

[23] R. J. Englar, "Overview of Circulation Control Pneumatic Aerodynamics: Blown Force and Moment Augmentation and Modification As Applied Primarily to Fixed-wing Aircraft." Proceedings of the 2004 NASA/ONR Circulation Control Workshop, NASA CP-2005-213509, 2005.

[24] R. ENGLAR, G. JONES, B. Allan, and J. Lin, "2-d Circulation Control Airfoil Benchmark Experiments Intended for ." 47th AIAA Aerospace sciences meeting including the new horizons forum and aerospace exposition, 2009.

[25] G. S. Jones and R. J. Englar, "Advances in Pneumatic-controlled High-lift Systems Through Pulsed Blowing." 21st Applied Aerodynamics Conference, 2003.

[26] W. E. Milholen, G. S. Jones, D. T. Chan, S. L. Goodliff, S. G. Anders, L. Melton, M. Allan, and F. Capone, "Enhancements to the ." 31st AIAA Applied Aerodynamics Conference, 2013.

[27] W. Milholen, G. Jones, D. Chan, and S. L. Goodliff, "High-reynolds Number Circulation Control Testing in the National Transonic Facility." 50TH AIAA AEROSPACE sciences meeting including the new horizons forum and aerospace exposition, 2012.

[28] W. E. Milholen, S. L. Goodliff, D. T. Chan, and G. S. Jones, "Transonic Drag Reduction Through Trailing-edge Blowing on the Fast-mac Circulation Control Model." 35th AIAA Applied Aerodynamics Conference, 2017.

[29] R. Radespiel and M. Burnazzi, "Fundamentals in Coanda Flap Design." Active Flow and Combustion Control 2014, 2015.

[30] M. Jahanmiri, "Aircraft Drag Reduction: an Overview," tech. rep., Chalmers University of Technology, 2011.

[31] A. F. S. Board, N. R. Council, *et al.*, *Assessment of wingtip modifications to increase the fuel efficiency of air force aircraft*. National Academies Press, 2007.

[32] P. Tokumaru and P. Dimotakis, "The Lift of a Cylinder Executing Rotary Motions in a Uniform Flow," *Journal of Fluid Mechanics*, vol. 255, pp. 1–10, 1993.

[33] V. E. Lockwood, "Lift Generation on a Circular Cylinder by Tangential Blowing from Surface Slots." NASA Technical Report, 1960.

[34] J. Seifert, "A Review of the Magnus Effect in Aeronautics," *Progress in Aerospace Sciences*, vol. 55, pp. 17–45, 2012.

[35] Lefebvre, A. and Zha, G.-C. , "Design of High Wing Loading Compact Electric Airplane Utilizing Co-flow Jet Flow Control." 53rd AIAA Aerospace Sciences Meeting, AIAA SciTech Forum, (AIAA 2015-0772), 2015.

[36] M. Hepperle, "Electric Flight - Potential and Limitations." AVT-209 Workshop on Energy Efficient Technologies and Concept Operation, 2224 October 2012, Lisbon, Portugal, 2012.

[37] A. aircraft, "ATR Family Booklet," 2014.

[38] C. Gologan, C. Kelders, A. Kuhlmann, and J. Seifert, "Extreme Short Take-off and Landing Regional Jets-economic Motivation and Technological Challenges," *The Aeronautical Journal*, vol. 113, no. 1147, pp. 563–574, 2009.

[39] G. J. Couluris, D. Signor, and J. Phillips, "Cruise-efficient Short Takeoff and Landing (CESTOL): Potential Impact on Air Traffic Operations." NASA Technical Report, NASA/CR-2010-216392, 2010.

[40] pwc and T. M. Institute, "Aviation's Second Golden Age: can the Us Aircraft Industry Maintain Leadership?." Tech Report, 2013. accessed 12/27/2017.

[41] M. A. Naqvi, *Prediction of Circulation Control Performance Characteristics for Super Stol and Stol Applications*. PhD thesis, Georgia Institute of Technology, 2006.

[42] NASA, "The NASA Aeronautics Blueprint - Toward a Bold New Era of Aviation." NASA Technical Report, 2002. accessed 12/27/2017.

[43] I. Sellers, William L., B. A. Singer, and L. D. Leavitt, "Aerodynamics for Revolutionary Air Vehicles," *21st Applied Aerodynamics Conference*, 2004.

[44] B. A. Seeley, "The Cafe Green Flight Challenge Program (cgfcp)." 51st AIAA Aerospace Sciences Meeting including the New Horizons Forum and Aerospace Exposition, 2012.

[45] S. W. Ashcraft, A. S. Padron, K. A. Pascioni, G. W. Stout Jr, and D. L. Huff, "Review of Propulsion Technologies for N+3 Subsonic Vehicle Concepts." NASA Technical Report, 2011.

[46] J. L. Felder, H. D. Kim, and G. V. Brown, "Turboelectric Distributed Propulsion Engine Cycle Analysis for Hybrid-wing-body Aircraft." 47th AIAA Aerospace Sciences Meeting, 2009.

[47] A. M. O. Smith and H. Roberts, "The Jet Airplane Utilizing Boundary Layer Air for Propulsion," *Journal of the Aeronautical Sciences*, vol. 14, pp. 97–109, 1947.

[48] R. T. Kawai, D. M. Friedman, and L. Serrano, "Blended Wing Body (bwb) Boundary Layer Ingestion (bli) Inlet Configuration and System Studies." NASA Technical Report, NASA/CR-2006-214534, 2006.

[49] E. Greitzer, "Subsonic Civil Transport Aircraft for a 2035 Time Frame." Oral presentation at University of Miami, 2012. accessed 12/27/2017.

[50] H. D. Kim, "Distributed Propulsion Vehicles." 27th International Congress of the Aeronautical Sciences, 2010.

[51] J. L. Felder, G. V. Brown, H. DaeKim, and J. Chu, "Turboelectric Distributed Propulsion in a Hybrid Wing Body Aircraft." 20th International Society for Airbreathing Engines (ISABE 2011), 2011.

[52] J. Zuk and D. A. Wardwell, "Summary of Nasa's Extreme Short Take-off and Landing (ESTOL) Vehicle Sector Activities," *SAE transactions*, vol. 114, no. 1, pp. 674–687, 2005.

[53] Spalart, P.R., Jou, W.H., Strelets, M., and Allmaras, S.R., "Comments on the Feasibility of Les for Wings, and on a Hybrid Rans/les Approach." Advances in DNS/LES, 1st AFOSR Int. Conf. on DNS/LES, Greyden Press, Columbus, H., Aug. 4-8, 1997.

[54] Spalart, P.R., Deck, S., Shur, M., and Squires, K.D., "A New Version of Detached-eddy Simulation, Resistant to Ambiguous Grid Densities," *Theoritical and Computational Fluid Dynamics*, vol. 20, pp. 181–195, DOI: 10.1007/s00162–006–0015–0, 2006.

[55] Travin, A.K., Shur, M.L., Spalart, P.R., and Strelets, M.K., "Improvement of Delayed Detached Eddy Simulation for Les With Wall Modelling." European Conference on Computational Fluid Dynamics, ECCOMAS CFD 2006, 2006.

[56] M. L. Shur, P. R. Spalart, M. K. Strelets, and A. K. Travin, "A Hybrid Rans-les Approach With Delayed-des and Wall-modelled Les Capabilities," *International Journal of Heat and Fluid Flow*, vol. 29, no. 6, pp. 1638–1649, 2008.

[57] C. Mockett, *A Comprehensive Study of Detached Eddy Simulation*. Univerlag-tuberlin, 2009.

[58] Morton, S.A., Forsythe, J.R., Squires, K.D., Cummings, R.M., "Detached-eddy Simulations of Full Aircraft Experiencing Massively Separated Flows." The 5th Asian Computational Fluid Dynamics Conference, Busan, Korea, 2003.

[59] N. Durrani and N. Qin, "Behavior of Detached-eddy Simulations for Mild Airfoil Trailing-edge Separation," *Journal of Aircraft*, vol. 48, no. 1, pp. 193–202, 2011.

[60] H.-S. Im and G.-C. Zha, "Delayed Detached Eddy Simulation of Airfoil Stall Flows Using High-order Schemes," *Journal of Fluids Engineering*, vol. 136, no. 11, p. 111104, 2014.

[61] G.-C. Zha and D. C. Paxton, "A Novel Flow Control Method for Airfoil Performance Enhancement Using Co-flow Jet." *Applications of Circulation Control Technologies*, Chapter 10, p. 293-314, Vol. 214, Progress in Astronautics and Aeronautics, AIAA Book Series, Editors: Joslin, R. D. and Jones, G.S., 2006.

[62] G.-C. Zha, W. Gao, and C. Paxton, "Jet Effects on Co-flow Jet Airfoil Performance," *AIAA Journal, No. 6,*, vol. 45, pp. 1222–1231, 2007.

[63] G.-C. Zha, C. Paxton, A. Conley, A. Wells, and B. Carroll, "Effect of Injection Slot Size on High Performance Co-flow Jet Airfoil," *AIAA Journal of Aircraft*, vol. 43, 2006.

[64] G.-C. Zha, B. Carroll, C. Paxton, A. Conley, and A. Wells, "High Performance Airfoil With Co-flow Jet Flow Control," *AIAA Journal*, vol. 45, pp. 2087–2090, 2007.

[65] Wang, B.-Y. and Haddoukessouni, B. and Levy, J. and Zha, G.-C., "Numerical Investigations of Injection Slot Size Effect on the Performance of Co-flow Jet Airfoil ," *AIAA Journal of Aircraft*, vol. 45, pp. 2084–2091, 2008.

[66] B. P. E. Dano, D. Kirk, and G.-C. Zha, "Experimental Investigation of Jet Mixing Mechanism of Co- Flow Jet Airfoil." AIAA-2010-4421, 5th AIAA Flow Control Conference, Chicago, IL, 28 Jun - 1 Jul 2010.

[67] B. P. E. Dano, G.-C. Zha, and M. Castillo, "Experimental Study of Co-flow Jet Airfoil Performance Enhancement Using Micro Discreet Jets." 49th AIAA Aerospace Sciences Meeting, AIAA-2011-0941, 2011.

[68] Lefebvre, A. and Dano, B. and Bartow, W. and Di Franzo, M. and Zha, G.-C., "Performance Enhancement and Energy Expenditure of Co-flow Jet Airfoil With Variation of Mach Number," *Journal of Aircraft*, no. 6, pp. 1757–1767, 2016.

[69] Liu, Z.-X. and Zha, G.-C., "Transonic Airfoil Performance Enhancement Using Co-flow Jet Active Flow Control." AIAA Paper 2016-3066, AIAA Aviation, 2016.

[70] Lefebvre, A. and Zha, G.-C., "Trade Study of 3d Co-flow Jet Wing for Cruise Performance." 54th AIAA Aerospace Sciences Meeting, AIAA SciTech Forum, (AIAA 2016-0570), 2016.

[71] J. Wimpress, "Aerodynamic Technology Applied to Takeoff and Landing," *Annals of the New York Academy of Sciences*, vol. 154, no. 1, pp. 962–981, 1968.

[72] R. H. Liebeck, "Design of Subsonic Airfoils for High Lift," *Journal of Aircraft*, vol. 15, no. 9, pp. 547–561, 1978.

[73] D. Florjancic, "Improved Design of a High Lift System for General Aviation Aircraft." Master Thesis, TU Delft, 2015.

[74] M. Gad-el Hak, "Modern Developments in Flow Control," *Applied Mechanics Reviews*, vol. 49, pp. 365–380, 1996.

[75] D. R. Williams and D. G. MacMynowski, *Fundamentals and Applications of Modern Flow Control, Progress in Astronautics and Aeronautics*. edited by Joslin, Ronald D and Miller, Daniel N and Lu, Frank K, American Institute of Aeronautics and Astronautics, 2009.

[76] L. D. Kral, "Active Flow Control Technology," *ASME FED, Technical Brief*, pp. 1–28, 2000.

[77] S. S. Collis, R. D. Joslin, A. Seifert, and V. Theofilis, "Issues in Active Flow Control: Theory, Control, Simulation, and Experiment," *Progress in Aerospace Sciences*, vol. 40, no. 4, pp. 237–289, 2004.

[78] A. Betz, *History of Boundary Layer Control in Germany*. Aerodynamische Versuchsanstalt, 1961.

[79] A. Seifert, A. Darabi, and I. Wyganski, "Delay of Airfoil Stall by Periodic Excitation," *Journal of aircraft*, vol. 33, no. 4, pp. 691–698, 1996.

[80] A. Seifert and L. Pack, "Oscillatory Control of Separation at High Reynolds Numbers," *AIAA journal*, vol. 37, no. 9, 1999.

[81] A. Seifert, T. Bachar, D. Koss, M. Shepshelovich, and I. Wygnanski, "Oscillatory Blowing: a Tool to Delay Boundary-layer Separation," *AIAA journal*, vol. 31, no. 11, pp. 2052–2060, 1993.

[82] D. Greenblatt, B. Nishri, A. Darabi, and I. Wygnanski, "Some Factors Affecting Stall Control With Particular Emphasis on Dynamic Stall." 30th Fluid Dynamics Conference, 1999.

[83] R. Seele, E. Graff, M. Gharib, L. Taubert, J. Lin, and I. Wygnanski, "Improving Rudder Effectiveness With Sweeping Jet Actuators." 6th AIAA Flow Control Conference, 2012.

[84] R. Seele, E. Graff, J. Lin, and I. Wygnanski, "Performance Enhancement of a Vertical Tail Model With Sweeping Jet Actuators." 51st AIAA Aerospace Sciences Meeting including the New Horizons Forum and Aerospace Exposition, AIAA 2013-0411, 2013.

[85] E. Graff, R. Seele, J. C. Lin, and I. Wygnanski, "Sweeping Jet Actuators-a New Design Tool for High Lift Generation." Innovative Control Effectors for Military Vehicles (AVT-215), 2013.

[86] M. Y. Andino, J. C. Lin, A. E. Washburn, E. A. Whalen, E. C. Graff, and I. J. Wygnanski, "Flow Separation Control on a Full-scale Vertical Tail Model Using Sweeping Jet Actuators." 53rd AIAA Aerospace Sciences Meeting, AIAA SciTech Forum, (AIAA 2015-0785), 2015.

[87] A. Glezer and M. Amitay, "Synthetic Jets," *Annual review of fluid mechanics*, vol. 34, no. 1, pp. 503–529, 2002.

[88] K. Mohseni and R. Mittal, *Synthetic Jets: Fundamentals and Applications*. CRC Press, 2014.

[89] B. L. Smith and A. Glezer, "The Formation and Evolution of Synthetic Jets," *Physics of fluids*, vol. 10, no. 9, pp. 2281–2297, 1998.

[90] R. Rathnasingham and K. S. Breuer, "Active Control of Turbulent Boundary Layers," *Journal of Fluid Mechanics*, vol. 495, pp. 209–233, 2003.

[91] M. Amitay and A. Glezer, "Aerodynamic Flow Control Using Synthetic Jet Actuators," *Control of Fluid Flow*, pp. 45–73, 2006.

[92] J. Kweder, C. C. Panther, and J. E. Smith, "Applications of Circulation Control, Yesterday and Today," *International Journal of Engineering*, vol. 4, no. 5, pp. 411–429, 2010.

[93] G. S. Jones, S. A. Viken, A. E. Washburn, L. N. Jenkins, and C. M. Cagle, "An Active Flow Circulation Controlled Flap Concept for General Aviation Aircraft Applications." 1st Flow Control Conference, Fluid Dynamics and Co-located Conferences, 2002.

[94] R. D. Joslin, "Aircraft Laminar Flow Control," *Annual review of fluid mechanics*, vol. 30, no. 1, pp. 1–29, 1998.

[95] D. Bushnell, "Aircraft Drag Reduction-a Review," *Proceedings of the Institution of Mechanical Engineers, Part G: Journal of Aerospace Engineering*, vol. 217, no. 1, pp. 1–18, 2003.

[96] J. C. Lin, "Review of Research on Low-profile Vortex Generators to Control Boundary-layer Separation," *Progress in Aerospace Sciences*, vol. 38, no. 4, pp. 389–420, 2002.

[97] S. L. Brunton and B. R. Noack, "Closed-loop Turbulence Control: Progress and Challenges," *Applied Mechanics Reviews*, vol. 67, no. 5, p. 050801, 2015.

[98] H. Choi, P. Moin, and J. Kim, "Active Turbulence Control for Drag Reduction in Wall-bounded Flows," *Journal of Fluid Mechanics*, vol. 262, pp. 75–110, 1994.

[99] K.-S. Choi, J.-R. Debisschop, and B. R. Clayton, "Turbulent Boundary-layer Control by Means of Spanwise-wall Oscillation," *AIAA journal*, vol. 36, no. 7, pp. 1157–1163, 1998.

[100] D. Knight, G. Zhou, N. Okong'o, and V. Shukla, "Compressible Large Eddy Simulation Using Unstructured Grids." AIAA Paper 98-0535, 1998.

[101] P. R. Spalart and S. R. Allmaras, "A One-equation Turbulence Model for Aerodynamic Flows." 30th Aerospace Sciences Meeting and Exhibit, Aerospace Sciences Meetings, AIAA Paper 92-0439, 1992.

[102] Zha, G.C., Shen, Y.Q. and Wang, B.Y., "An Improved Low Diffusion E-cusp Upwind Scheme ," *Journal of Computer and Fluids*, vol. 48, pp. 214–220, Sep. 2011.

[103] Shen, Y.Q., and Zha, G.C., "Improvement of the WENO Scheme Smoothness Estimator," *International Journal for Numerical Methods in Fluids*, vol. 64, pp. 653–675, 2009.

[104] Shen, Y.Q., Zha, G.C., and Wang, B.Y., "Improvement of Stability and Accuracy of Implicit WENO Scheme," *AIAA Journal*, vol. 47, pp. 331–334, 2009.

[105] Shen, Y.Q., and Zha, G.C., "Large Eddy Simulation Using a New Set of Sixth Order Schemes for Compressible Viscous Terms," *Journal of Computational Physics*, vol. 229, pp. 8296–8312, 2010.

[106] Shen, Y.Q., Zha, G.C., and Chen, X., "High Order Conservative Differencing for Viscous Terms and the Application to Vortex-induced Vibration Flows," *Journal of Computational Physics*, vol. 228(2), pp. 8283–8300, doi:10.1016/j.jcp.2009.08.004, 2009.

[107] G. C. Zha, D. Smith, M. Schwabacher, K. Rasheed, A. Gelsey, and D. Knight, "High Performance Supersonic Missile Inlet Design Using Automated Optimization." AIAA Paper 96-4142, 1996.

[108] Y.Q. Shen, B. Wang, and G.C. Zha, "Comparison Study of Implicit Gauss-seidel Line Iteration Method for Transonic Flows." AIAA Paper 2007-4332, 2007.

[109] B. Van Leer, "Flux Vector Splitting for the Euler Equations," *Eighth International Conference on Numerical Methods in Fluid Dynamics: Lecture Notes in Physics*, vol. 170, pp. 507–512, 1982.

[110] J. L Steger, and R.F Warming, "Flux Vector Splitting of the Inviscid Gasdynamic Equations With Application to Finite Difference Methods," *Journal of Computational Physics*, vol. 40, pp. 263–293, 1981.

[111] Edwards, J.R., "A Low-diffusion Flux-splitting Scheme for Navier-stokes Calculations," *Computer & Fluids*, vol. 6, pp. 635–659, 1997.

[112] Zha, G.C., Shen, Y.Q., and Wang, B.Y., "Calculation of Transonic Flows Using WENO Method With a Low Diffusion E-cusp Upwind Scheme." 46th AIAA Aerospace Sciences Meeting, AIAA Paper 2008-0745, 2008.

[113] Roe, P., "Approximate Riemann Solvers, Parameter Vectors, and Difference Schemes," *Journal of Computational Physics*, vol. 43, pp. 357–372, 1981.

[114] S. De Rango, and D. W. Zingg, "Aerodynamic Computations Using a Higher Order Algorithm." AIAA Paper 99-0167, 1999.

[115] D. W. Zingg, S. De Rango, M. Nemec, T. H. Pulliam, "Comparison of Several Spatial Discretizations for the Navier-stokes Equations," *Journal of Computational Physics*, vol. 160, pp. 683–704, 2000.

[116] Jameson, A., "Time Dependent Calculations Using Multigrid With Applications to Unsteady Flows Past Airfoils and Wings." AIAA Paper 91-1596, 1991.

[117] J. Alonso, L. Martinelli, and A. Jameson, "Multigrid Unsteady Navier-stokes Calculations With Aeroelastic Applications." AIAA Paper 95-0048, 1995.

[118] Shen, Y.Q., Wang, B.Y., and Zha, G.C., "Implicit WENO Scheme and High Order Viscous Formulas for Compressible Flows ." AIAA Paper 2007-4431, 2007.

[119] J. A. Ekaterinaris and M. F. Platzer, "Computational Prediction of Airfoil Dynamic Stall," *Progress in Aerospace Sciences*, vol. 33, no. 11, pp. 759–846, 1998.

[120] N. Nikitin, F. Nicoud, B. Wasistho, K. Squires, and P. Spalart, "An Approach to Wall Modeling in Large-eddy Simulations," *Physics of Fluids*, vol. 12, no. 7, pp. 1629–1632, 2000.

[121] V. Kolář, "Vortex Identification: New Requirements and Limitations," *International Journal of Heat and Fluid Flow*, vol. 28, no. 4, pp. 638–652, 2007.

[122] Hoerner, S.F., "Fluid-dynamic Drag." Hoerner Fluid Dynamics (June 25, 1993), 1965.

[123] Shur, M.L., Spalart, P.R., Strelets, M., and Travin, A., "Detached-eddy Simulation of an Airfoil at High Angle of Attack." 4th Int. Symp. Eng. Turb. Modelling and Measurements, Corsica, 1999.

[124] Jogansen, J. and Sorensen, N., "Application of a Detached Eddy Simulation Model on Airfoil Flows." IEA 2000, 2000.

[125] G. J. Couluris, C. Hange, D. Wardwell, D. Signor, and J. Phillips, "A Potential Impact Analysis of ESTOL Aircraft on Newark Airport Operations." AIAA Modeling and Simulation Technologies Conference and Exhibit, Guidance, Navigation, and Control and Co-located Conferences, 2007.

[126] Y. J and H. D., "Executive Summary of Calpoly/nasa Extreme Short Takeoff and Landing (ESTOL) Work." SAE International Powered Lift Conference, Warrendale, 2005.

[127] Rudolph, P. K. C., "High-lift Systems on Commercial Subsonic Airliners." NASA Contractor Report 4746, 1996.

[128] T. O. G. Prandtl, Ludwig, *Applied Hydro- and Aeromechanics*. Dover Publications, 1934.

[129] S. Mittal and B. Kumar, "Flow Past a Rotating Cylinder," *Journal of Fluid Mechanics*, vol. 476, pp. 303–334, 2003.

[130] R. J. Englar, "Overview of Circulation Control Pneumatic Aerodynamics: Blown Force and Moment Augmentation and Modification As Applied Primarily to Fixed-wing Aircraft," *Proceedings of the 2004 NASA/ONR Circulation Control Workshop, NASA CP-2005-213509*, pp. 23–66, 2006.

[131] R. J. Englar, "Circulation Control Pneumatic Aerodynamics: Blown Force and Moment Augmentation and Modifications; Past, Present and Future." AIAA 2000-2541, 2000.

[132] G. S. Jones, "Pneumatic Flap Performance for a 2D Circulation Control Airfoil, Steady & Pulsed." Applications of Circulation Control Technologies, Progress in Astronautics and Aeronautics, AIAA Book Series, 2006.

[133] Greitzer, E. M. and Slater, H. N., "N+3 Aircraft Concept Designs and Trade Studies, Final Report." NASA Technical Report, 2010.

[134] Hileman, J.I. and Spakovszky, Z.S. and Drela, M. and Sargeant, M.A., "Airframe Design for 'silent Aircraft'." AIAA Paper 2007-453, 45th AIAA Aerospace Sciences Meeting, Reno, NV, Jan 2007.

[135] Y.-Q. Shen and G.-C. Zha, "Large Eddy Simulation Using a New Set of Sixth Order Schemes for Compressible Viscous Terms ," *Journal of Computational Physics*, vol. 229, pp. 8296–8312, 2010.

[136] Y.-Q. Shen and G.-Z. Zha , "Generalized Finite Compact Difference Scheme for Shock/complex Flowfield Interaction," *Journal of Computational Physics*, vol. 230, pp. 4419–4436, 2011.

[137] Shen, Y.-Q. and Zha, G.-C. and Wang, B.-Y., " Improvement of Stability and Accuracy of Implicit WENO Scheme," *AIAA Journal*, vol. 47, No. 2, pp. 331–344, 2009.

[138] Shen, Y.-Q. and Zha, G.-C. and Chen, X.-Y., " High Order Conservative Differencing for Viscous Terms and the Application to Vortex-induced Vibration Flows," *Journal of Computational Physics*, vol. 228(2), pp. 8283–8300, 2009.

[139] Shen, Y.Q., and Zha, G.C., "Improvement of the WENO Scheme Smoothness Estimator," *International Journal for Numerical Methods in Fluids*, vol. 64, pp. 653–675, 2009.

[140] G.-C. Zha and E. Bilgen, "Numerical Study of Three-dimensional Transonic Flows Using Unfactored Upwind-relaxation Sweeping Algorithm," *Journal of Computational Physics*, vol. 125, pp. 425–433, 1996.

[141] B.-Y. Wang and G.-C. Zha, "A General Sub-domain Boundary Mapping Procedure for Structured Grid CFD Parallel Computation," *AIAA Journal of Aerospace Computing, Information, and Communication*, vol. 5, No.11, pp. 2084–2091, 2008.

[142] Wang, B. Y and Zha, G.-C. , "Detached-eddy Simulation of a Co-flow Jet Airfoil at High Angle of Attack." AIAA Paper 2009-4015, 2011.

[143] Im, H.-S. and Zha, G.-C. and Dano, B. P. E., "Large Eddy Simulation of Coflow Jet Airfoil at High Angle of Attack," *Journal of Fluid Engineering*, 2014.

[144] Y.-Q. Shen, G.-C. Zha, and B.-Y. Wang, "Improvement of Stability and Accuracy of Implicit WENO Scheme ," *AIAA Journal*, vol. 47, pp. 331–344, 2009.

[145] A. M. Lefebvre, *Investigation of Co-flow Jet Flow Control and Its Applications*. PhD thesis, University of Miami, Coral Gables, Florida, 2015.

[146] Y. Yang and G. Zha, "Simulation of Airfoil Stall Flows Using IDDES With High Order Schemes." 46th AIAA Fluid Dynamics Conference, AIAA Paper, 2016-3185, 2016.

[147] Y. Yang and G. Zha, "Super-lift Coefficient of Active Flow Control Airfoil: What Is the Limit?." 55th AIAA Aerospace Science Meeting, AIAA Paper 2017-1693, 2017.

[148] J. Jeong and F. Hussain, "On the Identification of a Vortex," *Journal of Fluid Mechanics*, vol. 285, pp. 69–94, 1995.

[149] E. N. Jacobs and R. M. Pinkerton, "Tests of NACA Airfoils in the Variable-density Wind Tunnel Series 44 and 64." NASA Technical Note, no. 392, 1931.

[150] S. Kumar, C. Cantu, and B. Gonzalez, "Flow Past a Rating Cylinder at Low and High Rotation Rates," *Journal of Fluids Engineering*, vol. 133, no. 4, p. 041201, 2011.

[151] S. Karabelas, B. Koumroglou, C. Argyropoulos, and N. Markatos, "High Reynolds Number Turbulent Flow Past a Rotating Cylinder," *Applied Mathematical Modelling*, vol. 36, no. 1, pp. 379–398, 2012.

[152] J. D. Brooks, "The Effect of a Rotating Cylinder at the Leading and Trailing Edges of a Hydrofoil," tech. rep., Naval Ordnance Test Station (China Lake, Calif.), 1963.

[153] A. Alvarez-Calderon, "High Lift and Control System for Aircraft," July 7 1964. US Patent 3,140,065.

[154] Y. Zhuang, X. Sun, D. Huang, and G. Wu, "Numerical Study on Aerodynamic Performances of the Wind Turbine Rotor With Leading-edge Rotation," *Journal of Renewable and Sustainable Energy*, vol. 4, no. 6, p. 063103, 2012.

[155] PCA engineers, "Design of a Mixed Flow Fan." Internal Report to University of Miami, 2017.

[156] Celeroton, "Design of a Mixed Flow Fan Prototype." Internal Report to University of Miami, 2017.

[157] J. Hoelzen, Y. Liu, B. Bensmann, C. Winnefeld, A. Elham, J. Friedrichs, and R. Hanke-Rauschenbach, "Conceptual Design of Operation Strategies for Hybrid Electric Aircraft," *Energies*, vol. 11, no. 1, p. 217, 2018.

[158] H. Kim, H.-D. Lim, J. Kim, and K. Kang, "Graphene for Advanced Li/s and Li/air Batteries," *Journal of Materials Chemistry A*, vol. 2, no. 1, pp. 33–47, 2014.

[159] S. Stückl, J. van Toor, and H. Lobentanzer, "Voltair–the All Electric Propulsion Concept Platform–a Vision for Atmospheric Friendly Flight." 28th International Congress of the Aeronautical Sciences (ICAS), 2012.